



National Library
of Canada

Acquisitions and
Bibliographic Services Branch

395 Wellington Street
Ottawa, Ontario
K1A 0N4

Bibliothèque nationale
du Canada

Direction des acquisitions et
des services bibliographiques

395, rue Wellington
Ottawa (Ontario)
K1A 0N4

Your file - Votre référence

Our file - Notre référence

NOTICE

The quality of this microform is heavily dependent upon the quality of the original thesis submitted for microfilming. Every effort has been made to ensure the highest quality of reproduction possible.

If pages are missing, contact the university which granted the degree.

Some pages may have indistinct print especially if the original pages were typed with a poor typewriter ribbon or if the university sent us an interior photocopy.

Reproduction in full or in part of this microform is governed by the Canadian Copyright Act, R.S.C. 1970, c. C-30, and subsequent amendments.

AVIS

La qualité de cette microforme dépend grandement de la qualité de la thèse soumise au microfilmage. Nous avons tout fait pour assurer une qualité supérieure de reproduction.

S'il manque des pages, veuillez communiquer avec l'université qui a conféré le grade.

La qualité d'impression de certaines pages peut laisser à désirer, surtout si les pages originales ont été dactylographiées à l'aide d'un ruban usé ou si l'université nous a fait parvenir une photocopie de qualité inférieure.

La reproduction, même partielle, de cette microforme est soumise à la Loi canadienne sur le droit d'auteur, SRC 1970, c. C-30, et ses amendements subséquents.

Canada

University of Alberta

Transport Phenomena in Stable Linear Laminar Rivulet Flows

by

Paul A. Nawrocki



A thesis
submitted to the Faculty of Graduate Studies and Research
in partial fulfillment of the requirements for the degree of

Doctor of Philosophy

Department of Chemical Engineering

Edmonton, Alberta

Spring 1993



National Library
of Canada

Acquisitions and
Bibliographic Services Branch

395 Wellington Street
Ottawa, Ontario
K1A 0N4

Bibliothèque nationale
du Canada

Direction des acquisitions et
des services bibliographiques

395, rue Wellington
Ottawa (Ontario)
K1A 0N4

Your file *Votre référence*

Our file *Notre référence*

The author has granted an irrevocable non-exclusive licence allowing the National Library of Canada to reproduce, loan, distribute or sell copies of his/her thesis by any means and in any form or format, making this thesis available to interested persons.

L'auteur a accordé une licence irrévocable et non exclusive permettant à la Bibliothèque nationale du Canada de reproduire, prêter, distribuer ou vendre des copies de sa thèse de quelque manière et sous quelque forme que ce soit pour mettre des exemplaires de cette thèse à la disposition des personnes intéressées.

The author retains ownership of the copyright in his/her thesis. Neither the thesis nor substantial extracts from it may be printed or otherwise reproduced without his/her permission.

L'auteur conserve la propriété du droit d'auteur qui protège sa thèse. Ni la thèse ni des extraits substantiels de celle-ci ne doivent être imprimés ou autrement reproduits sans son autorisation.

ISBN 0-315-81989-8

Canada

K.T. Chuang
Department of Chemical Engineering
Rm. 536 Chemical-Mineral Bldg.
University of Alberta
Edmonton, AB
T6G 2G5

January 9, 1993

Graduate Studies & Research
University Hall
University of Alberta
Edmonton, AB

To whom it may concern:

I hereby grant permission to **Paul A. Nawrocki** to use the information contained in the paper **Mass Transfer in Structured Corrugated Packing**, published in the **Canadian Journal of Chemical Engineering** **1991, 69(12):1336-1343**, in his thesis entitled **Transport Phenomena in Stable Linear Laminar Rivulet Flows**.

Sincerely yours,

A handwritten signature in cursive script, appearing to read 'K.T. Chuang'.

K.T. Chuang

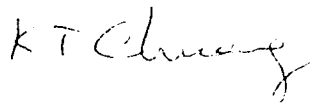
Department of Chemical Engineering
Room 536 Chemical-Mineral Building
University of Alberta
Edmonton, AB T6G 2G6
1993 02 08

Faculty of Graduate Studies & Research
University Hall
University of Alberta
Edmonton, AB

To whom it may concern:

I hereby grant permission to **Paul A. Nawrocki** to use the information contained in the paper **Hysteresis in Stable Rivulet Flows**, submitted to the **Canadian Journal of Chemical Engineering**, in his thesis entitled **Transport Phenomena in Stable Linear Laminar Rivulet Flows**.

Sincerely yours,

A handwritten signature in cursive script, appearing to read 'K.T. Chuang'.

K.T. Chuang

Z.P. Xu
Department of Chemical Engineering
Rm. 536 Chemical-Mineral Bldg.
University of Alberta
Edmonton, AB
T6G 2G5

January 9, 1993

Graduate Studies & Research
University Hall
University of Alberta
Edmonton, AB

To whom it may concern:

I hereby grant permission to **Paul A. Nawrocki** to use the information contained in the paper **Mass Transfer in Structured Corrugated Packing**, published in the **Canadian Journal of Chemical Engineering** **1991, 69(12):1336-1343**, in his thesis entitled **Transport Phenomena in Stable Linear Laminar Rivulet Flows**.

Sincerely yours,


Z.P. Xu

University of Alberta

Release Form

Name of Author:

Paul A. Nawrocki

Title of Thesis:

Transport Phenomena in Stable Linear
Laminar Rivulet Flows

Degree:

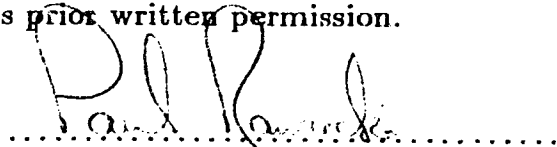
Doctor of Philosophy

Year this degree granted:

Spring 1993

Permission is hereby granted to the University of Alberta Library to reproduce single copies of this thesis and to lend or sell such copies for private, scholarly or scientific research purposes only.

The author reserves all other publication and other rights in association with the copyright in the thesis, and except as hereinbefore provided neither the thesis nor any substantial portion thereof may be printed or otherwise reproduced in any material form whatever without the author's prior written permission.



(Student's signature)

Paul A. Nawrocki

79 Hudson Drive

Regina, Saskatchewan

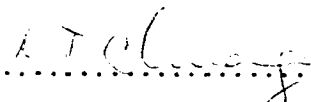
Canada

S4S 2W1

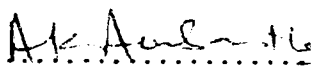
Date : 1993 03 03

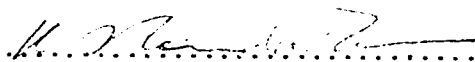
University of Alberta
Faculty of Graduate Studies and Research

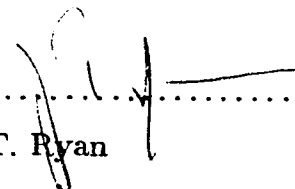
The undersigned certify that they have read, and recommend to the Faculty of Graduate Studies and Research for acceptance, a thesis entitled **Transport Phenomena in Stable Linear Laminar Rivulet Flows** submitted by **Paul A. Nawrocki** in partial fulfillment of the requirements for the degree of **Doctor of Philosophy**.


.....
K.T. Chuang (Supervisor)


.....
R.G. Moore (University of Calgary)


.....
A.K. Ambastha


.....
K. Nandakumar


.....
J.T. Ryan

Date : 1995 03 03

To My Grandfather
Who Taught Me To Value My Education
And To My Wife
Who Taught Me How To Live With It

Abstract

The wetting of the flow surfaces in heat exchangers, trickle-bed reactors and columns containing structured packing has been shown to be discrete in nature involving rivulets. For this reason, simple film models are inadequate in describing processes occurring in these types of operations. Detailed, fundamental modelling of the rivulet flow structure and transport processes occurring in these flows is, therefore, required in order to provide a basis from which more complex models can be built describing the overall processes occurring in the particular application of interest. To demonstrate the applicability of detailed rivulet modelling, theoretical analysis of the velocity and mass transfer characteristics in rivulet flows in both an inclined, flat plate absorber and in columns containing structured, corrugated packing has been performed. These theoretical results are compared with experimental data.

To study the performance of a column containing structured, corrugated packing, mechanistic models are established for liquid distribution, liquid flow on the packing surface and mass transfer. These models are used to investigate the effect of packing height, liquid load, initial maldistribution as well as differing initial distribution and liquid–solid contact angle on the packed column performance. Wetted area is the primary value of interest and the simulated results compare very well with those predicted by Onda [109]. The results clearly demonstrate that the wetted

surface area is a strong function of the liquid–solid contact angle. Other predicted values such as the mass transfer coefficient and overall height of a transfer unit show reasonable agreement with published data.

In the inclined, flat plate absorber, theoretical work on the structure of and absorption in rivulet flows is performed by combining the Laplace equation for curved interfaces with the Navier-Stokes and convection-diffusion equation. For the flow structure analysis, the theoretically predicted values of rivulet width and height are compared with experimental data for the stainless steel–water system and it is found that the combination of the Laplace and Navier-Stokes equations accurately predicts the dimensions of a flowing rivulet on an inclined flat plate. The comparison of the theoretical and experimental absorption results indicate enhanced absorption in the experimental data due, possibly, to a secondary flow cell in the rivulet.

The results of this study show that detailed, theoretical modelling of rivulet flows is a suitable approach in the analysis of gas absorption in columns utilizing structured packing. Further, this type of work must be pursued to determine its applicability in other applications such as trickle-bed reactors and heat exchangers. The results also demonstrate that, although the rivulet dimensions of width and height are well characterized by the theoretical relationships developed in this work, the mass transfer process is more complex than that described by the two-dimensional diffusion, one-dimensional convection equation used in this analysis.

Acknowledgments

My parents deserve a big thank you for supporting me throughout my life and during my years at university. You taught me to value that which I have and not to take for granted the gifts which God has bestowed upon me. I particularly appreciate your words of encouragement during my first semester of university when I could have easily packed it in and gone home. Without you I may not have finished my first year of university.

My brother also deserve a big thank you. I was fortunate enough to be able to live with both of you after we left home and got to know you as you really are. I could not have asked for two better people to have as my brothers and I hope you realize that you are a part of this degree.

Next, I would like to thank my supervisor, Dr. K.T. Chuang, who supported me over the course of my Ph.D. and taught me how to do research. I appreciate the independence which I was given and the fact that I was allowed to make mistakes and learn from them.

The numerical work in this thesis could not have been completed without the help of Dr. K. Nandakumar. I thank you for your patience and help as I developed the code which was used to simulate the experimental results. Also, a big thanks to Dr. S. Liu, who informed me that I could not use the ADI scheme to solve the

convection-diffusion equation. Finally, thanks to Bob Barton, without whose help I would have had to figure out how to use UNIX and the workstations all by myself.

The office staff here at the Department of Chemical Engineering also deserve a special thank you for all the friendly advice and pleasant conversation over the years. Thank you also for attending to all the administrative matters which have required your attention on my behalf.

I am indebted to the people in the Machine and Instrument Shops who have helped me with the construction and debugging of my experimental apparatus—your technical skills make the experimental research in this department possible. I also thank you for your friendship and for allowing me to find out just what goes on in your shops—even a little hands on training!

Thanks is also due to Andrée Koenig for supplying me with numerous chemicals, keeping my GC going and making sure that I always had enough distilled water.

Thanks also goes to my fellow grad students, both past and present, who have truly made this degree memorable. Those lunchtime table hockey and card games were great and were surpassed only by the numerous trips to Maxwell Taylors for wings. I must also mention the many hours we spent in the fluid dynamics lab, which kept me from going crazy when my research was going nowhere.

To you Rayna, who is presently too young to read—the work contained in this thesis is what I was working on during the first few years of your life. I apologize for missing all that I did during those years but hope that when you are older you will understand.

Finally, I would like to thank my wife, Wendy Rae Novakowski, not only for your love and support, but also for your love of horses and your dream of having a ranch someday. I, too, dream of owning our own ranch and hope that this degree will, in some small way, allow us to realize this dream.

Contents

Chapter 1

Introduction	1
1.1 Background	1
1.2 Purpose	3
1.3 Overview of Thesis	4

Chapter 2

Literature Review	7
2.1 Surface Phenomena	7
2.2 Contact Angle Analysis	15
2.3 Rivulet Flow Analysis	19
2.4 Application to Structured Packing	23

Chapter 3

Applications	28
3.1 Mechanistic Models	29
3.1.1 Liquid Distribution	29

3.1.2	Effective Area	34
3.1.3	Mass Transfer	34
3.2	Results and Discussion	36
3.2.1	Effect of Packing Height	36
3.2.2	Effect of Liquid Load	39
3.2.3	Effect of Number of Initial Distribution Points	39
3.2.4	Effect of Liquid–Solid Contact Angle	43
3.2.5	Effect of Initial Maldistribution	46
3.2.6	Comparison With Published Results	48

Chapter 4

	Governing Equations	57
4.1	Derivation	58
4.1.1	Profile Equations	58
4.1.2	Flow Equations	60
4.1.3	Convection-Diffusion Equation	62
4.2	Generalized Curvilinear Coordinates	63
4.2.1	Physical–Computational Spaces	64
4.2.2	Equation Transformation	66
4.3	Numerical Solutions	76
4.3.1	Profile Equations	76
4.3.2	Flow Equations	82

4.3.3	Convection-Diffusion Equation	84
4.3.4	Mixing Cup Calculations	88
4.3.5	Grid Refinement	92

Chapter 5

	Experimental System	96
5.1	Description of Apparatus	96
5.2	Auxiliary Systems	105
5.3	Experimental Techniques and Measurements	107
5.4	Additional Procedures	116

Chapter 6

	Investigation of Rivulet Dimensions	118
6.1	Experimental Contact Angles	119
6.2	Experimental Widths	126
6.2.1	Width Data	127
6.3	Experimental Heights	136
6.3.1	Height Data	136
6.4	Theoretical Rivulet Dimensions	138
6.4.1	Width and Height	138
6.4.2	Interfacial and Cross-Sectional Area	144
6.4.3	Rivulet versus Film Model	149

Chapter 7

Investigation of Rivulet Absorption	153
7.1 Effect of Sampling Mechanism	153
7.2 Effect of Calculation Method	156
7.3 Effect of Carbon Dioxide Flow Rate	156
7.4 Absorption Results	159
7.4.1 Concentration versus Liquid Flow Rate	160
7.4.2 Boundary Layer Development	161
7.4.3 Analytical versus Numerical Solution	169
7.4.4 Experimental versus Theoretical Absorption	170
7.4.5 Flow Structure	170

Chapter 8

Conclusions and Recommendations	175
8.1 Conclusions	175
8.2 Recommendations	176

References	178
-------------------	------------

Appendix A

Equipment Specifications	195
---------------------------------	------------

Appendix B

Physical Properties	198
----------------------------	------------

Appendix C

Calibration Technique	199
C.1 Gas Chromatograph	199

Appendix D

Sample Calculations	202
D.1 Absorption Results	202
D.1.1 Carbon Dioxide Concentration in Water Before Absorption . .	202
D.1.2 Converting Carbon Dioxide Peak Area to Concentration . . .	204
D.1.3 Overall Liquid-Side Mass Transfer Coefficient	206
D.1.4 Dimensionless Number Analysis	207
D.2 Analytical Diffusion Model	210
D.3 Negligible Z-Diffusion Assumption	212
D.4 Error Analysis	213

Appendix E

Best Fit Lines	217
-----------------------	------------

Appendix F

Raw Experimental Data	222
F.1 Experimental Absorption Data	222
F.2 Surface Roughness Analysis	223

Appendix G

Computer Code and Implementation	238
G.1 Generation of Theoretical Results	239

List of Tables

3.1	Geometric Information, Structured Corrugated Packing	29
3.2	Wetted Area and Mass Transfer in Packing Elements for the System Air- NH_3 - H_2O , $ND=7$, $\theta=50^\circ$, $L_T=15\text{ m}^3/(\text{m}^2\text{ h})$	37
4.1	Effect of Computational Grid Density on the Solution of the z-momentum Navier-Stokes Equation Used to Determine the Volumetric Flow Rate Inside a Rivulet Profile. Most Sensitive Profile. $\alpha=15^\circ$, $\theta=90^\circ$, $\text{Log}_{10}B=-1.0$	94
4.2	Effect of Computational Grid Density on the Solution of the Convection-Diffusion Equation Used to Determine the Concentration Inside a Rivulet Profile at the Specified Flow Distance. Most Sensitive Profile. $\alpha=15^\circ$, $\theta=10^\circ$, $\text{Log}_{10}B=3.0$, $\text{Dist}=0.5\text{ m}$	95
5.1	Gas Chromatograph Settings	106
5.2	Integrator Settings	107
6.1	Contact Angle Measurements, in degrees, Using Sessile Drops on Horizontal and Inclined Surfaces for the Stainless Steel-Water System in Both Air and CO_2	124
6.2	Contact Angle Measurements in a Flowing Rivulet for the Stainless Steel-Water System in Air. $\alpha=30^\circ$	125
6.3	Average and Standard Deviation Values for Experimentally Determined Contact Angles in Sessile Drops and Flowing Rivulets ($\alpha=30^\circ$) for the Stainless Steel-Water System in Air.	125
7.1	Effect of CO_2 Flow Rate on Absorption. $\alpha=45^\circ$	159

A.1	Experimental Equipment and Specifications	196
A.2	Experimental Equipment and Specifications	197
F.1	Experimental Absorption Data for a Plate Inclination of 15°.	224
F.2	Experimental Absorption Data for a Plate Inclination of 15°.	225
F.3	Experimental Absorption Data for a Plate Inclination of 30°.	226
F.4	Experimental Absorption Data for a Plate Inclination of 30°.	227
F.5	Experimental Absorption Data for a Plate Inclination of 45°.	228
F.6	Experimental Absorption Data for a Plate Inclination of 45°.	229
F.7	Experimental Absorption Data for a Plate Inclination of 45°.	230
F.8	Experimental Absorption Data for a Plate Inclination of 45°. Effect of CO ₂ Flow on the Degree of Absorption.	231
F.9	Experimental Absorption Data for a Plate Inclination of 60°.	232
F.10	Experimental Absorption Data for a Plate Inclination of 60°.	233
F.11	Experimental Absorption Data for a Plate Inclination of 60°.	234
F.12	Experimental Absorption Data for a Change in Plate Inclination from 30° to 60°.	235
G.1	Input File for Computer Code	240

List of Figures

3.1	Flow Channel Arrangement and Geometry of Packing	30
3.2	Model of Flow Splitting	31
3.3	Model of Liquid Distribution Inside the Idealized Packing Structure Including Interactions at the Column Wall	32
3.4	Liquid Flow Patterns a) First element b) Second element c) Fifth element	38
3.5	Packing Wettability as a Function of Liquid Flow Rate for Various Packing Heights	40
3.6	Mass Transfer Performance as a Function of Liquid Flow Rate for Various Packing Heights	41
3.7	Packing Wettability as a Function of Liquid Flow Rate for Various Packing Heights	42
3.8	Wettability as a Function of Packing Height for Various Number of Initial Liquid Distribution Points	44
3.9	Number of Rivulets as a Function of Packing Height for Various Number of Initial Liquid Distribution Points	45
3.10	Effect of Contact Angle on Wettability for Various Initial Liquid Flow Rates	47
3.11	Liquid Distribution Arrangement for Unequal Area Maldistribution. a) 1/4-area b) 1/2-area c) 3/4-area	49
3.12	Liquid Distribution Arrangement for Unequal Flow Maldistribution. a) Even Distribution b) First Shift c) Second Shift	50

3.13	Effect of Unequal Flow Initial Maldistribution on Wetted Area as a Function of Packing Height	51
3.14	Effect of Unequal Area Maldistribution on Wetted Area as a Function of Packing Height	52
3.15	Comparison of Reported and Calculated Wetted Areas as a Function of Liquid Flow Rate	54
3.16	Comparison of Reported and Calculated Liquid-Side Mass Transfer Coefficients as a Function of Liquid Flow Rate	55
3.17	Comparison of Reported and Calculated Height of an Overall Gas-Phase Mass Transfer Unit as a Function of the Number of Distribution Points	56
4.1	Geometry and Nomenclature For a Half Profile of a Sessile Drop Resting on a Flat, Horizontal Solid Surface. Solid Surface Not Shown	58
4.2	Coordinate Systems for the Physical and Computational Spaces . . .	65
4.3	Grid Structure Inside Rivulet Profile. Largest Width Rivulet Case. $\alpha=15^\circ$, $\theta=15^\circ$, $\text{Log}_{10}B=1.7$. Every fifth ξ -line shown.	67
4.4	Grid Structure Inside Rivulet Profile. Largest Height Rivulet Case. $\alpha=15^\circ$, $\theta=88^\circ$, $\text{Log}_{10}B=-0.26$	68
4.5	Grid Structure Inside Rivulet Profile. Average Rivulet Size For Stainless Steel-Water System. $\alpha=45^\circ$, $\theta=50^\circ$, $\text{Log}_{10}B=-0.17$	69
4.6	Grid Structure Inside Rivulet Profile. Half Circle Profile Case From Which Results Were Used to Check Against the Analytical Conduction Problem In an Infinite Cylinder. $\alpha=45^\circ$, $\theta=90^\circ$, $\text{Log}_{10}B=-1.0$	70
4.7	Grid Structure Inside Rivulet Profile. Smallest Height Rivulet Case. $\alpha=89^\circ$, $\theta=15^\circ$, $\text{Log}_{10}B=0.2$. Every fifth ξ -line shown.	71
4.8	Grid Structure Inside Rivulet Profile. Smallest Width Rivulet Case. $\alpha=89^\circ$, $\theta=88^\circ$, $\text{Log}_{10}B=-1.0$	72
4.9	Boundary Conditions for Solution of the z -momentum Navier-Stokes Equation	75
4.10	Boundary Conditions for Solution of Convection-Diffusion Equation .	75

4.11	Contour Plot of the Metric Coefficient $\frac{\partial \xi}{\partial x}$ in Computational Space. $\alpha = 45^\circ, \theta = 50^\circ, \text{Log}_{10} B = -0.17$	77
4.12	Contour Plot of the Metric Coefficient $\frac{\partial \xi}{\partial y}$ in Computational Space. $\alpha = 45^\circ, \theta = 50^\circ, \text{Log}_{10} B = -0.17$	78
4.13	Contour Plot of the Metric Coefficient $\frac{\partial \eta}{\partial x}$ in Computational Space. $\alpha = 45^\circ, \theta = 50^\circ, \text{Log}_{10} B = -0.17$	79
4.14	Contour Plot of the Metric Coefficient $\frac{\partial \eta}{\partial y}$ in Computational Space. $\alpha = 45^\circ, \theta = 50^\circ, \text{Log}_{10} B = -0.17$	80
4.15	Contour Plot of the Streamlines Inside the Rivulet Profile. Average Rivulet Size for the Stainless Steel–Water System. Velocity is in m/s . $\alpha = 45^\circ, \theta = 50^\circ, \text{Log}_{10} B = -0.17$	85
4.16	Dimensionless Concentration Inside the Rivulet Profile. Average Rivulet Size for the Stainless Steel–Water System. $\alpha = 45^\circ, \theta = 50^\circ$, $\text{Log}_{10} B = -0.17$, Dist = 0.114 m	89
4.17	Dimensionless Concentration Inside the Rivulet Profile. Average Rivulet Size for the Stainless Steel–Water System. $\alpha = 45^\circ, \theta = 50^\circ$, $\text{Log}_{10} B = -0.17$, Dist = 0.256 m	90
4.18	Dimensionless Concentration Inside the Rivulet Profile. Average Rivulet Size for the Stainless Steel–Water System. $\alpha = 45^\circ, \theta = 50^\circ$, $\text{Log}_{10} B = -0.17$, Dist = 0.368 m	91
5.1	Schematic of Experimental Apparatus	97
5.2	Schematic of Top and Bottom Views of the Inclined Flow Plate and Plexiglass Cover Sheet. All Dimensions in mm	99
5.3	Schematics of Liquid Sampling Mechanism, Gas Distribution Box, Liquid Collection Box and Constant Head Tank. All Dimensions in mm	101
6.1	Representative Sessile Drop Used in the Determination of Appropriate Values for the Static Equilibrium Contact Angle for the System Stainless Steel–Water. The Surface Upon Which the Rivulet is Resting is Horizontal. The Drop Profile Rises Above the Solid Surface and a Reflection of the Drop Profile Can Be Seen in the Solid Surface. Air Environment.	121

6.2	Representative Sessile Drop Used in the Determination of Appropriate Values for the Advancing and Receding Static Contact Angles for the System Stainless Steel–Water. The Surface Upon Which the Drop is Resting is Inclined 15° from the Horizontal. The Drop Profile Rises Above the Solid Surface and a Reflection of the Drop Profile Can Be Seen in the Solid Surface. Air Environment.	122
6.3	Representative Flowing Rivulet Used in the Determination of Appropriate Values for the Contact Angle in a Flowing Rivulet for the System Stainless Steel–Water. The Surface Upon Which the Rivulet is Flowing is Inclined 30° from the Horizontal. The View of the Photograph is Looking Down the Plate. Air Environment.	123
6.4	Theoretical and Experimental Rivulet Width as a Function of Flow Rate for a Plate Inclination of 15°	130
6.5	Theoretical and Experimental Rivulet Width as a Function of Flow Rate for a Plate Inclination of 30°	131
6.6	Theoretical and Experimental Rivulet Width as a Function of Flow Rate for a Plate Inclination of 45°	132
6.7	Theoretical and Experimental Rivulet Width as a Function of Flow Rate for a Plate Inclination of 60°	133
6.8	Theoretical and Experimental Rivulet Width as a Function of Flow Rate for a Plate Inclination of 90°	134
6.9	Theoretical and Experimental Rivulet Height versus Flow Rate. $\alpha = 15^\circ$, $Dist = 0.098\text{ m}$	139
6.10	Theoretical and Experimental Rivulet Height versus Flow Rate. $\alpha = 30^\circ$, $Dist = 0.147\text{ m}$	140
6.11	Theoretical and Experimental Rivulet Height versus Flow Rate. $\alpha = 45^\circ$, $Dist = 0.176\text{ m}$	141
6.12	Theoretical and Experimental Rivulet Height versus Flow Rate. $\alpha = 60^\circ$, $Dist = 0.167\text{ m}$	142
6.13	Theoretical and Experimental Rivulet Height versus Flow Rate. $\alpha = 90^\circ$, $Dist = 0.156\text{ m}$	143
6.14	Theoretical Rivulet Width versus Volumetric Flow Rate as a Function of Plate Inclination. $\theta = 46^\circ$	145

6.15	Theoretical Rivulet Height versus Volumetric Flow Rate as a Function of Plate Inclination. $\theta = 46^\circ$	146
6.16	Theoretical Interfacial Area per Length versus Volumetric Flow Rate as a Function of the Plate Inclination. $\theta = 46^\circ$	147
6.17	Theoretical Cross-Sectional Area versus Volumetric Flow Rate as a Function of the Plate Inclination. $\theta = 46^\circ$	148
6.18	Theoretical Rivulet Width versus Volumetric Flow Rate. Rivulet versus Film Model Comparison. Flow Plate Inclination as Indicated. $\theta = 46^\circ$	150
6.19	Theoretical Rivulet Height versus Volumetric Flow Rate. Rivulet versus Film Model Comparison. Flow Plate Inclination as Indicated. $\theta = 46^\circ$	151
6.20	Theoretical Rivulet Interfacial Area per Length, m , versus Volumetric Flow Rate, m^3/s . Rivulet versus Film Model Comparison. Flow Plate Inclination as Indicated. $\theta = 46^\circ$	152
7.1	Absorption Results for a Plate Inclination of 45° Showing the Effect of Flow Rate and Flow Distance. Absorption Results Calculated Using Volume Method. Reproducible Data. Fixed Weir Sampling Mechanism.	155
7.2	Absorption Results for a Plate Inclination of 45° Showing the Effect of Volumetric Flow Rate and Flow Distance. Absorption Results Calculated Using Volume Method. All of the Data Collected. Fixed Weir Sampling Mechanism.	157
7.3	Absorption results for a Plate Inclination of 45° Showing the Effect of Flow Rate and Flow Distance. Absorption Results Calculated Using Difference in Weight Method. All of the Data Collected. Fixed Weir Sampling Mechanism.	158
7.4	Absorption Results for a Plate Inclination of 15° Showing the Effect of Flow Rate and Flow Distance.	162
7.5	Absorption Results for a Plate Inclination of 30° Showing the Effect of Flow Rate and Flow Distance.	163
7.6	Absorption Results for a Plate Inclination of 45° Showing the Effect of Flow Rate and Flow Distance.	164

7.7	Absorption Results for a Plate Inclination of 60° Showing the Effect of Flow Rate and Flow Distance.	165
7.8	Dimensionless Number Analysis for Experimental and Theoretical Absorption Results Indicating Development of the Concentration Boundary Layer.	168
7.9	Transient Conduction/Diffusion Problem in a Cylinder of Infinite Length	169
7.10	Comparison of Analytical and Computational Solutions for Transient Diffusion (Mass or Heat) in an Infinite Cylinder. Dimensionless Time as Indicated.	171
7.11	Comparison of Corrected Experimental and Theoretical CO_2 Absorption versus Flow Rate. Experimental Data are for the Plate Inclinations as Shown. Theoretical Prediction is For $\alpha=15^\circ$	172
7.12	Effect of Change in Flow Plate Inclination on Experimental Absorption Results. $\alpha=60^\circ$, $Dist=0.368\text{ m}$	174
C.1	Calibration Curve for Analyzing Dissolved CO_2 in Water. $T=20^\circ\text{C}$.	201
F.1	Surface Roughness Profiles. a) Flow Plate. Vertical Scale $= 5.08 \times 10^{-6}\text{ m}$ b) Stainless Steel Sample. Vertical Scale $= 10.16 \times 10^{-6}\text{ m}$. .	237
G.1	Flowsheet Structure for Computer Code	241

Nomenclature

a_e	effective mass transfer area, m^2/m^3
a_p	geometrical surface area, m^2/m^3
a_w	wetted area, m^2/m^3
A_i	abscissas for Gaussian Quadrature
b', B	radius of curvature at apex of rivulet, m
B_c	half-channel base dimension, m
c	non-dimensionalizing parameter, $1/m^2$
C', C	concentration, $kmol/m^3$
d_{eq}	equivalent diameter, m
\mathcal{D}	diffusion coefficient, m^2/s
Dis	flow distance, m
D_1	diameter of a packing element, m
g	gravitational constant, $9.807 m/s^2$
\tilde{G}	molar velocity of gas, $kmol/(m^2 s)$
h	crimp height, m
H	Henry's Law constant, $MPa/(mol\ frac)$
H_i	weighting factors for Gaussian Quadrature
H_{OG}	height of an overall gas-phase transfer unit, m

H_1	height of a packing element, m
HTU	height of an individual transfer unit, m
i, j, k	coordinates of intersection points in packing
I	number of intersection points per packing element
$ J^{-1} $	determinant of the inverse Jacobian matrix
J, K	denote array element position
k_L	individual liquid-phase mass transfer coefficient, m/s
k_0	maximum value of the coordinate direction k
$K_{\bar{z}}$	overall liquid-side mass transfer coefficient based on mole fraction driving force
l_{xy}	length of flow channel in the x and y -directions, m
l_z	length of flow channel in the z -direction, m
\tilde{L}	molar velocity of liquid, $kmol/(m^2 s)$
L_T	initial liquid distribution flow rate in column, $m^3/(m^2 h)$
m	slope of equilibrium line
M	number of packing elements
MW	molecular weight, $kg/kmol$
n	number of moles
N	number of rivulets per element of packing
ND	number of initial distribution points
$N_{Gz^{-1}}$	inverse Graetz number
N_{Pe}	Peclet number
N_{Re}	Reynolds number
N_{Sc}	Schmidt number

N_{Sh}	Sherwood number
P', P	pressure, kPa
PA	peak area of CO_2 from integrator
q	volumetric flow rate, m^3/s
Q_0	initial liquid flow rate matrix
r_1	radius of meridional curvature, m
r_2	radius of cylindrical curvature, m
R	ideal gas law constant, $82.05 L atm/(kmol K)$
\mathcal{R}	roughness ratio
s	number of corrugated sheets per element
S	length of corrugation side, m
s'_p, S_p	surface area per unit length, m^2/m
t', t	time, s
T	temperature, $^{\circ}C$ or K as indicated
u', u	velocity in convection-diffusion equation, m/s
U	superficial velocity, m/s
U_e	effective velocity, m/s
v', v	velocity in Navier-Stokes equation, m/s
v'_p, V_p	volume per unit length, m^3/m
V	volume, m^3
W_A	reversible work of adhesion, N/m
\tilde{x}	liquid-phase mole fraction
x'_p, X_p	half-width of rivulet, m
\tilde{y}	gas-phase mole fraction
y'_p, Y_p	height of rivulet profile, m

Subscripts

A	solute
B	solvent
CO_2	carbon dioxide
dyn	dynamic
G	gas-phase
H_2O	water
L	liquid-phase
lm	logarithmic mean
p	rivulet profile
sat	saturation
x	x -direction
y	y -direction
z	z -direction

Superscripts

$'$	dimensional quantity
$*$	equilibrium condition

Greek Letters

α	angle of flow channel or plate from horizontal, degrees
β	discount factor
δ	liquid film thickness, m
γ	interfacial tension, N/m

ϵ	void fraction of packing
μ	absolute viscosity, $Pa\ s$
ν	kinematic viscosity, m^2/s
θ	liquid–solid contact angle, degrees
ρ	density, kg/m^3
σ	surface tension, N/m

Chapter 1

Introduction

1.1 Background

There has been a renewed interest in the modelling of rivulet flows since the introduction of structured packings for use in distillation, absorption and stripping columns. In these packings, the liquid can flow as a film or in discrete rivulets depending upon the type of packing and its wettability by the liquid. This type of modelling also has applications in heat exchangers applications where rivulet flow can occur—often with disastrous results. It is in this area that much work has been done recently in determining the stability of film flows and subsequent breakdown of these films into stable rivulet flows. Meandering of rivulet flows has also been a topic of much interest in the current literature with papers discussing the stability criteria as applicable to these types of flows. Finally, trickle-bed reactors often experience rivulet flow since the catalyst surfaces are not always fully wetted by the liquid. Despite the widespread applications for models describing rivulet flow and mass and heat transfer, the literature in this area is very limited.

For application in absorption columns, rivulet modelling must be combined with models describing the liquid distribution and mass transfer processes occurring within the packing. For the liquid distribution models, various authors have used dispersion and random walk models to describe the random nature of liquid flow in trickle-bed reactors and random packing. With structured packing, its ordered nature has led to the development of mechanistic liquid distribution models, which attempt to track the liquid through the column by making assumptions about how it is distributed at the packing junctions. This type of mechanistic approach to liquid distribution requires rivulet modelling when it can be shown that the liquid flows in this manner—the reason being that once the liquid can be quantified at a certain location and in a certain flow structure, the Navier-Stokes and relevant mass transfer equations can be utilized.

The above method of incorporating liquid distribution, flow and mass transfer models to describe processes utilizing structured packing has been attempted recently by a number of authors. The results have been promising considering the complex interactions which exist inside a full scale absorption column. By developing intricate liquid distribution mechanisms based upon observations of liquid flow in various types of structured packing, the distribution models have become more complex and closer to the actual process occurring in the packing.

Modelling of the fluid flow and mass transfer process has received less attention than the liquid distribution models and it is in this area that more work is required. Although the Navier-Stokes equation has been applied to rivulet flows assuming a simple one-dimensional velocity profile and the theoretical results shown to agree with the experimental data, there is evidence that the flow is one-dimensional with secondary flow. These studies incorporating secondary flow, while complex in nature, require theoretical analysis and verification by experimental work.

For the mass transfer process occurring within a rivulet, even less work than that for the flow field has been done. The application of the convection-diffusion equation to a stable, linear, laminar rivulet flow to predict the mass transfer rate has never been adequately demonstrated and, based upon the above arguments of secondary flow, the mass transfer problem is indeed complex. Coupled with the secondary flow described above is the secondary flow which would be induced by Marangoni effects. For the full mass transfer process then, the governing equation would be considerably more complex than the simplified convection-diffusion equation which is used in this analysis.

Underlying the above work is the more basic phenomena of interfacial tension and its relationship to contact angles in gas-liquid-solid systems. The application of these surface phenomena to this research is fundamental since the size and shape of the rivulet which is formed on a given plate for a particular liquid is determined by the value of the contact angle. The conflicting reports of contact angle and interfacial tension data in the literature serve as an indicator that this area is far from well understood. As was found after surveying the literature, lack of cleanliness, contamination of the surface, roughness of the surface or lack of information about these three criteria has led to much of the confusion concerning contact angle measurements. Nevertheless, by measuring the contact angle for the system of interest and by taking suitable precautions to ensure cleanliness, useful values of contact angle can be obtained.

1.2 Purpose

The work contained in this thesis is comprised of two separate components, each of which compliment the other. The first component demonstrates how a

simple film approximation to the full rivulet flow model can be used to describe an absorption process using classical relationships to describe the fluid flow and mass transfer processes occurring on the packing in the process. The second component involves the study of rivulet flows at a fundamental level to better characterize the flow field and mass transfer process. This second component requires a more fundamental approach utilizing both theoretical derivation and numerical solutions of the equations governing the system. To complete this work, experimental data is collected to verify the theoretical predictions. This latter goal comprises the bulk of this thesis.

1.3 Overview of Thesis

Chapter 2 reviews the relevant literature concerning surface phenomena, contact angle measurements, rivulet flow analysis and its applications to structured packing. Arguments concerning the use of the equations of Young and Dupré are presented along with a discussion of the theoretical modelling of surfaces as it relates to contact angle. Discussions concerning the measurement of contact angles and the variability in this data is also presented in an attempt to sort out the disparate data which exist in the literature. The section concerning rivulet flow analysis presents the relevant rivulet modelling and experimental results which have been published. The final section of this chapter deals with the application of rivulet modelling to characterize the process of mass transfer and liquid distribution in structured packing. Relevant research in this area is presented and discussed to show that a rivulet model as presented here is applicable.

In Chapter 3, a simplified rivulet model is applied to the process of gas stripping in a column containing structured packing. The system modelled is air-NH₃-H₂O

and the results presented show the effect of system parameters including flow rate, contact angle, packing height, number of initial distribution points and maldistribution. Comparisons are also done with published experimental data to show that rivulet modelling is a suitable approach to a problem of this sort.

Chapter 4 presents the theoretical equations describing the free interface of the rivulet profile and the governing equations for the flow field and mass transfer process occurring inside this profile. Once these equations are simplified and the appropriate boundary conditions are applied, the numerical techniques used to solve these equations are presented. The theory of grid generation is also presented in this chapter along with a discussion of how it was applied to the rivulet flow problem.

The experimental system used to gather the raw experimental data is described in detail in Chapter 5. Each component of the system is discussed as are the experimental techniques used to gather the relevant data. This chapter concludes with a brief discussion of some of the experimental procedures which were tested but proved to be unsatisfactory for this type of investigation.

Chapter 6 presents the experimental and theoretical results for the width and height of a flowing rivulet. A discussion of these results and the relevance of hysteresis in flows of this type is presented. Additional theoretical results for the cross-sectional and interfacial areas of a flowing rivulet are presented along with a comparison of the simplified rivulet model used in Chapter 3 with the full rivulet model.

The experimental and theoretical absorption results are presented in Chapter 7. A discussion of end effects and the method used to calculate the absorption results is first discussed as these two items proved to be vital in acquiring reliable results. This discussion is followed by the actual absorption results which are presented both in terms of concentration and dimensionless Sherwood number.

Chapter 8 presents the conclusions and recommendations from this study together with suggestions for future work in this area.

Chapter 2

Literature Review

2.1 Surface Phenomena

Contact angle analysis has received much attention in the literature because of its seemingly simple relationship to the liquid–solid system being studied via Young’s equation. This equation predicts the contact angle of a given system from values of the interfacial tension of the phases present. While simple in form, this equation has evoked much discussion because it has not been verified experimentally. The following section presents an overview of the discussion regarding Young’s equation as well as several other important aspects of surface phenomena as they relate to this research.

Thomas Young [150] was the first to propose a relationship for the static equilibrium of an interface on a solid surface. He stated qualitatively that the three material boundaries—gas–liquid, liquid–solid and gas–solid—each possesses a constant surface tension and that for the system to be in static equilibrium, each of the horizontal components must sum to zero at the point of contact. This qualitative

statement has since been expressed mathematically as shown

$$\gamma_{GS} = \gamma_{LS} + \gamma_{GL} \cos \theta \quad (2.1)$$

and is often referred to as Young's equation.

Thermodynamic treatments of surface phenomena have also been developed. Thompson [140, 141] was the first to use this approach, while Gibbs [65] generalized this method. Dupré [51] used this idea also and, in 1869, derived the following expression for the reversible work of adhesion between a liquid and solid in terms of the interfacial tensions present in the system.

$$W_A = \gamma_{GS} + \gamma_{GL} - \gamma_{LS} \quad (2.2)$$

This expression is a thermodynamic statement of the fact that the reversible work of separating the liquid and solid phases must be equal to the change in free energy of the system. This change in the free energy arises due to changes in the surface area of the gas-solid, gas-liquid and liquid-solid interfaces and can be written in terms of the interfacial tensions.

While Young used a static equilibrium approach, Sumner [135] has shown that it is possible to derive this same equation thermodynamically for an ideal plane solid surface using the same assumptions inherent in Young's equation and assuming the system is treated as being in thermal and mechanical equilibrium. In his analysis, the interfacial tensions are expressed in terms of the partial derivatives of the Helmholtz free energy (work function) of the system with respect to the areas of the liquid-solid, gas-solid and gas-liquid phases. Recent authors [77, 127] have given more general thermodynamic derivations of the equations of Young and Dupré.

The equations of Young and Dupré provide a powerful, theoretical approach to the study of surface phenomena. Assuming that values of interfacial tension required

in these equations can be measured, the work of wetting and the contact angle of the system of interest can both be predicted—two very useful quantities. Measurement of these interfacial tension values, however, has proven to be the major complication in experimentally verifying these two equations thus leading to many discussions concerning the validity of these equations—Young’s equation in particular.

Young’s equation, as stated, invites criticism because it originates as a static equilibrium relationship and, as such, requires that the forces in the planar and perpendicular direction both sum to zero. The actual statement of Young’s equation, however, deals only with resolution of forces in the planar direction. It has been observed [3, 25] that the perpendicular direction seemingly has an unresolved force arising from the gas–liquid interfacial tension thereby invalidating the equation. Dussan V. [53], Lester [93] and Michaels and Dean [104], however, state that the counteracting force is indeed present in the solid and causes deformation in low yield strength materials, such as soft silica gels and thin mica sheets [6]. For high yield strength materials, in which no deformation is observed, Lester [92] theoretically shows that this equation is indeed correct. Experimentally, Bailey and Kay [7], claim verification of Young’s equation for the water–mica and hexane–mica systems using measurements of the energies involved in the bifurcation of mica under different conditions to provide values for the interfacial tension terms.

A further criticism of Young’s equation arises because of the inconsistent values of contact angle reported in the literature. Young’s equation predicts but a single value, while contact angle hysteresis is an accepted phenomena in this area. Years of research have failed to resolve this issue, although some studies have provided insight into this problem [3, 13, 14, 15, 24, 37, 38, 46, 66, 78, 120, 127, 144, 145].

Adamson [3] has identified three causes for hysteresis of contact angles: contamination of either the liquid or the solid surface, roughness of the solid surface,

and immobility of the solid surface on a macromolecular scale. The first two have received much attention in the literature as they are the major sources of hysteresis in systems exhibiting contact angle phenomena; the third is limited to specific types of solid surface (eg. agar gels) and is not applicable to this research.

The study of hysteresis of contact angles gained credibility when the following relationship between contact angle and surface roughness was developed theoretically by Wenzel [144, 145], using Young's equation.

$$\mathcal{R} = \frac{\cos \theta_{macro}}{\cos \theta_{micro}} \quad (2.3)$$

This relationship illustrated for the first time how hysteresis could occur on rough surfaces and demonstrated that two angles are actually present in a system exhibiting hysteresis—the readily observable (macroscopic) angle and the microscopic angle, the latter of which cannot, as yet, be measured. The microscopic angle defines the liquid–solid contact, has a constant value and is the value required by Young's equation, whereas the macroscopic angle is the one observed in practical situations and exhibiting vastly different values.

Various authors have used this idea of a microscopic–macroscopic angle to illustrate how surface roughness affects contact angle. Shuttleworth and Bailey [127] stated that the experimentally observed contact angle is the sum of the intrinsic angle and the slope of the surface at the point of contact. The slope angle can be positive or negative, giving a definite range of contact angle values. The maximum value is the advancing angle while the minimum is the receding angle.

Building upon Shuttleworth and Bailey's ideas, Johnson and Dettre [78, 79] have theoretically described the wettability of idealized rough surfaces using computer analysis. By studying an ideal surface of known roughness characteristics, they showed that Wenzel's equation and the idea of a microscopic–macroscopic contact

angle can be used to simulate observed hysteresis. Agreement of this model with hysteresis data on real surfaces was only qualitative but did predict the correct behaviour of the contact angle.

The theoretical relationship of Wenzel and the computer modelling of Johnson and Dettre begin to draw together the seemingly disjointed contact angle data reported in the literature. The observations of Bartell and Smith [16], Guastalla [70], Murray and Darvell [106], Ryley and Khoshaim [116], Wenzel [144, 145] and Zisman [152] that polishing a surface reduces the difference of the advancing and receding angle can now be explained at least qualitatively. Zisman [153] also reports similar behaviour and finds that, as long as there were no surface pores or crevices into which the liquid can penetrate, the advancing and receding angles are equal. A progressive series of papers by Baker [8], Levine [94], Schulman [119] and Shafrin [123] confirm this statement. Conversely, where penetration of the liquid can occur, these two angles can differ significantly.

On idealized, rough surfaces, Johnson and Dettre's series of papers [47, 48, 49, 78, 79] bring together the qualitative arguments of Bikerman [23, 24], Cassie and Baxter [38], Derjaguin [46], Good [66], Harkins [71], Schwartz and Minor [120] and Shuttleworth and Bailey [127]. Their work shows that the advancing and receding angles occur at situations of high free energy in the system, that energy barriers exist between these states and that the lowest energy situation on a rough surface is that predicted by Wenzel's equation. These results from their thermodynamic analysis suggest that an observable, macroscopic angle equal to the equilibrium contact angle value will occur only on a smooth surface since, on rough surfaces, the observable macroscopic angle is different than the microscopic angle (equilibrium value), the latter value not being readily observable.

Adamson [3] describes contamination of the solid surface and liquid in the system

studied as the other major causes of hysteresis in contact angle analysis. Impurities in the liquids used in these types of studies have been discussed [116, 121, 148] and are not considered to be a problem if careful preparation and storage practices are observed [148]. Contamination of the solid surface, however, presents a different challenge as discussed by several authors [9, 10, 11, 12, 20, 21, 68, 70, 89, 116, 124] since surface contamination originates from adsorbed films and films remaining after surface preparation is complete. For films arising from surface preparation, Fowkes and Harkins [60], for example, found that rigorous cleaning of the solid surface and using very pure liquids significantly reduced the hysteresis. Yekta-Fard and Ponter [148] note four causes of surface contamination and observe the same behaviour as stated previously but state that cleaning of solid surfaces with some usually accepted procedures (detergent, absolute ethanol or distilled water) may not result in a clean surface. Their procedure of using organic acids to clean polished metal surfaces appears to remove any traces of impurities and leaves a surface which is clean enough for contact angle studies. Results of contact angle studies appearing in the literature which do not utilize meticulous cleaning procedures must be used with the knowledge that surface contamination may be present. This contamination must be considered even if not reported by the authors.

While contamination of the surface from films due to polishing can be removed with cleaning, adsorbed films on the surface present an entirely different problem. In a series of papers, Bernett and Zisman [21], Shafrin and Zisman [124] and Zisman [153] have described how water vapour can have a significant effect on the contact angle. These studies showed the large effect of even one adsorbed monolayer of water on the solid upon the contact angle of hydrophobic liquids. Langmuir [89] was the first to document these effects and recent work by Yekta-Fard and Ponter [113, 149] have shown that by carefully controlling the environment in

these studies, one may obtain reliable results.

The work by Yekta-Fard and Ponter [113, 148, 149] has clarified many of the problems of roughness and contamination associated with contact angle measurements. By carefully preparing their solid samples and then meticulously cleaning them and eliminating any impurities in the liquids used, they were able to attain reproducible values of contact angle in both inert and liquid saturated environments at different temperatures. The procedures set out by these studies attempt to standardize the approach used in measuring equilibrium contact angle values and demonstrate that while contact angle values do vary, the reasons for these variations are readily explainable in terms of surface roughness and contamination of the solid and liquid.

With contact angle being a function of surface roughness and preparation as well as liquid and solid contamination, the effects of temperature and drop size require investigation to determine their relative contributions. Studies of temperature effects on contact angle indicate a small, negative contribution—a value of $-0.1^{\circ}/^{\circ}C$ being an average figure for a large number of surfaces with water as the wetting liquid [2, 3, 44, 60, 68, 112, 144]. This small value of variation indicates that very close control of temperature is unnecessary when measuring contact angles since the error in the angle caused by temperature fluctuations is smaller than the error in the measuring technique used.

Using the above observations and expressing Wenzel's equation in terms of the cosine of the angle, Adam [1] suggests that temperature must affect the interfacial tension and the adhesion to the solid to very nearly the same proportionate extent. This proportionate decrease in the interfacial tension and adhesion forces arises from increased thermal motions in the liquid and allows for a nearly constant contact angle for large temperature variations. As shown by Griffith and Wallis [68], the stainless

steel–water system exhibits this behavior over a large range of temperature.

For the effect of drop size on contact angle values, the literature seems to indicate that they are independent of each other [153]. Based upon the previously presented ideas and arguments concerning microscopic–macroscopic contact angles, this statement is justified for the microscopic angle since nowhere in the derivation of Young’s or Dupré’s equation does a gravitational term appear; for the macroscopic angle, however, the same conclusion cannot be drawn. Recently, Ponter and Yekta-Fard [113, 148, 149], have shown that drop size has a definite effect on the macroscopic contact angle for very small drop size ($<3\text{ mm}$ for stainless steel–water at 25°C) and no effect for larger drop sizes.

Studies of drops on solid surfaces have concentrated not only on the contact angle which the liquid makes with the solid surface but also on the shape of the profile of the drop. In the absence of a gravitational field, a drop which does not spread will lie on the solid surface in the form of a segment of a circle. In a gravitational field, if the drop is very small, surface forces will predominate over the force of gravity, and the shape of the droplet will not differ greatly from a true segment of a sphere. If the drop is quite large, the gravitational force will dominate, and the sessile drop will be distorted such that it is horizontal on top. The degree of flattening occurring in the drop, therefore, is related to its size.

The equation which explains the above behavior and predicts the profile of small drops or drops in the absence of gravitational fields was first described by Laplace [45]. This equation can be expressed as follows

$$\Delta P = \sigma_L \left(\frac{1}{r_1} + \frac{1}{r_2} \right) \quad (2.4)$$

Thermodynamic derivations [39] of this equation have made it widely accepted, although its use is limited, because it applies strictly to small drops [99, 146].

Bashforth and Adams [17] used this equation to derive similar relationships which would apply in gravitational fields; however, their equations, while predicting the profile of any drop, were as complex as the Laplace equation for profile shape and could not be solved easily or explicitly. To overcome this drawback, Bashforth and Adams published a set of tables containing solutions for the profile of drops as a function of the implicit parameter, the radii of curvature of the drop at its apex. These tables allow one to find the profile of the drop without solving the equations.

Hartland and Hartley [72], using computer analysis, have recently rederived and solved the equations of the profile of a sessile 3-D drop and a sessile 2-D surface in a gravitational field and tabulated the solutions in dimensionless form. Their results can, thus, be used to describe the profile for any sessile 2-D surface or 3-D drop for any system of interest. Alternatively, their equations can be used directly in any drop or surface profile analysis.

To use the equations of Bashforth and Adams in analysing 2-D surfaces when the solid surface is inclined requires inclusion of the angle of inclination. This step was done by Tien and Rothfeld [142] to analyze rivulet flows on inclined plates.

2.2 Contact Angle Analysis

There are a number of techniques in the literature which have been used to measure contact angle values of liquids on solid surfaces. While certain methods are considered to be more accurate than others, it has been stated [80] that the limitation on the accuracy is not in the measuring technique itself, but rather in the reproducibility of the surfaces being studied—instruments that measure to an accuracy of 1° are usually more than adequate. Interestingly, Murray and Darvel [106] claim that there can be good agreement between the methods if suitable

precautions of measuring technique and materials preparation are followed. This statement is verified by the work of Ponter and Yekta-Fard [113, 148, 149].

Johnson and Dettre [80] discuss the more popular techniques of contact angle measurement and categorize them into six different groupings: drop or bubble methods, vertical rod method, tensiometric methods, horizontal liquid surface methods, capillary methods, and dynamic or static angle method. Except for the first method, the other ones, while widely used, do not allow measurement of the contact angle directly on the working surface where the angle is required. In these methods, some type of sample of the solid must be prepared and used in place of the real surface for contact angle determination. Due to this restriction, method one was chosen for use and will be discussed further.

In the drop or bubble methods, there are different techniques from which to choose. Perhaps the most interesting and simplest technique is that developed by Langmuir [90] in which the angle is determined from the reflection of a point light source from the drop surface at the point of contact of the liquid with the solid. While not requiring any optical equipment for the approximation of the tangent of the line of contact of the liquid with the solid surface, it can only be used for angles less than 90° and unwanted reflections from the drop surface often cause problems.

Another drop technique involves determining the angle indirectly by measurement of its dimensions. For small drops, the shape can be approximated as a portion of a sphere and the appropriate equation used to calculate the angle [97]. Contact angles for larger drops, in which gravity effects distort the shape, can be determined from the equations of Bashforth and Adams [17, 55, 98].

The most commonly used method of measuring contact angles involves direct measurement of the angle from the profile of a liquid drop resting on a plane solid surface. The contact angle is determined by constructing a tangent to the profile of

a liquid drop resting on a plane solid surface at the point of contact with the solid surface using a projected image [84] or a photograph [137] of the drop profile, or directly, using a telescope fitted with a goniometer eyepiece [22, 61]. This technique is very popular because it does not require knowledge of the liquid density or surface tension, it can employ very simple instruments, it can be used on very small solid samples with very little liquid and control of the temperature or environment can easily be accomplished by enclosing the drop in a controlled environment cell. As well, accuracy of $1-2^\circ$ can be achieved by a trained observer. This last method is the one of choice not only because of its simplicity but because it also allows for direct determination of advancing and receding contact angles using a liquid drop which is allowed to advance or recede at will. While possibly not excelling in the measurement of any one particular angle (advancing, receding, equilibrium), by measuring all three angles with one method, errors associated with multiple methods are reduced and direct comparison of the contact angles are possible. Lastly, but most importantly, it has been shown [53, 67, 80] that this technique is the only satisfactory method for measuring true advancing and receding angles.

The literature contains a vast array of experimental studies in which the contact angle of liquids on solid surfaces have been determined; however, in these studies there is very limited information on the stainless steel–water system. For the limited number of studies which were found, the measurement techniques and subsequent contact angle values determined were surprisingly consistent. Although no single study can be regarded as providing a definitive result for what the true contact angle is, a limited range of angle values is shown to exist.

Krell [86] studied the effect of surface roughness on contact angle using 18/9 stainless steel. Using a goniometric technique to measure the contact angle of a sessile drop, he found that the equilibrium angle has its highest value of 89° at 0.1

micron roughness, drops to a low of 52° at 2 micron roughness and then rises again to 82° at 6.5 micron roughness. The wide range of values of contact angle was not expected, as stated by the author, since Wenzel's equation predicts a change in angle of only 2° . A possible explanation in terms of opposing forces due to open capillaries on the solid surface is given and seems to be supported by high speed photography, but was not further substantiated.

Two studies by Ponter and Yekta-Fard [113, 149] give equilibrium values for water on Type-303 stainless steel using a goniometer and sessile drop technique. These studies show a definite change in angle with drop size with the type of change being dependent upon the environment in which the drop is contained. For a saturated air environment at 25°C , the contact angle is 52° for a 1.5 mm diameter drop and rises to 57° for drops larger than 6 mm. Similar behavior occurs in a saturated argon environment at 25°C where the angle is 52° for a 1.5 mm drop and rises to 57° for drops larger than 5 mm. In a saturated water vapor environment at 100°C , a decrease in contact angle occurs as the drop size increases— 79° at 1 mm to 66° for drops larger than 7 mm. No explanation is given for the results for this system.

Griffith and Wallis [68] used a horizontal liquid surface method to measure advancing and receding contact angle over a wide range of temperature and found a large degree of scatter in the value obtained. Typical results at 30°C range from 38° to 79° with 58° possibly representing the equilibrium value. Surface contamination was believed to be the cause of the lack of reproducibility of an advancing or receding angle.

A recent study by Schmuki and Laso [118] reports advancing, receding and dynamic contact angle values for water on AISI 316L stainless steel. The advancing and receding values were measured by determining the tangent to a magnified profile

of a sessile drop on a horizontal plate while the dynamic measurements were made from the width and height of a linear, laminar rivulet by assuming the rivulet cross-section to be a segment of a circle. Advancing angles of $62 \pm 3^\circ$ and receding angles of $49 \pm 3^\circ$ are reported with the dynamic angle being $68 \pm 8^\circ$. An important point which is made by the authors is that the dynamic contact angles are very close to the static advancing angles in every case and can be considered equal with experimental error.

2.3 Rivulet Flow Analysis

The first detailed analysis of rivulet flow on inclined flat plates was performed in 1966 by Towell and Rothfeld [142] who successfully showed that the Laplace and Navier-Stokes equations could be combined to characterize both the free interface describing the cross-sectional profile of a flowing rivulet and the velocity profile of the fluid flowing inside. Later work by Allen and Biggin [5], Bentwich *et al.* [19], Dassori *et al.* [43], Fedotkin *et al.* [57], Kern [82], Peier *et al.* [111] and Semiat [122] brought a generalizing of the solution techniques for the governing equations and a vast array of new problems to which rivulet analysis could be applied. Semiat [122], for example, used the above described rivulet analysis in characterizing both concave and convex rivulets on inclined surfaces with straight edged grooves. Dassori *et al.* [43] successfully showed that rivulet analysis could be used to describe mass transfer with chemical reaction in partially wetted flat plate catalyst pellets.

In their original paper, Towell and Rothfeld [142] applied the Navier-Stokes and Laplace equation to the general case of rivulet flow. They also presented the assumptions necessary in the analysis of the simplified situations of wide, flat rivulets and small rivulets. The numerical work solved the general rivulet flow problem

and the results were presented in comparison with the experimental data for the glass–water system; excellent agreement was obtained. This particular system, however, is characterized by a contact angle of not greater than 20° which is very low and produces rivulets which tend to be wide and flat making analysis of rivulet dimensions other than the width difficult.

Kern [82], using rivulet height as the characteristic dimension and not width as did Towell and Rothfeld, solved the rivulet equations using numerical finite difference and the assumption of constant interfacial curvature. His results showed good agreement with his experiments in the range of contact angle up to 100° . However, because he did not consider all of the wettability parameters in his analysis, some doubt remains as to whether his results are applicable to systems whose wettability characteristics are vastly different than those specifically studied in his work.

Allen and Biggin [5] used a series expansion approach to solve the applicable equations describing the flow of liquid in a linear, laminar rivulet. The validity of this solution again depends on the ratio of the rivulet's height to its width. The smaller the ratio, the better the approximation. These approximate solutions are compared with exact numerical ones generated using finite element methods and it is shown that in the interior of the rivulet, the two solutions agree quite well. Nearer the free interface, however, the series approximation solutions are not satisfactory.

To avoid numerical analysis techniques, Bentwich *et al.* [19] used a bipolar conformal transformation to derive an exact analytical solution for the case of a vertical plate. Results for the non-vertical case are derived from the vertical case in the form of a polynomial solution using a Ritz-Galerkin method. Using this technique, the results describing velocity profiles in a linear, laminar rivulet are presented graphically over the range of interest in terms of the contact angle and rivulet height. In this analysis the rivulet height is made dimensionless via the

capillary constant.

Subsequent analysis by various authors use one of the above general techniques of simplification of the equation governing the process [111, 122], direct numerical solution [43], or analytical techniques [57].

Experimental studies of rivulet widths, heights, velocity profiles and contact angle have been few in number, but have incorporated several different techniques to obtain the values of interest. In their original work, Towell and Rothfeld [142] measured the rivulet width and contact angle in the flowing rivulet. The width measurements were obtained from enlarged photographs of pictures taken of flowing rivulets, while the contact angle was measured using a method developed by Langmuir and Schaeffer [90] and used by Tomlinson and Patterson [59] and Peier *et al.* [111]. Nakagawa and Scott [107] used a pin and depth micrometer apparatus to obtain not only widths and heights of a flowing rivulet, but also the profile of the rivulet. Schmuki and Laso [118] measured both rivulet width and height in their study employing enlarged images of flowing rivulets via a video camera to obtain their width measurements and the pin and micrometer apparatus of Nakagawa and Scott [107] to measure the heights. A unique method of obtaining rivulet height values and rivulet profiles was developed by Kern [82, 83] in which the height values were obtained by using a light source located to one side of the rivulet to cast a shadow of the rivulet onto the plate. Knowing the location of the light source and the length of the shadow the rivulet height was determined. For rivulet profiles, the distortion by the rivulet of straight lines on the plate gave a method of determining the rivulet profiles. Fedotkin *et al.* [57] incorporated a laser doppler velocity meter to measure the rivulet width, height and also profile and the velocity distribution inside a rivulet flowing on a vertical surface.

The wettability of the surface used in rivulet studies is of primary importance

since this factor determines the rivulet characteristics of size, shape and linearity. Schmuki and Laso [118], while pointing out that a completely clean stainless steel surface is hydrophilic, concede that a contaminating film (possibly organic) is always present leading to a surface which is not completely clean and, therefore, hydrophobic. The crucial criteria for any cleaning procedure used in the experimental study then must be that it produce a surface of reproducible wetness.

With regard to the actual formation of the rivulet on the plate once it has been cleaned, several authors [42, 107, 118] have shown that reproducibility of the rivulet dimensions is dependent upon the history of formation of the rivulet. Both Nakagawa and Scott [107] and Schmuki and Laso [118] found that a rivulet would tend to flow on parts of the plate which had previously been wetted. Drying the plate between runs eliminated this problem. Nakagawa and Scott [107] further discuss the differences between rivulets which have been formed by starting with dropwise flow, increasing the flow rate to form a linear rivulet and those which have been formed by starting with dropwise flow, increasing the flow rate to form a linear rivulet, then decreasing the flow rate and finally increasing the flow rate again. They conclude that as long as a consistent method of rivulet formation is followed, reproducible results can be obtained.

Fundamental studies into the process of mass transfer in rivulet flows has received almost no attention in the literature to date, although this very process is often used to model such systems as trickle-bed reactors and packed columns. A recent study by Dassori *et al.* [43] modelled a mass transfer process with chemical reaction in partially wetted flat plate catalyst pellets using a rivulet flow model to describe the hydrodynamic problem and a diffusion-reaction model to describe the mass transfer-reaction process. The results of their theoretical model, which models the flow at the most basic level, show qualitative agreement with the global, macroscopic

results in real process equipment to which their results were compared. Of note is the fact that their mass transfer model considers only diffusion through the rivulet and not diffusion with convection as occurs in the real situation.

Another recent series of studies by Funk *et al.* [62, 63] employed a similar diffusion–reaction model to characterize reactions on partially-wetted catalyst pellets. They found that this simple rivulet flow model adequately described the reaction process which occurs on the catalyst pellet and confirmed their results with experimental work [64]. The experiments clearly demonstrated the effect of flow rate, liquid composition, wetting efficiency and liquid inlet conditions on the reaction rate.

2.4 Application to Structured Packing

Modelling of liquid distribution in random and structured packings has produced several different and interesting approaches to the solution of this problem. One approach used for both random and structured packings has been to simply model the packing as a series of tubes with liquid flowing down the wall of each. Shi and Mersmann [125] assumed equal flow in all channels in their study of the hydraulics in random packings while Stikkelmair and Stemmer [131] used experimental observations to determine the percentage of flow in each. These models, while providing some insight into liquid distribution and hydraulics in packings, do not adequately describe the process occurring in the packing.

Another approach used for random packings has been to apply a diffusion analogy to the liquid flow and derive the diffusion coefficient or dispersion term either from experimental data or a more theoretical approach. Cihla and Schmidt [41] used a gaussian distribution function to model the flow of liquid through

random packing and derived what is essentially the diffusion analogy for flow in random packings. This approach has subsequently been adopted by many authors [4, 18, 54, 74, 110, 114, 115, 129, 130] most of whom derive their diffusion coefficient from experimental observations.

The above described diffusion model of liquid flow through random packing suffers one serious drawback as pointed out by Groenhof [69] and Lespinasse [91]. The model assumes film flow of the liquid and not flow along discrete paths as is often observed experimentally. Several of the above models have corrected this deficiency and can, therefore, describe, to varying degrees of success, the overall flow distribution. Further problems with this diffusion model approach arise since the local distribution is not well characterized as many different local distributions can give rise to the same overall distribution. As pointed out by Bemer and Zuiderweg [18], the local flow distribution is of primary importance as it is the key to understanding the hydrodynamics and mass transfer in the packing.

The modelling of the distribution of liquid in structured packing has proceeded along similar lines as for random packing but because of the highly ordered structure of the packing, more mechanistic models have developed. These models, inspired by the work in random packings and attempting to overcome their weaknesses, have modelled the distribution by following the liquid through the packing describing its movement at each point. The simplest of these models is that of Bravo *et al.* [30], which uses a wetted-wall analogy to describe the flow and subsequent distribution in gauze-type packings. The problem here, as in random packings, is that the flow is often in discrete channels or rivulets for non-gauze packings. In subsequent work, Fair and Bravo [56] introduce a discount factor to describe the degree of total wetting of the packing but the factor itself is based only on known efficiency data and not on theoretical work.

More complete modelling of the distribution has been done by Nawrocki *et al.* [108], Stikkelman and Wesselingh [132], Stoter *et al.* [133] and Xu *et al.* [147]. These models use a discrete block model to determine where the liquid flows in the packing. In this method, the dimension of the blocks and their communication with each other depends on the type, size and surface characteristics of the packing itself as well as the local liquid flow rate in each block. Determination of the splitting factors required by these models is still done through experimental work but the fundamental nature of this approach makes it very promising for analyzing both liquid distribution and flow.

In modelling the distribution of the liquid in the column, the goal is to describe where the liquid is, and once the liquid can be tracked through the column, determine the amount of liquid at each location. Knowing the details of liquid location and quantity, more accurate predictions of the flow structure (film, rivulet, drops, jets, spray), interfacial area and mass transfer in the packing or column of interest can be made.

The predominant flow structure in the packing, as observed in experiments, is that of rivulet flow. While this type of flow is well accepted, little work has been done in this area. Several early authors [69, 91, 114, 126, 129, 130] disputed the film flow models of the liquid in the packing and instead assumed discrete flow (rivulet) models, the idea for which was based on experimental observations. While not actually modelling the rivulet flow, these studies provided the groundwork necessary for the application of their ideas by such people as Nawrocki *et al.* [108], Shi and Mersmann [125] and Zech and Mersmann [151]. These rivulet models, however, simplify the rivulet to a film flow approximation of the actual flow but, as stated by Michell and Furzer [105], the difference between laminar films and laminar rivulets decreases as the rivulet width increases.

Apart from the above studies, most research in this area avoids the previously described techniques and utilizes correlations of performance data. The literature is exhaustive in the experimental aspects of examining the performance data to determine the flow structure and interfacial area and only a relevant overview will be presented here.

From an experimental viewpoint, evaluation of the flow structure is not done directly but is inferred from measurements of the interfacial area using methods, such as the dye method (staining the packing surface using a dye) [85], the chemical method (absorption of a gas into or reaction of a gas with the liquid) [136], the photographic method [87, 126], light transmission method [33, 34, 87, 96, 143] and the ultrasonic pulse transmission [134]. An excellent overview of the above methods has been given by Landau *et al.* [88]. These methods provide indirect evidence of such phenomena as channelling, excessive wall flow, flooding and packing dryout by showing the change in interfacial area and mass transfer coefficients when the above phenomena occur.

By far the most experimentally studied area in packing research is that of column performance under actual operating conditions. These data provide direct values of the volumetric mass transfer coefficient as a function of material of packing [31, 40], height of packing [102], type of packing [28, 31, 100, 128], liquid flow rate [26, 28, 101], gas flow rate [27, 28, 30, 76, 101, 103], column diameter [30, 75, 102], gas-liquid system [30, 102, 128], reflux ratio [28] and column pressure [30, 75, 76, 100, 102, 103]. Upon tabulating and correlating these data, a large enough body of knowledge is acquired to allow design of new columns in the range of parameters studied [29, 76]. Outside this envelope, however, no reliable design is possible.

From a fundamental modelling aspect, these studies are useful since they provide

real data to which to compare theoretical predictions of interfacial area and mass transfer coefficients. These comparisons are invaluable, but the problem with this approach is that different experimental systems are used incorporating different distributors, packings, liquid and gas flow rates and column pressures. More importantly, no understanding of the fundamental process occurring in the column is gained. Using fundamental modelling, the contribution of the various parameters listed above can be quantified and analyzed allowing a more detailed knowledge of the transfer process.

Chapter 3

Applications¹

The analysis of fluid flow and mass transfer in linear, laminar rivulet flow began as an overall design study of mass transfer in structured packing in an industrial absorption process. The purpose of this study was to investigate the validity of modelling the liquid distribution, liquid flow and mass transfer occurring in the structured packing using a separate mechanistic model for each of the three processes. This type of basic approach to the complex interactions occurring in the packing would, if successful, help to disseminate some of the characteristics of this type of process and lead to a better understanding of the processes involved.

The model which was developed incorporated three separate models: one for liquid distribution, one for effective area (liquid flow) and one for mass transfer. The resulting simulations were used to investigate the effect of packing height, liquid load, initial maldistribution as well as differing initial distribution and liquid-solid contact angle on the packed column performance. The details of the construction of the model along with relevant results are contained in the following chapter.

¹A version of this chapter has been published. Nawrocki, Xu and Chuang 1991, Can. J. Chem. Eng. 69(6):1336-1343

Packing Type	10 MCP
Packing Material	Stainless Steel
Crimp Height, h , mm	10
Channel Base, $2 B_c$, mm	26
Height, H_1 , mm	100
Diameter, D_1 , mm	300
Surface Area, a_p , m^2/m^3	298
Void Fraction, ϵ	0.978
Channel flow angle from horizontal, α	45°

Table 3.1: Geometric Information, Structured Corrugated Packing

3.1 Mechanistic Models

To predict mass transfer in structured corrugated packing, mechanistic models were established for liquid distribution, effective area and mass transfer. These models are described below.

3.1.1 Liquid Distribution

The geometry of the structured corrugated packing used in this research is shown in Figure 3.1. The dimensions are shown in Table 3.1. The liquid distribution model was established based on the model presented by Xu *et al.* [147]. The following assumptions were made:

1. The liquid flowing on the surface of any channel is split at the next intersection point into two portions with fraction S_f flowing down through the intersection point and fraction $(1-S_f)$ flowing along the original channel. Figure 3.2 details the liquid flow at a specific packing junction while Figure 3.3 details the liquid flow and its distribution in the packing.
2. No mass transfer occurs between the two sides of the packing plate. The structure is similar to that of Mellapak but there are no holes in the plate surface.

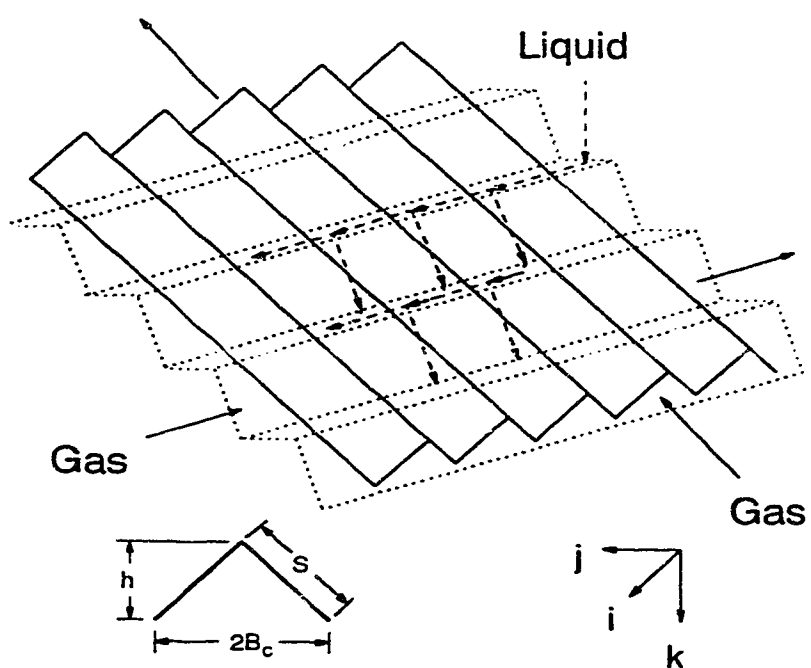


Figure 3.1: Flow Channel Arrangement and Geometry of Packing

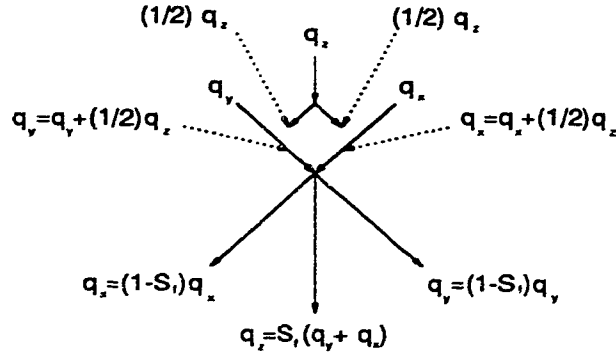


Figure 3.2: Model of Flow Splitting

3. No radial mixing occurs in the junction between two elements of packing.
4. The liquid reaching the column wall is partially reflected into the packing and partially flows down the wall according to the factor, S_f .

The liquid distribution (flow rate) matrix was established to calculate the flow rates at each intersection point. Together, Figures 3.1, 3.2 and 3.3 show the liquid distribution inside the packing and the assignment of the specific flow rate variables, q_x , q_y and q_z to each intersection point. The subscripts, i , j and k define the particular intersection point.

The flow rate matrix for the initial liquid distribution and at the top of each subsequent packing element is expressed as

$$Q_0 = [q(i, j, k)]_{s \times s} \quad \text{where } k = 0 \quad (3.1)$$

and the number of corrugated sheets per element can be determined from

$$s = \text{INT} \left(\frac{D_1}{h} \right) \quad (3.2)$$

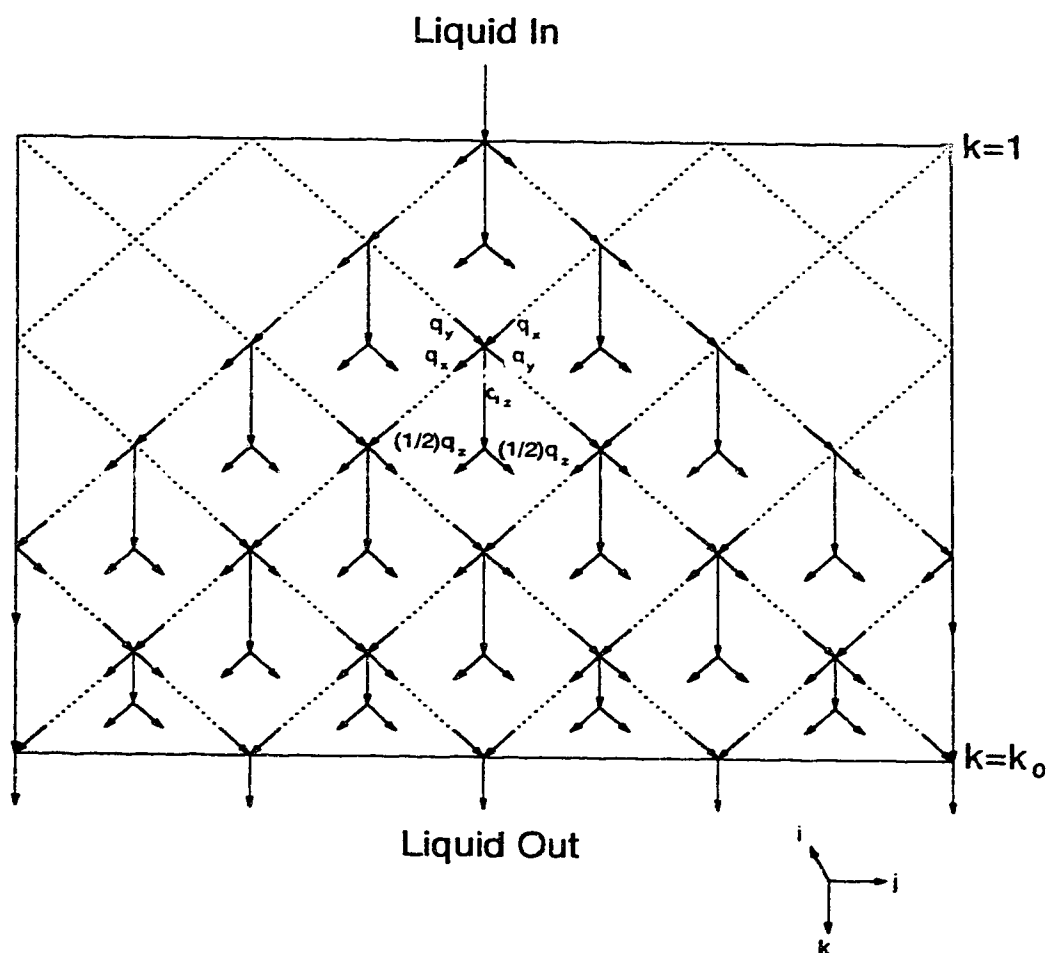


Figure 3.3: Model of Liquid Distribution Inside the Idealized Packing Structure Including Interactions at the Column Wall

Within each packing element, the flow rates are described by the following equations:

when $k = 1$

$$q_x(i, j, 1) = \frac{1}{2} (1 - S_f) q(i, j, 0) \quad (3.3)$$

$$q_y(i, j, 1) = \frac{1}{2} (1 - S_f) q(i, j, 0) \quad (3.4)$$

$$q_z(i, j, 1) = S_f q(i, j, 0) \quad (3.5)$$

when $k = 2$

$$q_x(i, j, 2) = (1 - S_f) \left[\frac{1}{2} q(i, j, 0) + q_x(i, j+1, 1) \right] \quad (3.6)$$

$$q_y(i, j, 2) = (1 - S_f) \left[\frac{1}{2} q(i, j, 0) + q_y(i, j-1, 1) \right] \quad (3.7)$$

$$q_z(i, j, 2) = S_f [q(i, j, 0) + q_x(i, j+1, 1) + q_y(i, j-1, 1)] \quad (3.8)$$

when $2 < k < k_0$

$$q_x(i, j, k) = (1 - S_f) \left[q_x(i, j+1, k-1) + \frac{1}{2} q_x(i, j, k-2) \right] \quad (3.9)$$

$$q_y(i, j, k) = (1 - S_f) \left[q_y(i, j+1, k-1) + \frac{1}{2} q_x(i, j, k-2) \right] \quad (3.10)$$

$$q_z(i, j, k) = S_f [q_x(i, j+1, k-1) + q_y(i, j-1, k-1) + q_x(i, j, k-2)] \quad (3.11)$$

when $k = k_0$

$$q(i, j, k_0) = q_x(i, j, k_0-2) + q_x(i, j+1, k_0-1) + q_y(i, j-1, k_0-1) + \frac{1}{2} [q_x(i, j+1, k_0-1) + q_x(i, j-1, k_0-1)] \quad (3.12)$$

The variable k_0 in the above equations is defined as

$$k_0 = \text{INT} \left(\frac{H_1 \tan \alpha}{B_c} + \frac{1}{2} \right) + 1 \quad (3.13)$$

For this packing, successive elements are rotated 90° from the preceding one which makes it necessary in the calculations to rotate the flow rate matrix at the top of each subsequent element before beginning the calculations for that element.

Using the above model, the liquid flow in the packing is determined completely. The model parameter S_f is obtained by fitting experimental liquid distribution data.

3.1.2 Effective Area

From the liquid distribution model, the flow rates in the three directions, x , y and z , at each intersection point are determined. The assumption is made that four rivulets are formed at each intersection point with flow rates q_x , q_y , $\frac{1}{2} q_z$, $\frac{1}{2} q_z$, respectively, where rivulets q_x and q_y flow along the channels and rivulets $\frac{1}{2} q_z$ and $\frac{1}{2} q_z$ flow vertically down the packing surface to the next intersection point.

The half-width of each rivulet is determined by Shi and Mersmann's empirical correlation [125]

$$x'_p = 1.745 q_L^{0.4} \nu_L^{0.2} \left(\frac{\rho_L}{\sigma_L g} \right)^{0.15} (1 - \cos \theta)^{-1} \quad (3.14)$$

This correlation assumes that the real rivulet, which has a curved profile, can be approximated as a rectangle with the same width and cross-sectional area as the real rivulet. This approximation is referred to in this work as the film model approximation to the full rivulet.

From the geometry of the particular packing, the specific wetted area for an element can be determined from

$$a_w = \frac{\sum_{i=1}^I 2 (x'_{p,x,i} + x'_{p,y,i}) l_{xy} + 8 x'_{p,z,i} l_z}{\pi D_1^2 (H/4)} \quad (3.15)$$

Assuming the stagnant zones in the corrugated sheet packing are small

$$a_e = a_w \quad (3.16)$$

3.1.3 Mass Transfer

The effective gas velocity in the packing is determined from the equation proposed by Bravo *et al.* [30]

$$U_{G,e} = \frac{U_G}{\epsilon \sin \alpha} \quad (3.17)$$

Using the relationship of Johnstone and Pigford [81], Bravo *et al.* [30] have expressed the gas-side mass transfer coefficient for structured packing as

$$N_{Sh,G} = 0.0338 N_{Re,G}^{\frac{4}{5}} N_{Sc,G}^{\frac{1}{3}} \quad (3.18)$$

where the dimensionless numbers in the above equation are defined as follows:

$$N_{Sh,G} = \frac{k_G d_{eq}}{\mathcal{D}_{AB}} \quad (3.19)$$

$$N_{Re,G} = \frac{d_{eq} \rho_G U_{G,e}}{\mu_G} \quad (3.20)$$

$$N_{Sc,G} = \frac{\mu_G}{\rho_G \mathcal{D}_{AB}} \quad (3.21)$$

and

$$d_{eq} = 2 B_c h \left(\frac{1}{2 B_c + 2 S} + \frac{1}{2 S} \right) \quad (3.22)$$

Using the falling film relationship for laminar flow, the effective liquid velocity is

$$U_{L,e} = \frac{3 q_L}{4 x_p' \delta_{dyn}} \quad (3.23)$$

where the liquid film thickness, δ_{dyn} , is defined as follows:

$$\delta_{dyn} = \left(\frac{3 \mu_L q_L}{x_p' \rho_L g \sin \alpha} \right)^{\frac{1}{3}} \quad (3.24)$$

The liquid-side mass transfer coefficient is based on penetration theory as described by Higbie [73] and for structured packing Bravo *et al.* [30] have expressed it as

$$k_L = 2 \left(\frac{\mathcal{D}_{AB} U_{L,e}}{\pi S} \right)^{\frac{1}{2}} \quad (3.25)$$

Since q_L , x_p' and δ_{dyn} vary throughout the packing, $U_{L,e}$ and k_L are not constant. In this study, the local effective liquid velocity $U_{L,e,i}$ and the liquid-side mass transfer coefficient $k_{L,i}$ are first calculated for each rivulet at each intersection point in the packing and the average liquid-side mass transfer coefficient of a layer is calculated from

$$k_L = \frac{1}{N} \sum_{i=1}^N k_{L,i} \quad (3.26)$$

The height of a transfer unit (HTU) for the individual phases can be calculated from

$$HTU_G = \frac{U_G}{k_G a_e} \quad (3.27)$$

$$HTU_L = \frac{U_L}{k_L a_e} \quad (3.28)$$

The height of an overall transfer unit is obtained from

$$H_{OG} = HTU_G + \frac{\tilde{G}}{\tilde{L}} HTU_L \quad (3.29)$$

3.2 Results and Discussion

With the above described models, the flow rate, width, dynamic thickness, effective velocity and liquid-side mass transfer coefficient of each liquid rivulet in the packing can be determined from the liquid flow mechanism. From these data, the wetted area and mass transfer coefficients for an entire element of packing were calculated. In this research, 300 mm diameter structured, corrugated packing was simulated. The packing contains approximately 340 intersection points at the cross-section and 3800 for each element. The mass transfer process simulated was the absorption of ammonia from air by water.

3.2.1 Effect of Packing Height

Figure 3.4 shows the liquid flow patterns as a function of packing height while Table 3.2 lists the number of liquid rivulets, wetted area, and mass transfer properties for varying numbers of packing elements. From these data it can be seen that the liquid spreads quickly in the first several elements of packing sharply increasing the wetted area (a_w) and sharply decreasing the overall height of a gas-phase transfer unit (H_{OG}). After the fifth element of packing (500 mm packing

	Number of Packing Elements			
	1	2	5	10
N	1322	9198	13172	13172
$a_w, m^2/m^3$	26.36	90.55	130.35	133.72
$k_G, m/s$	0.0176	0.0176	0.0176	0.0176
$k_L, m/s$	0.000321	0.000206	0.000207	0.000211
HTU_G, m	2.15	0.626	0.435	0.424
HTU_L, m	0.492	0.224	0.155	0.148
H_{OG}, m	2.22	0.658	0.457	0.445

Table 3.2: Wetted Area and Mass Transfer in Packing Elements for the System Air- NH_3 - H_2O , $ND = 7$, $\theta = 50^\circ$, $L_T = 15 m^3/(m^2 h)$

height) though, the flow pattern develops quickly as indicated by the constant number of rivulets and the differences due to packing height of both a_w and H_{OG} decrease. However, even with the stable flow pattern, the values of a_w and H_{OG} continue to improve with packing height because of the improving liquid distribution in the rivulets.

The above description of a stable flow pattern does not imply that no redistribution is required. As the liquid flows down the column, the percentage of the total liquid which is on the wall increases and must eventually be redistributed to reduce losses in column efficiency. Stoter *et al.* [133] have clearly demonstrated that a relatively flat flow pattern in the packing still has significant wall flow which requires redistribution.

It is interesting to note the change in k_L with increasing packing height. In the first several elements of packing, k_L decreases with an increase in packing height. In subsequent elements, k_L increases slightly. This behavior may be attributed to the fact that, in the first several elements, the number of rivulets increases steeply resulting in a decrease in the effective rivulet velocity. However, after the fifth

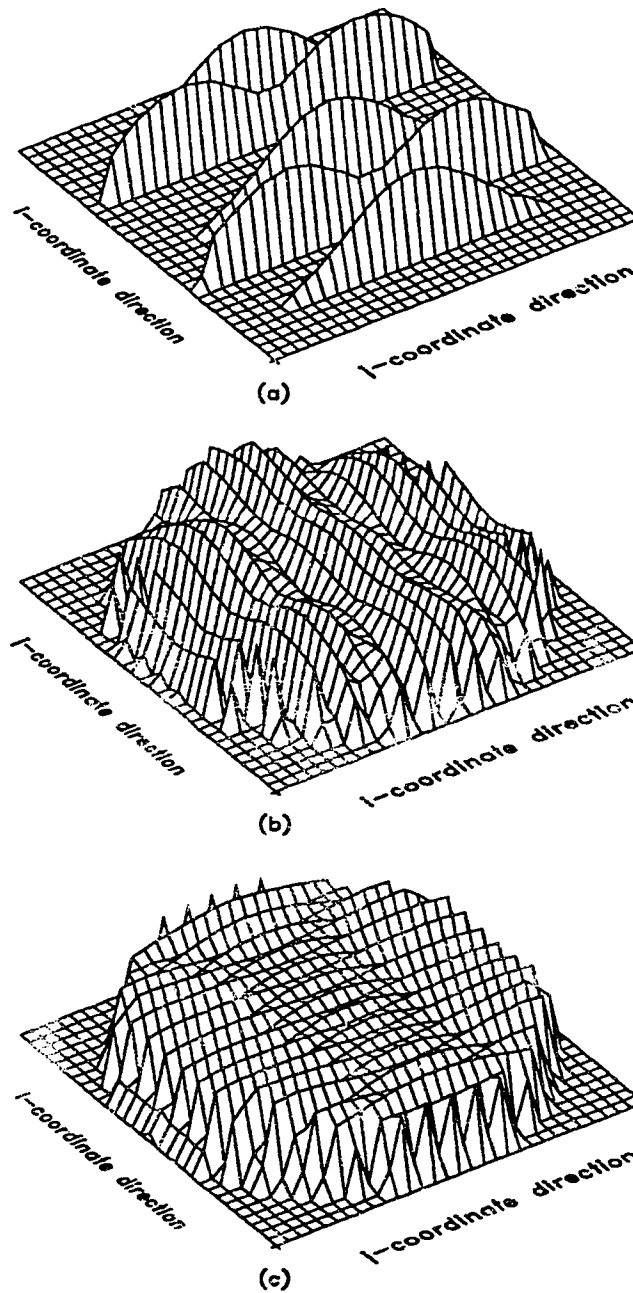


Figure 3.4: Liquid Flow Patterns a) First element b) Second element c) Fifth element

element, the number of rivulets becomes constant while the liquid distribution continues to improve. The end result is a decrease in the difference in rivulet velocities and an increase in the value of k_L within the element. With traditional correlations, only one superficial value for k_L is used which does not reflect the true situation in the packing.

3.2.2 Effect of Liquid Load

With increasing liquid load, the number of rivulets does not change except at very high loads. However, the wetted area and the liquid-side mass transfer coefficient both increase, as shown in Figures 3.5 and 3.6, respectively. For the air- NH_3 - H_2O system, the liquid-side mass transfer coefficient does not affect the mass transfer process significantly and the decrease in H_{OG} as shown in Figure 3.7 is attributed mainly to the increase in wetted area. The simulations also show that even under as high a liquid load as $60 \text{ m}^3/(\text{m}^2 \text{ h})$, the packing is not wetted totally regardless of the height of packing because of the large value for the surface tension of water.

3.2.3 Effect of Number of Initial Distribution Points

Figure 3.8 illustrates how the wetted area of the packing increases with an increase in the number of initial distribution points. However, after several elements, the wetted area assumes a constant, maximum value as the number of rivulets, shown in Figure 3.9, which determine wetted area, also attain their maximum value. These maxima are attained quite quickly for cases with more than four distribution points indicating that the structured corrugated packing exhibits good self-distributing properties. For this reason, this kind of packing is often used in some types of gas-liquid distributors. Even though the packing has good self-distribution properties,

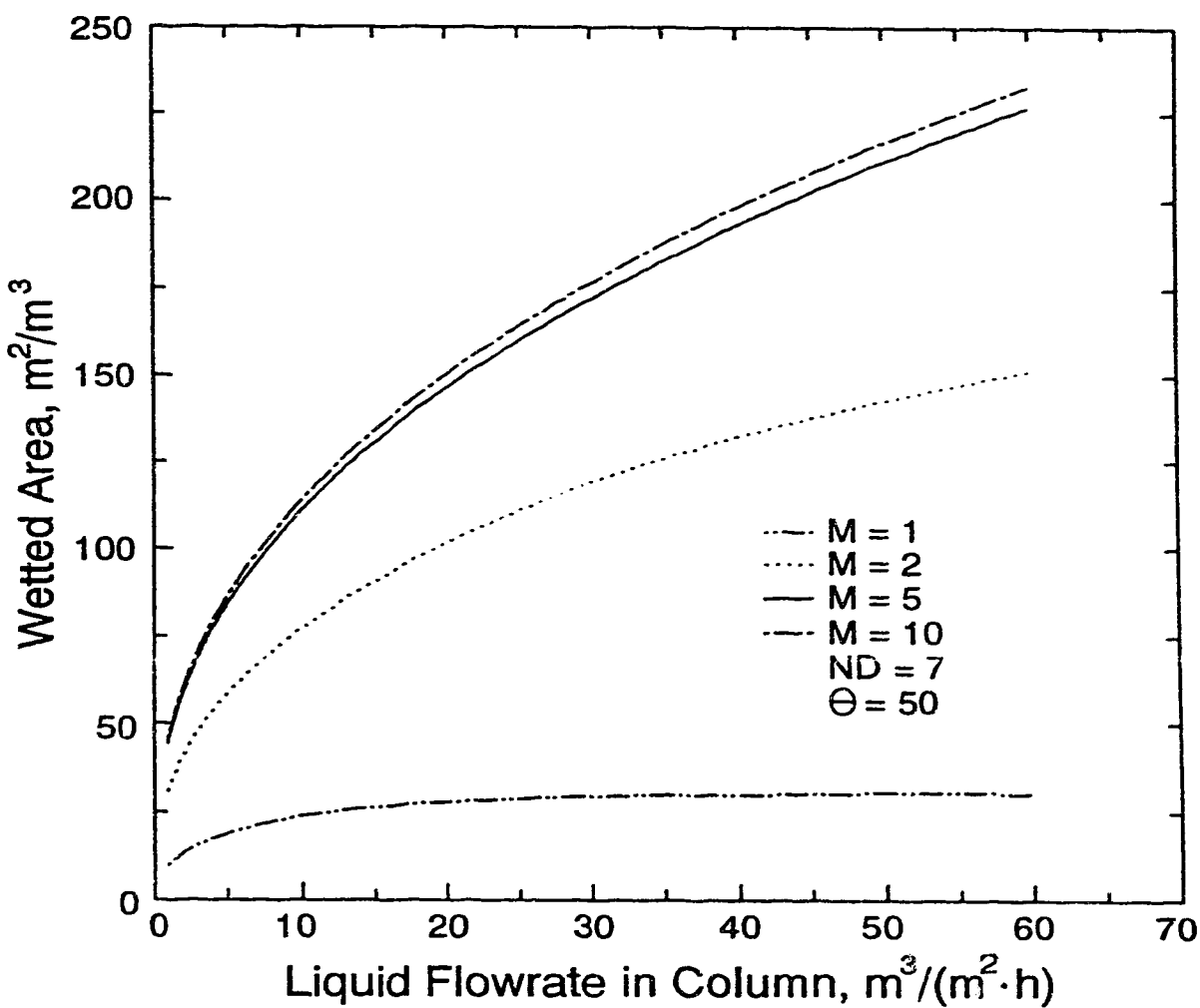


Figure 3.5: Packing Wettability as a Function of Liquid Flow Rate for Various Packing Heights

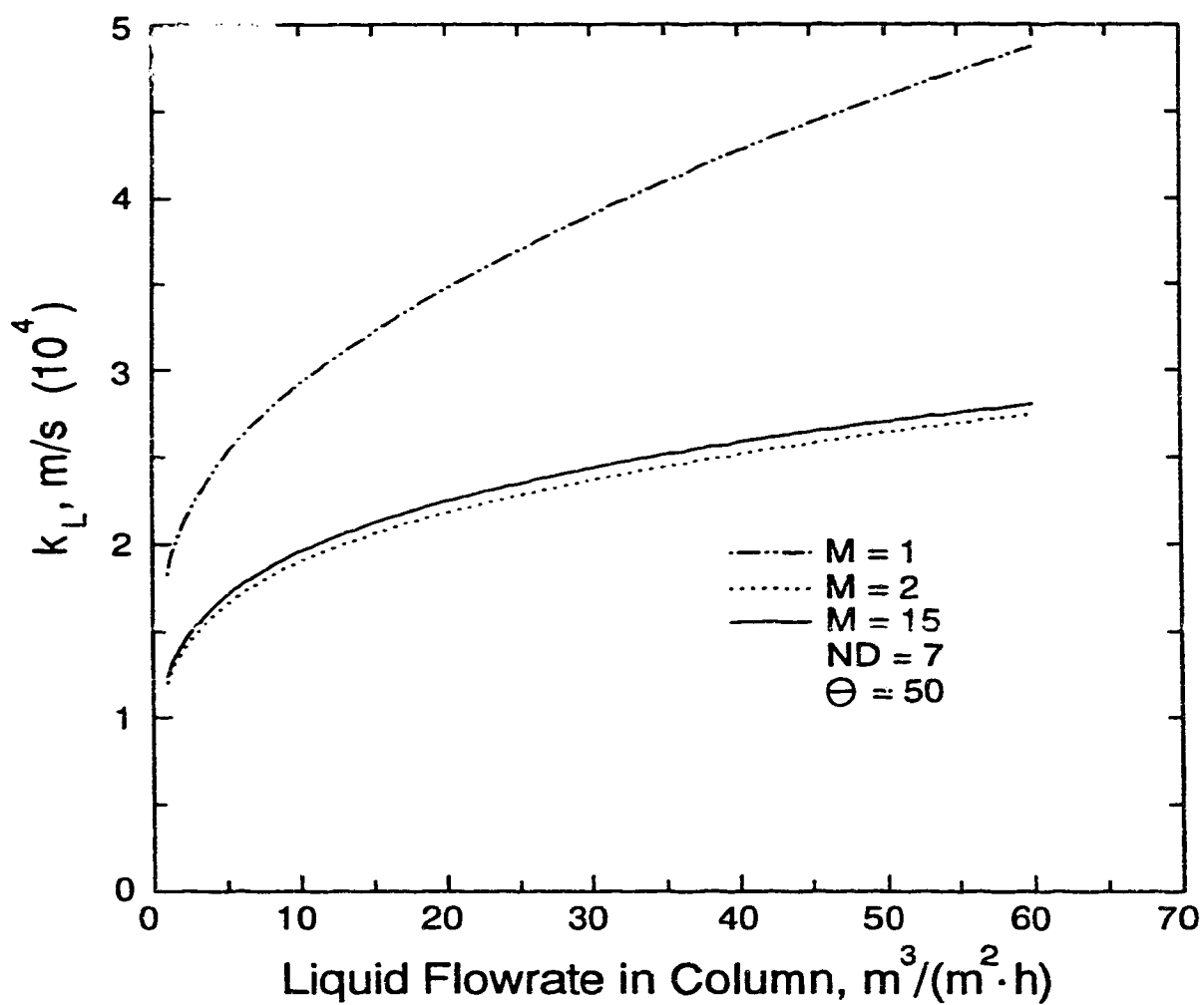


Figure 3.6: Mass Transfer Performance as a Function of Liquid Flow Rate for Various Packing Heights

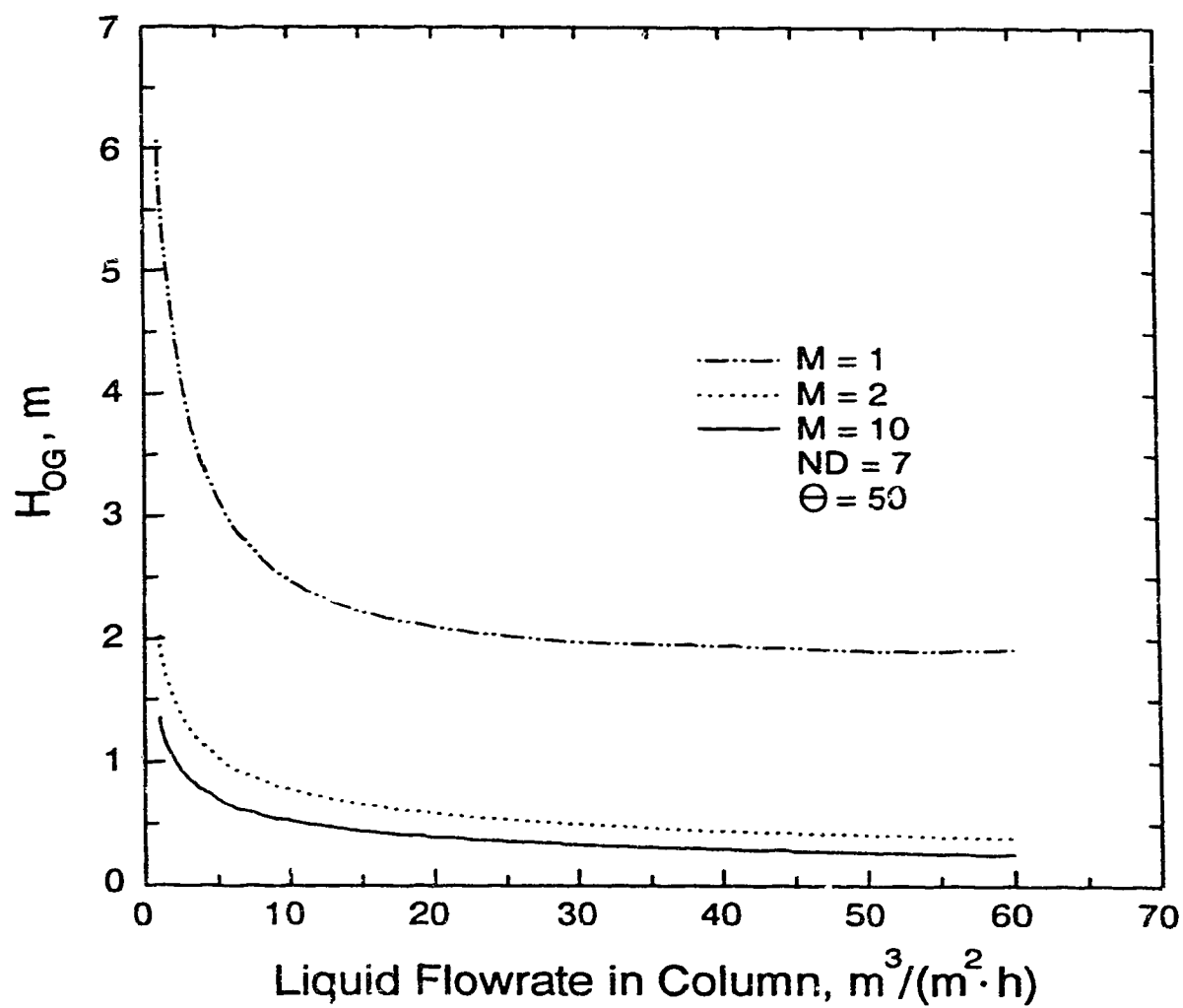


Figure 3.7: Packing Wettability as a Function of Liquid Flow Rate for Various Packing Heights

the initial distributor is still very important since, with good initial distribution, the packed height for liquid pre-distribution can be decreased greatly. This characteristic is seen quite clearly in Figure 3.9 for one distribution point where the number of rivulets increases very slowly especially in packing element five. In this element, the liquid has travelled through the preceding elements in such a way that it is not effectively distributed at the top of element five and therefore does not wet this element properly. The wetted areas of Figure 3.8 show this trend as they are far smaller in the case of one distribution point than they are for any of the other number of distribution points.

3.2.4 Effect of Liquid–Solid Contact Angle

The wettability of the packing surface depends mainly on the liquid–solid contact angle while the contact angle itself is related to the liquid's physical properties especially surface tension and the surface energy of the packing material. The measured values for the contact angle given in the literature often do not agree since the geometric condition of the solid surface has not been taken into account. In this study the contact angle value used was for a typical stainless steel surface as described by Krell [86].

Figure 3.10 shows that the wettability of the packing surface is very sensitive to the liquid–solid contact angle. It can be seen in this figure that the wetted area of packing decreases significantly with increasing contact angle which results in an increase in H_{OG} . In the past 20 years, much research work has been done to decrease the liquid–solid contact angle by treating the packing surface either physically or chemically thereby increasing wettability. Chuang and Miller [40] demonstrated that by increasing the wettability of a surface the efficiency would similarly increase. Figure 3.10 clearly shows that any decrease in the contact angle greatly increases

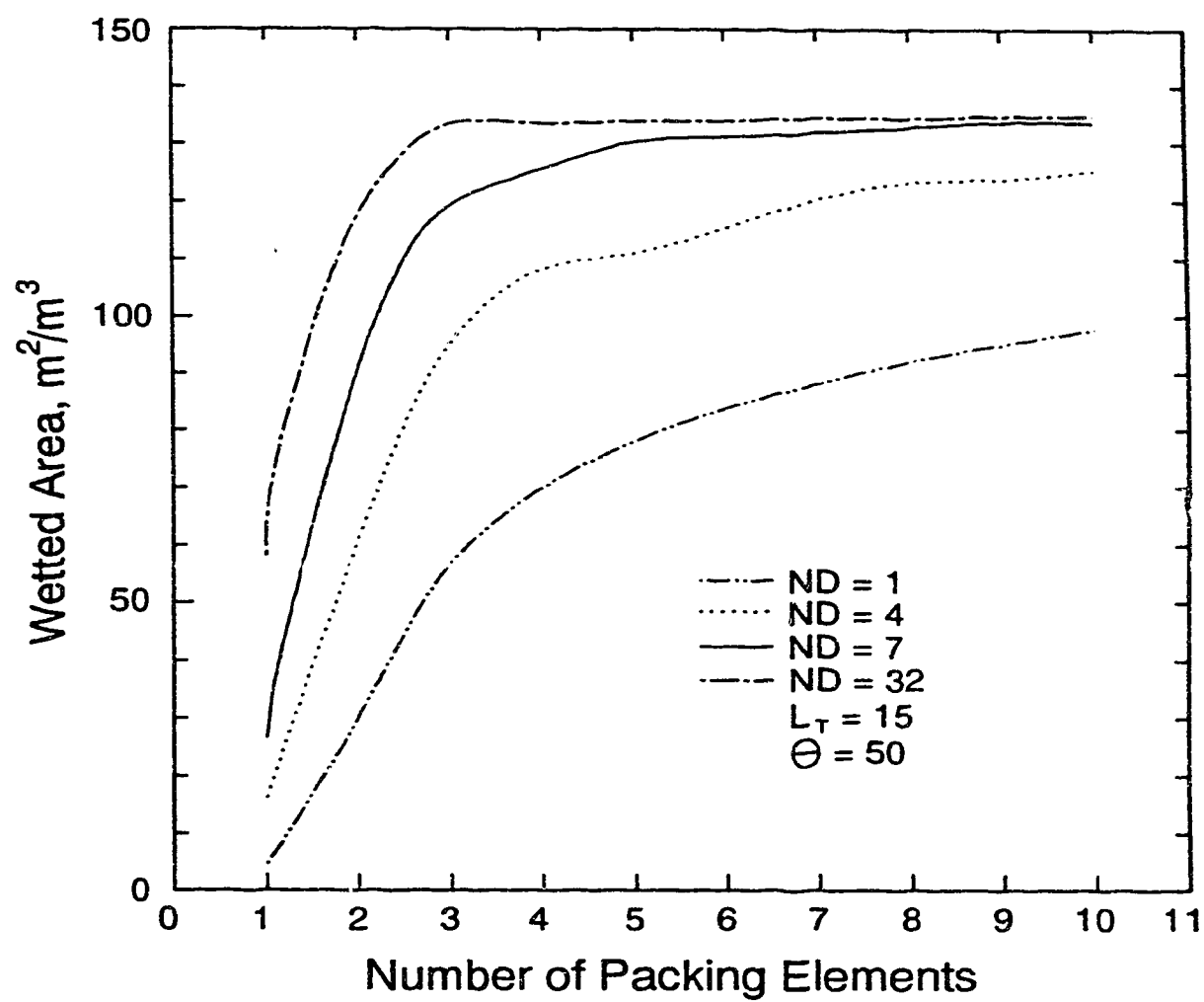


Figure 3.8: Wettability as a Function of Packing Height for Various Number of Initial Liquid Distribution Points

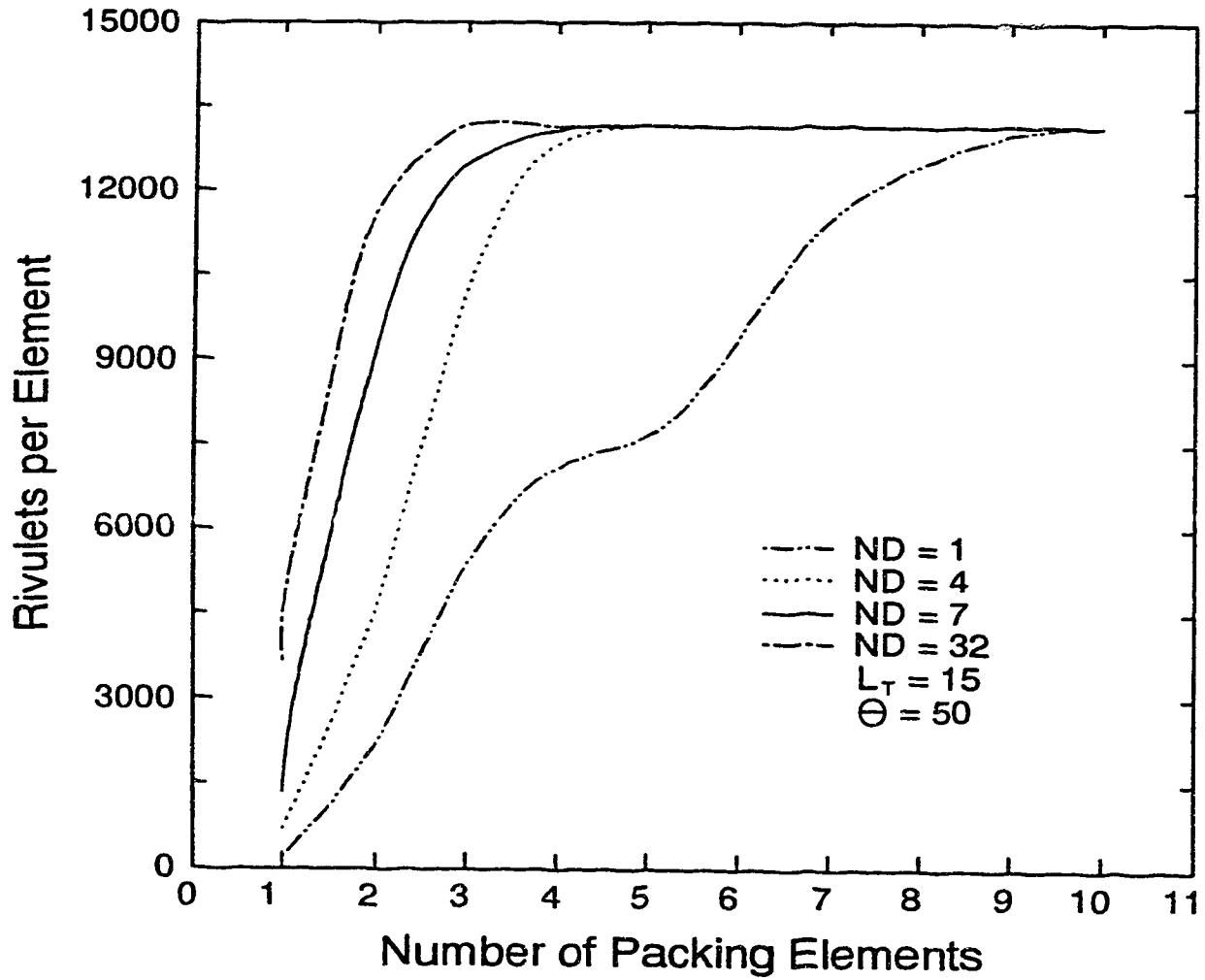


Figure 3.9: Number of Rivulets as a Function of Packing Height for Various Number of Initial Liquid Distribution Points

the wetted area with a resulting increase in the efficiency of the packing.

Figure 3.10 also indicates that the liquid-side mass transfer coefficient would decrease with improving packing surface wettability because the effective liquid velocity would decrease. Most of the published literature assumes that the packing is totally wetted in the determination of k_L from penetration theory. If the packing is not totally wetted, the calculated value of k_L will be smaller than the true value. For evenly and totally wetted packing like that used in this study, k_L is approximately $5.6 \times 10^{-5} - 2.2 \times 10^{-4} \text{ m/s}$, while if the packing is partially wetted k_L is $1.2 \times 10^{-4} - 2.7 \times 10^{-4} \text{ m/s}$. The comparison of these k_L values can be seen in Figure 3.16. It can be seen that as the contact angle decreases, the values of k_L predicted by the model presented here approach those predicted by the model of Bravo *et al.* [30]. This result is reasonable since, if the value of the contact angle is zero, the packing can be assumed to be totally wetted given a sufficient liquid load and the two models become equivalent.

3.2.5 Effect of Initial Maldistribution

In this research, two kinds of initial maldistribution are considered. The first is uneven distribution points in the cross-section with even distribution from each point while the second is uneven liquid flow from the distribution points with evenly spaced points in the cross-section. The first case is illustrated in Figure 3.11 where six of the seven distribution points are put in a circular pattern around the seventh one with an inner zone of $\frac{1}{4}$, $\frac{1}{2}$ and $\frac{3}{4}$ of the total cross-sectional area of the column. The distribution points for the $\frac{1}{2}$ -inner area case are geometrically evenly spaced where as for the $\frac{1}{4}$ and $\frac{3}{4}$ -area cases they are not. The unevenly distributed liquid analysis is illustrated in Figure 3.12 where equally spaced distribution points were used with the flow first being evenly distributed in the column cross-section (1-1-1)

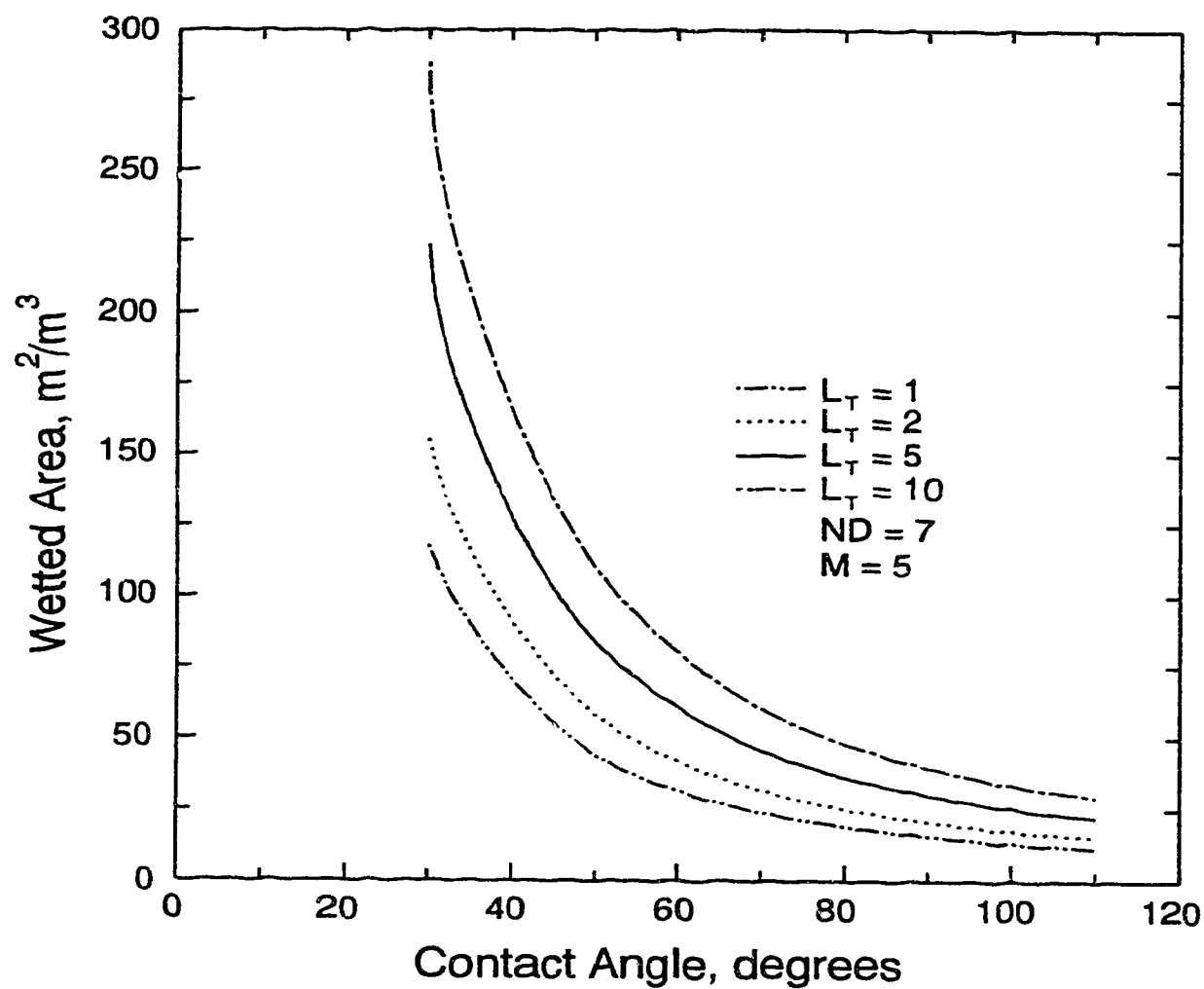


Figure 3.10: Effect of Contact Angle on Wettability for Various Initial Liquid Flow Rates

and then shifted to one-half of the column cross-section in two steps. The first shift used a distribution of (0.5–1–1.5) in the cross-section while the second was (0–1–2) which meant that only half of the packing was being irrigated.

Figure 3.13 shows the results of the unequal flow maldistribution from evenly spaced distribution points and demonstrates that uneven liquid distribution has a significant negative effect on the wetted area. Figure 3.14 illustrates the effect of unequally spaced distribution points. In this case, the negative effect on the wetted area is present but is not as significant as in the previous case and is restricted to the first five elements. Interestingly, the packing recovers very well from this type of maldistribution due to its idealized structure as well as its inherent good distribution properties.

A final note is that the results shown in this section have been generated using a rather small diameter column and that more significant decreases in wetted area would occur in larger diameter columns as maldistribution effects are enhanced as the column diameter increases.

3.2.6 Comparison With Published Results

The packing surface simulated in this research is roughened so that the surface can be wetted well. Krell [86] has given the relationship of the contact angle for the stainless steel–water system as a function of the mean depth of roughness. On the basis of Krell's results, a contact angle of 50° was used in these simulations.

Figure 3.15 compares the simulated values of wetted area with those predicted by the correlation of Onda [109] and demonstrates that the method presented in this study can predict reasonable values of wetted area in structured, corrugated packing. In using Onda's correlation to compare the values of wetted area, it must

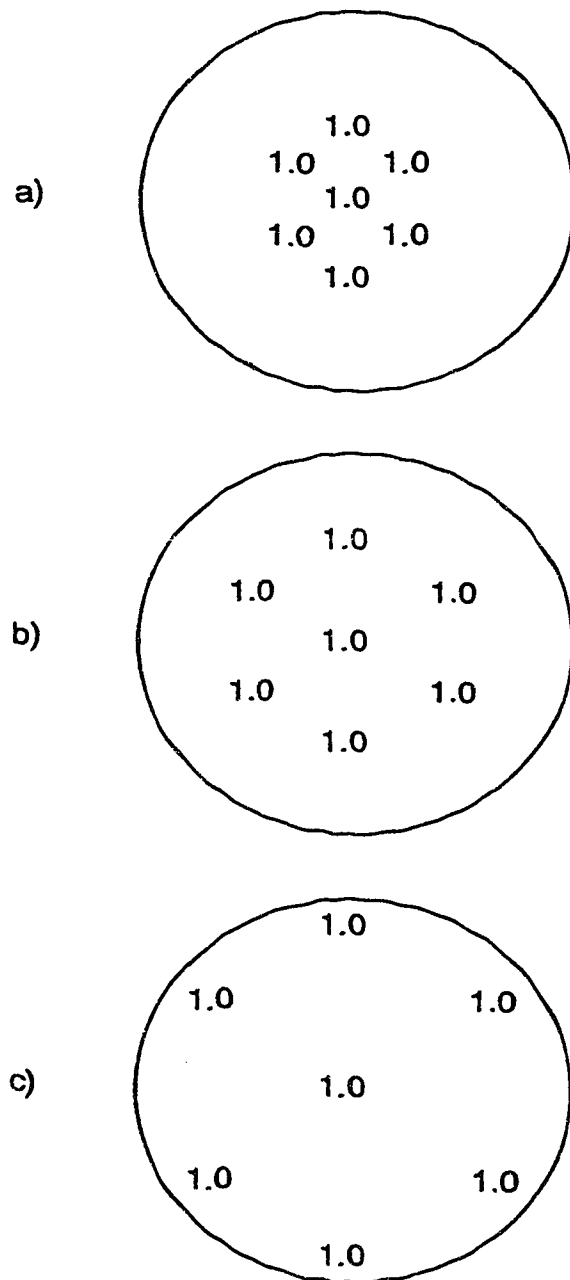


Figure 3.11: Liquid Distribution Arrangement for Unequal Area Maldistribution.
a) 1/4-area b) 1/2-area c) 3/4-area

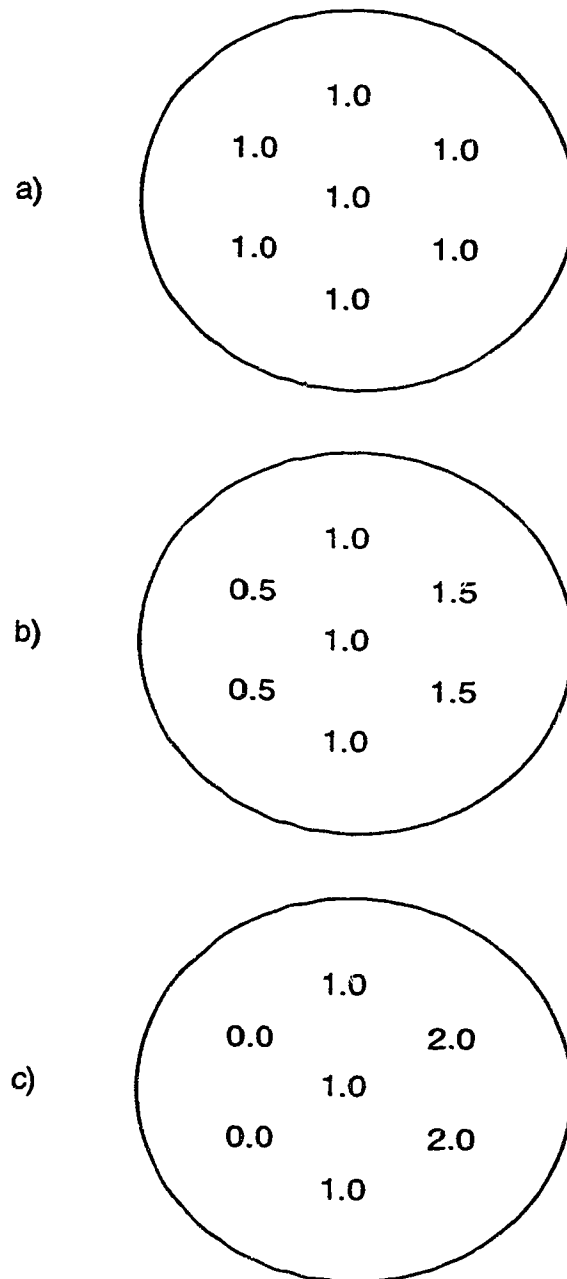


Figure 3.12: Liquid Distribution Arrangement for Unequal Flow Maldistribution. a) Even Distribution b) First Shift c) Second Shift

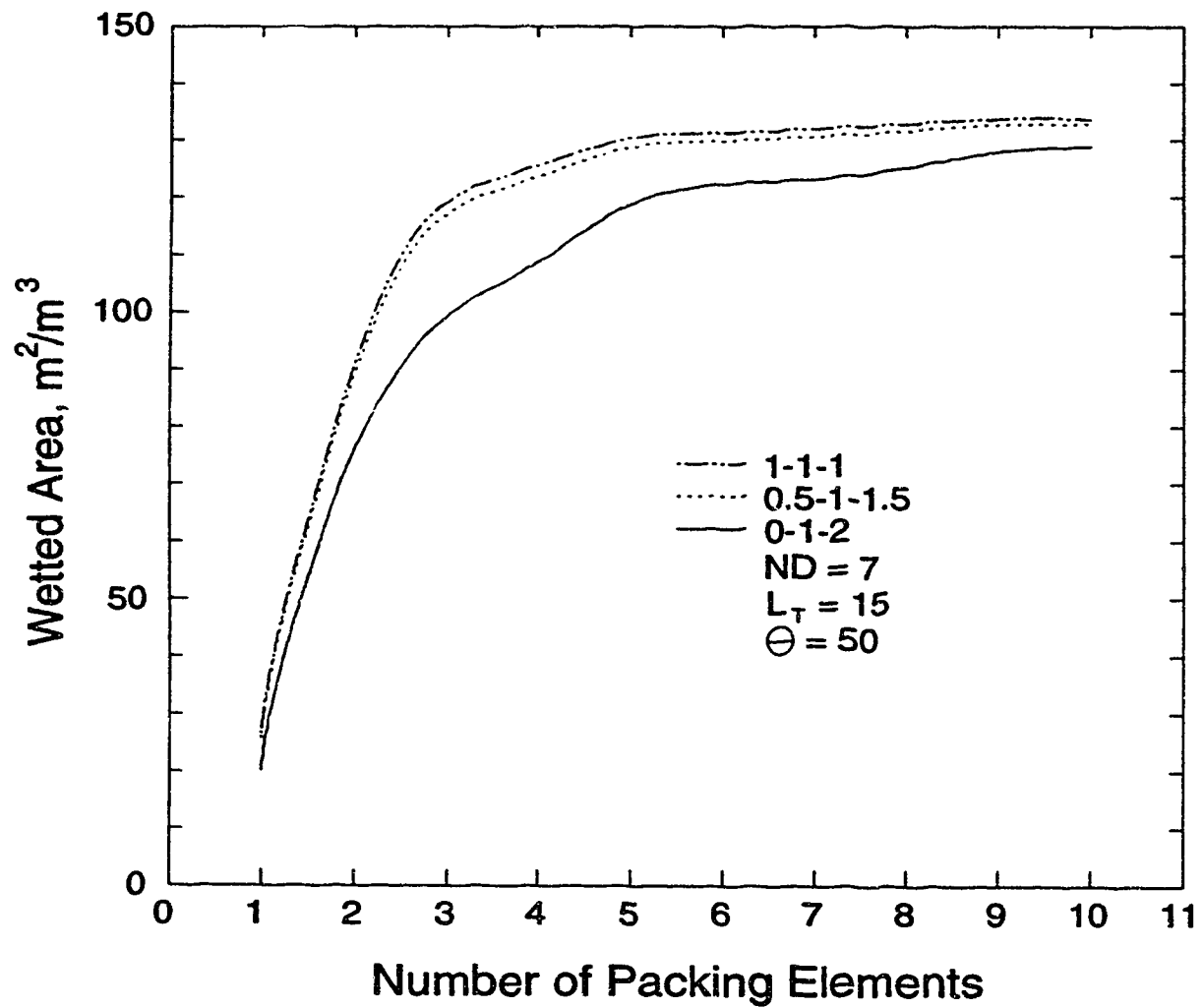


Figure 3.13: Effect of Unequal Flow Initial Maldistribution on Wetted Area as a Function of Packing Height

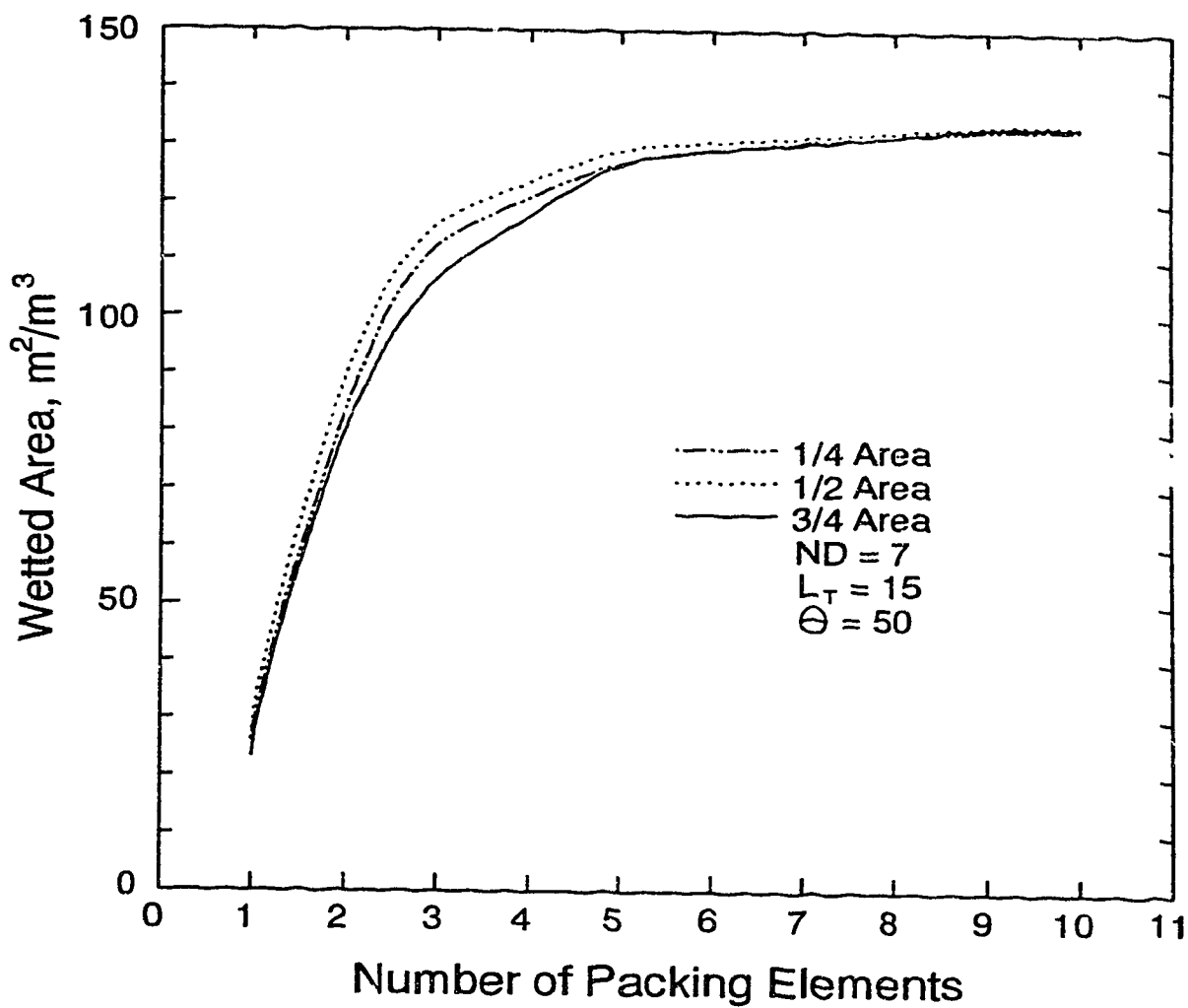


Figure 3.14: Effect of Unequal Area Maldistribution on Wetted Area as a Function of Packing Height

be recognized that, in fact, Onda's correlation is based solely on data from random packing. The reason for choosing this correlation as the basis of comparison is because it is the only general predictive method for determining values of wetted area.

Figure 3.16 compares the values of k_L predicted by the method presented in this study with those predicted by the method of Bravo *et al.* [30]. As stated previously, because the method presented here does not use the assumption of totally wetted packing, the simulated values of k_L must be larger than those predicted by Bravo *et al.* [30] when the packing is partially wetted and equal to them when the liquid flow rate is high enough to totally wet the packing ($>60 \text{ m}^3/(\text{m}^2 \text{ h})$). Clearly then, Figure 3.16 indicates that this method predicts consistent results for k_L .

In Figure 3.17, experimental absorption data for the air- NH_3 - H_2O system are compared with simulated values of H_{OG} . The difference between the experimental and theoretical values of H_{OG} is quite large although some of the difference may result from enhanced absorption due to end effects in the experimental data, which is not accounted for in the simulations. The major problem with the experimental data of Xu *et al.* [147] appears to be due to end effects since this data was obtained from a column with a very small packed height (0.6 m) where these effects become very significant especially with a system such as air- NH_3 - H_2O . Further uncertainty with this experimental data arises since it does not agree with data published by Meier *et al.* [103] who used a smaller diameter column and larger packing height. Clearly, more experimental data are required to test the simulated H_{OG} data. What is clear is that the simulated H_{OG} results show the correct trend and are reasonable when compared with the limited experimental data available.

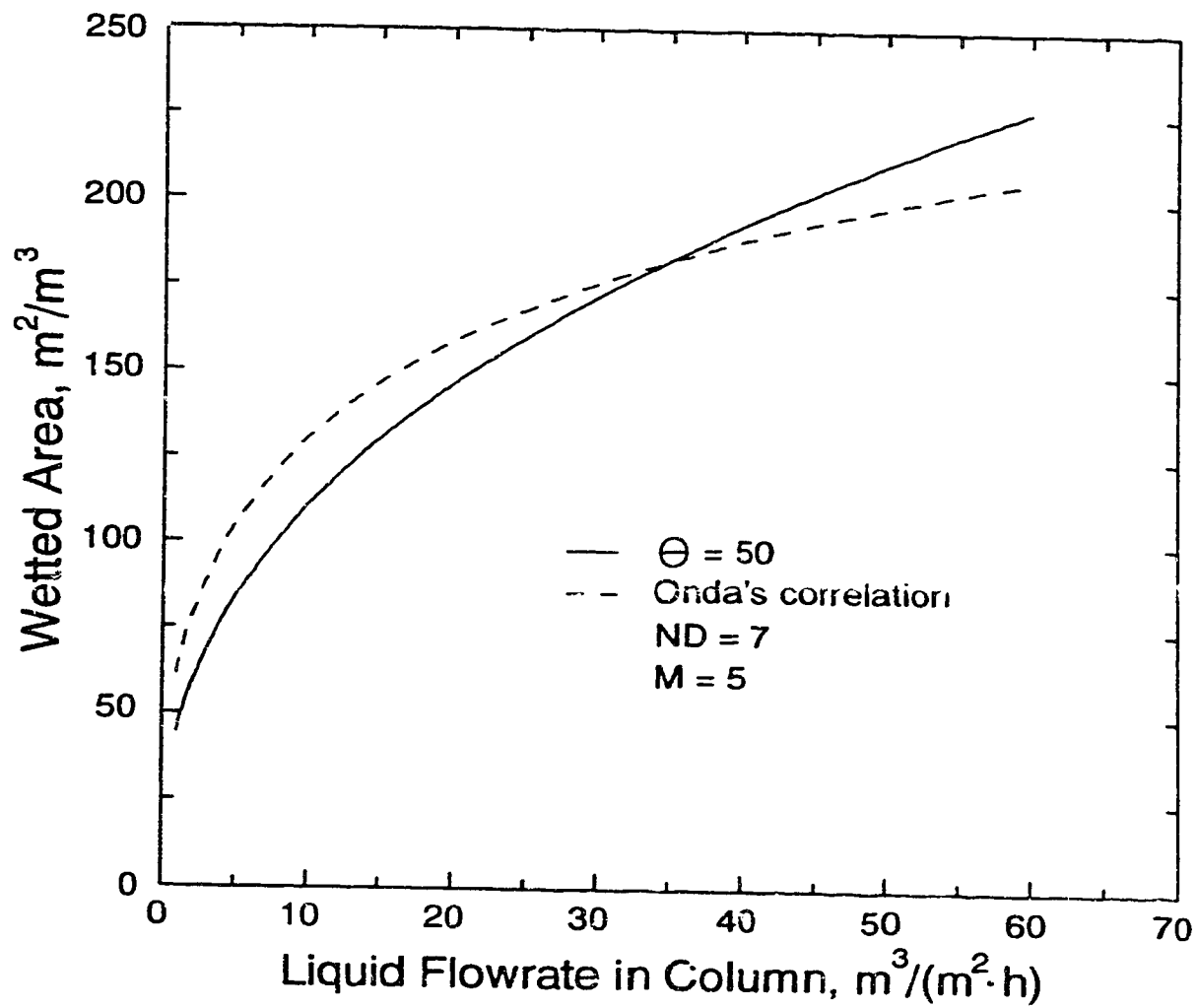


Figure 3.15: Comparison of Reported and Calculated Wetted Areas as a Function of Liquid Flow Rate

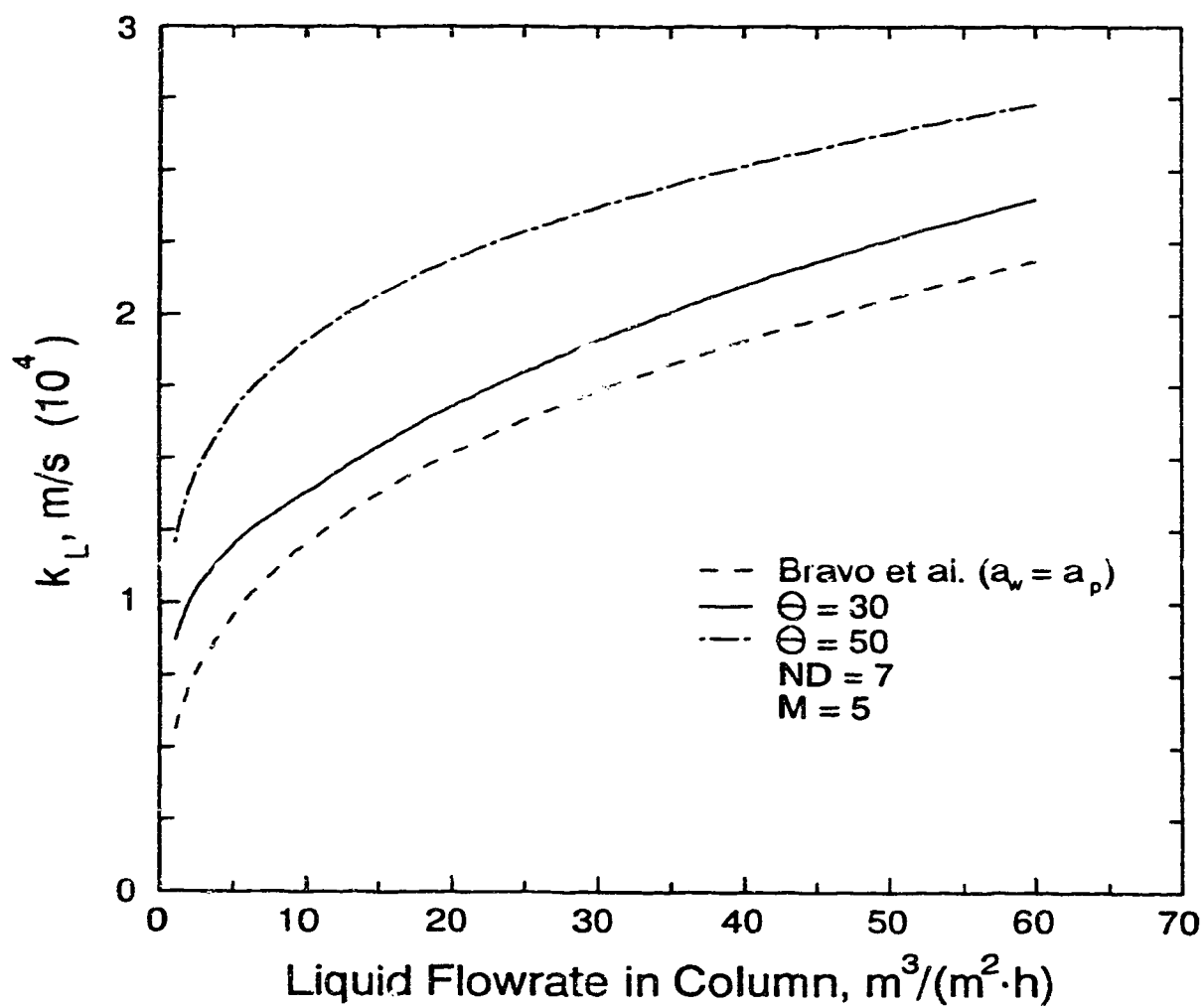


Figure 3.16: Comparison of Reported and Calculated Liquid-Side Mass Transfer Coefficients as a Function of Liquid Flow Rate

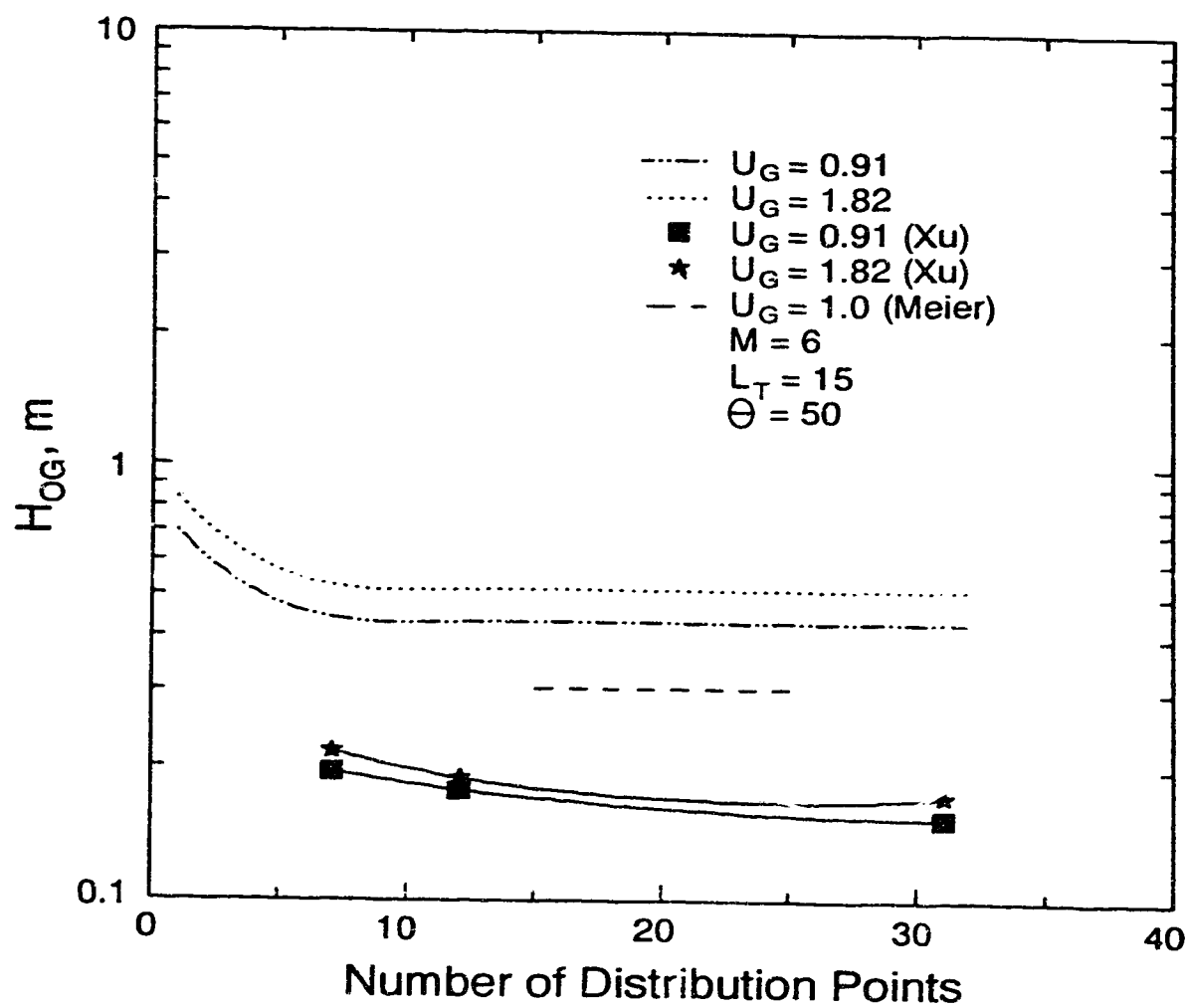


Figure 3.17: Comparison of Reported and Calculated Height of an Overall Gas-Phase Mass Transfer Unit as a Function of the Number of Distribution Points

Chapter 4

Governing Equations¹

The rivulet flow problem studied in this research is composed of three distinct portions, each of which requires a separate solution formulation. This chapter outlines the methodology used to arrive at the governing equations for each portion and the appropriate solution technique used.

Before proceeding however, some qualifying remarks must be made. For the coordinate systems used in the following methods, the cartesian system used in the solution of the profile equations has the y -axis pointed in a direction opposite to the normal y -axis direction as shown in Figure 4.1. This change in direction is done to provide positive values of rivulet height and does not affect the solution in any manner. All other coordinate systems are either normal cartesian, x, y, z , or bipolar-type, ξ, η, z , systems.

The scaling of the three sets of governing equations was done separately as no common scaling variables are possible. The profile equations are scaled using

¹A version of this chapter has been submitted for publication. Nawrocki and Chuang, 1993, Can. J. Chem. Eng.

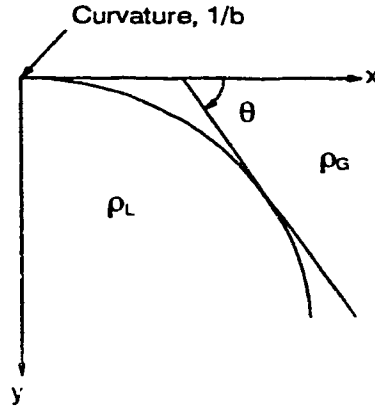


Figure 4.1: Geometry and Nomenclature For a Half Profile of a Sessile Drop Resting on a Flat, Horizontal Solid Surface. Solid Surface Not Shown

the parameter, c . The length variables in both the Navier-Stokes and convection-diffusion equations are scaled utilizing the aspect ratio of the rivulet. The velocity terms in these latter two equations are scaled differently, however, since the convection-diffusion equation has differentials with respect to the z -direction. The exact scaling variables have been outlined in the following sections along with the development of the equations.

4.1 Derivation

4.1.1 Profile Equations

The equations which describe the two-dimensional free interface of the rivulet are derived from the Laplace equation, which for the case of a sessile drop resting

on a horizontal surface, is expressed as follows:

$$\Delta P = \sigma_L \left(\frac{1}{r_1} + \frac{1}{r_2} \right) \quad (4.1)$$

In the case of rivulet flow, there is symmetry about one meridional cross-section but no cylindrical symmetry as is the case for sessile drops. The cylindrical curvature is, in fact, equal to zero leaving only the meridional curvature to be considered and reducing the above equation to the following:

$$\Delta P = \sigma_L \left(\frac{1}{r_1} \right) \quad (4.2)$$

Using this reduced form of the Laplace equation, and assuming that the profile is not affected by the flow inside but only by surface tension and gravity effects, the latter of which change if the plate is inclined, it is possible to equate the excess hydrostatic pressure at any point along the interface to the excess pressure as expressed above via the Laplace equation. The solution of the resulting equation is

$$\sigma_L \sin \left(\frac{\theta}{s'_p} \right) = \frac{\sigma_L}{b'} + \Delta \rho g y'_p \cos \alpha \quad (4.3)$$

and leads to the relationships for the height, width, surface area per unit length, and volume per unit length of the rivulet shape as listed below [72].

height:

$$Y_p = -\frac{1}{B \cos \alpha} + \sqrt{\frac{1}{B^2 \cos^2 \alpha} + \frac{2}{\cos \alpha} (1 - \cos \theta)} \quad (4.4)$$

width:

$$\frac{dX_p}{d\theta} = \frac{\cos \theta}{\left[\frac{1}{B^2} + 2 \cos \alpha (1 - \cos \theta) \right]^{\frac{1}{2}}} \quad (4.5)$$

surface area per unit length:

$$\frac{dS_p}{d\theta} = \frac{1}{\left[\frac{1}{B^2} + 2 \cos \alpha (1 - \cos \theta) \right]^{\frac{1}{2}}} \quad (4.6)$$

volume per unit length:

$$V_p = 2X_p \left[Y_p + \frac{1}{B \cos \alpha} \right] - \frac{2 \sin \theta}{\cos \alpha} \quad (4.7)$$

The above variables have been non-dimensionalized as follows

$$\begin{aligned} X_p &= x'_p c^{\frac{1}{2}} & Y_p &= y'_p c^{\frac{1}{2}} & B &= b' c^{\frac{1}{2}} \\ S_p &= s'_p c^{\frac{1}{2}} & V_p &= v'_p c & \epsilon &= \frac{(\rho_L - \rho_G)g}{\sigma_L} \end{aligned} \quad (4.8)$$

where the prime denotes dimensional quantities.

The boundary conditions for the solution of the above equations arise from the fact that at the apex of the interface the contact angle is zero as are the width, height, surface area and volume.

$$\theta = 0 \quad X_p = Y_p = S_p = V_p = 0 \quad (4.9)$$

4.1.2 Flow Equations

Once the profile of the two-dimensional interface, which determines the free interface of the rivulet, is obtained, the flow field inside this domain can be determined. This flow field is generated through the solution of the Navier-Stokes equations, which have been simplified according to the assumptions applicable to this type of problem. The assumptions involved are:

1. The shape of the free interface is not affected by the flow inside it.
2. The rivulet is of constant height and width.
3. One-dimensional flow parallel to the z -axis, $v_x = v_y = 0$
4. Fully developed flow, $\frac{\partial}{\partial z} = \frac{\partial^2}{\partial z^2} = 0$
5. Steady, uniform, laminar flow, $\frac{\partial}{\partial t} = 0$
6. Incompressible, Newtonian liquid, $\Delta \rho_L = 0$

7. No shear at the gas-liquid interface, $\frac{\partial v_x}{\partial n}(\text{interface}) = 0$
8. No slip at the liquid-solid interface, $v_z(x, 0) = 0$

With the above assumptions, the Navier-Stokes equations reduce to the following:

continuity:

$$\frac{\partial v_z}{\partial z} = 0 \quad (4.10)$$

x -momentum:

$$\frac{\partial P}{\partial x} = 0 \quad (4.11)$$

y -momentum:

$$\frac{\partial P}{\partial y} = -1 \quad (4.12)$$

z -momentum:

$$\frac{\partial^2 v_z}{\partial x^2} + \left(\frac{x'_p}{y'_p}\right)^2 \frac{\partial^2 v_z}{\partial y^2} = -1 \quad (4.13)$$

The above equations have been non-dimensionalized as follows

$$x = \frac{x'}{x_p} \quad y = \frac{y'}{y_p} \quad v_z = \frac{v'_z}{(x'_p)^2 (g/\nu_L)} \quad P = \frac{P'}{\rho_L g y'_p \sin \alpha} \quad (4.14)$$

where the prime denotes dimensional quantities.

The boundary conditions required for the solution of the above equations are found in the simplifying assumptions listed previously. Specifically, they are zero slip of the fluid at the liquid-solid interface and zero shear at the gas-liquid interface. These two conditions are expressed as follows:

$$v_z(x, 0) = 0 \quad \frac{\partial v_z}{\partial n}(\text{interface}) = 0 \quad (4.15)$$

Using these boundary conditions to solve the z -momentum equation produces the desired flow field inside the rivulet.

4.1.3 Convection-Diffusion Equation

The development of the equations describing the mass transfer process occurring within the flowing rivulet begins with the full form of the convection-diffusion equation without reaction

$$\frac{\partial(u_x C_A)}{\partial x} + \frac{\partial(u_y C_A)}{\partial y} + \frac{\partial(u_z C_A)}{\partial z} + \frac{\partial C_A}{\partial t} = \mathcal{D}_{AB} \left(\frac{\partial^2 C_A}{\partial x^2} + \frac{\partial^2 C_A}{\partial y^2} + \frac{\partial^2 C_A}{\partial z^2} \right) \quad (4.16)$$

For the particular flow field to which this equation is to be applied, the following assumptions can be made:

1. One-dimensional flow parallel to the z -axis, $u_x = u_y = 0$
2. Density of the mixture is constant, $\frac{\partial u_x}{\partial x} + \frac{\partial u_y}{\partial y} + \frac{\partial u_z}{\partial z} = 0$
3. No accumulation of component A , $\frac{\partial C_A}{\partial t} = 0$
4. Neglect z -diffusion, $\frac{\partial^2 C_A}{\partial z^2} = 0$
5. No diffusive flux through the solid surface, $\frac{\partial C_A}{\partial y}(x, y=0) = 0$

The above assumptions reduce the full convection-diffusion equation to

$$u_z \frac{\partial C_A}{\partial z} = \mathcal{D}_{AB} \frac{\partial^2 C_A}{\partial y^2} + \left(\frac{x'_p}{y'_p} \right)^2 \frac{\partial^2 C_A}{\partial x'^2} \quad (4.17)$$

The variables have been non-dimensionalized as follows

$$x = \frac{x'}{x'_p} \quad y = \frac{y'}{y'_p} \quad z = \frac{z' \mathcal{D}_{AB}}{u_z (x'_p)^2} \quad u_z = \frac{u'_z}{u_z} \quad C_A = \frac{C'_A}{C_{A,sat}} \quad (4.18)$$

where the prime denotes dimensional quantities.

The boundary conditions which allow for the solution of the convection-diffusion equation are zero diffusive flux at the solid surface and saturation of the liquid by

the diffusing gas at the gas-liquid interface. Using the non-dimensionalized variables listed above, these two conditions can be summarized as follows,

$$\frac{\partial C_A}{\partial y}(x, y=0) = 0 \quad C_A(\text{interface}) = 1 \quad (4.19)$$

Solution of the simplified convection-diffusion equation using the above boundary conditions gives the concentration profile of the diffusing gas.

4.2 Generalized Curvilinear Coordinates

The solution of the Navier-Stokes and convection-diffusion equation in the domain of interest posed some interesting computational challenges which required attention before the actual equations could be solved. Firstly, the free interface is curved which means that some type of cylindrical or elliptical coordinate system is required upon which the calculations can be performed. Secondly, the shape of the free interface changes depending upon the flow rate of the fluid and the angle of inclination of the flow surface. Thirdly, the interface is not a portion of a circle or an ellipse except in rare instances. It becomes apparent then, that any numerical solution of the governing equations for the rivulet flow problem must be done using a grid which is flexible enough to fit the variety of shapes which the rivulet can assume and sufficiently orthogonal that convergence of the solution can still be obtained. This latter point will be discussed further in Section 4.3.2. The technique which proved to be the solution to the above problems was that of generalized curvilinear coordinates.

4.2.1 Physical-Computational Spaces

Using generalized curvilinear coordinates essentially implies that a distorted region in physical space can be mapped into a rectangular region in the generalized coordinate space, herein called computational space. The appealing characteristics of this method are that there is a one-to-one correspondence of each point in the computational space with a point in the physical space and that the computational space, now rectangular in shape, accurately represents an oddly shaped physical space and allows classical differencing techniques to be used in the solution of the governing equations.

Figure 4.2 shows each space with its respective coordinate system. It can be seen that the curved interface has been replaced with a straight edge of the rectangle, $\xi = 1$, and that the two singular points have become singular lines in the computational domain, $\eta = 0$ and $\eta = 1$. Several different types of physical grids were studied to determine which one would allow for the best solution of the governing equations with the grid shown in figure chosen for several reasons. Firstly, the physical grid, as shown, can adequately describe the free interface (ie. the largest constant ξ -line is the free interface). Secondly, although two singular points appear in this pseudo-bipolar coordinate system, they both lie at dirichlet boundary condition locations for both governing equations, $u_z = 0$ for the Navier-Stokes equation and $C_A = 1$ for the convection-diffusion equation. This fact greatly simplifies the computational technique on this grid. Thirdly, the intersection of the constant η -lines with both the free interface and the solid surface is orthogonal making the imposition of the boundary conditions in the numerical technique far easier than it would be if the coordinate lines were not orthogonal at these two surfaces. Lastly, the grid in the interior of the domain is nearly orthogonal at all locations reducing the magnitude of the cross-derivative terms in the transformed

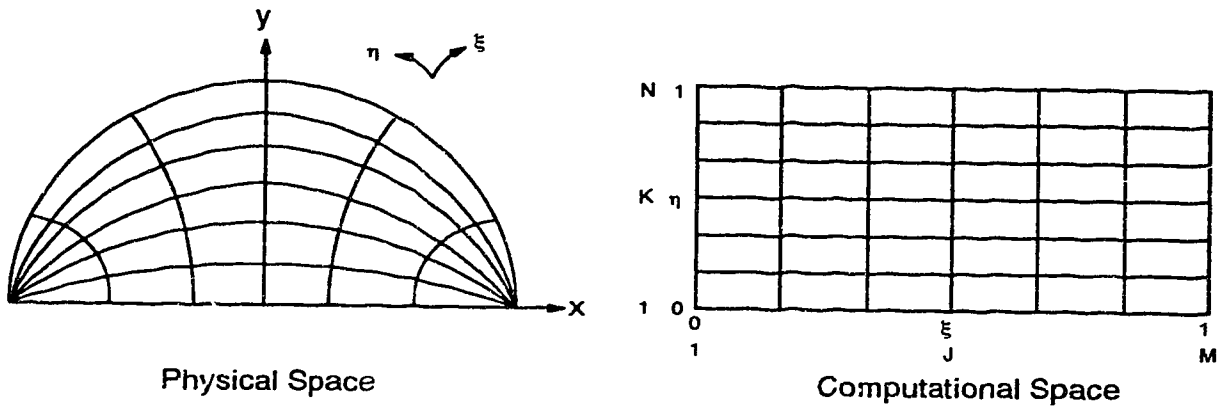


Figure 4.2: Coordinate Systems for the Physical and Computational Spaces

governing equations making the solution of these equations possible.

Since this grid is not a true bipolar coordinate system, some description of how it was constructed is necessary. The technique used was suggested by Dorma [50] and is as follows:

1. On the free interface of the profile being analysed, determine the intersection of each constant η -line with this surface using the criteria that the η -lines are to be equally spaced.
2. At each of the designated points, construct a tangent to the surface.
3. Locate the intersection of this tangent with the x -axis.
4. Using this intersection as the centre of a circle, draw an arc from the free interface to the solid surface. The radius of the arc is equal to the distance from the x -axis intersection of the tangent to the interface intersection of the tangent. This arc is the constant η -line.
5. Divide each η -line into segments of equal length.
6. Connect these equal segments to form the grid as shown in the figure.

This technique was used to produce the grids shown in Figures 4.3 to 4.8 which had the desired characteristics described above. Additionally, because they were constructed geometrically rather than through techniques such as orthogonal mapping [52, 117], they could be generated quickly and efficiently.

Figures 4.3 to 4.8 show the range of rivulet profiles simulated and the grids which were constructed inside them on which to solve the Navier-Stokes and convection-diffusion equations. In these figures, it can be seen that the constant η -lines do intersect both the free interface and the solid surface orthogonally and that the grid itself is nearly orthogonal everywhere.

It should be noted that the orthogonal mapping technique of Ryskin and Leal [117] would, at first glance, appear to be an ideal method for the generation of grids for this type of problem. In fact, this method was investigated, and it was found that this method is a special case of the more general class of grid generation techniques known as conformal mapping. As pointed out by Duraiswami and Prosperetti [52], in order to generate an orthogonal grid inside an arbitrary domain, the conformal module of the domain must be computed, something which is lacking in the method of Ryskin and Leal [117]. Once this fact was discovered, the attempt to construct a truly orthogonal grid inside the domain was discontinued since the general method of construction of an orthogonal grid in an arbitrary domain, as described by Duraiswami and Prosperetti [52], was too computationally intensive.

4.2.2 Equation Transformation

With construction of a suitable computational grid complete, the governing equations must be expressed in terms of this new space. A number of authors [58, 138, 139] have described the transformation procedure which essentially involves application of the chain rule to the differentials present in the governing equations

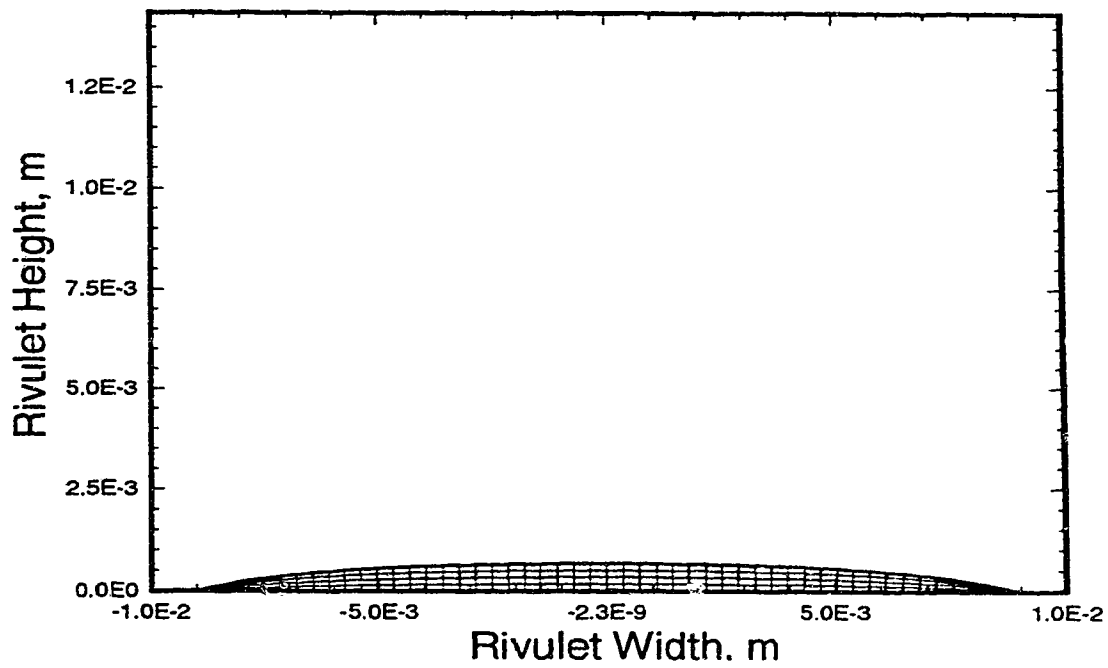


Figure 4.3: Grid Structure Inside Rivulet Profile. Largest Width Rivulet Case. $\alpha = 15^\circ$, $\theta = 15^\circ$, $\text{Log}_{10} B = 1.7$. Every fifth ξ -line shown.

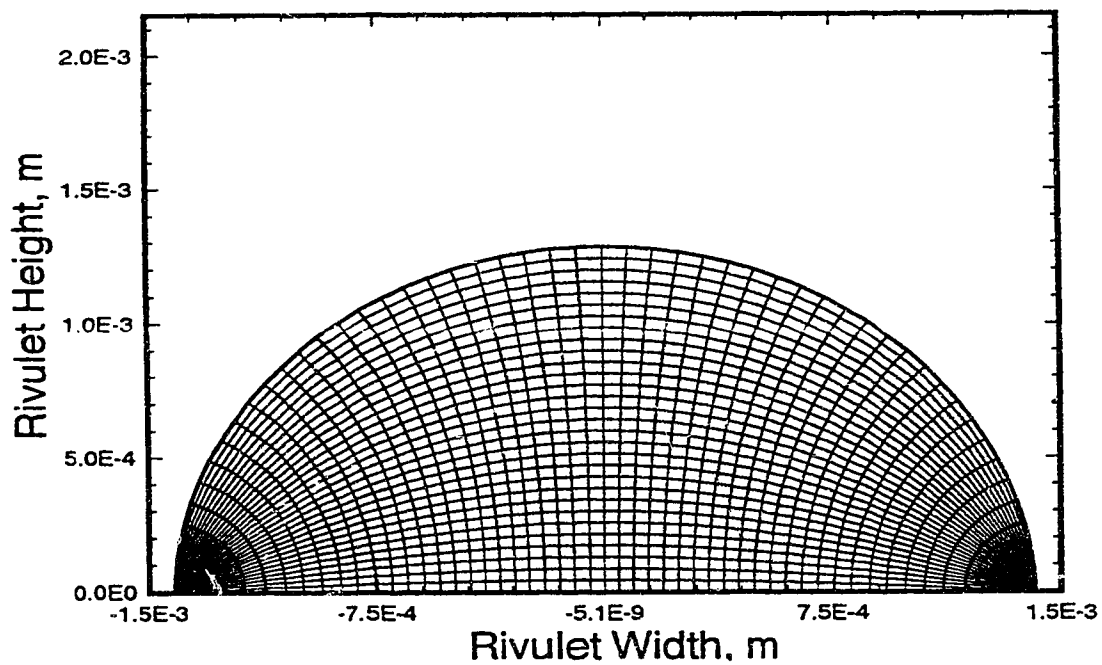


Figure 4.4: Grid Structure Inside Rivulet Profile. Largest Height Rivulet Case. $\alpha = 15^\circ$, $\theta = 88^\circ$, $\text{Log}_{10} B = -0.26$.

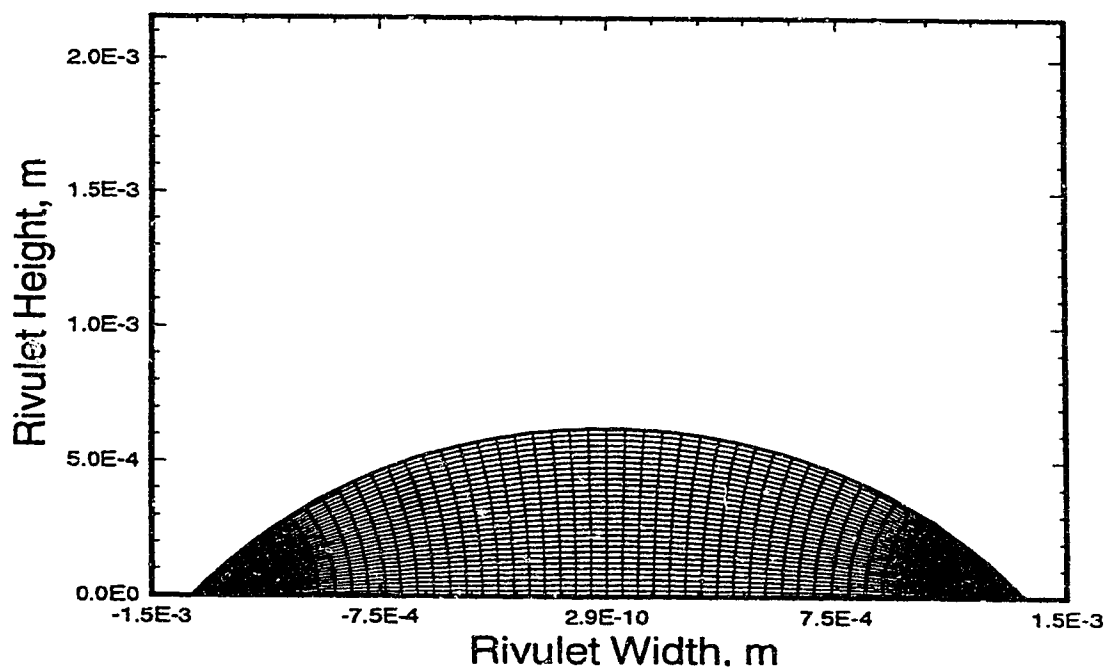


Figure 4.5: Grid Structure Inside Rivulet Profile. Average Rivulet Size For Stainless Steel–Water System. $\alpha = 45^\circ$, $\theta = 50^\circ$, $\text{Log}_{10} B = -0.17$.

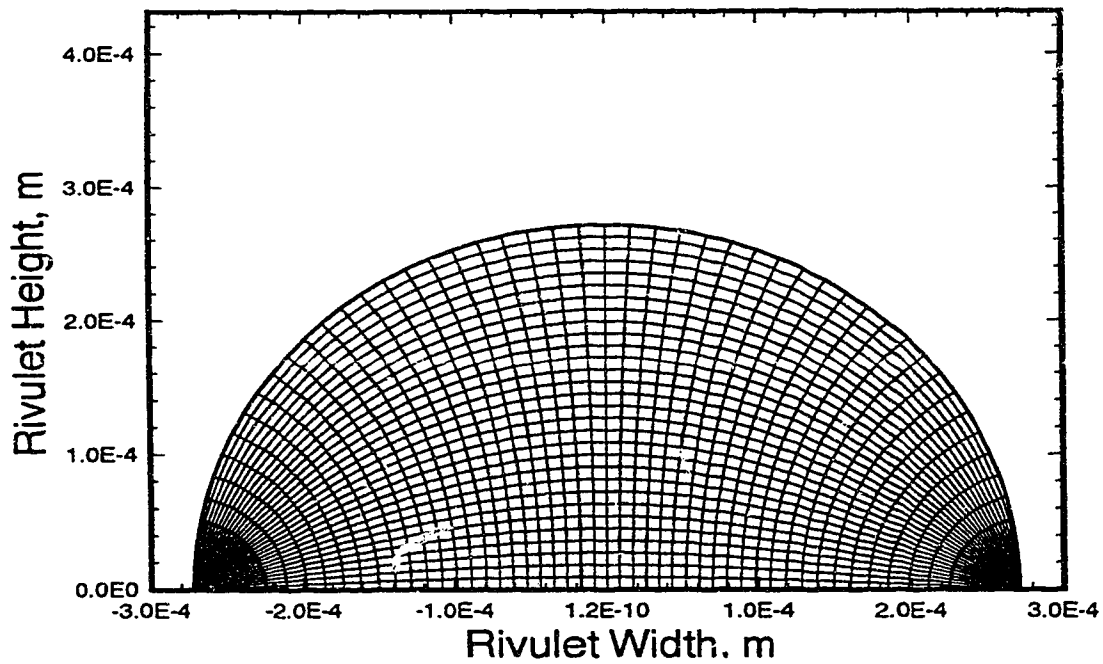


Figure 4.6: Grid Structure Inside Rivulet Profile. Half Circle Profile Case From Which Results Were Used to Check Against the Analytical Conduction Problem In an Infinite Cylinder. $\alpha = 45^\circ$, $\theta = 90^\circ$, $\text{Log}_{10} B = -1.0$.

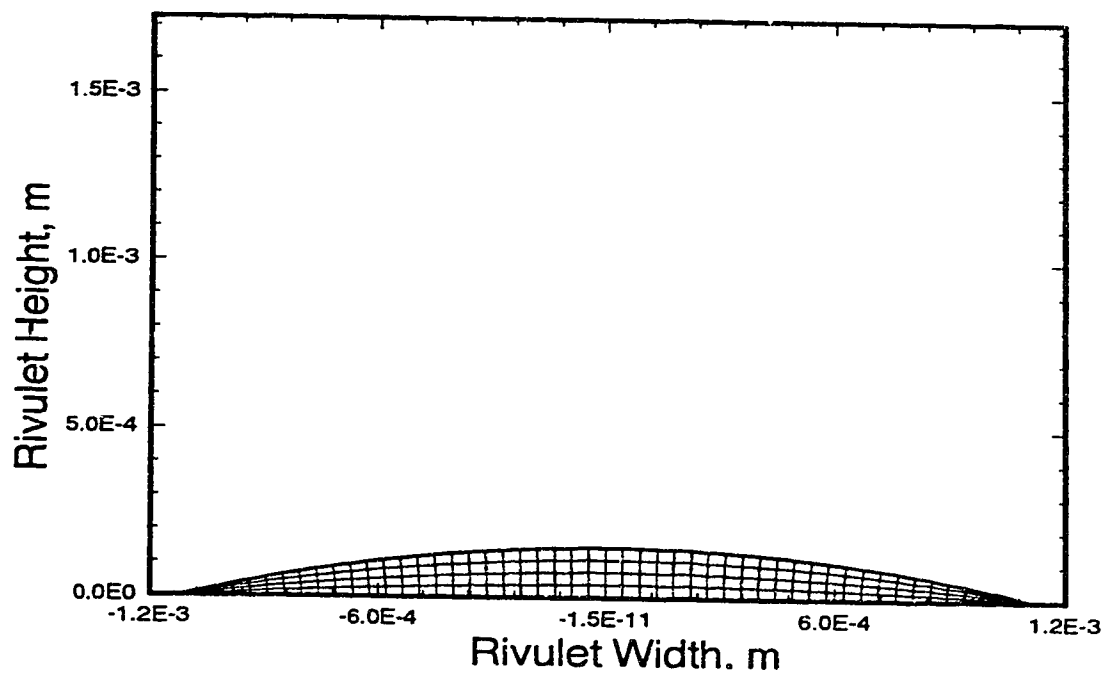


Figure 4.7: Grid Structure Inside Rivulet Profile. Smallest Height Rivulet Case. $\alpha = 89^\circ$, $\theta = 15^\circ$, $\text{Log}_{10} B = 0.2$. Every fifth ξ -line shown.

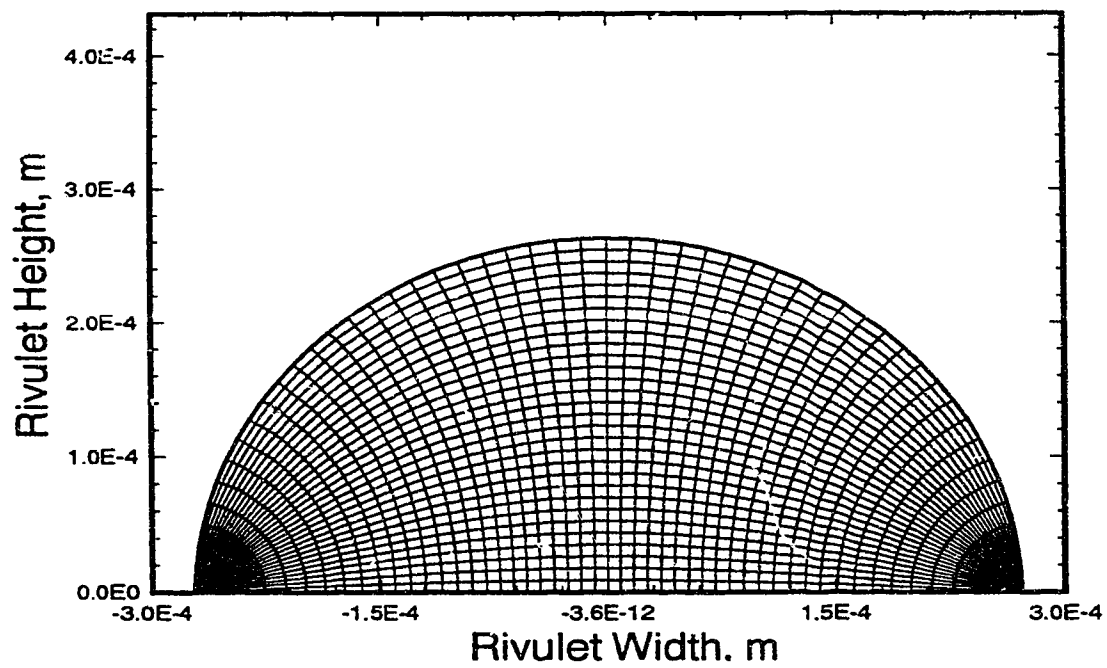


Figure 4.8: Grid Structure Inside Rivulet Profile. Smallest Width Rivulet Case.
 $\alpha = 89^\circ$, $\theta = 88^\circ$, $\text{Log}_{10} B = -1.0$.

to relate the two coordinate systems. For the equations used in this study, the appropriate relationships are

$$\frac{\partial}{\partial x} = \frac{\partial}{\partial \xi} \frac{\partial \xi}{\partial x} + \frac{\partial}{\partial \eta} \frac{\partial \eta}{\partial x} \quad \frac{\partial}{\partial y} = \frac{\partial}{\partial \xi} \frac{\partial \xi}{\partial y} + \frac{\partial}{\partial \eta} \frac{\partial \eta}{\partial y} \quad (4.20)$$

The above relationships contain the metric coefficients of the transformation and require evaluation in order to solve the governing equations. For the coordinate system used, the relationships for the metric coefficients can be expressed as

$$\begin{aligned} \frac{\partial \xi}{\partial x} &= + \frac{1}{|J^{-1}|} \frac{\partial y}{\partial \eta} & \frac{\partial \xi}{\partial y} &= - \frac{1}{|J^{-1}|} \frac{\partial x}{\partial \eta} \\ \frac{\partial \eta}{\partial x} &= - \frac{1}{|J^{-1}|} \frac{\partial y}{\partial \xi} & \frac{\partial \eta}{\partial y} &= + \frac{1}{|J^{-1}|} \frac{\partial x}{\partial \xi} \end{aligned} \quad (4.21)$$

$$\text{where} \quad |J^{-1}| = \frac{\partial x}{\partial \xi} \frac{\partial y}{\partial \eta} - \frac{\partial x}{\partial \eta} \frac{\partial y}{\partial \xi} \quad (4.22)$$

With the above relationships substituted into the governing equations, the equations become, after simplifying and rearranging
z-momentum:

$$\begin{aligned} & \left[\frac{1}{|J^{-1}|} \frac{\partial y}{\partial \eta} \frac{\partial}{\partial \xi} \left(\frac{1}{|J^{-1}|} \frac{\partial u_z}{\partial \xi} \frac{\partial y}{\partial \eta} - \frac{1}{|J^{-1}|} \frac{\partial u_z}{\partial \eta} \frac{\partial y}{\partial \xi} \right) - \right. \\ & \quad \left. \frac{1}{|J^{-1}|} \frac{\partial y}{\partial \xi} \frac{\partial}{\partial \eta} \left(\frac{1}{|J^{-1}|} \frac{\partial u_z}{\partial \xi} \frac{\partial y}{\partial \eta} - \frac{1}{|J^{-1}|} \frac{\partial u_z}{\partial \eta} \frac{\partial y}{\partial \xi} \right) \right] + \\ & \left(\frac{x'_p}{y'_p} \right)^2 \left[- \frac{1}{|J^{-1}|} \frac{\partial x}{\partial \eta} \frac{\partial}{\partial \xi} \left(- \frac{1}{|J^{-1}|} \frac{\partial u_z}{\partial \xi} \frac{\partial x}{\partial \eta} + \frac{1}{|J^{-1}|} \frac{\partial u_z}{\partial \eta} \frac{\partial x}{\partial \xi} \right) + \right. \\ & \quad \left. \frac{1}{|J^{-1}|} \frac{\partial x}{\partial \xi} \frac{\partial}{\partial \eta} \left(- \frac{1}{|J^{-1}|} \frac{\partial u_z}{\partial \xi} \frac{\partial x}{\partial \eta} - \frac{1}{|J^{-1}|} \frac{\partial u_z}{\partial \eta} \frac{\partial x}{\partial \xi} \right) \right] = -1 \quad (4.23) \end{aligned}$$

convection-diffusion equation:

$$\begin{aligned} & \left[\frac{1}{|J^{-1}|} \frac{\partial y}{\partial \eta} \frac{\partial}{\partial \xi} \left(\frac{1}{|J^{-1}|} \frac{\partial C_A}{\partial \xi} \frac{\partial y}{\partial \eta} - \frac{1}{|J^{-1}|} \frac{\partial C_A}{\partial \eta} \frac{\partial y}{\partial \xi} \right) - \right. \\ & \quad \left. \frac{1}{|J^{-1}|} \frac{\partial y}{\partial \xi} \frac{\partial}{\partial \eta} \left(\frac{1}{|J^{-1}|} \frac{\partial C_A}{\partial \xi} \frac{\partial y}{\partial \eta} - \frac{1}{|J^{-1}|} \frac{\partial C_A}{\partial \eta} \frac{\partial y}{\partial \xi} \right) \right] + \\ & \left(\frac{x'_p}{y'_p} \right)^2 \left[-\frac{1}{|J^{-1}|} \frac{\partial x}{\partial \eta} \frac{\partial}{\partial \xi} \left(-\frac{1}{|J^{-1}|} \frac{\partial C_A}{\partial \xi} \frac{\partial x}{\partial \eta} + \frac{1}{|J^{-1}|} \frac{\partial C_A}{\partial \eta} \frac{\partial x}{\partial \xi} \right) + \right. \\ & \quad \left. \frac{1}{|J^{-1}|} \frac{\partial x}{\partial \xi} \frac{\partial}{\partial \eta} \left(-\frac{1}{|J^{-1}|} \frac{\partial C_A}{\partial \xi} \frac{\partial x}{\partial \eta} + \frac{1}{|J^{-1}|} \frac{\partial C_A}{\partial \eta} \frac{\partial x}{\partial \xi} \right) \right] = u_z \frac{\partial C_A}{\partial z} \quad (4.24) \end{aligned}$$

As with the governing equations, the boundary conditions must also be transformed. The same technique as was used for the governing equations is used for the boundary conditions although, in this case, the resulting equations are not as complex. The transformed boundary conditions are

z -momentum:

$$\begin{aligned} u_z(\xi=0, \eta) &= 0 & u_z(\xi, \eta=0) &= 0 & u_z(\xi, \eta=1) &= 0 \\ \frac{\partial u_z}{\partial \xi}(\xi=1, \eta) &= 0 \end{aligned} \quad (4.25)$$

convection-diffusion:

$$\begin{aligned} C_A(\xi=1, \eta) &= 1 & C_A(\xi, \eta=0) &= 1 & C_A(\xi, \eta=1) &= 1 \\ \frac{\partial C_A}{\partial \xi}(\xi=0, \eta) &= 0 \end{aligned} \quad (4.26)$$

and are illustrated in Figures 4.9 and 4.10. It is interesting to note that in both sets of boundary conditions, one of the boundary conditions in the physical space has been transformed into three separate statements of the same condition. This result arises because of the presence of the two singular points in the domain and does not cause any problems in the solution technique. As referred to earlier, it is because these singular points have dirichlet boundary conditions that this grid is so desirable.

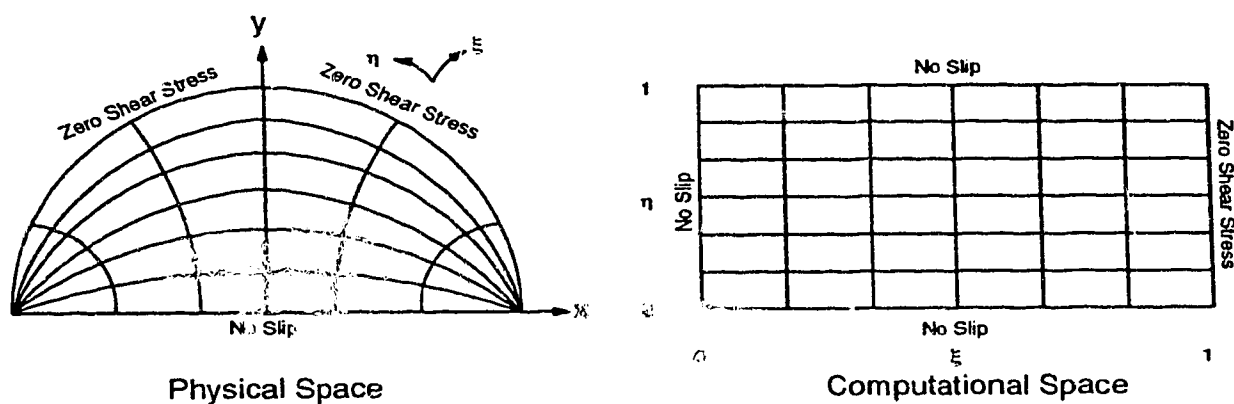


Figure 4.9: Boundary Conditions for Solution of the z -momentum Navier-Stokes Equation

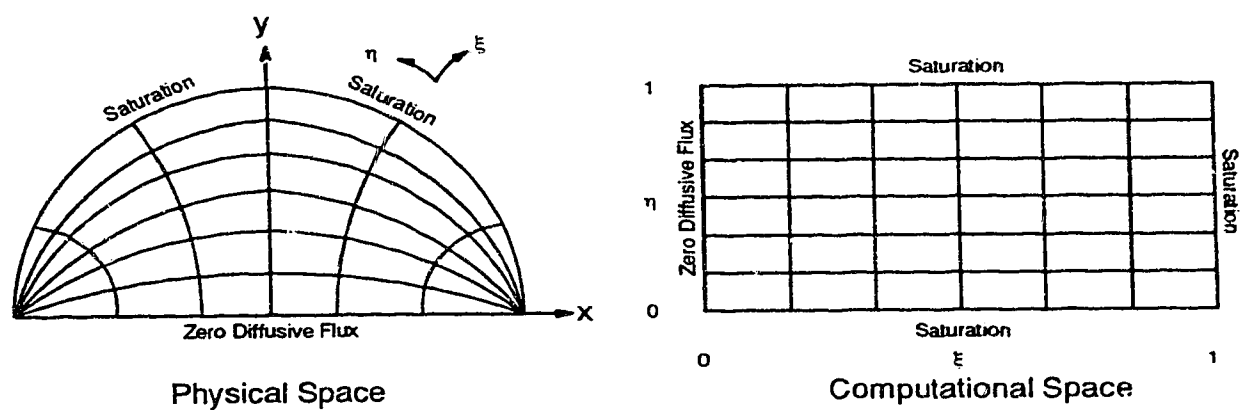


Figure 4.10: Boundary Conditions for Solution of Convection-Diffusion Equation

Metric Coefficients

The technique of generalized curvilinear coordinates requires values for the metric coefficients in order to perform the necessary equation and boundary condition transformations shown previously. Figures 4.11 to 4.14 show typical contour plots of the four metric coefficients used in this study and it can be seen that, in all cases, the contours vary smoothly with both flat and steep regions present. Also, the contours are continuous in all cases except at the two singular points in the domain where the Jacobian of the transformation is zero making the value of the metric coefficients undefined. For this reason, the contour lines in the figure do not extend to $\eta = 0$ or $\eta = 1$. It must be noted that each rivulet shape will have its own unique set of metric coefficients but that they will be similar to those shown in Figures 4.11 to 4.14, the differences being in the steepness or flatness of the contours.

4.3 Numerical Solutions

4.3.1 Profile Equations

While the solution to the equations describing the height and volume per unit length of the rivulet are analytical, the equations for rivulet width and arc length require numerical solution techniques. In order to solve these ordinary differential equations, Gaussian Quadrature using Laguerre Integration was chosen. A twelfth degree polynomial was selected as it gave sufficiently accurate results for the variety of rivulet shapes studied.

The technique itself involves rewriting the integral in the proper format using

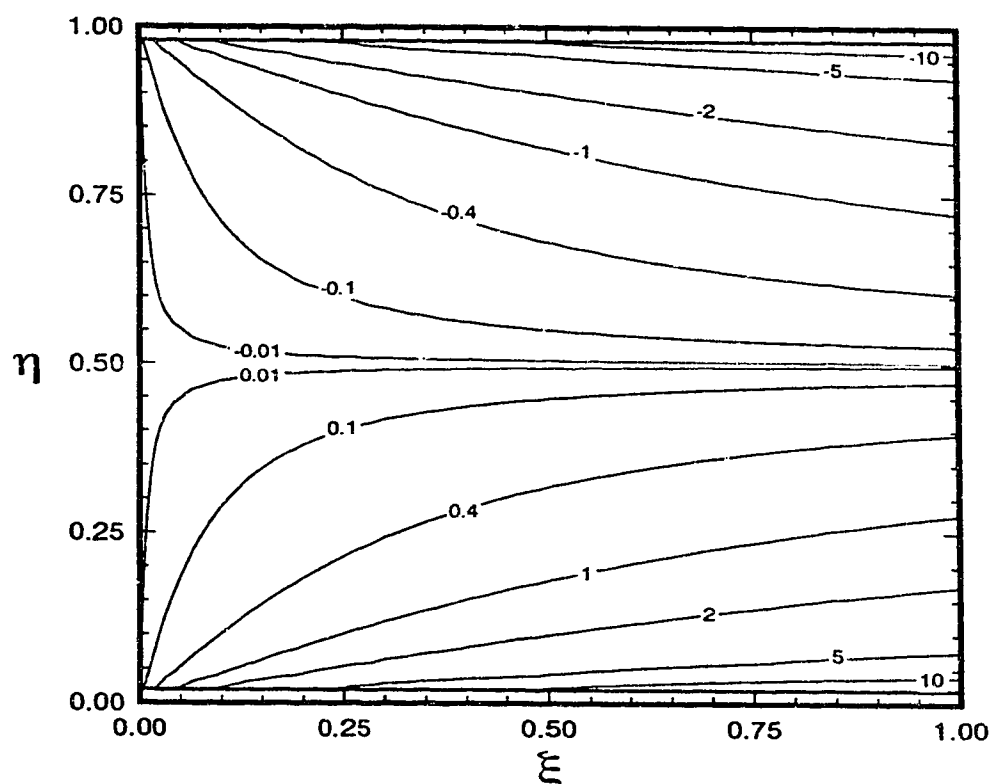


Figure 4.11: Contour Plot of the Metric Coefficient $\frac{\partial \xi}{\partial x}$ in Computational Space.
 $\alpha = 45$, $\theta = 50$, $\text{Log}_{10} B = -0.17$

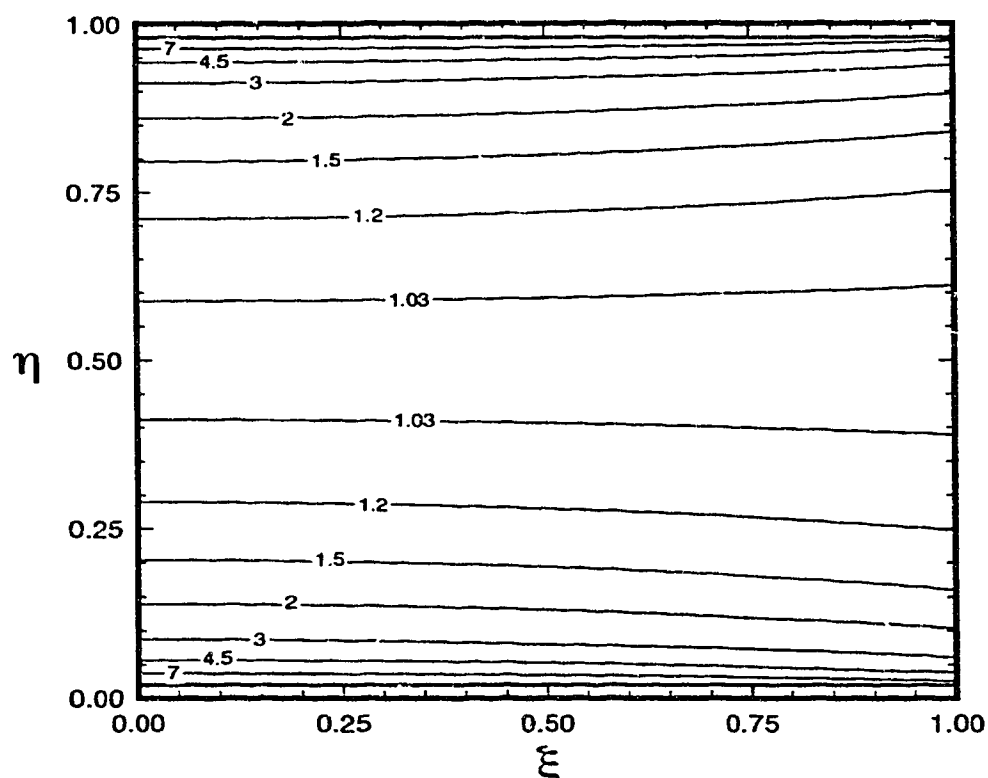


Figure 4.12: Contour Plot of the Metric Coefficient $\frac{\partial \xi}{\partial y}$ in Computational Space.
 $\alpha = 45$, $\theta = 50$, $\text{Log}_{10} B = -0.17$

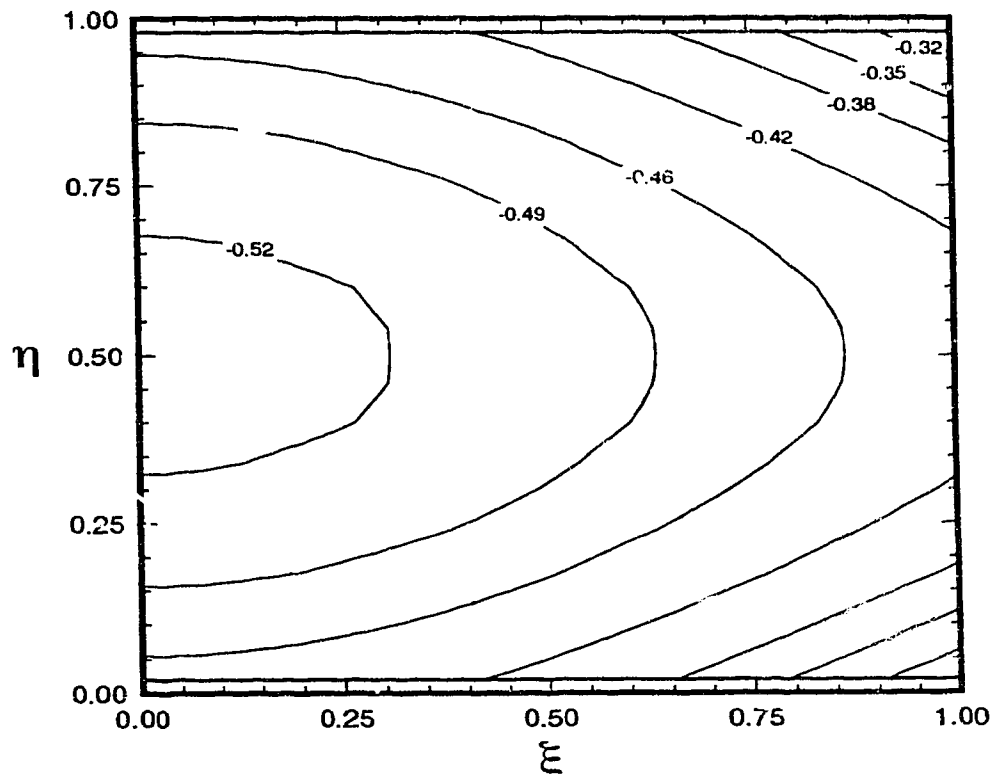


Figure 4.13: Contour Plot of the Metric Coefficient $\frac{\partial \eta}{\partial x}$ in Computational Space.
 $\alpha=45$, $\theta=50$, $\text{Log}_{10}B=-0.17$

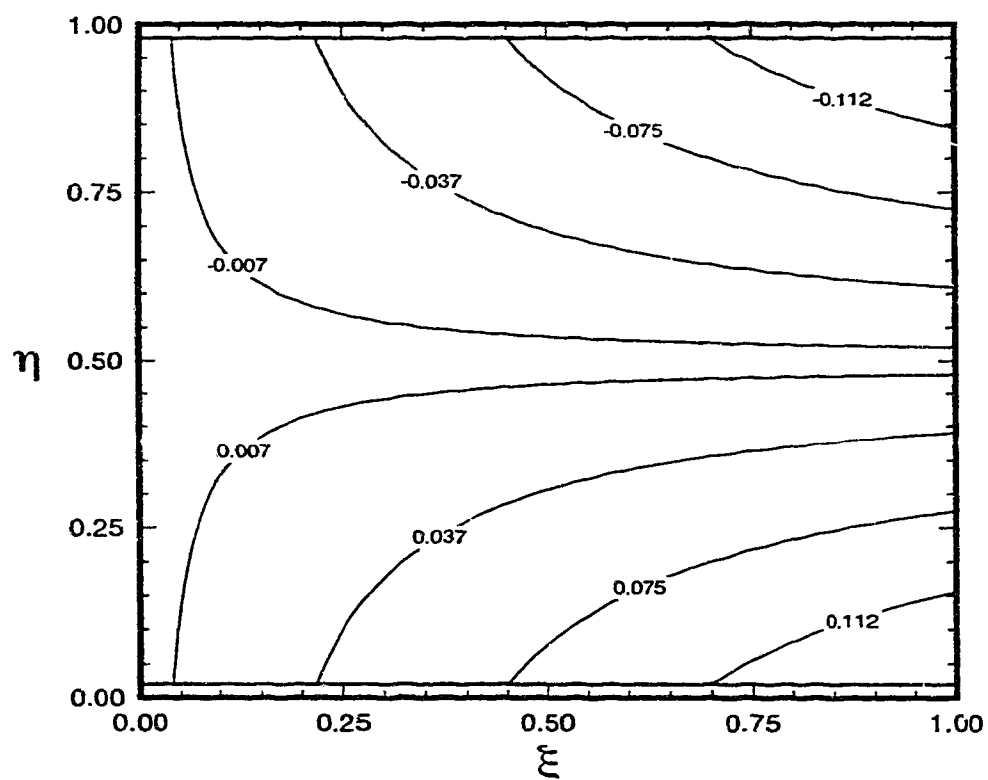


Figure 4.14: Contour Plot of the Metric Coefficient $\frac{\partial \eta}{\partial y}$ in Computational Space.
 $\alpha=45$, $\theta=50$, $\text{Log}_{10}B=-0.17$

the following relationship

$$\int_{\theta_1}^{\theta_2} f(y) dy = \frac{\theta_2 - \theta_1}{2} \sum_{i=1}^n H_i f(y_i) \quad (4.27)$$

$$\text{where } f(y_i) = f\left(\frac{(\theta_2 - \theta_1)W_i + (\theta_2 + \theta_1)}{2}\right)$$

When applied to the equations for the width and the arc length, Equations 4.5 and 4.6 respectively, the result is

width

$$X_p = \frac{\theta_2 - \theta_1}{2} \sum_{i=1}^n H_i \left(\frac{\cos A_{1,i}}{\left(\frac{1}{B^2} + 2 \cos \alpha (1 - \cos A_{1,i})\right)^{\frac{1}{2}}} + \frac{\cos A_{2,i}}{\left(\frac{1}{B^2} + 2 \cos \alpha (1 - \cos A_{2,i})\right)^{\frac{1}{2}}} \right) \quad (4.28)$$

surface area per unit length

$$S_p = \frac{\theta_2 - \theta_1}{2} \sum_{i=1}^n H_i \left(\frac{1}{\left(\frac{1}{B^2} + 2 \cos \alpha (1 - \cos A_{1,i})\right)^{\frac{1}{2}}} + \frac{1}{\left(\frac{1}{B^2} + 2 \cos \alpha (1 - \cos A_{2,i})\right)^{\frac{1}{2}}} \right) \quad (4.29)$$

where : $n = 12$

θ_1 = smaller value of contact angle (lower limit of integration)

θ_2 = contact angle of liquid studied (upper limit of integration)

$$A_{1,i} = \frac{(\theta_2 - \theta_1)W_i + (\theta_2 + \theta_1)}{2}$$

$$A_{2,i} = \frac{(\theta_1 - \theta_2)W_i + (\theta_2 + \theta_1)}{2}$$

To determine the value of the width and surface area of a particular profile, the input parameters required were the smaller value of the contact angle, the contact angle of the liquid-solid system being studied, the value of the radius of curvature

at the apex of the rivulet and the angle of inclination of the flow surface from the horizontal. Integration of the equations was then performed from the lower to the upper contact angles with the results being the width and the surface area per unit length of the rivulet.

The above procedure was also used to generate the entire profile of the rivulet. By integrating the equation for rivulet width from the lower contact angle to intermediate values of the contact angle, intermediate width values were obtained. By using the analytical height equation to determine intermediate height values, the appropriate x and y -coordinate positions along the rivulet profile were found and used to construct the profile.

4.3.2 Flow Equations

The numerical solution of the transformed z -momentum Navier-Stokes equation utilized the Thomas algorithm to solve the sparse matrix resulting from the centered, three-point discretization of the appropriate differential terms. Successive over-relaxation was also used as it significantly reduced the computational time required to solve the equation.

A complication inherent in the technique of generalized curvilinear coordinates now appears when the discretization of the z -momentum equation is performed. As can be observed from Equation 4.23, cross-derivative terms appear in the formulation which add to the complexity of the problem. Centered, three-point difference formulations for these differentials are readily available, however, depending upon the orthogonality of the grid upon which the equations are solved, the solution can be either unstable in the case of a highly non-orthogonal grid or stable in the case of a nearly orthogonal grid. In the evaluation of the particular grid to use to solve the governing equations, it was found that polar grids with one singular

point (cylindrical-type coordinate systems) produced highly non-orthogonal grids for low contact angles and the solution of the governing equations became unstable in these instances. The bipolar-type coordinate system shown in Figure 4.2 allowed for a nearly orthogonal grid and stable solutions for both governing equations in the range of contact angles studied.

The actual solution of the discretized equation was performed row by row along rows of constant η starting at $\eta = 2$ and proceeding to $\eta = N - 1$. The direction of the solution sweeps did not affect the final solution as a steady-state result was the only solution of interest. The above described sweep direction was chosen, however, because it allowed for the fastest propagation of the zero shear stress boundary condition into the computational domain. It can be visualized that sweeps done along constant ξ -lines would not allow as fast a propagation of the boundary condition information as would sweeps done along lines of constant η .

Incorporating the zero shear stress boundary condition into the problem formulation was greatly simplified due to the orthogonality of the grid at the free interface. The statement of this boundary condition has been shown in Equation 4.25, and discretizing it for a grid which is orthogonal at the free interface results in the following simple relationship

$$u_z(K, J-1) = u_z(K, J+1) \quad (4.30)$$

Using this result, the unknown, imaginary point, $u_z(K, J-1)$, is eliminated from the formulation of the discretized equations resulting in a simpler set of equations than would have been realized had the grid not been orthogonal at the free interface. In fact, discretization of this boundary condition using a non-orthogonal grid was performed using a polar-type grid with the result being a more cumbersome and difficult equation to solve than the case just described.

Finally, the solution of the velocity field was iterated upon until the difference in the values of the velocity obtained in successive iterations was less than a specified tolerance. To determine a suitable tolerance which would be consistent for all computations of the velocity field, a value of 1×10^{-4} times the value of the velocity at the point ($K=2, J=2$) in the first iteration was used. This point was chosen as it had the smallest velocity value of any point in the domain and, for the first iteration, its value was small, non-zero and of the same order of magnitude as the final solution.

Figure 4.15 shows the streamlines inside an average size rivulet for the stainless steel–water system. It can be seen that the streamlines are perpendicular to the free interface as they must be due to the zero stress boundary condition used in the solution of the Navier-Stokes equation. Also, the velocity profile is parabolic as expected at any vertical cross-section. Finally, for rivulets with different contact angles and plate inclinations, similar figures could be constructed although the differences would be only in the profile shape and magnitude of the velocity—the contour lines themselves would be similar to the ones shown in this figure.

4.3.3 Convection-Diffusion Equation

The solution of the convection-diffusion equation is more complex than the solution of the z -momentum Navier-Stokes equation due to the presence of the convection term on the left hand side of the equation as can be seen from Equation 4.17. It is interesting to note, however, that once this equation is non-dimensionalized and transformed into computational space, the diffusion side of the equation is identical to the momentum side of the z -momentum equation as can be seen from Equations 4.23 and 4.24. Another interesting feature of this equation arises because of the fact that, at the solid surface, there is no convection. Not only

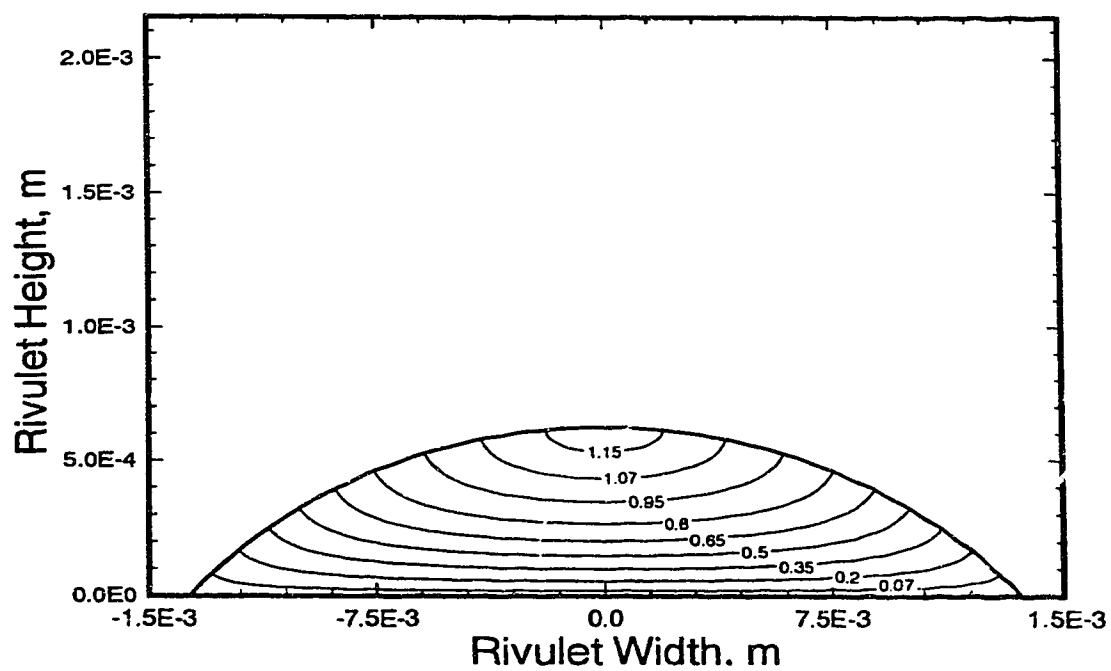


Figure 4.15: Contour Plot of the Streamlines Inside the Rivulet Profile. Average Rivulet Size for the Stainless Steel–Water System. Velocity is in m/s . $\alpha=45$, $\theta=50$, $\text{Log}_{10}B=-0.17$

does this change the form of the equation from parabolic to homogeneous elliptic but it also means that standard implicit techniques for the solution of marching problems (ADI) are no longer applicable [95]. As there are other techniques available for the solution of these types of problems, most notably Crank-Nicolson, this change in the form of the equation from non-homogeneous to homogeneous requires only a change in the numerical method used to solve the equation.

As suggested above, the method of Crank-Nicolson was used to solve the convection-diffusion equation. In the particular form of the method chosen, which in this case was implemented in a two-dimensional domain, the discretized differentials were evaluated at the $z + \frac{1}{2}$ level. The centered, three-point discretization of the differential term, $\frac{\partial^2 C_A}{\partial \xi^2}$, would be

$$\frac{\partial^2 C_A}{\partial \xi^2} = \frac{C_{K,J+1}^{n+1} - 2C_{K,J}^{n+1} + C_{K,J}^{n+1} + C_{K,J+1}^n - 2C_{K,J}^n + C_{K,J-1}^n}{2(\Delta \xi)^2} \quad (4.31)$$

where K and J represent grid point positions and n is the iteration number for each marching step.

The discretization of the other differentials follows the pattern shown above, and as can be seen from this formulation, iteration of each marching step is required since the values of the concentration at the next level, $z+1$, are not known. In the solution of the convection-diffusion equation for rivulet flow, approximately ten iterations were usually required for suitable convergence of the concentration values for each z -level.

The discretized equations from the Crank-Nicolson formulation produced a tridiagonal matrix structure which was subsequently solved using the Thomas algorithm. The order of solution of the equations in the computational domain was as follows:

1. Starting at $K = 2$ and stopping at $K = N - 1$, solve for the concentration at the next z -level sweeping lines of constant η .

2. Check for convergence of the newly calculated concentration values.
3. If convergence not attained, iterate for the values at the same next z -level sweeping this time along lines of constant ξ starting at $J = M-1$ and stopping at $J = 1$. Use updated values for the $z+1$ level as calculated in the η sweeps above as the guess values for the $z+1$ level.
4. Check again for convergence.
5. If convergence is not attained return to sweeping the η -direction, then the ξ -direction checking for convergence after each set of sweeps is complete. Always use updated values from the previous iteration as guess values for the concentration at the $z+1$ level.
6. When convergence is attained, the newly calculated values of concentration at the $z+1$ level become the z -level values and the entire procedure is repeated until the required flow distance is reached.

The above method of sweeping in both directions was implemented as it allowed for faster propagation of information throughout the computational domain than would have occurred by simply sweeping in the ξ or η -directions.

Implementation of the zero diffusive flux boundary condition at the solid surface was done exactly as described for the zero shear stress condition in the z -momentum equation. In this case, the discretization of the boundary condition, as shown in Equation 4.26, produces the result

$$C_A(K, J+1) = C_A(K, J-1) \quad (4.32)$$

As with the z -momentum equation, this relationship is used to eliminate the unknown, imaginary point $C_A(K, J-1)$ from the discretised convection-diffusion equation. Solution of the equation then proceeds as explained above.

One last feature of this solution which requires some mention is the fact that a variable step size was used in the z -direction. In order to track the solution accurately from start to finish, it was found that a very small step size was required

at the start of calculations since the gradients at this point are very high. As the solution proceeds, a larger step size can be used without loss of accuracy in the solution. For solutions for long flow distances, large step sizes produce the same final result as small step sizes or variable step sizes. In the simulations performed for this flow system, a maximum step size of 1 mm was used, while the smallest starting step size depended upon the size of the rivulet cross-section.

Figures 4.16 to 4.18 show the developing concentration profile of CO_2 in the flowing rivulet. It can be seen that the penetration of CO_2 is very limited in the ideal convection-diffusion case shown here and that penetration is largest at the solid surface where convection is smallest and decreases as the apex of the rivulet is approached because of increasing convection. There is a small central region in the rivulet to which CO_2 penetrates last, the reason for this behaviour being that diffusion near the solid surface is not hindered by convection as it is in the region near the apex of the rivulet. Finally, the concentration profiles in these diagrams are orthogonal at the solid surface as required by the boundary conditions used to solve the convection-diffusion equation. As with the contour plot of the streamlines shown in the Section 4.3.2, these plots are for an average size rivulet for the stainless steel-water system. Similar diagrams could be drawn for each rivulet simulated with the differences being in the size of the rivulet profile and specific location of the contour lines—the shape of the contours would be very similar to the ones shown in Figures 4.16 to 4.18.

4.3.4 Mixing Cup Calculations

The solutions which result from the numerical computations described above are flow and concentration profiles and must be converted to mixing cup velocities and concentrations to be useful in comparisons with the experimental data. The

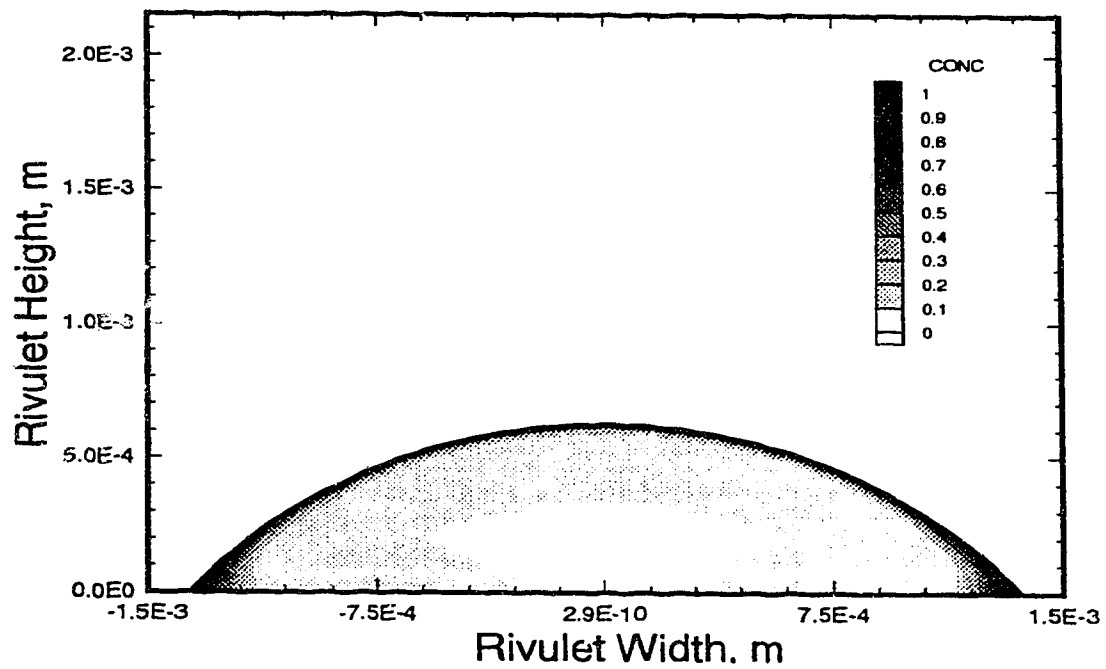


Figure 4.16: Dimensionless Concentration Inside the Rivulet Profile. Average Rivulet Size for the Stainless Steel–Water System. $\alpha = 45^\circ$, $\theta = 50^\circ$, $\text{Log}_{10} B = -0.17$, $\text{Dist} = 0.114 \text{ m}$

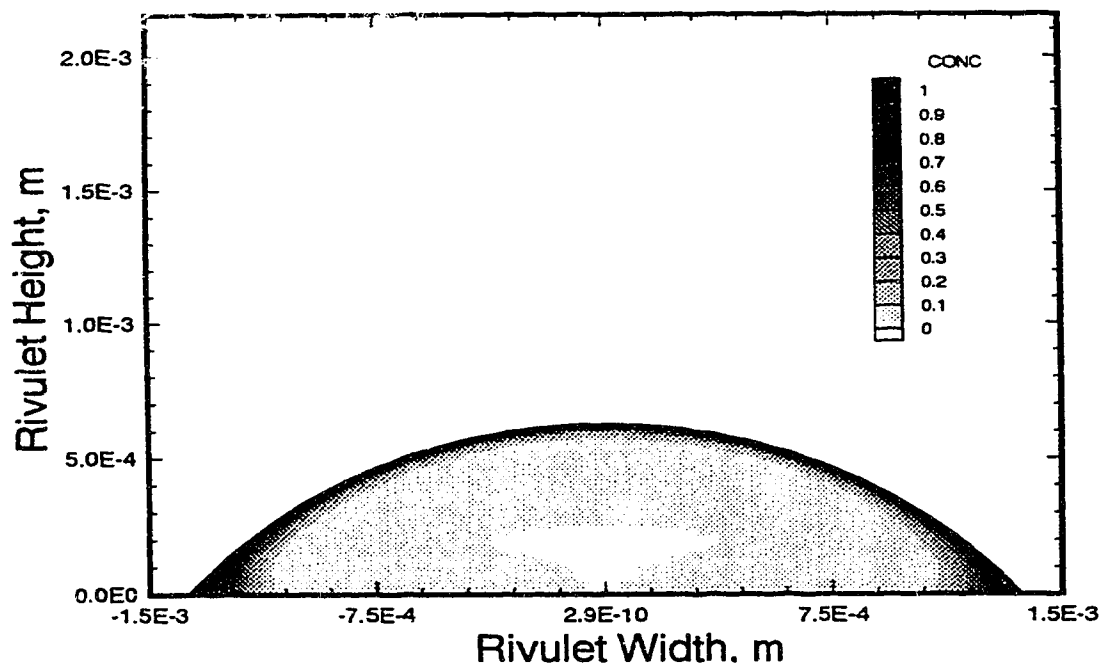


Figure 4.17: Dimensionless Concentration Inside the Rivulet Profile. Average Rivulet Size for the Stainless Steel–Water System. $\alpha = 45^\circ$, $\theta = 50^\circ$, $\text{Log}_{10}B = -0.17$, $\text{Dist} = 0.256 \text{ m}$

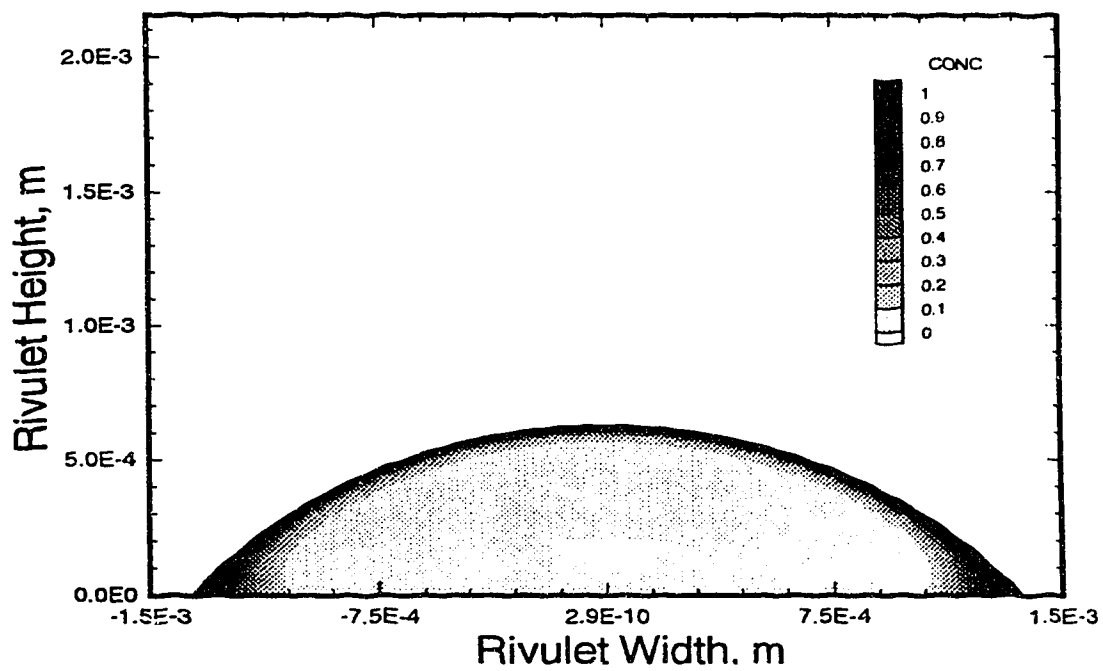


Figure 4.18: Dimensionless Concentration Inside the Rivulet Profile. Average Rivulet Size for the Stainless Steel–Water System. $\alpha = 45^\circ$, $\theta = 50^\circ$, $\text{Log}_{10} B = -0.17$, $\text{Dist} = 0.368 \text{ m}$

equations for the mixing cup velocity and concentration for the rivulet system can be written in cartesian coordinates as follows

cross-sectional area:

$$V_p = \iint_{V_p} dx dy \quad (4.33)$$

velocity profile:

$$u_{z, av} = \frac{1}{V_p} \iint_{V_p} u_z dV_p = \frac{1}{V_p} \iint_{V_p} u_z(x, y) dx dy \quad (4.34)$$

concentration profile:

$$C_{A, av} = \frac{1}{u_{z, av} V_p} \iint_{V_p} u_z C_A dV_p = \frac{1}{u_{z, av} V_p} \iint_{V_p} u_z(x, y) C_A(x, y) dx dy \quad (4.35)$$

In order for these equations to be implemented in the computer code, they must be rewritten in terms of ξ and η . The final expressions are

cross-sectional area:

$$V_p = \iint_{V_p} |J^{-1}| d\xi d\eta \quad (4.36)$$

velocity profile:

$$u_{z, av} = \frac{1}{V_p} \iint_{V_p} u_z [f(\xi, \eta), g(\xi, \eta)] |J^{-1}| d\xi d\eta \quad (4.37)$$

concentration profile:

$$C_{A, av} = \frac{1}{u_{z, av} V_p} \iint_{V_p} u_z [f_1(\xi, \eta), g_1(\xi, \eta)] C_A [f_2(\xi, \eta), g_2(\xi, \eta)] |J^{-1}| d\xi d\eta \quad (4.38)$$

4.3.5 Grid Refinement

Grid refinement was done for both the flow and mass transfer equations to determine the effect of the grid density on the respective solutions. The rivulet

profiles shown in the following tables were chosen for illustration, as they were the rivulet profiles which were most sensitive to grid refinement. The particular variables chosen as the test variables were cross-sectional area and average velocity for the flow equation and the average concentration for the mass transfer equation. These variables were chosen as they were the ones of interest in this study and showed suitable sensitivity to grid density.

Table 4.1 shows the simulations done to test the velocity computations, and as can be seen from the table, the solutions are quite good for all but the coarsest grids. Based on the results of these computations, a grid of at least $\xi = 31$, $\eta = 51$, (31×51) is required to obtain a satisfactory solution for the flow field.

Table 4.2 lists the simulations for the convection-diffusion equation and the effect of the grid density on these solutions. Grids courser than 31×51 were not tested for this situation as a grid of at least this density is required for the solution of the flow field and the same grid is to be used for both equations. From Table 4.2 it can be seen that there is very little improvement in the solution for grids finer than the 31×51 grid determined previously. Based on these results, a grid density of 31×51 was chosen and used in all successive computations.

Grid Density	Cross-Sectional Area (m^2)	Volumetric Flow Rate (mL/min)
7×7	0.1153	0.29352
11×11	0.1158	0.29584
21×21	0.1159	0.29736
31×31	0.1159	0.29770
41×41	0.1159	0.29781
51×51	0.1159	0.29788
11×21	0.1158	0.29692
11×31	0.1158	0.29718
11×41	0.1158	0.29726
11×51	0.1158	0.29731
21×11	0.1158	0.29629
31×11	0.1158	0.29637
41×11	0.1158	0.29640
51×11	0.1158	0.29642
21×51	0.1159	0.29775
31×51	0.1159	0.29784
41×51	0.1159	0.29787

Table 4.1: Effect of Computational Grid Density on the Solution of the z -momentum Navier-Stokes Equation Used to Determine the Volumetric Flow Rate Inside a Rivulet Profile. Most Sensitive Profile. $\alpha = 15^\circ$, $\theta = 90^\circ$, $\text{Log}_{10} B = -1.0$.

Grid Density	Specified Step Size (m)	Rate of Step Size Increase	Concentration At Distance
31×51	1×10^{-2}	1.0	0.2392
31×51	1×10^{-3}	1.0	0.2392
31×51	1×10^{-4}	1.0	0.2392
31×51	1×10^{-4}	1.1	0.2392
31×51	1×10^{-2}	1.2	0.2391
31×41	1×10^{-4}	1.1	0.2390
41×51	1×10^{-4}	1.1	0.2390
51×51	1×10^{-4}	1.1	0.2390

Table 4.2: Effect of Computational Grid Density on the Solution of the Convection-Diffusion Equation Used to Determine the Concentration Inside a Rivulet Profile at the Specified Flow Distance. Most Sensitive Profile. $\alpha = 15^\circ$, $\theta = 10^\circ$, $\text{Log}_{10} B = 3.0$, $\text{Dist} = 0.5 m$.

Chapter 5

Experimental System

5.1 Description of Apparatus

A schematic of the inclined flow plate apparatus is shown in Figure 5.1. The components of the experimental system include the inclined flow plate proper, plexiglass cover sheet, liquid collection box and cooling water chamber cover, liquid sampling mechanism, gas distribution box, constant head tank, storage tank, liquid supply system, constant temperature bath and cooling water system, CO₂ supply system and temperature monitoring system. Each of these components will be discussed in detail in the following paragraphs.

The inclined flow plate, shown in Figure 5.2, was machined from a solid block of AISI-304 stainless steel so as to provide a flat, smooth surface on the top side and a separate chamber underneath to allow for cooling water flow. The top flow surface was 510 *mm* long and 204 *mm* wide and was not machined completely flat but had 25 *mm* wide by 5 *mm* high ridges running the complete length of the plate on each side, to which the plexiglass cover sheet could be attached to enclose the flow surface

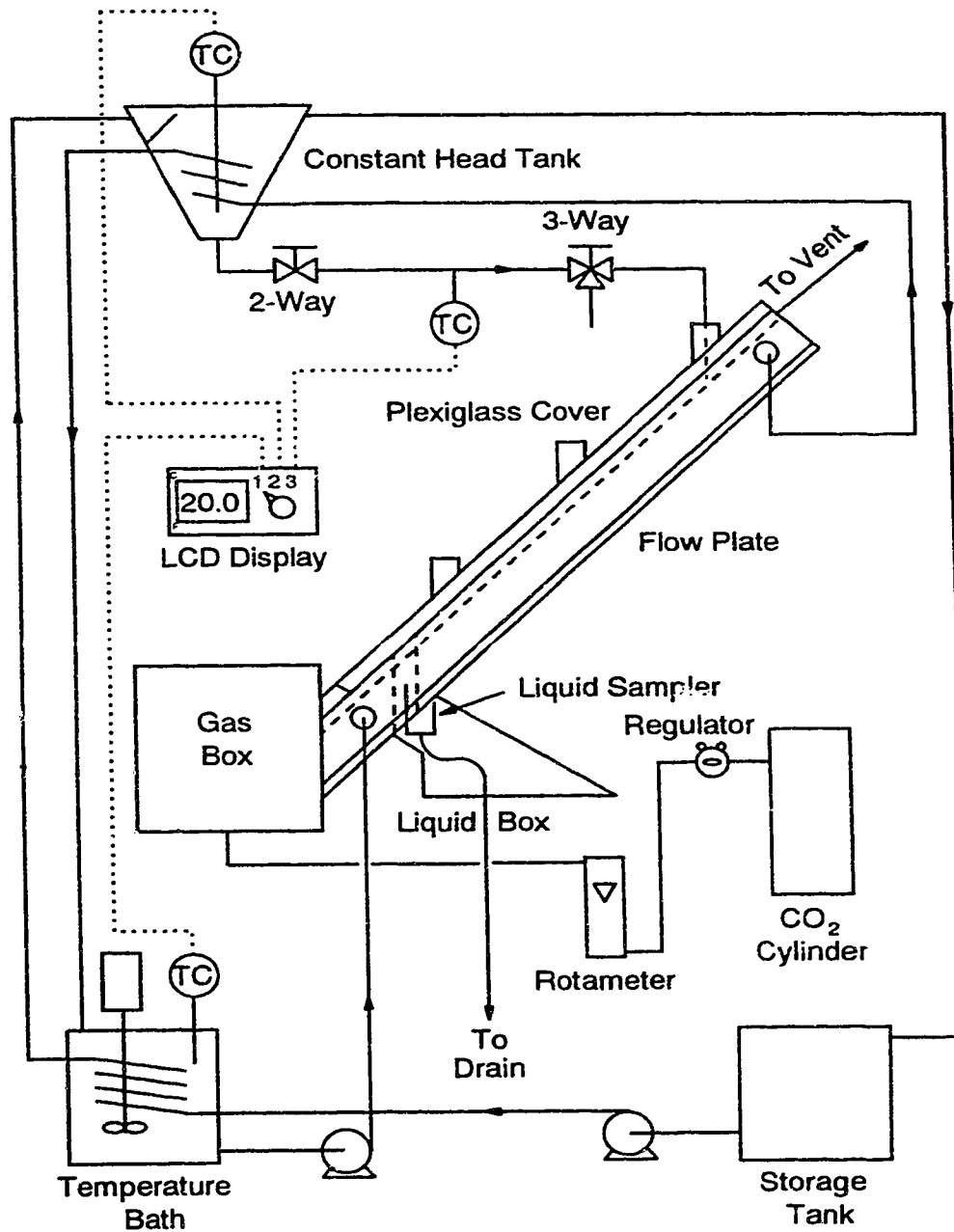


Figure 5.1: Schematic of Experimental Apparatus

and allow absorption studies to be done. As well, an inclined slot 10 *mm* wide was cut through the flow surface to the other side of the plate to allow for removal of liquid before it reached the end of the plate. Into the side of the plate were cut two 6.35 *mm* diameter holes to provide for cooling water flow into and out of the cooling jacket. This chamber in the bottom of the plate was divided into four interconnected sections to provide for adequate distribution of the cooling water to all parts of the plate. Finally, the top end of the plate was cut square, while the bottom end was cut at 45° to allow for better attachment of the gas distribution box.

The flow surface of the inclined flow plate was the one surface which required special attention and preparation. The surface was first machined to specification along with the rest of the plate, but following this procedure, additional care was taken to ensure that the surface was sufficiently smooth. The machining of the surface had left small, but significant, grooves in the plate which were removed by hand sanding of the surface using progressively finer grades of sandpaper (240 emery cloth, 320 wet-dry, 600 wet-dry and crocus cloth). This hand sanding removed the machining marks completely and left a surface that was smooth to the touch. The plate was washed thoroughly and then hand buffed on a cloth buffing wheel to ensure that all of the grit from the sandpaper was removed and that the surface was as smooth as required. This final buffing procedure produced a surface that was of the desired smoothness.

A final design feature of the inclined flow plate was that it was required to operate at inclination angles of 0° to 90°. This criterion was satisfied by attaching two metal dowels, 15.875 *mm* in diameter by 98 *mm* in length, one to each side of the flow plate, and inserting these dowels into clamping devices on the triangular support stand which held the flow plate (not shown for clarity in Figure 5.1). Due to the large rotation of the flow plate, all attachments to the plate (cooling water

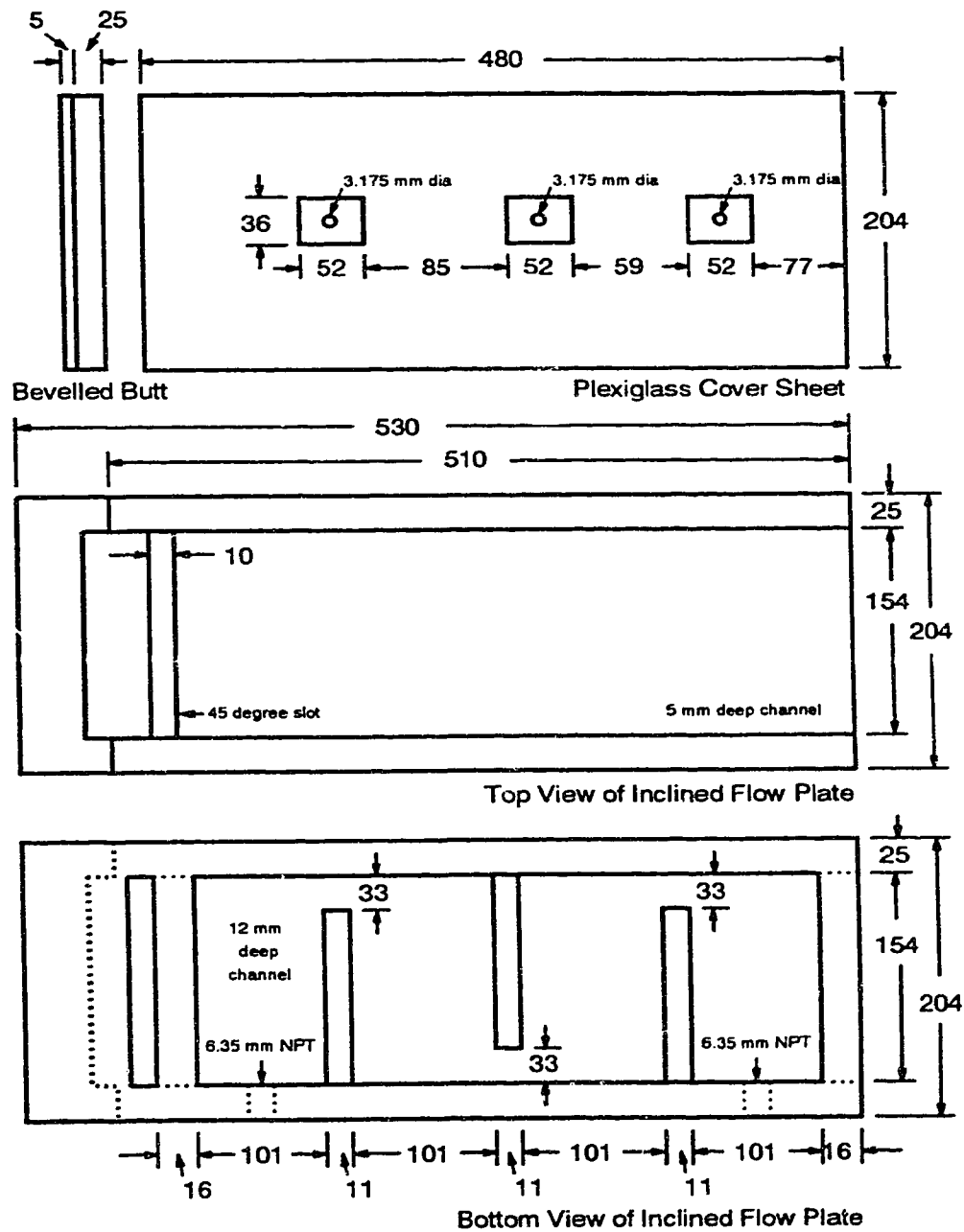


Figure 5.2: Schematic of Top and Bottom Views of the Inclined Flow Plate and Plexiglass Cover Sheet. All Dimensions in *mm*.

lines, liquid distributor and liquid sampling mechanism) were designed so that they could be adjusted to compensate for the plate rotation.

The gas distribution box, shown in Figure 5.3, was a cube 180 *mm* long on each side. It contained a 19.05 *mm* diameter hole in the bottom to allow for gas entry and had a slit 5 *mm* high and 154 *mm* long cut into one side, which matched the slit in the plate once the plexiglass cover was attached. This slit allowed for gas to pass from this box to the inclined flow plate.

To catch the liquid which left the plate through the inclined slot, a liquid collection box was designed which could serve both as an overflow for excess liquid and as a support for the liquid sampling mechanism. The box is illustrated in Figure 5.3. It was irregular in shape, with two 12.7 *mm* diameter liquid outlet ports in the bottom and was attached to the stainless steel sheeting which served as the cover plate for the cooling jacket in the bottom of the flow plate.

The liquid sampling mechanism, shown in Figure 5.3, was simply a small, specially designed cup which was flexibly mounted into the liquid collection box so that it could be moved back and forth along the bottom edge of the inclined slot and catch the liquid which was flowing off the plate. This cup was designed with a 3.175 *mm* diameter hole in the bottom, as shown, to which was connected flexible tygon tubing, running out of the bottom of the box through one of the overflow holes. In this manner, the liquid could quickly be removed from the plate and sampled with very little end effects present for the absorption studies. For the other experiments, the liquid was allowed to flow into the box and overflow through the bottom hole at which time the flow rate was measured.

The plexiglass cover used during the absorption studies had to serve as both a sealing cover for the flow plate and, in some capacity, as the medium through which the liquid could be delivered to the plate. The design, as shown in Figure 5.2, was

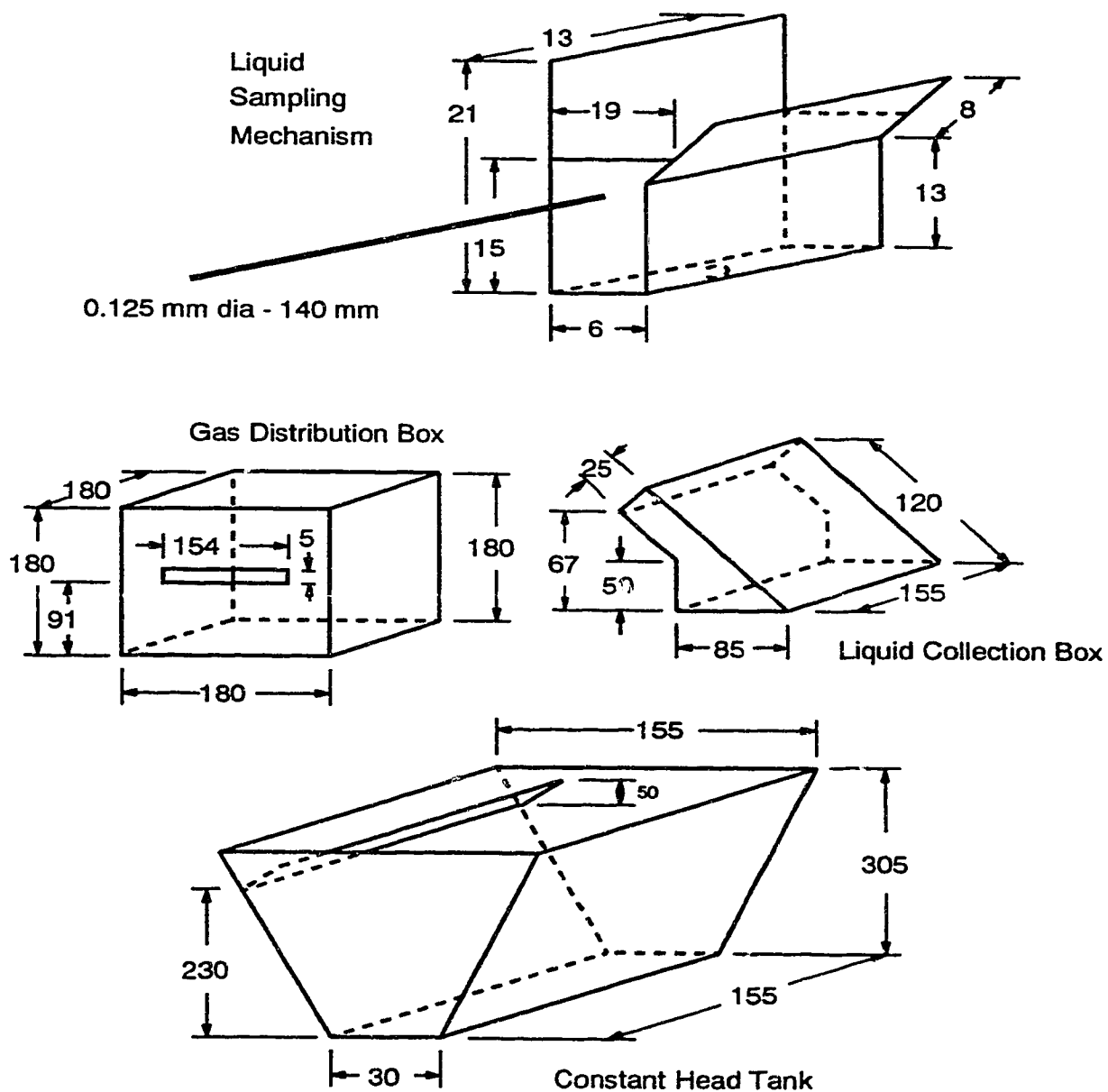


Figure 5.3: Schematics of Liquid Sampling Mechanism, Gas Distribution Box, Liquid Collection Box and Constant Head Tank. All Dimensions in *mm*.

a flat piece of 4.75 mm thick, clear cast acrylic sheet, with three specially designed blocks of plexiglass attached at pre-determined locations through which tubing could be inserted to deliver liquid to the plate. With this setup, the cover adequately sealed the flow surface, and liquid could be delivered to the plate at three locations.

To provide for a steady supply of constant temperature liquid, a gravity fed system was designed. The overhead tank, shown in Figure 5.3, was triangular in shape to allow for adequate stilling time for the liquid entering and yet a reasonably short residence time. Additional features included 2 m of 6.35 mm copper tubing cooling coils to provide temperature control and a 12.7 mm copper tubing overflow line back to the storage tank to keep the level in the constant head tank at the desired level. This tank also had a removable lid to allow for inspection of the inside and cleaning.

The storage tank, from which the water for the constant head tank was supplied, was simply a cylindrical tank 565 mm in diameter and 610 mm high, complete with a lid to keep the water supply clean. A 19.05 mm diameter outlet in the side of the tank near the bottom allowed for delivery of the water from the tank to the pump which circulated the water to the constant head tank. Water for the tank was supplied from a distilled water source to be discussed later.

The constant temperature bath was a 30 L water bath capable of providing 2.5 kW of refrigeration or 1 kW of heating. Water from this bath was circulated using a second magnetically coupled pump through 12.7 mm tygon tubing to the cooling jacket in the inclined flat plate and then on to the coils in the constant head tank to provide adequate temperature control in these systems. Control of the temperature in the bath itself was accomplished by setting the controller to automatic or by controlling the temperature manually, the latter being the mode of preference because of the low cooling load. A 1/15 hp stirrer in the bath as well as

water returning from the cooling system loop kept the temperature bath adequately mixed.

To supply liquid from the supply tank to the flow plate, a Cole-Parmer variable speed, magnetically coupled gear pump was employed. This pump was located near the supply tank and pumped the water from this location through the constant temperature bath and then to the constant head tank. This liquid line was constructed from 6.35 *mm* copper tubing with 6 *m* of the total 11 *m* length consisting of a coiled section in the temperature bath to provide for better temperature control. From the constant head tank, the liquid flowed through 6.35 *mm* stainless steel tubing to a 6.35 *mm* Whitey high accuracy brass valve. Subsequently, the liquid passed through a second length of similar tubing containing a 6.35 *mm* stainless steel Swagelok "T", through a 6.35 *mm* Whitey three-way brass valve, and then finally through a last section of 3.175 *mm* stainless steel tubing which was the liquid distributor. The tip of this last section nearest the flow plate was filed such that the end of the tubing was parallel to the flow surface. This filing of the end of the tubing was done to all the sections of tubing used as distributors because it provided for better liquid distribution.

To prevent heat losses in the crucial components of the system, self-adhering foam insulating tape was installed on the constant head tank and the sections of tubing just described. This insulation was effective in preventing heat losses in both the tubing sections leading from the constant head tank and in the constant head tank itself. It should be noted, however, that the system was also run without the insulation described above and, apart from a slightly higher heat load on the temperature bath, the temperature of the liquid being delivered to the plate with the system uninsulated was only 0.1–0.2°C lower than the liquid delivered with the insulated system.

In order to monitor the temperature of the system while it was in operation, several "type-J" thermocouples were installed. A 3.175 *mm* thermocouple was installed in the lid of the constant head tank and measured the liquid temperature at a point three-quarters of the way down the tank. A 1.588 *mm* thermocouple was used in the constant temperature bath to monitor the temperature of the liquid in this system. This second thermocouple, being easily accessible and removable, was also used to measure the ambient temperature in the lab and the temperature of the CO₂ flowing on the plate during absorption runs. The third 1.588 *mm* thermocouple was placed in the "T", which was part of the liquid supply line between the constant head tank and the flow plate, the exact location being halfway between the first high accuracy valve and the second three-way valve.

The temperature reading from the thermocouples was displayed using an LCD housed in a box which collected the thermocouple signals. To obtain the temperature from a particular thermocouple, the three-way switch on the front of the box was adjusted to the proper position. The thermocouples themselves were calibrated using a standard calibration technique by the instrument shop in the department and were accurate to within 0.5°C for the temperature range in these studies.

The CO₂ supply system for the absorption studies consisted of a commercial grade CO₂ cylinder, a Matheson single stage CO₂ regulator, a Matheson gas-liquid rotameter to measure the flow rate and 6.35 *mm* stainless steel tubing to connect the above components to the gas distribution box. The gas from the cylinder was delivered directly to the plate without scrubbing it to remove impurities or humidifying it.

5.2 Auxiliary Systems

The distilled water used in these experiments was taken from the distilled water supply located in a separate laboratory. The distillation system itself was of the kettle type which used a water-cooled, inverted, funnel-shaped cone near the top of the apparatus to condense the vapour generated from the liquid flowing through the system. The distilled water produced by this system was not of the highest quality since the system was very old and essentially removed only the hardness from the water. This water was used despite the obvious concerns about its quality because a better source of water was not easily accessible.

No degassing of the water used in these studies was performed as it was deemed unnecessary. The dissolved content of the CO_2 in the water remained steady at a low value over the course of the studies performed, with representative values being listed in Appendix D.

The absorption studies done in this work required the use of a gas chromatograph (GC) and integrator to determine the amount of CO_2 present in the liquid of interest. The GC used was a Varian Model 3700 with a Porapak Q column 2.65 *m* in length. The integrator was a Hewlett-Packard Model 3380A, which used thermal paper to record the peak and area data. The operating parameters of the GC are shown in Table 5.1, while the parameters for the integrator are shown in Table 5.2. The low temperature of the oven in the GC was necessary to provide an adequate difference in retention times of the CO_2 and water peaks. At higher temperatures, not enough separation was realized, and the peaks were often merged. The value of the slope sensitivity used for the integrator was chosen as 0.03 *mV/min* since this value gave the best consistency of integrated peak areas (start and end ticks used by the integrator in determining the peak area).

Parameter		Setting
Temperatures	Injector A	180°C
	Injector B	10°C
	Column	105°C
	Therm. Cond. Det.	180°C
	Ion Detector	180°C
	Filament	180°C
Det. Mod. Zero	Upper	-12.0
	Lower	0.0
Carrier Gas Flow Settings	A	30 mL/min
	B	30 mL/min
Carrier Gas Flow rate	LHS Port	60 mL/min
	RHS Port	40 mL/min
Thermal Conductivity Detector	Range	0.5 mV
	Output	+
	Power	ON
	Current	144 mA
Column Pressure	A	29 psig
	B	29 psig
Attenuator		1
Carrier Gas Line Pressure (Regulator)		40 psig

Table 5.1: Gas Chromatograph Settings

Parameter	Setting
Report	Area %
Start Delay	OFF
Stop Timer	15 <i>min</i>
Area Reject	OFF
Chart Speed	0.5 & 2.0 <i>cm/min</i>
Chart	Auto
Slope Sensitivity	0.03 <i>mV/min</i>
Attenuation	1

Table 5.2: Integrator Settings

The camera which was used to take pictures of the rivulet widths and contact angles was a Nikon 35 *mm* camera with a Nikon Micro-NIKKOR 55 *mm*, 1:35 closeup lens. The film which was used was Kodak tungsten 160 colour slide film. A tripod was used to take the pictures to ensure that the camera did not move while the pictures were taken.

5.3 Experimental Techniques and Measurements

The following section outlines the experimental techniques used to gather the measurements required in order to make meaningful comparisons of the experimental and theoretical work. The measurements required in the various components of this study (temperature, barometric pressure, inclined flow plate angle, liquid and gas flow rates, contact angle of flat, sessile and inclined, flowing drops, rivulet widths and heights, and dissolved CO₂ concentrations) have been described in detail below along with the techniques involved in obtaining these measurements. Several of the more involved techniques are described first.

To provide the GC with a sample to analyze, liquid samples were withdrawn

from the inclined flow plate at the conditions of interest. Normally, steady state of the absorption system was realized in 10–15 *min* depending upon flow rate of the liquid. Samples of 10 *mL* were collected in a test tube of that size and filling of the test tube was done by always keeping the end of the sample line below the liquid level in the tube. In this manner, changes in hydrostatic pressure of the liquid as it exited the sample line were reduced. More importantly, it was found that if the liquid flowed down the edge of the test tube when it was being filled abnormally low results were obtained. The test tube was rinsed twice before being filled with an actual sample to ensure that it did not contain any liquid from the previous sample.

To actually draw a sample from the test tube once it was filled, a 10 μL Hamilton gas-tight microsyringe was used as it was found that regular 10 μL Hamilton liquid microsyringes gave very inconsistent results, presumably due to CO_2 leakage in the syringe. The procedure of drawing a sample was quite involved because of the insolubility of CO_2 and is outlined below:

1. Withdraw the plunger from the barrel and, using a wash bottle or some other similar device, flush the barrel. This procedure removes any gas bubbles which were formed when the previous sample was injected as some of the liquid in the needle of the syringe is vapourized during the injection.
2. Insert the plunger into the barrel and depress it at least halfway. DO NOT blot the end of the needle to remove the excess liquid at this point as this has the tendency to allow some of the liquid in the needle to evaporate before the next sample is drawn producing a gas bubble.
3. When a sample is ready to be drawn, carefully depress the plunger to the bottom of the barrel while holding the end of the needle just below the level of the liquid in the test tube. When depressing the plunger it is important to be very gentle as the teflon tip of the plunger is very delicate. A bubble will usually be formed on the end of the needle during this step and this bubble can be removed by simply withdrawing the needle from the liquid momentarily.
4. With the end of the needle just below the surface of the liquid in the test tube, slowly draw in a sample of liquid, always drawing in more sample than will

ultimately be used and then expel this liquid slowly into the test tube. Repeat twice more taking care not to introduce any bubbles into the syringe.

5. To draw a real sample, insert the needle of the syringe as far as possible without wetting the glass barrel and overfill the syringe. Depress the plunger to the desired volume, blot the end of the needle and inject the sample into the GC.

A syringe guide was used in the above procedure as the barrel of these syringes is easily damaged.

To determine the amount of CO_2 in the liquid sample injected into the GC, calibration of the GC was required. The procedure which was selected was as follows:

1. Ensure that the settings on the GC and integrator are set to the same values as those which will be used for the liquid injections.
2. Record the ambient temperature, CO_2 temperature, barometric pressure.
3. Using a gas-tight syringe, inject into the GC varying known volumes of CO_2 whose peak areas are in the range of the peak areas obtained from the liquid samples.
4. Based on the known volumes injected, the temperature and the pressure, calculate the moles of gas injected.
5. Construct a calibration curve of the CO_2 content versus peak area with the information obtained.

The procedure outlined above was adopted not only because it was straightforward and gave adequate reproducibility of the gas peak area in terms of volume injected, but also because it avoided the problems of trying to obtain standards of dissolved CO_2 in water. The calibration curve and the experimental conditions at which the curve was constructed are described in detail in Appendix C.

For the flow and absorption experiments done in this study, a flow surface of reproducible cleanliness was required in order to maintain consistency in the results obtained. The procedure which was used to clean the plate then had this requirement as its basic criteria. As well, simplicity and ease of procedure were required since frequent cleaning of the plate was necessary. Cleaning procedures involving acetone, methylene chloride, and soap and water were all tried and it was found that soap and water produced as reproducibly clean a surface as acetone or methylene chloride. The soap and water procedure was the one adopted in these studies, however, it must be pointed out that in using this procedure a contaminating film may have still been left on the surface. The important point, as pointed out by Schmuki and Laso [118], is that the surface was reproducible. By measuring the contact angle, as discussed earlier, some idea of the degree of contamination is possible since a residual film on the flow surface will affect the contact angle. The exact cleaning procedure used in these studies was as follows:

1. Rinse the plate under tap water to wet it.
2. Using ordinary dishwashing soap, scrub the surface using a paper towel.
3. Rinse the soap from the plate and using another clean paper towel, scrub the surface.
4. Rinse the plate with distilled water and wipe it dry with a paper towel.
5. Using a lint free cloth, gently wipe the surface to remove the lint left from the paper towel.
6. Allow the plate to air dry before use.

The procedures used to establish the rivulet on the flow plate, from which the measurement of the width or height were taken, can be classified into three distinct groupings as follows: increasing flow procedure, decreasing flow procedure and interrupted flow procedure. For the absorption studies, only the interrupted

flow procedure was used. In the increasing flow procedure, for which it was hoped the advancing contact angle would be most applicable, the flow was first started as dropwise and slowly increased until a continuous rivulet was formed. The flow was slowly and incrementally increased after this point and measurements taken after each increment until unstable, meandering flow resulted. For the decreasing flow procedure, for which it was hoped the decreasing contact angle would be most applicable, a maximum flow rate at which a linear, laminar rivulet could be maintained was found and the flow rate subsequently decreased slowly and incrementally. At each incremental decrease, measurement of the width or height was performed until the rivulet was no longer continuous. The interrupted flow procedure, for which it was hoped the equilibrium contact angle would be most applicable, involved setting the flow rate at a certain value via the three-way valve (liquid not flowing to the plate at this point), directing the liquid to the plate at the set flow rate and then taking the desired width or height measurement. When a new flow rate was required, the flow was stopped, set at the new value and then reintroduced to the plate. In this procedure, it was hoped that rivulets of intermediate dimensions between the previous two cases would result. The measurement of the height and width was not done at the same time on the same rivulet, but was performed at different times on different rivulets, although the procedure to establish the rivulets was always as described above for both sets of measurements. The reason for not doing both measurements on one rivulet was because of the logistics of having to use a camera to measure the widths and a micrometer to measure the heights—one would interfere with the other.

The widths of the flowing rivulets were measured from colour slides taken with a 35 *mm* camera of the rivulet as it was flowing on the plate. The exact method involved attaching a scale, calibrated to 1/32 *in*, beside the flowing rivulet, taking

a photograph of the rivulet looking perpendicularly down at it and then projecting the developed slide on a wall to obtain an image 15–20 times larger than normal. In order to obtain the width of a rivulet at a certain set of conditions, approximately ten width measurements were taken from each slide and averaged to obtain a rivulet width representative of the actual rivulet. These averaged values are the ones which appear in the figures in Chapter 6, Section 6.2.1.

To measure the heights of the flowing rivulets, a depth micrometer was securely mounted to the inclined flow plate at a specified distance down the flow plate and a small pin attached to the actual shaft of the micrometer. This pin produced no significant change in the rivulet as the measurement of the height took place. The actual procedure to measure the height of the rivulet was as follows:

1. Mount the micrometer to the inclined flow plate using the mounting brackets at a specified distance from the start of the flow.
2. Obtain a zero reading which is the distance to the flow surface.
3. Start the flow of liquid and measure the height of the rivulet.
4. Change the rate to the next value and measure the rivulet height.
5. At the conclusion of each run, check the zero reading.
6. The rivulet height is the difference between the zero reading and the height reading.

The measurement of the top of the rivulet was relatively easy to determine especially at higher flow rates since as the pin encountered the liquid it produced small ripples in the fluid. At the lower flow rates no ripples were produced, but by moving the pin back and forth across the rivulet, the point at which the liquid no longer “clung” to the pin indicated the height of the rivulet. This simple procedure produced the results which are shown in the figures of Chapter 6, Section 6.3.1. The height values reported are not averaged as were the width values but represent

single measurements. Tests were also performed to see if the rivulet height changed along the length of the flow plate by mounting the micrometer at different distances down the plate.

The angle of inclination of the inclined plate was measured using an adjustable protractor and plumb line. The protractor was capable of measuring to within 1° and this value was considered to be the accuracy of the measurement of the plate angle itself. A small, fixed protractor, calibrated to the nearest 5° , was also attached to the inclined flow plate mounting bracket to function as a quick second check of the angle during actual experiments to see that the plate angle did not change.

The barometric pressure was measured using a standard mercury barometer which was located on the first floor near the center and one end of the building. It was a Nova barometer calibrated in both millimetres and inches of mercury. A thermometer was attached to the barometer and measured temperature to within 1°C . For the absorption studies, the barometer was read at the start of each day a run was performed.

The flow of liquid on the plate was measured using the classic "bucket-and-stopwatch" method. Liquid was collected in various size graduated cylinders (10, 25 or 50 *mL*) depending upon the flow rate from the end of the plate either through the overflow holes in the bottom of the liquid collection box during the height and width studies or through the sampling line during the absorption studies. Very steady flows were realized in the experimental runs and this simple method proved to be satisfactory for measuring the flow rate.

The flow rate of CO_2 was monitored during the course of the absorption runs using a rotameter which had previously been calibrated using a Singer dry gas meter for the higher flow rates and a Hewlett-Packard 100 *mL* bubble meter for the lower flow rates. Periodic checks of the rotameter were performed to ensure that the

rotameter was indeed delivering the proper amount of gas.

For the absorption runs, the CO₂ pressure on the outlet side of the regulator was set at 15 *psig* and the rotameter set to deliver a flow of 750 *mL/min*. This flow rate was large enough to produce a pure CO₂ environment on the plate yet small enough that increased absorption due to shear of the liquid by the gas at the gas-liquid interface was not significant. As well, this flow rate was low enough to allow for adequate heat transfer into the cylinder to vapourize the liquid and provide a steady flow of gas.

The measurement of the liquid temperatures was accomplished by inserting the thermocouple into the liquid of the vessel of interest and recording the temperature. For the constant head tank, the thermocouple was located near the exit of the tank to record the temperature of the liquid at this point. For the constant temperature bath, the thermocouple was located in one corner but, because the bath was well stirred, there were no significant temperature gradients. In order to record the temperature of the liquid as it flowed to the liquid distributor, a "T" was inserted in the liquid line. A thermocouple was then carefully inserted into the side port of this "T" in such a manner that the tip of the thermocouple was in contact with the liquid stream and not touching the far wall of the fitting. In this manner, an accurate reading of the liquid temperature at this point could be obtained.

For measurement of the gas temperature, the thermocouple from the temperature bath was used. This thermocouple was removed from the bath and inserted a distance equal to at least half the length of the thermocouple into the gap between the plexiglass cover and the flow plate. By leaving the thermocouple in the gas stream until a constant temperature was obtained, an accurate reading of the temperature of the gas on the plate was found.

The measurement of the contact angle of the liquid on the plate also involved

using a camera—the same one as in the width measurements. For the measurement of the static contact angle, a drop of known quantity was placed on the inclined flow surface and allowed to remain there for one to five minutes. When the proper time had passed, a photograph was taken of the profile of the drop from an angle which was not quite parallel to the flow surface. By taking the picture from a slight inclination down onto the plate surface, a more sharply defined interface between the liquid and the solid surface was realized. These photographs were again colour slides and were projected onto a wall to provide a 10–15 times magnification. A protractor was used to measure the angle of contact of the liquid with the solid from profiles which had been traced onto sheets of paper.

The above described method provided values of advancing, receding and equilibrium contact angles. The equilibrium angles were determined from sessile drops resting on the inclined flow plate which was horizontal at the time. The advancing and receding values were taken from profiles of drops which were slowly moving or just about to move on the inclined flow plate which was tilted at an angle of 15° sideways—the entire mounting bracket for the inclined flow plate was tipped. All the values of the contact angle used in this study were taken from pictures looking “end on” at the inclined flow plate. Finally, the contact angle measurements reported used both air and CO_2 as the surroundings to see if the environment had a significant effect on the angle.

Contact angles from flowing rivulets were also taken using the above described camera and the resulting colour slides were analyzed as described above for the static contact angle case. The increasing, decreasing and interrupted flow procedures were used to vary the value of the contact angle in the system.

To better characterize the flow surface, measurements of the surface roughness were taken using a Taylor-Hobson Talysurf 4 Surface Measuring Instrument. This

equipment measured the center-line-average roughness of the surface in micro-inches by means of a stylus which traveled across the surface of interest and recorded the heights and depths of the hills and valleys on the surface using a rectilinear recorder. The equipment automatically gave the results of the analysis as an average reading, and by utilizing the rectilinear recorder, a graph representing the cross-sectional profile of the surface irregularities on the plate surface was obtained.

5.4 Additional Procedures

In order to finalize some of the procedures outlined above, preliminary procedures were tested with interesting results sometimes obtained. Several of the more significant procedures attempted will be outlined below.

In the measuring of the contact angle using the sessile and flowing-stagnant drop, photographs were also taken looking across the plate when the plate was horizontal and when it was tipped 15° in the proper inclination direction. This procedure was performed to determine if the final polishing procedure for the plate had any effect on the contact angle since the polishing was done in the direction of the length of the plate. As well, small amounts of Food Club red food colouring (water, colour, benzoic acid) was added to the liquid which was used to make the drops on the plate. This colouring was tried in order to better highlight the contact angle of the drop with the plate.

Another important procedure tested involved the collection of the liquid samples during the absorption studies. Before the design of the liquid collection cup, a fixed weir in the liquid collection box was used to collect the liquid and direct it to the sampling line from which the samples were drawn. Using this setup, the liquid was required to flow off the end of the plate, fall approximately 1 cm, pool

in the weir and then flow out of the liquid collection box through a one-eighth inch Swagelok fitting. This setup proved to be unsatisfactory resulting in the design of the previously described liquid collection cup.

One last procedure which was tested was that of weighing the gas-tight microsyringe to determine the amount of liquid injected into the GC. The procedure required filling the syringe with $5\ \mu\text{L}$ of liquid, weighing it, injecting the sample and then reweighing the syringe—the difference in the weights being the amount of liquid injected. Although this procedure works well for larger amounts of liquid, it was found that for a $5\ \mu\text{L}$ sample, which weighs approximately $50/10000^{\text{th}}$ of a gram, the reproducibility in the weight was not satisfactory even using an analytical balance which weighed to within $1/10000^{\text{th}}$ of a gram. The errors which could be associated with the weighing of the syringe included liquid on the outside of the syringe which remained between the syringe and guide after flushing of the syringe, oil from the fingers of the person handling the syringe (eliminated by wearing gloves), evaporation of the liquid either from the outside of the syringe or from the end of the needle due to the length of time associated with weighing the syringe, and errors associated with weighing the syringe on the balance. Since this procedure did not improve the accuracy of the results and, in fact, produced more scatter in the data than reading the volume from the scale on the syringe, the amount of liquid injected was determined directly from the volume markings on the syringe. As a quick secondary check of the volume injected, the peak area of the water from the GC trace was compared to the peak area of the previous water peaks. When the peak area was not similar to the previous ones, the sample was rejected since when a common volume of liquid was properly injected, the peak areas for the water were very reproducible.

Chapter 6

Investigation of Rivulet Dimensions¹

To investigate the size and shape of flowing rivulets, measurements of the widths and heights of flowing rivulets were performed at a variety of inclined plate angles and flow rates. The measurements of the widths of the rivulets were done photographically while the values of height were determined using a depth micrometer. Using the theoretical equations for the profile of a rivulet and the solution of the velocity field inside, as outlined in Chapter 4, theoretical predictions of the rivulet width and height were generated and compared with the experimental data. All of the data in this chapter were obtained at a temperature of 20°C.

¹A version of this chapter has been submitted for publication. Nawrocki and Chuang, 1993, Can. J. Chem. Eng.

6.1 Experimental Contact Angles

One of the key input parameters required to generate theoretical rivulet profiles was the value of the contact angle in the liquid–solid system studied. As described in Chapter 5, Section 5.3, a photographic technique was used to record the drop profile and the subsequent picture projected on a wall to obtain a 15–20-fold magnification. Figures 6.1 and 6.2 are pictures which are representative of the ones taken in the determination of the equilibrium and advancing–receding contact angles, respectively. Figure 6.3 illustrates the contact angle as determined from a flowing rivulet. As can be seen from the first two pictures, the outline of the drops is quite sharp, and with the large magnification used to analyze the angle of contact of the drop with the solid surface, reproducible results were obtained. The pictures used in the determination of the flowing contact angle were not ideal, however, they did provide direct evidence of the magnitude of the contact angle in this situation.

Tables 6.1 and 6.2 list the values of static and flowing rivulet contact angles, respectively, which were determined from photographs similar to the ones just mentioned. As can be seen from the tables, there is significant variation in the values of the contact angle for certain sets of data but, overall, these data are quite good as can be seen from Table 6.3 which lists the mean values and standard deviation of each set of contact angles in the previous two tables. From this last table some conclusions can be drawn and appropriate values of the contact angle deduced. For the case of sessile drops in air and CO_2 , there is a significant difference in the average values determined for both the advancing and receding contact angle. However, for equilibrium contact angle values, there is no significant difference between those values recorded using an air environment and those recorded using a CO_2 environment.

For the contact angles measured from a flowing rivulet, some interesting results were also obtained. For the increasing flow case, the contact angle varied from a low of 27° to a high of 80° while, for the decreasing flow case, the values varied from 21° to 47° . For the interrupted flow angles, where the interrupted flow procedure was used, the value of the contact angle determined was $46^\circ \pm 4^\circ$. These contact angle results from a flowing rivulet are significant when compared with the sessile drop studies in that the same variation in contact angle, from advancing to receding angle, is observed. Clearly, the range of contact angles measured using a sessile drop can be realized in a flowing rivulet system. Finally, it must be noted that the value of the interrupted flow angle in the flowing rivulet case is significantly different than the sessile drop contact angle.

From the above results, the interrupted flow value of the contact angle from the flowing rivulet was used in the theoretical simulations as it most accurately reflected the true contact angle in the flowing rivulet. For the advancing and receding contact angles, however, the values determined from the sessile drop case were used for several reasons. Firstly, although a wide range of contact angles were determined in the flowing rivulet study, the complete range of contact angles (advancing to receding) was not always observed as can be seen from the decreasing flow data in Table 6.2. Secondly, the photographic technique used to determine the contact angles worked well only for larger values of the contact angle ($> 25^\circ$). For contact angles smaller than this value, the data are unreliable. In the simulated data which follow, the contact angles which were used were 26° , 46° , 72° , 88° . In the simulated width data reported later in Section 6.2.1, the contact angle value of 72° is used to show that this normally reported value of the static contact angle for the stainless steel–water system does not characterize the rivulet width data for a flowing rivulet system.

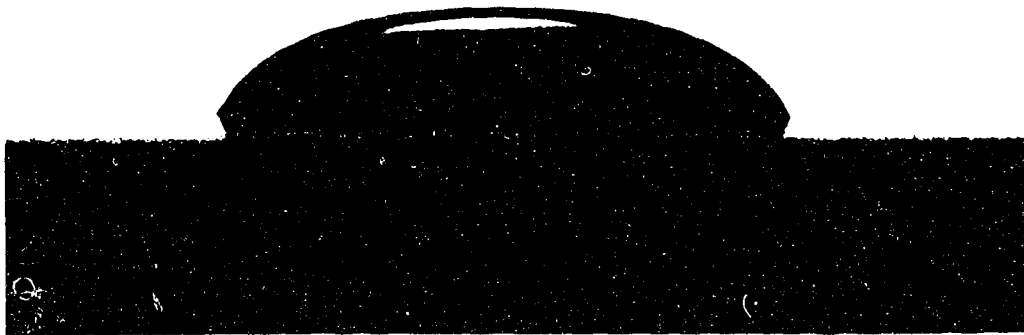


Figure 6.1: Representative Sessile Drop Used in the Determination of Appropriate Values for the Static Equilibrium Contact Angle for the System Stainless Steel–Water. The Surface Upon Which the Rivulet is Resting is Horizontal. The Drop Profile Rises Above the Solid Surface and a Reflection of the Drop Profile Can Be Seen in the Solid Surface. Air Environment.



Figure 6.2: Representative Sessile Drop Used in the Determination of Appropriate Values for the Advancing and Receding Static Contact Angles for the System Stainless Steel–Water. The Surface Upon Which the Drop is Resting is Inclined 15° from the Horizontal. The Drop Profile Rises Above the Solid Surface and a Reflection of the Drop Profile Can Be Seen in the Solid Surface. Air Environment.

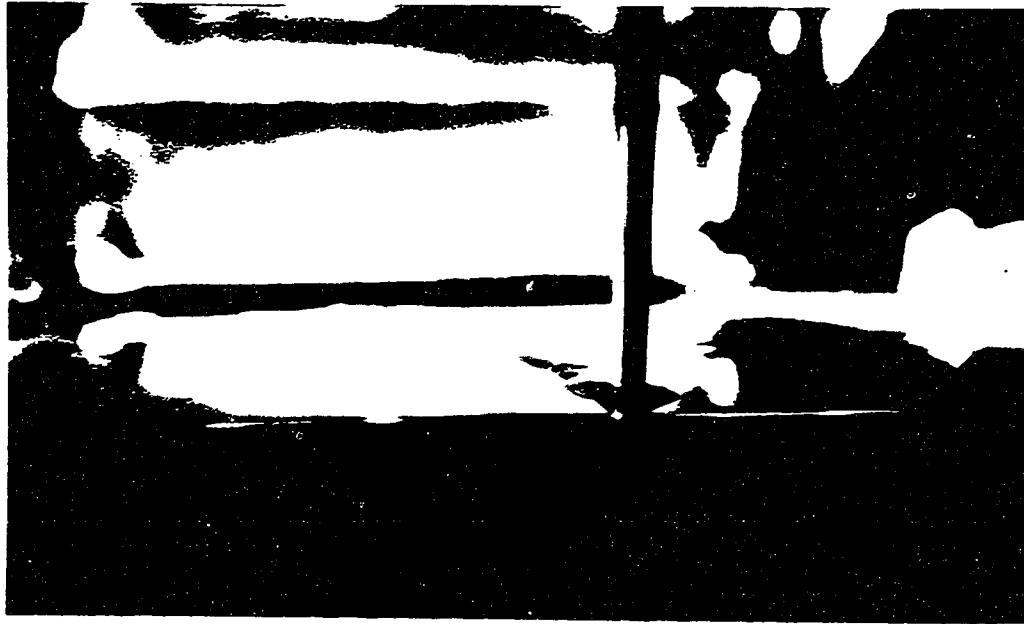


Figure 6.3: Representative Flowing Rivulet Used in the Determination of Appropriate Values for the Contact Angle in a Flowing Rivulet for the System Stainless Steel–Water. The Surface Upon Which the Rivulet is Flowing is Inclined 30° from the Horizontal. The View of the Photograph is Looking Down the Plate. Air Environment.

Contact Angles in Drops					
In Air			In CO ₂		
Receding	Equilibrium	Advancing	Receding	Equilibrium	Advancing
26	80	81	15	61	80
26	82	90	15	64	86
26	72	92	16	59	73
24	80	90	17	63	80
27	73		14	62	77
27	75		18	68	74
20	66		18	66	83
31	64		10	68	78
28	77		14	67	81
24	80		14	69	82
	73			71	83
	73			73	80
	72			70	
	74			62	
	73			69	
	73			64	
	71			70	
	69			58	
	71			70	
	73				
	67				
	72				
	72				
	67				
	72				
	65				

Table 6.1: Contact Angle Measurements, in degrees, Using Sessile Drops on Horizontal and Inclined Surfaces for the Stainless Steel-Water System in Both Air and CO₂.

Contact Angles In Flowing Rivulets					
Increasing Flow		Decreasing Flow		Interrupted Flow	
Flow (mL/min)	Angle (°)	Flow (mL/min)	Angle (°)	Flow (mL/min)	Angle (°)
10	33 46	62	47 31	23	43
24	27 61	41	27 23	37	42
34	40 56	26	25 21	55	45
54	53 80			64	51 47

Table 6.2: Contact Angle Measurements in a Flowing Rivulet for the Stainless Steel–Water System in Air. $\alpha = 30^\circ$.

Summary of Contact Angle Data		
	Average Value (°)	Standard Deviation (°)
Contact Angles in Air		
Receding	26	3
Equilibrium	72	5
Advancing	88	5
Contact Angles in CO ₂		
Receding	15	3
Equilibrium	66	4
Advancing	80	4
Contact Angles in Flowing Rivulets		
Interrupted	46	4

Table 6.3: Average and Standard Deviation Values for Experimentally Determined Contact Angles in Sessile Drops and Flowing Rivulets ($\alpha = 30^\circ$) for the Stainless Steel–Water System in Air.

6.2 Experimental Widths

The investigation of rivulet widths was performed in such a manner as to provide information on the hysteresis of rivulet flow and to show that this phenomenon can be controlled, at least in an experimental setting.

A variety of flow rates were required to perform the desired analysis and the smallest and largest flow rates attained for any one experimental condition varied slightly due to the effect of plate inclination on the stability of the rivulet. In the figures which follow, the experimental data simply indicate the region for which stable, linear, laminar rivulet flow was obtained. A short description of the largest and smallest flow rates used in this study is presented here but for a complete description of the experimental method for establishing the rivulet flow refer to Chapter 5, Section 5.3.

The plate inclination controlled the size of the largest stable rivulet which could be obtained—smaller plate inclinations resulted in larger rivulets. Also, the rivulet exhibited its largest width at low plate angles. For the smallest flow rate studied, plate angle and type of flow analysis were both contributors with the latter being the controlling factor in determining whether the rivulet was stable or not. For the increasing flow rate studies, the smallest flow rate which could be obtained depended upon the size of the drop which would flow down the plate before the flow became continuous. Obviously, at larger plate angles smaller drops were formed which meant that the flow could become continuous sooner. It was also found that for the decreasing flow studies, it was easier to obtain smaller flow rates than for the increasing flow studies since the flow was already continuous in the decreasing flow case.

In these studies, two different size distributors were used. For all plate

inclinations a 3.175 *mm* diameter tubing section was used except for the 90° case where a 1.5875 *mm* diameter tubing section was used. This change in the size of distributor did not affect the results obtained.

For the photographs taken of the flowing rivulet, the picture captured the first 150 *mm* of the flow including the point at which it was introduced onto the plate. This technique allowed the direct observation of any change in the rivulet in the field of view of the picture. In all cases, visually observed entrance effects on the rivulet were restricted to the first 12.5 *mm* of the flow and no measurements were taken in this region.

Finally, while the rivulets studied in this research were quite uniform in width and height, they were not always completely linear as there was always some meandering in many of the flows, especially for the increasing flow studies. Notwithstanding this fact, the results indicate that the assumption of linearity is quite good in the case of measuring rivulet widths and heights.

6.2.1 Width Data

Figures 6.4 to 6.8 show the experimental rivulet width data as a function of flow rate for inclined plate angles of 15–90°. The triangles represent the increasing flow data, the squares the decreasing flow data and the circles the interrupted flow data. The theoretical curves which are shown represent the advancing (88°), receding (26°) and equilibrium (72°) contact angles as well as the contact angle measured for a flow rivulet (46°).

Figure 6.4 is the width data for a plate inclination of 15° and the data clearly show the effect a non-constant value of the contact angle. For the increasing flow data, the width remains constant at approximately 2.2 *mm* until the flow reaches

a value of $1 \times 10^{-6} \text{ m}^3/\text{s}$ at which point it begins to increase sharply. For the decreasing flow case, the width remains constant at 4.6 mm until the flow decreases to $5 \times 10^{-7} \text{ m}^3/\text{s}$ at which point it drops to 3.7 mm and remains steady at this value.

Using the idea of a varying contact angle, the above behaviour is readily explained and expected. For the increasing flow data, the rivulet assumes a certain width and height characterized by the interrupted flow case contact angle when it is introduced onto the plate and becomes continuous. As the flow rate is slowly increased, the height and the contact angle in the rivulet increase while the width remains constant as long as there are no disturbances to the system. When the contact angle in the rivulet begins to approach the value of the static advancing contact angle, the flow becomes unstable, and with further increases in the flow rate, the angle will decrease forcing the rivulet to expand in width.

For the decreasing flow data, the opposite occurs in the rivulet. When the rivulet is first formed on the plate with a large flow rate, the contact angle is close to that of the interrupted flow contact angle. As the flow rate is decreased, however, the contact angle decreases as the height of the rivulet decreases and width remains constant. When the contact angle approaches the value of the receding contact angle, the rivulet narrows and the height increases to return the contact angle to a value close to that observed in the interrupted flow case.

The interrupted flow data in Figure 6.4 links the above two data sets as it illustrates the case where the effect of contact angle variation has been reduced as much as possible. By interrupting the flow at each measurement, the chance of producing a rivulet with an abnormally high or low contact angle is reduced. The data confirm this fact as they follow the theoretical line for a contact angle of 46° .

The data in Figure 6.5 are for the case of a 30° plate inclination and exhibit the same contact angle variation as observed in Figure 6.4. In this case though, the

interrupted flow data follow the 46° line more closely and the decreasing flow data do not exhibit the same degree of variation.

Figure 6.6 shows the data for the 45° plate inclination and is similar to Figure 6.5. In this figure, there is one point in the interrupted set which does not lie as close to the 46° line as all the other points. This discrepancy shows that careful control of the flow system must be maintained in order to produce meaningful results since rivulet flows are very sensitive to surface contamination and disturbances to the system.

The data in Figure 6.7 are for a plate inclination of 60° and, again, are very similar to the previous data showing clear variation of the contact angle—the width values in the decreasing and increasing flow cases have both constant and rapidly changing regions and the interrupted flow case lacks this behaviour.

Finally, the data in Figure 6.8 are for the case of a 90° plate inclination and have several interesting features. In the increasing flow data, two contact angle variation regions are present. The first one occurs at a flow of $3.8 \times 10^{-7} \text{ m}^3/\text{s}$ and the second at $7.5 \times 10^{-7} \text{ m}^3/\text{s}$. Clearly, more than one contact angle variation region can occur in a given data set if the experiment is performed carefully enough and the flow remains stable over a large flow range. In the interrupted flow data, there are three points which deviate from the 46° line by a significant, uniform amount. As in the interrupted flow data of Figure 6.6, these points show that the contact angle in the flowing rivulet can assume different values and, without careful control, no meaningful data can be obtained.

Looking at Figures 6.4 to 6.8 as a group, some interesting characteristics become evident. In each figure, there is a common ending point where the data for each of the three separate sets converge. This point occurs at lower flow rates as the plate inclination increases because the flow becomes unstable sooner as the plate angle

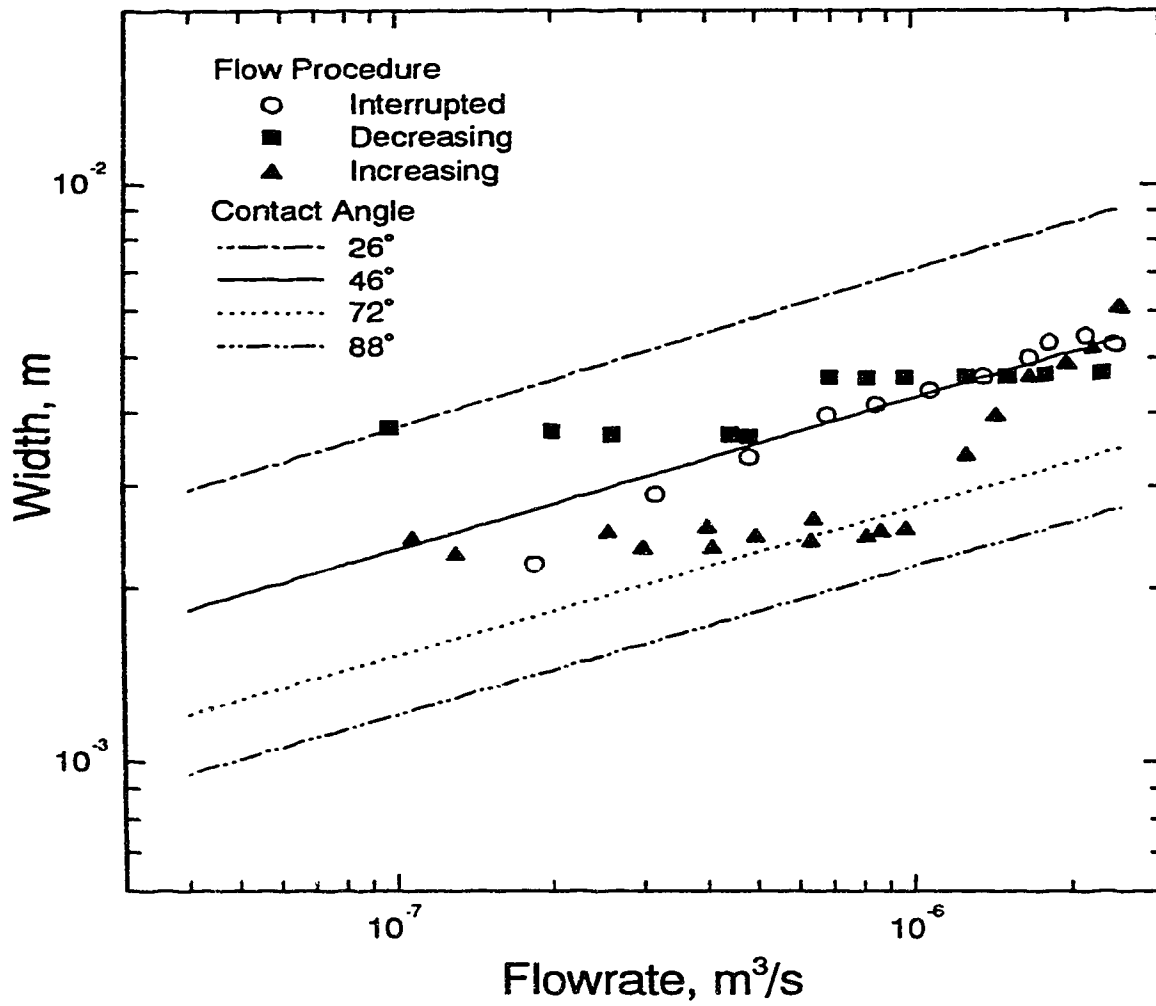


Figure 6.4: Theoretical and Experimental Rivulet Width as a Function of Flow Rate for a Plate Inclination of 15° .

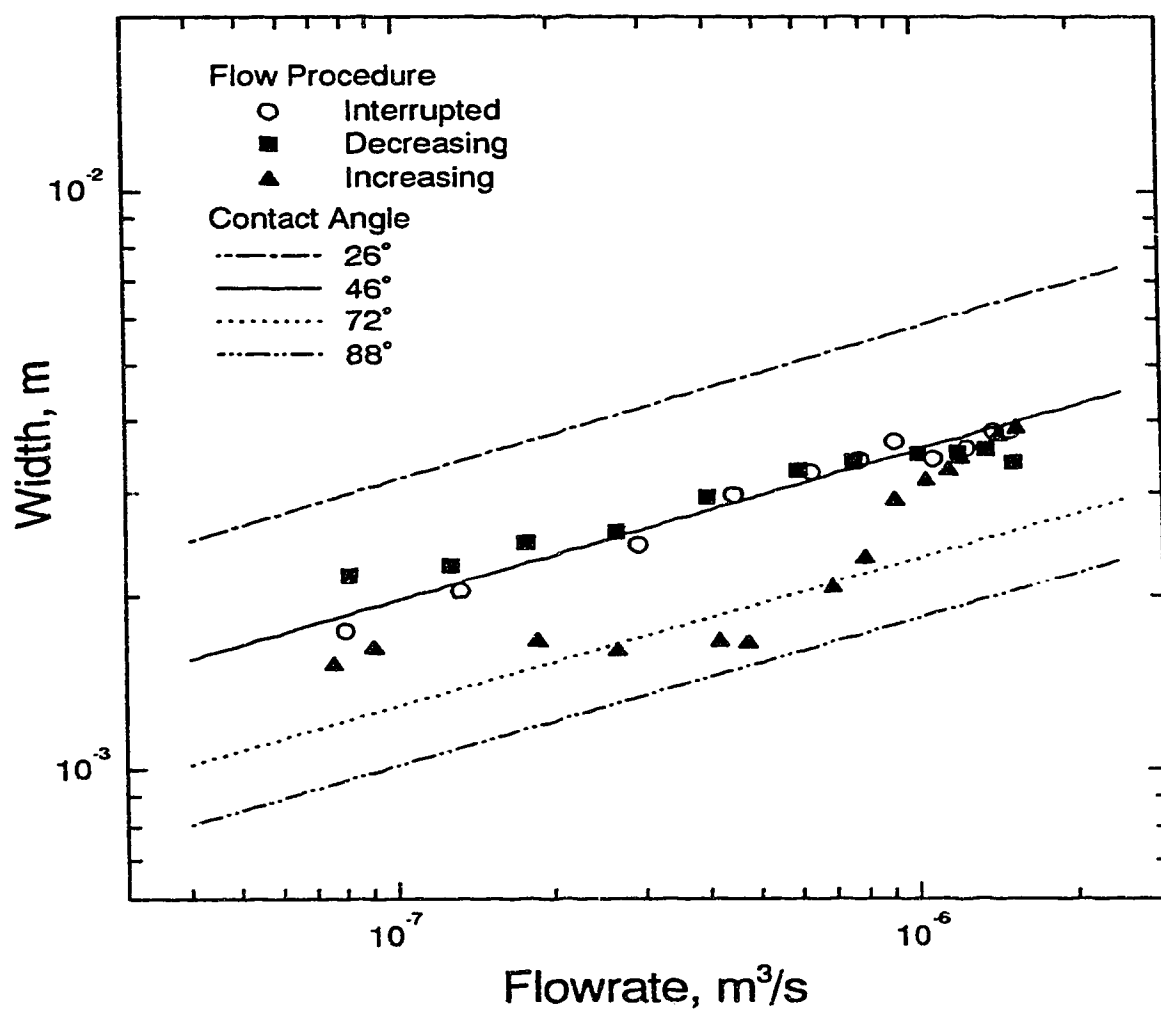


Figure 6.5: Theoretical and Experimental Rivulet Width as a Function of Flow Rate for a Plate Inclination of 30° .

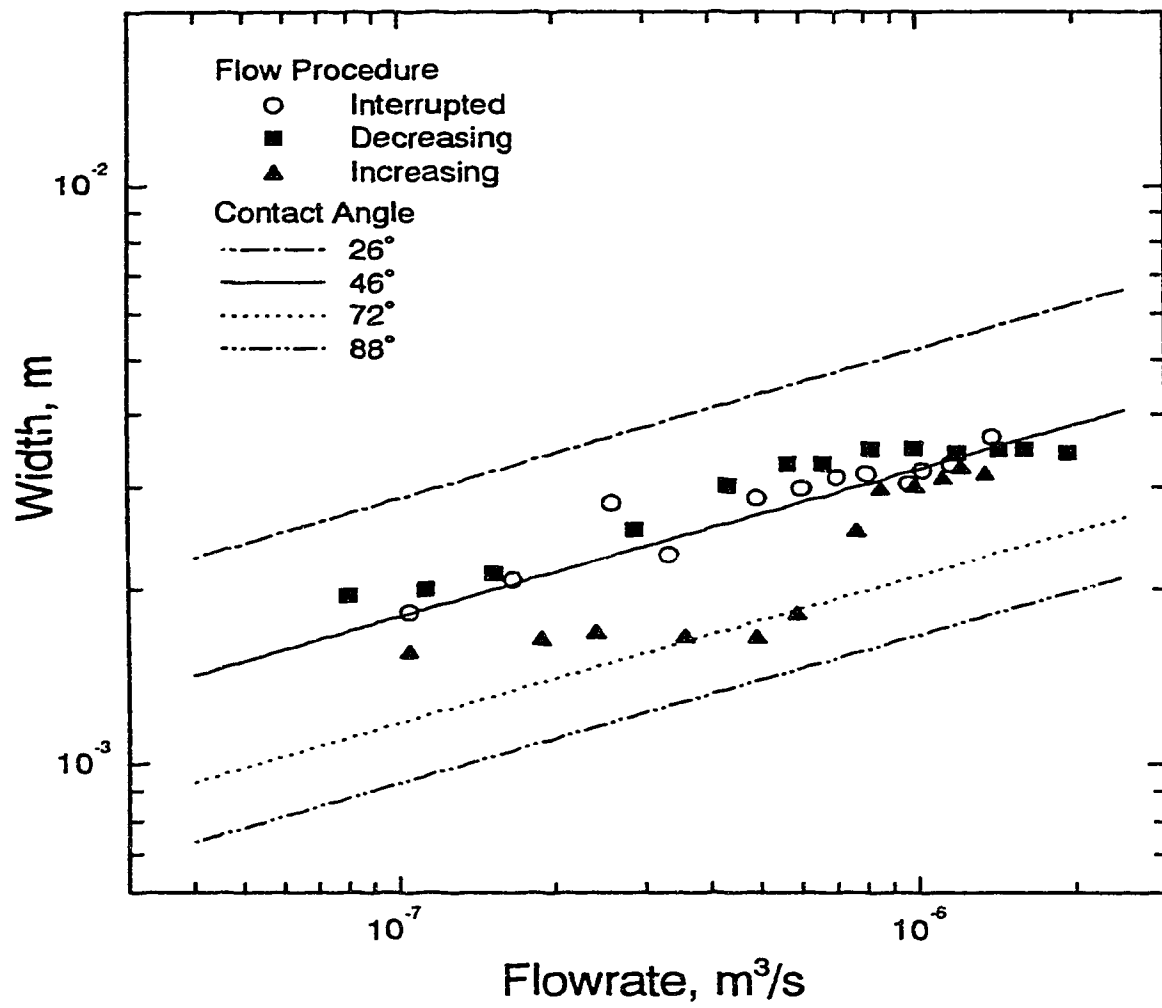


Figure 6.6: Theoretical and Experimental Rivulet Width as a Function of Flow Rate for a Plate Inclination of 45°.

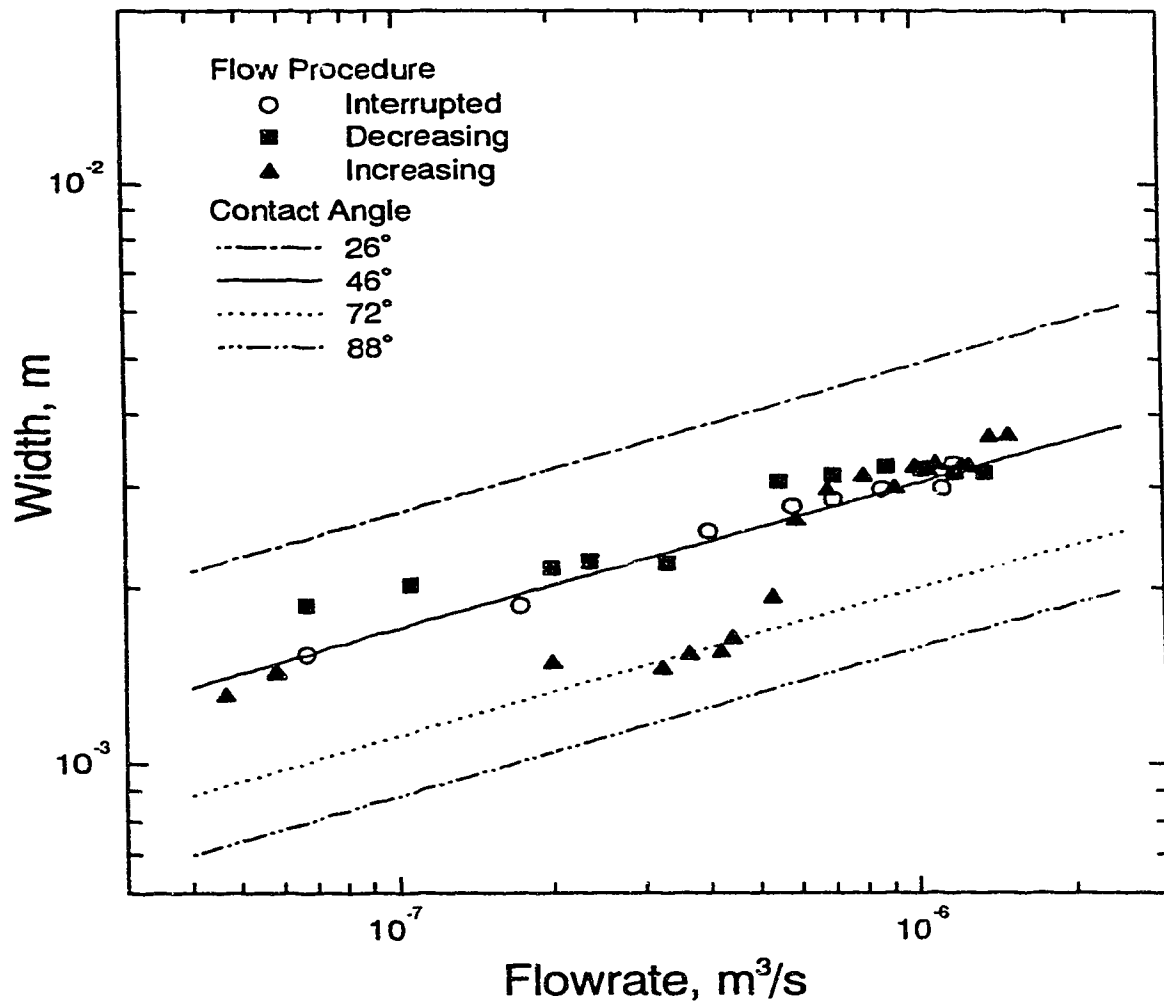


Figure 6.7: Theoretical and Experimental Rivulet Width as a Function of Flow Rate for a Plate Inclination of 60° .

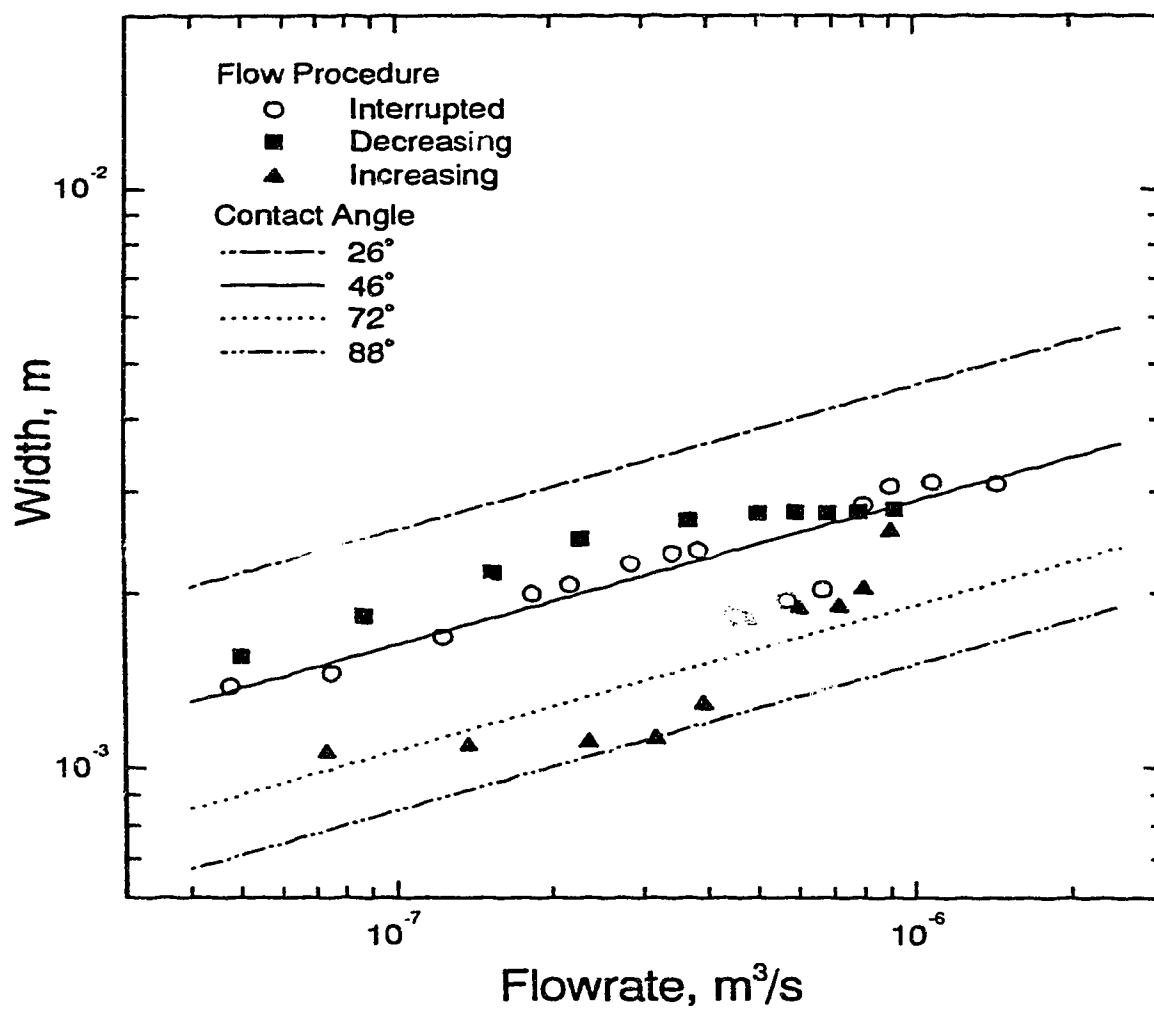


Figure 6.8: Theoretical and Experimental Rivulet Width as a Function of Flow Rate for a Plate Inclination of 90° .

increases. As with the ending point, there is a common starting point at the lowest flow rate in each figure except Figure 6.4 and this point occurs at lower flow rates as the plate angle increases.

The five figures clearly show that the width of the rivulet decreases for a given flow rate as the plate angle is increased. This behaviour is expected from a qualitative standpoint since as the plate is inclined, the effect of gravity acting to flatten the rivulet is reduced, allowing the rivulet to become higher and narrower. As well, the average liquid velocity in the rivulet increases as the plate inclination increases meaning that more liquid can pass through the same size rivulet. Referring to the theoretical curves in each of the figures, it is clear that this behaviour is also predicted theoretically.

The data in Figures 6.4 to 6.8 have already been shown to be well characterized by the contact angle observed in a flowing rivulet but it is also interesting to note that the advancing and receding contact angles bound the data in all of the figures. The contact angle in the width data for the increasing flow study can be seen to be approaching the advancing contact angle as it should and, in the case of Figure 6.8, touches it before the contact angle decreases in value. Similarly, for the decreasing flow study, the contact angle for the width data decreases toward the value of the receding contact angle until the flow begins to narrow and the value of the contact angle again rises. In Figure 6.4, the angle in the rivulet is equal to the receding contact angle at the lowest flow value used.

Finally, a clear hysteresis loop is present in each of the figures if one simply looks at the increasing and decreasing flow data. The increasing flow data trace out the bottom half of the loop and the decreasing flow data complete the top half. This characteristic is most noticeable in Figure 6.8.

6.3 Experimental Heights

The investigation of rivulet heights was performed in such a manner as to provide information on the height of the rivulet under increasing, decreasing and interrupted flow conditions. The same procedure of starting the flow, changing the flow in increments and measuring after each increment was used in this study. The difference between this study and the width studies is that a micrometer was used to measure the height values instead of a camera. Due to this difference, the values shown in the following figures are values measured a predetermined distance from the distributor.

6.3.1 Height Data

Figure 6.9 shows the height data for the case of a 15° plate inclination. Increasing, decreasing and interrupted flow data are shown and it can be seen that, unlike the widths measurements, the data deviate outside the theoretical bounding lines for the data in the increasing flow study. Although these data go outside the theoretical bounds, it is interesting to note that there is a large contact angle variation occurring at approximately the same flow rate as the contact angle variation for the width data at the same conditions. This correlation in the contact angle variation for data taken at different times on different rivulets using the same techniques further justifies the statement that the phenomena presented in this study are reproducible. In the height values for the decreasing flow study, the contact angle variation is more subtle but is present as can be seen toward the lower flow rates where the contact angle values in the rivulet move toward the receding contact angle as they did in the width studies. The interrupted flow data deviate randomly at the lower flow rates but are more consistent toward the larger flow rates and follow the

46° line. These data are quite well represented by the 46° line although not as well as the width values for the same conditions.

In Figure 6.10, contact angle variation is present in both the increasing and decreasing data although it is quite subtle. For the increasing data, the contact angle variation occurs at a flow rate of $7 \times 10^{-7} \text{ m}^3/\text{s}$ while for the decreasing flow data, it occurs around $2 \times 10^{-7} \text{ m}^3/\text{s}$. The flow rate values for the occurrence of contact angle variation in the height values are in the same range as the contact angle variation seen in the width values.

The contact angle values in the increasing flow data span the entire range of values from the receding to the advancing angle while those in the decreasing flow data are limited to values equal to or less than the receding contact angle. The data in this figure are different than the other sets in that the increasing flow data just barely passes outside the advancing contact angle theoretical line and the decreasing flow data lies almost entirely below the receding contact angle theoretical line.

The data in Figure 6.11 are again similar to the data for the 15° plate inclination in that the increasing flow data pass above the height values predicted by the advancing contact angle. As well, the decreasing flow data pass below the receding contact angle data. In the middle region of the data however, the data are quite well characterized by the 46° line especially the decreasing flow data.

Figure 6.12, for a plate inclination of 60°, is very similar to Figure 6.11 with regard to the upper limits on the data, however, in this figure, the lowest values of height recorded are considerably lower than those in Figure 6.11. For the lowest values of height recorded for both the decreasing and increasing flow cases, the values lie below the receding contact angle line. For the decreasing flow data this data point is quite good but for the increasing flow data this point seems to be out of place. Contact angle variation again appears in both of the data sets around a

flow of $3 \times 10^{-7} \text{ m}^3/\text{s}$.

Finally, Figure 6.13 shows the height data for the case of a 90° plate inclination. Contact angle variation is clearly evident in the increasing and decreasing flow data at $1 \times 10^{-7} \text{ m}^3/\text{s}$ and $3.5 \times 10^{-7} \text{ m}^3/\text{s}$, respectively. The contact angle in the increasing flow data starts at a value near 46° and increases past 88° at the higher flow rates. The contact angle in the decreasing flow data does the opposite, starting at a value of just over 88° and ending at a value near the receding contact angle of 26° . Interestingly, the interrupted flow data follow the increasing flow data in this figure whereas in Figure 6.9 these same data more appropriately followed the decreasing flow data. This discrepancy in the character of the height data and the fact that the height values taken were very small ($<1 \text{ mm}$) were the primary reasons why interrupted flow data was not reported in all five figures.

Looking at all of the figures, it can be seen that the decreasing flow data are adequately represented by the 46° line in the middle region of flow rates studied while the increasing flow data lie in a region above this line. Also, as with the width values, the height values decrease for a given flow rate when the plate inclination is increased. The behaviour is again due to the fact that gravity does not squash the rivulet as much when the plate is vertical and that the linear velocity in the rivulet increases with increasing plate angle.

6.4 Theoretical Rivulet Dimensions

6.4.1 Width and Height

Figure 6.14 is a compilation of the theoretical rivulet widths versus flow rate as a function of the plate inclination presented in Section 6.2.1. The specific curves

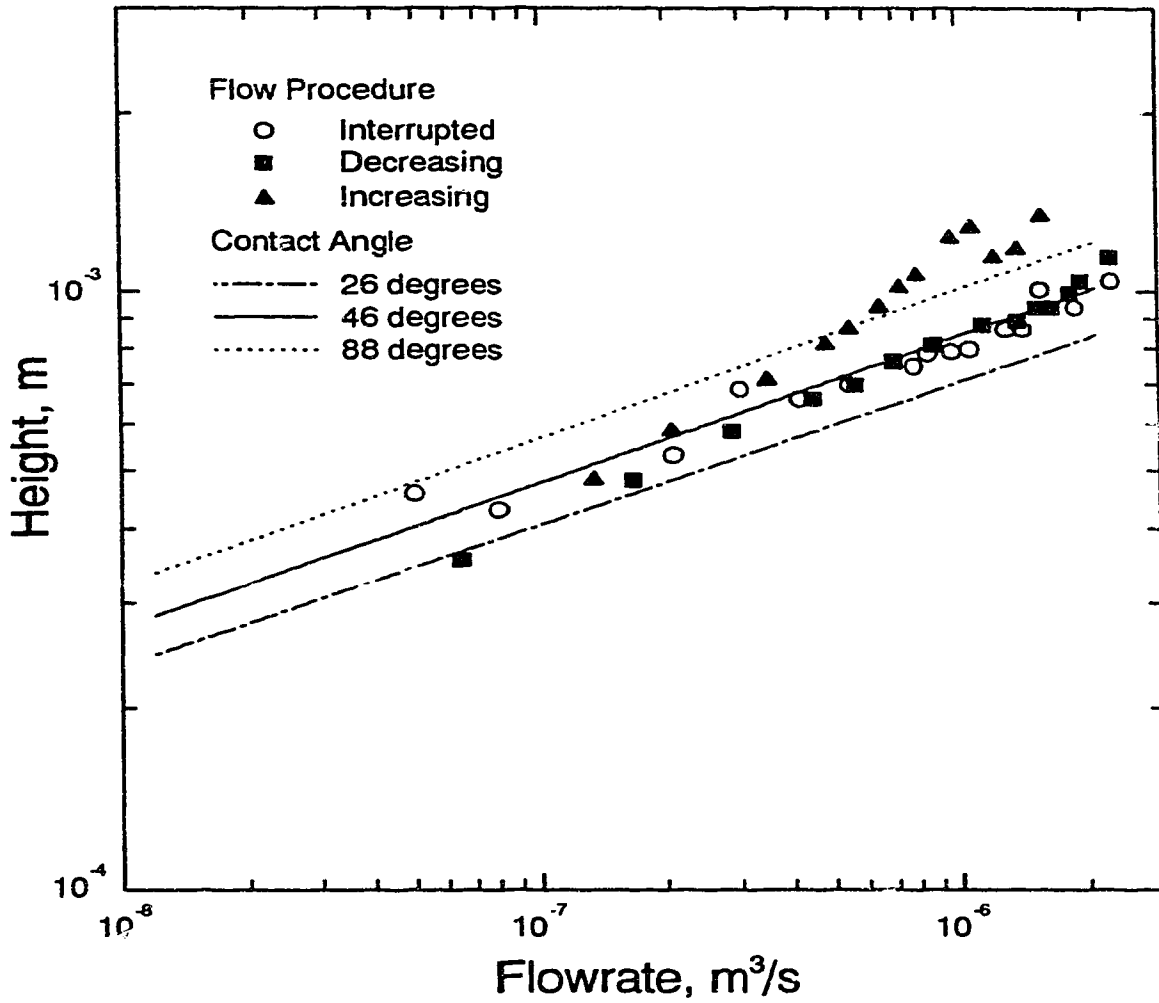


Figure 6.9: Theoretical and Experimental Rivulet Height versus Flow Rate.
 $\alpha = 15^\circ$, $Dist = 0.098\text{ m}$.

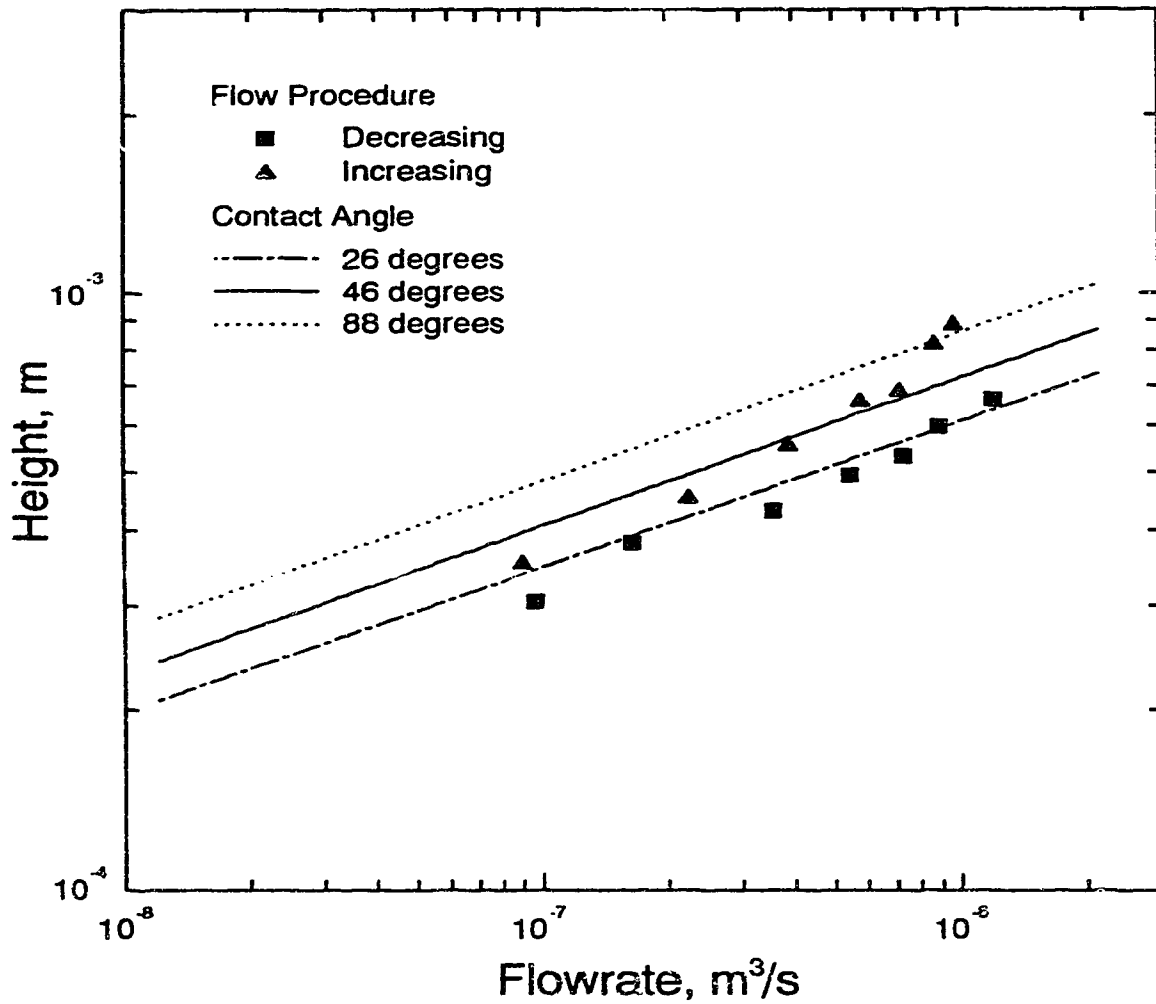


Figure 6.10: Theoretical and Experimental Rivulet Height versus Flow Rate. $\alpha = 30^\circ$, $Dist = 0.147 \text{ m}$.

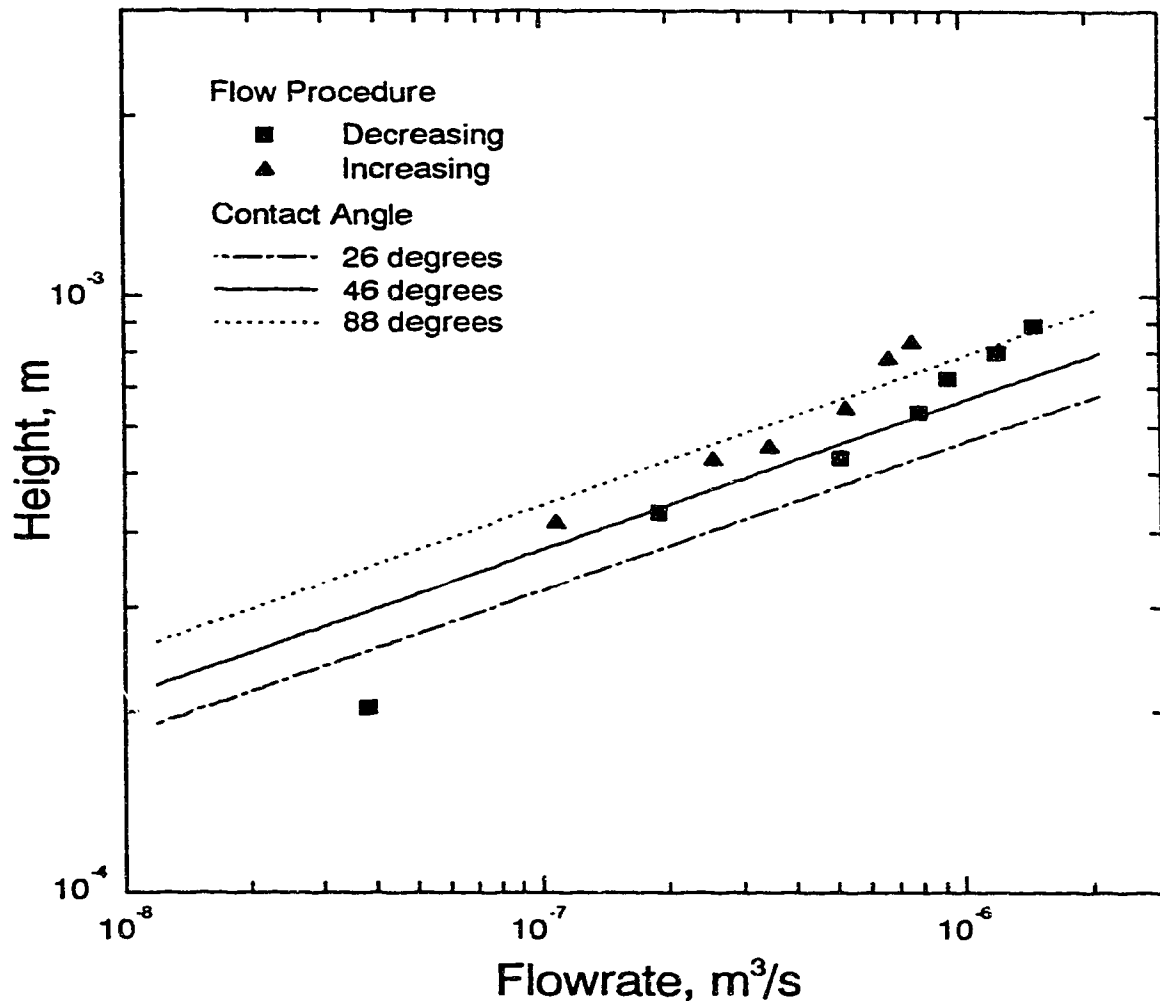


Figure 6.11: Theoretical and Experimental Rivulet Height versus Flow Rate. $\alpha = 45^\circ$, $Dist = 0.176\text{ m}$.

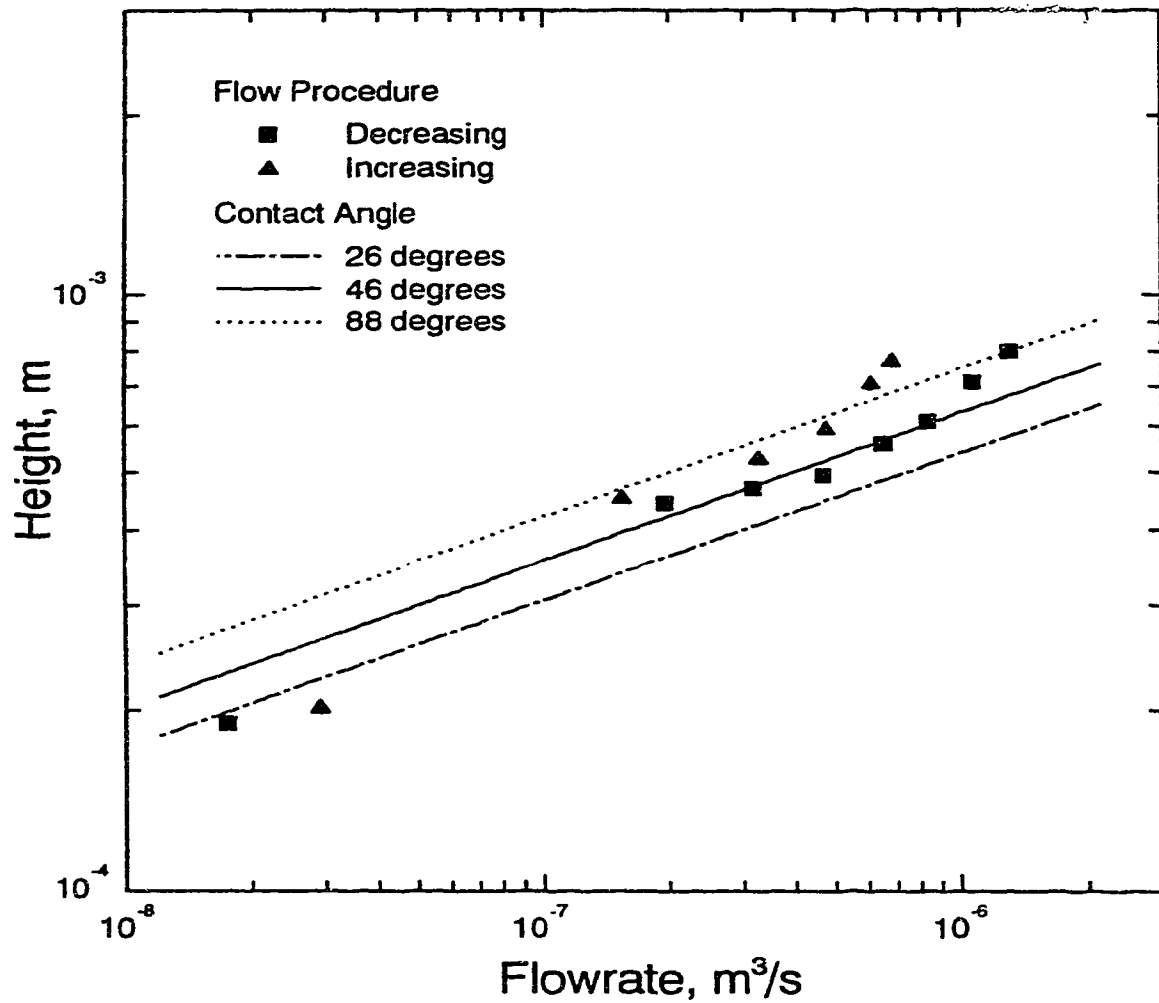


Figure 6.12: Theoretical and Experimental Rivulet Height versus Flow Rate.
 $\alpha = 60^\circ$, $Dist = 0.167\text{ m}$.

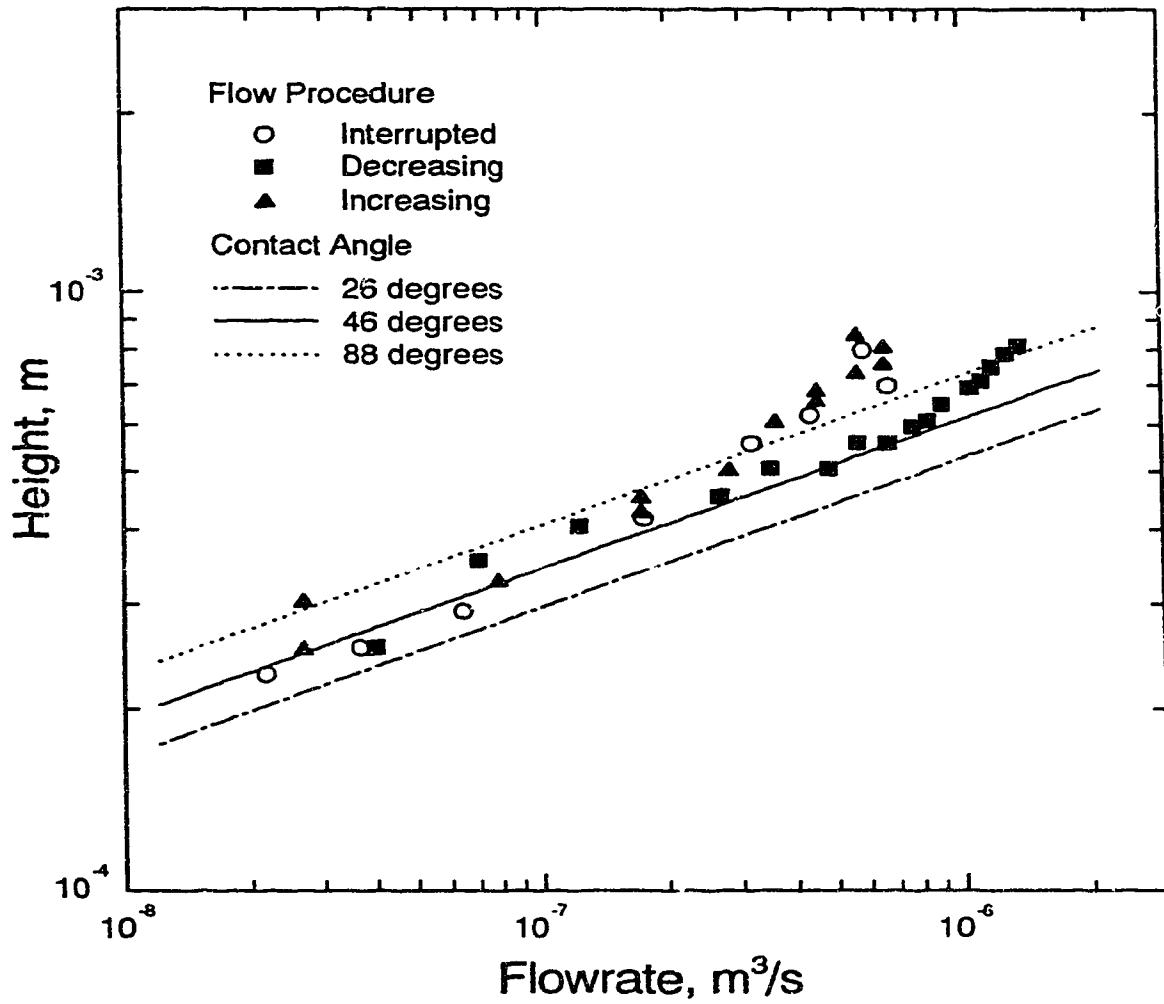


Figure 6.13: Theoretical and Experimental Rivulet Height versus Flow Rate.
 $\alpha = 90^\circ$, $Dist = 0.156 \text{ m}$.

shown in this figure are the widths for a contact angle of 46° . As can be seen from the figure the width of the rivulet decreases as the plate inclination is increased for a constant volumetric flow rate.

As with the rivulet widths, similar results can be presented for the rivulet heights versus flow rate as a function of the plate inclination and these results are illustrated in Figure 6.15. The same characteristic of decreasing rivulet height with increasing plate inclination at a constant volumetric flow rate is seen in this figure as was seen in the widths just presented. The reason for this behaviour is that, as the plate inclination is increased, the linear velocity inside the rivulet increases, and as the velocity increases, the same amount of liquid can flow through a smaller sized profile or smaller rivulet. This increase in linear velocity means that for the same flow rate both the rivulet width and height decrease when the plate inclination is increased.

6.4.2 Interfacial and Cross-Sectional Area

Of particular importance to the mass transfer process analyzed in this study is the value of the interfacial area of the rivulet. Figure 6.16 illustrates the effect of volumetric flow rate and plate inclination on the interfacial area per unit length of rivulet (arc length) and it can be seen that this value decreases with increasing plate inclination at a constant flow rate. This behaviour is expected based on the previous arguments for the theoretical rivulet widths and heights.

Figure 6.17 shows the change in cross-sectional area of the rivulet profile as a function of the volumetric flow rate and the plate inclination and further reinforces the fact that the rivulet profile decreases with increasing plate inclination at a constant flow rate.

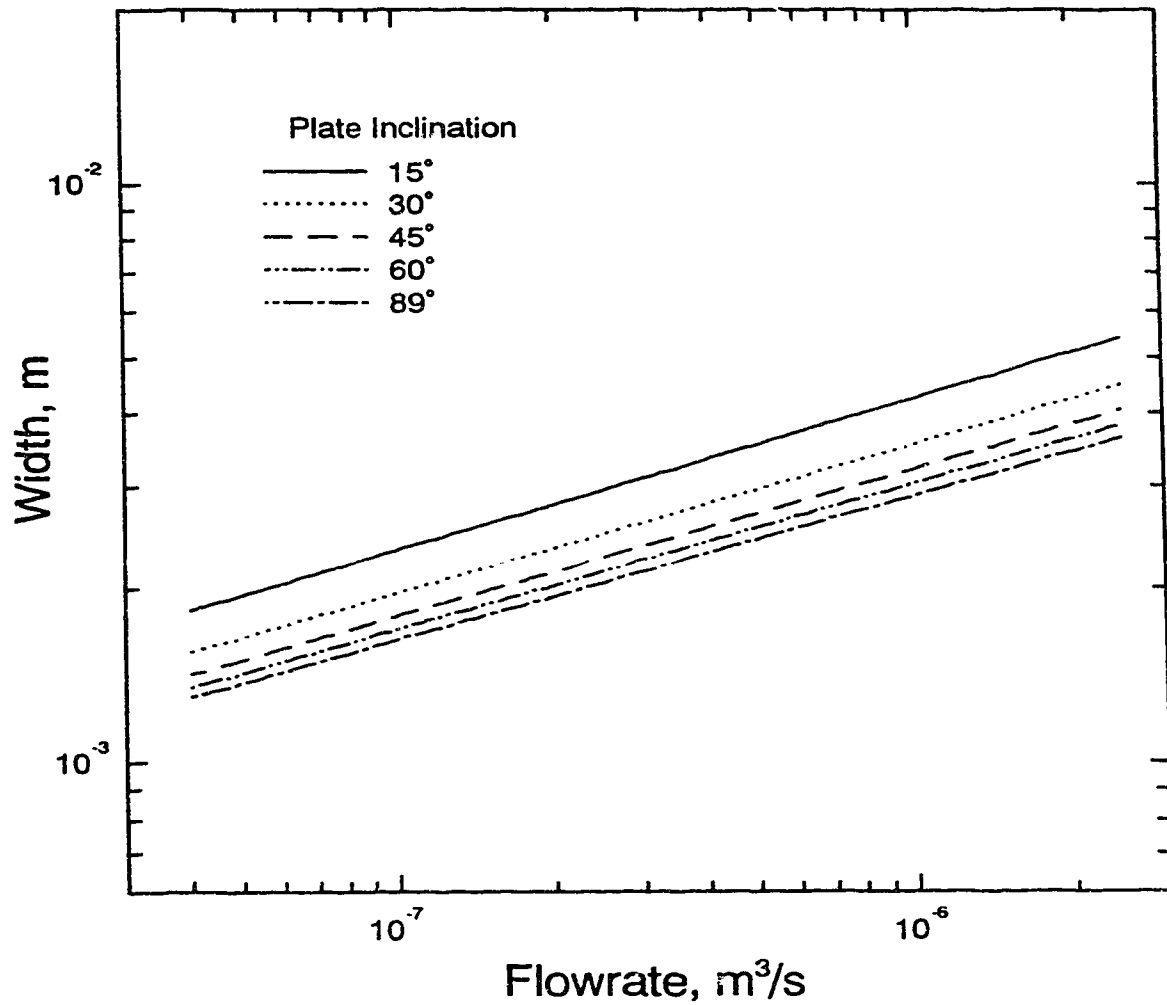


Figure 6.14: Theoretical Rivulet Width versus Volumetric Flow Rate as a Function of Plate Inclination. $\theta=46^\circ$.

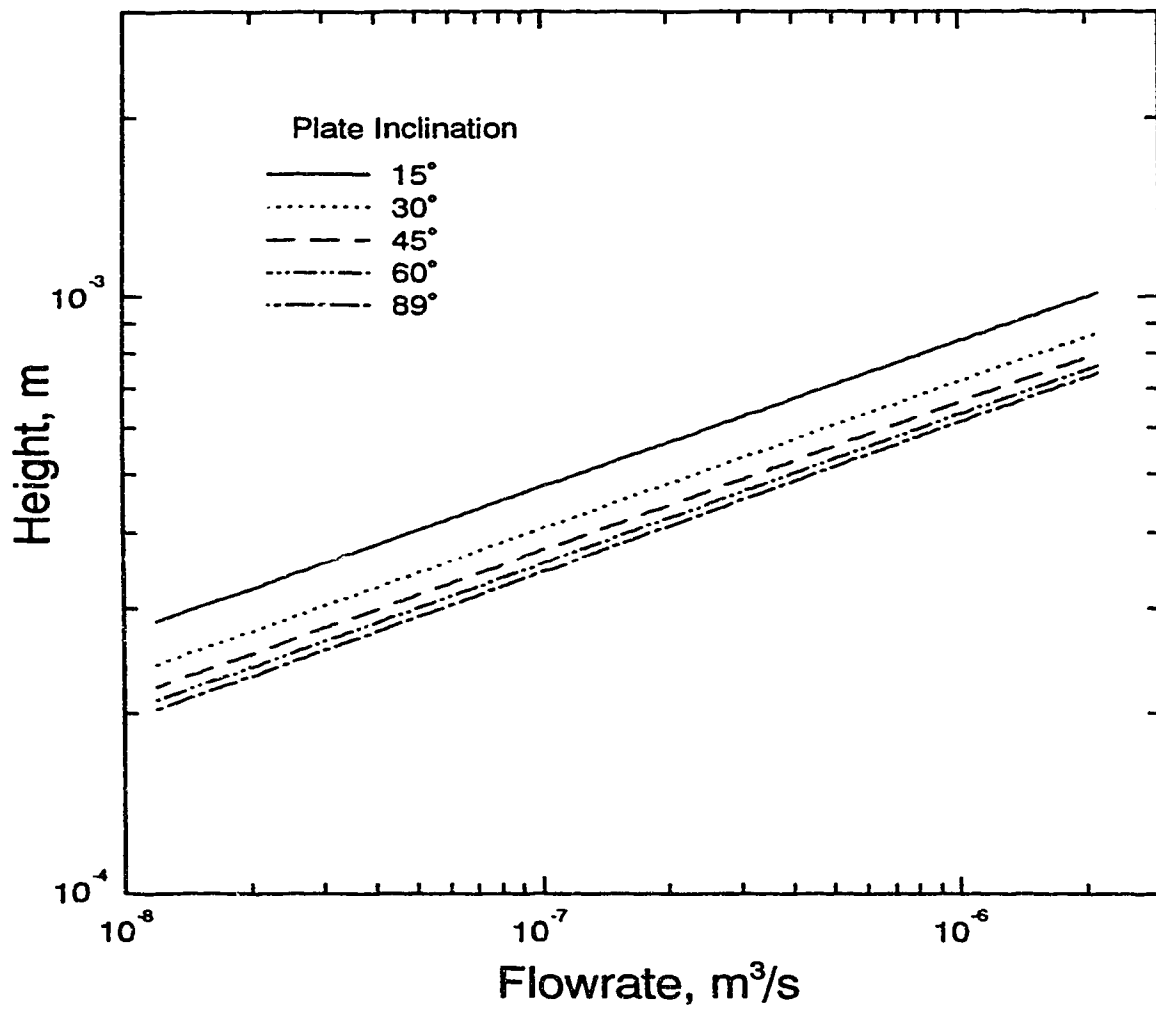


Figure 6.15: Theoretical Rivulet Height versus Volumetric Flow Rate as a Function of Plate Inclination. $\theta = 46^\circ$.

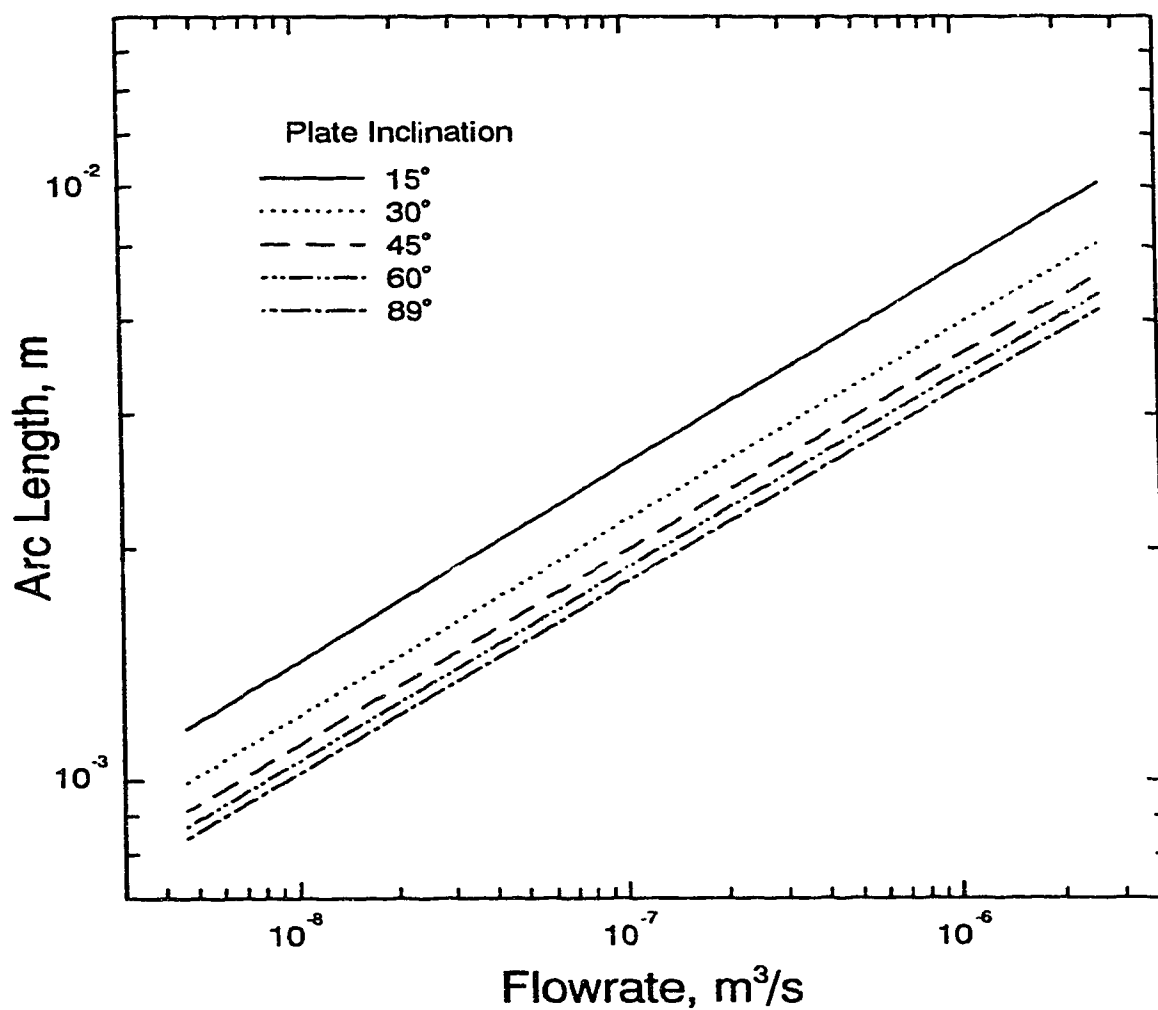


Figure 6.16: Theoretical Interfacial Area per Length versus Volumetric Flow Rate as a Function of the Plate Inclination. $\theta = 46^\circ$.

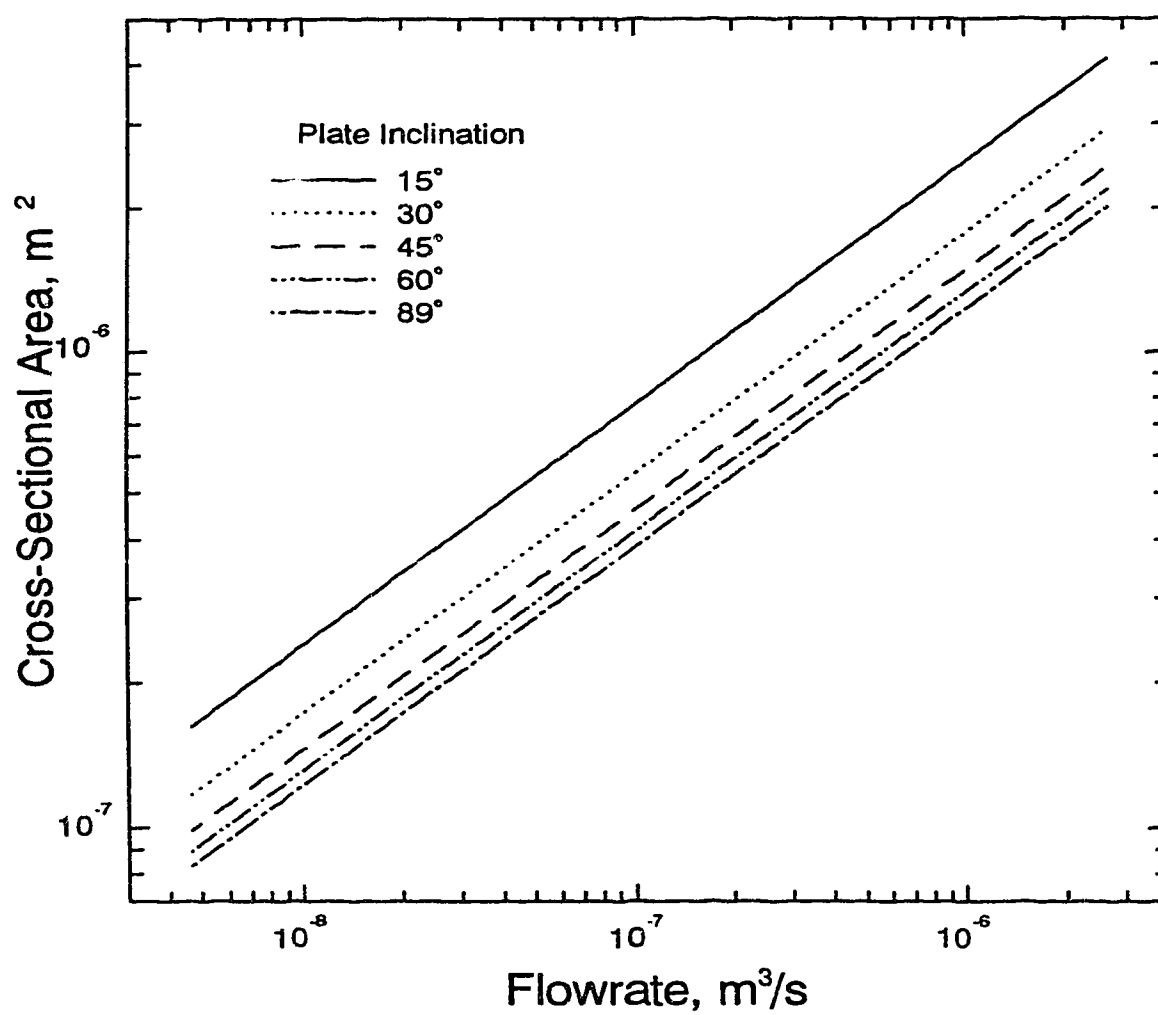


Figure 6.17: Theoretical Cross-Sectional Area versus Volumetric Flow Rate as a Function of the Plate Inclination. $\theta = 46^\circ$.

6.4.3 Rivulet versus Film Model

The theoretical analysis presented in this study is computationally intensive and a much simpler method of calculating the flow rate inside a rivulet profile would be to reduce the rivulet to a rectangle of the same width and cross-sectional area as in this analysis wherein the height of the rectangle would be smaller than that in the rivulet model. This approximation has been presented by Shi and Mersmann [125] and is the model which was used in the analysis of the gas absorption system in Chapter 3. However, as will be shown in this section, this analysis is not satisfactory.

Figures 6.18 and 6.19 show the discrepancy between the rivulet and film models in terms of the width and height versus volumetric flow rate. These plots show the rivulet widths and heights plotted as a function of the volumetric flow rate calculated using both models and it can be seen that the error between these methods is considerable—28% for the range studied here. Clearly, the film model approximation to rivulet flow is not satisfactory in this situation. It must be noted, however, that for rivulets of larger widths, the film approximation does gain validity since a rivulet with a very large width is essentially a film with curved edges which become insignificant for large rivulet widths.

Figure 6.20, which compares the interfacial area versus volumetric flow rate for both the film and rivulet models, combines the previous plots of width and height and clearly shows that the interfacial area is significantly overpredicted by the film model.

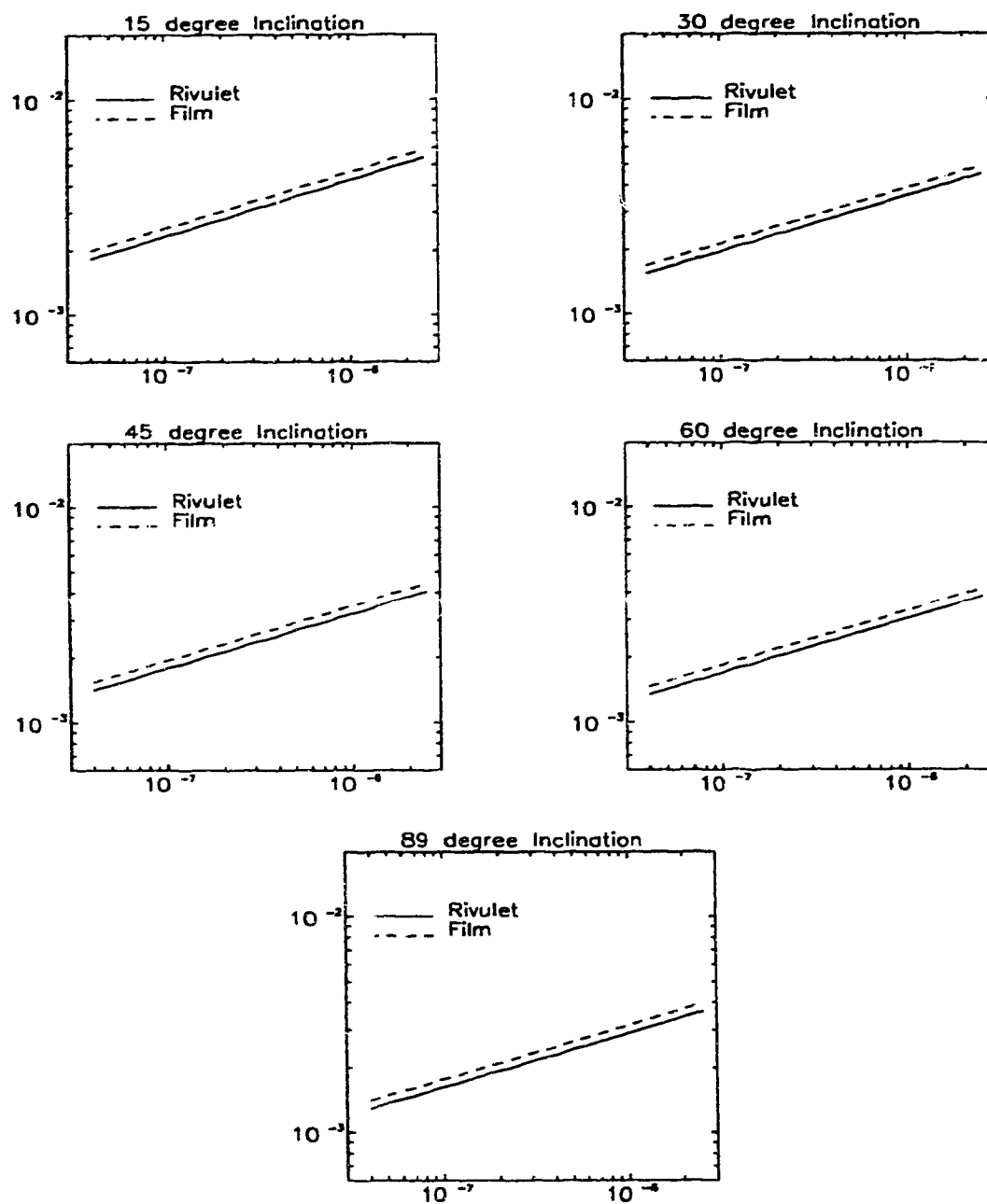


Figure 6.18: Theoretical Rivulet Width versus Volumetric Flow Rate. Rivulet versus Film Model Comparison. Flow Plate Inclination as Indicated. $\theta = 46^\circ$.

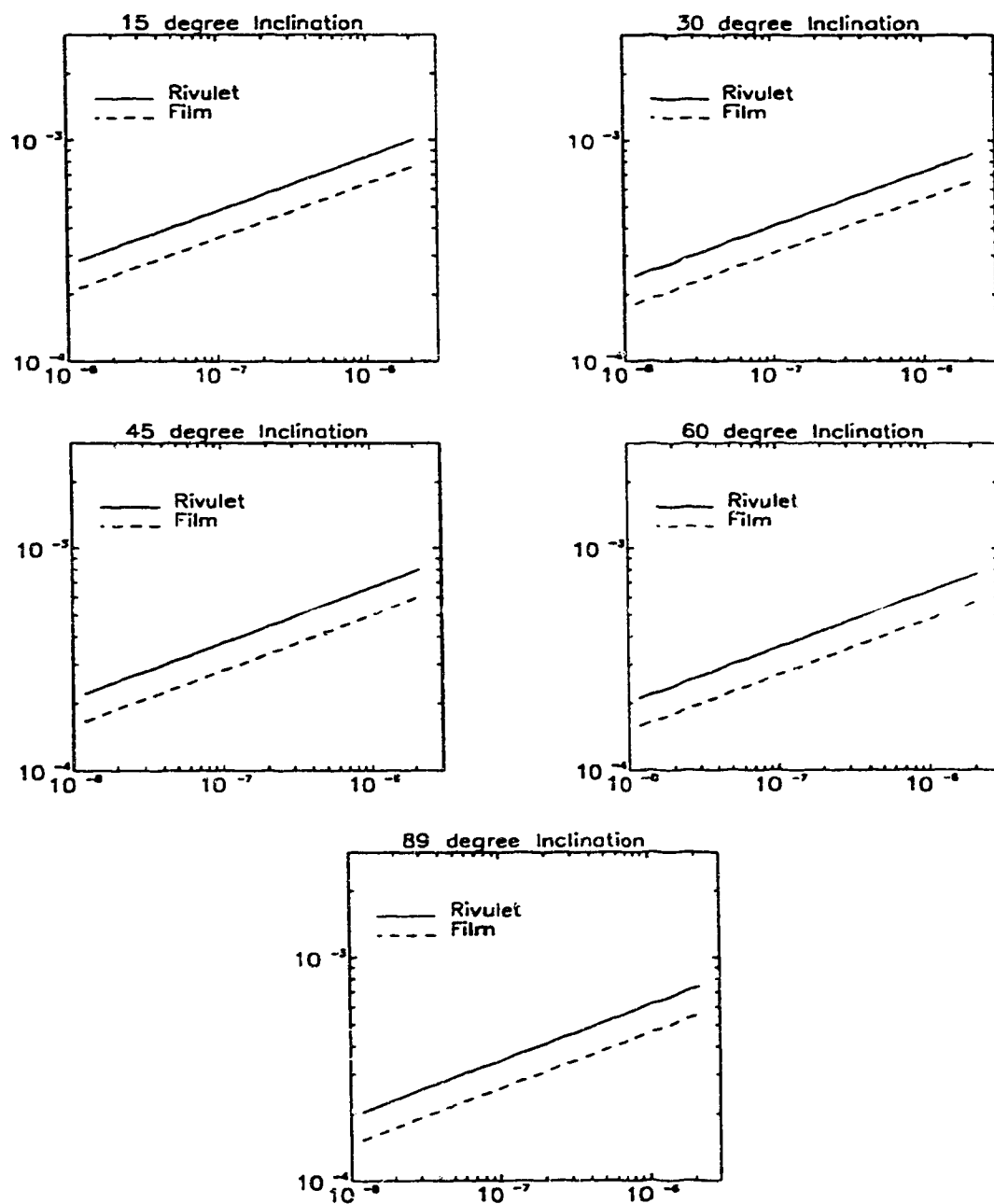


Figure 6.19: Theoretical Rivulet Height versus Volumetric Flow Rate. Rivulet versus Film Model Comparison. Flow Plate Inclination as Indicated. $\theta = 46^\circ$.

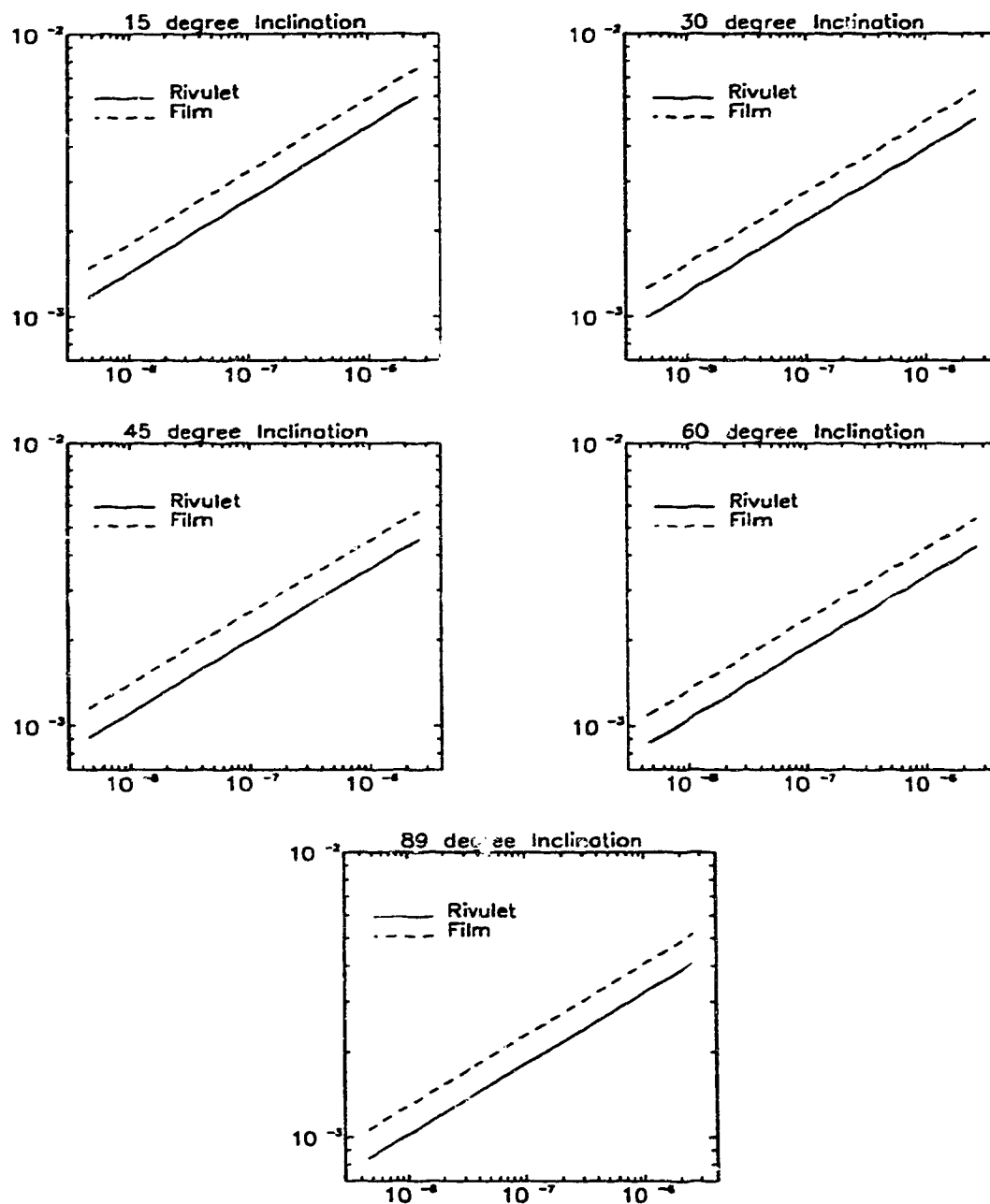


Figure 6.20: Theoretical Rivulet Interfacial Area per Length, m , versus Volumetric Flow Rate, m^3/s . Rivulet versus Film Model Comparison. Flow Plate Inclination as Indicated. $\theta = 46^\circ$.

Chapter 7

Investigation of Rivulet Absorption

The results presented in this chapter are the reproducible results which were gathered in the absorption studies. The complete set of absorption data is contained in Appendix F. Data was rejected for a number of reasons including poor water peaks on the integrator trace, incorrect number of peaks on the integrator trace, incorrect retention time in the gas chromatograph and leakage of the liquid sample past the GC injection septum. All of the data in this chapter were obtained at a temperature of 20°C .

7.1 Effect of Sampling Mechanism

Figure 7.1 shows the CO_2 absorption data for a plate angle of 45° using a fixed weir sampling mechanism. The three lines drawn in the figure represent the best fit line for each of the three flow distances studied. Looking individually at each

cluster of data points representing a certain flow distance and flow rate, the results are seemingly reproducible in nature. However, looking at all the data as a group it is clear that the results are not consistent. In this type of figure showing absorption versus flow rate with flow distance as the parameter, the expected results are three parallel lines sloping downward from left to right. These data do have the second characteristic but the lines are definitely not parallel and, in the case of the 0.114 m flow distance, the lines cross. Clearly, these data show unacceptably high end effects present in the experimental setup and no meaningful results can be extracted. As well, while the data seem to be reproducible, the results are highly dependent upon exactly how the liquid flowed into the weir. For example, if the liquid flowed into the weir at the exact location where the liquid was removed from the weir, very small end effects would be present in the data. The data in Figure 7.1 for a flow distance of 0.368 m are an example of this behaviour. Conversely, if the liquid flowed into the weir at a location which was not near the liquid exit, abnormally high end effects would occur because of excess mixing of the liquid in the weir as it flowed to the exit hole. The data for a flow distance of 0.114 m in Figure 7.1 show this behaviour very clearly as the absorption at the lowest flow rate for this data set is higher than that for either of the other two data sets. The above described flow patterns of the liquid into the weir were also observed visually during the experimental runs.

This lack of reproducibility and the abnormally high end effects in the data led to the design of the liquid sampling cup which is described in Chapter 5, Section 5.1. All of the data reported in this study, except where otherwise noted, was gathered using the liquid sampling cup.

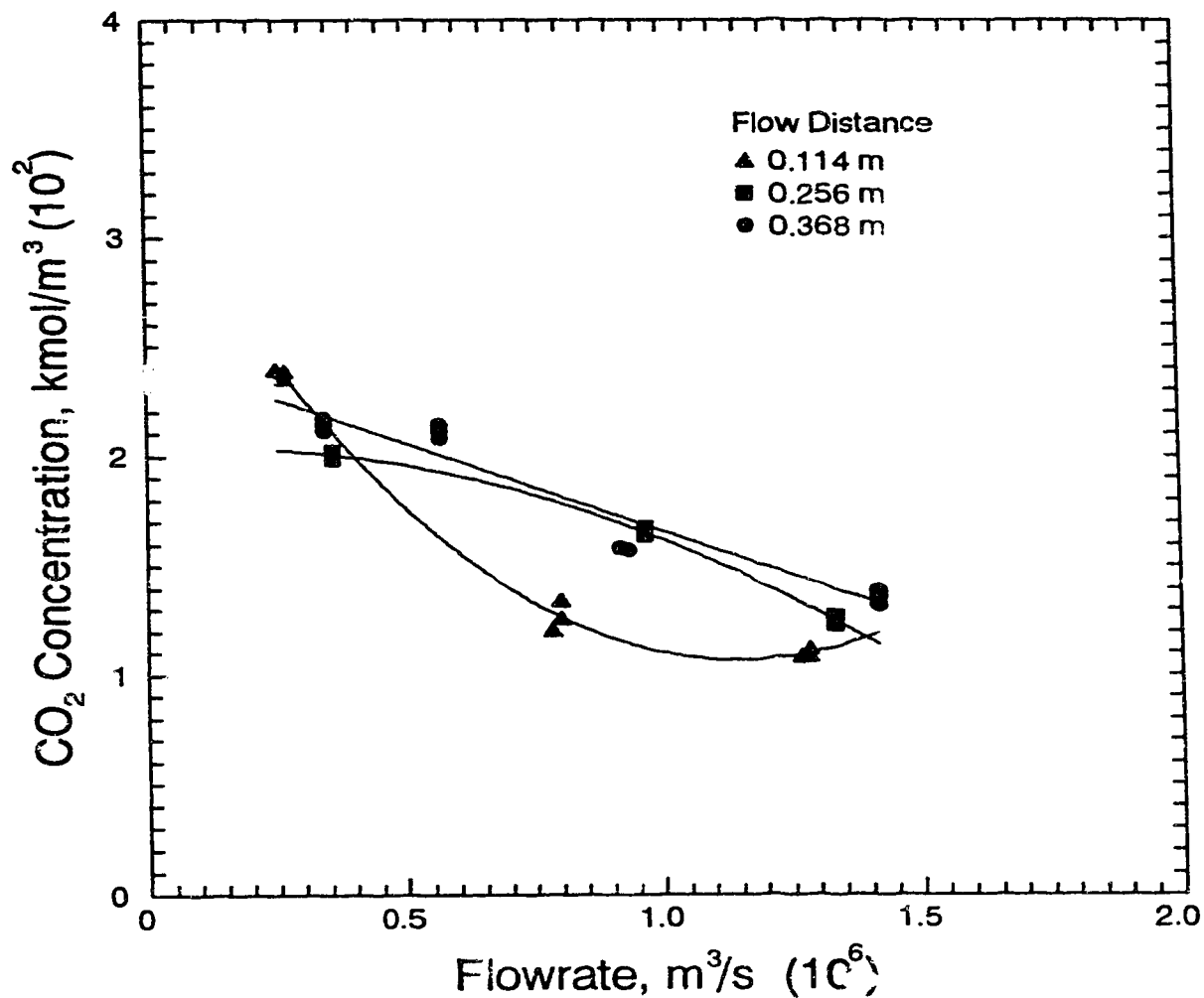


Figure 7.1: Absorption Results for a Plate Inclination of 45° Showing the Effect of Flow Rate and Flow Distance. Absorption Results Calculated Using Volume Method. Reproducible Data. Fixed Weir Sampling Mechanism.

7.2 Effect of Calculation Method

The calculation of the concentration of the $\text{CO}_2\text{-H}_2\text{O}$ samples required either measurement or calculation of the volume of the liquid sample since the absorption results were reported as kmol/m^3 . To determine the volume of the sample, the volume could either be read directly from the syringe, which was used to inject the sample, or the sample could be weighed both before and after the injection, and volume calculated from the difference in the weights. To determine which method would be more appropriate for this type of study, both methods were investigated using one set of absorption experiments. Figure 7.2 shows the absorption results calculated by reading the volume directly from the syringe while the results in Figure 7.3 were calculated by the difference in weight technique.

The results from these two figures are similar, as expected, but the data in Figure 7.3 have considerably more scatter. Chapter 5, Section 5.4 discusses, in detail, the reasons for this increased scatter which include size of liquid sample, handling of liquid syringe, presence of liquid on the outside of the syringe and errors associated with weighing the syringe. Based on the results of this study and the problems just listed, the absorption calculations were based upon reading the volume of the liquid from the syringe itself and not upon the difference in the weight of the syringe.

7.3 Effect of Carbon Dioxide Flow Rate

In an absorption experiment of the type studied in this research, the effect of the gas flow rate on the amount of absorption must be investigated. The reason that this type of analysis is required is that as the gas velocity increases, it creates shear

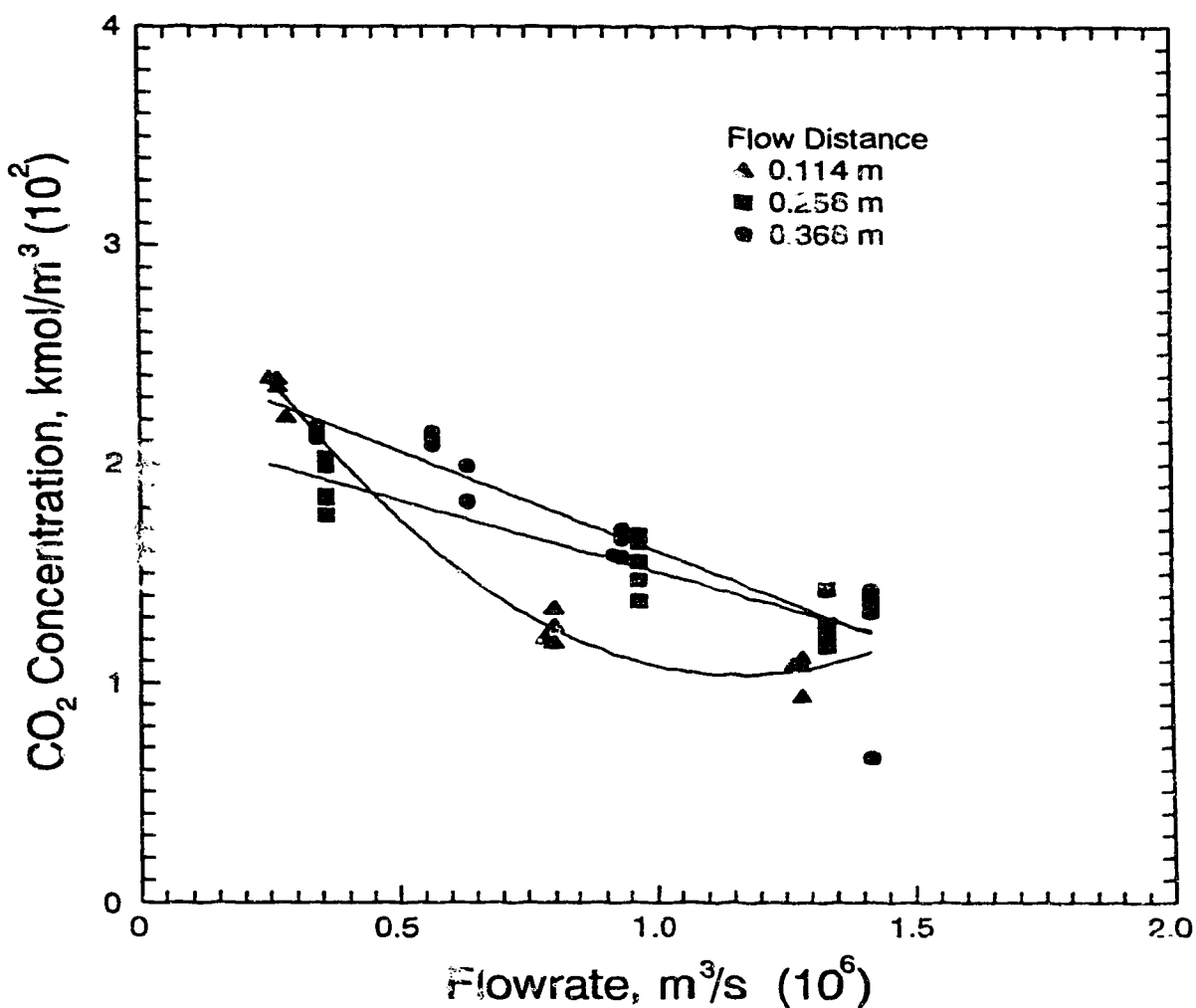


Figure 7.2: Absorption Results for a Plate Inclination of 45° Showing the Effect of Volumetric Flow Rate and Flow Distance. Absorption Results Calculated Using Volume Method. All of the Data Collected. Fixed Weir Sampling Mechanism.

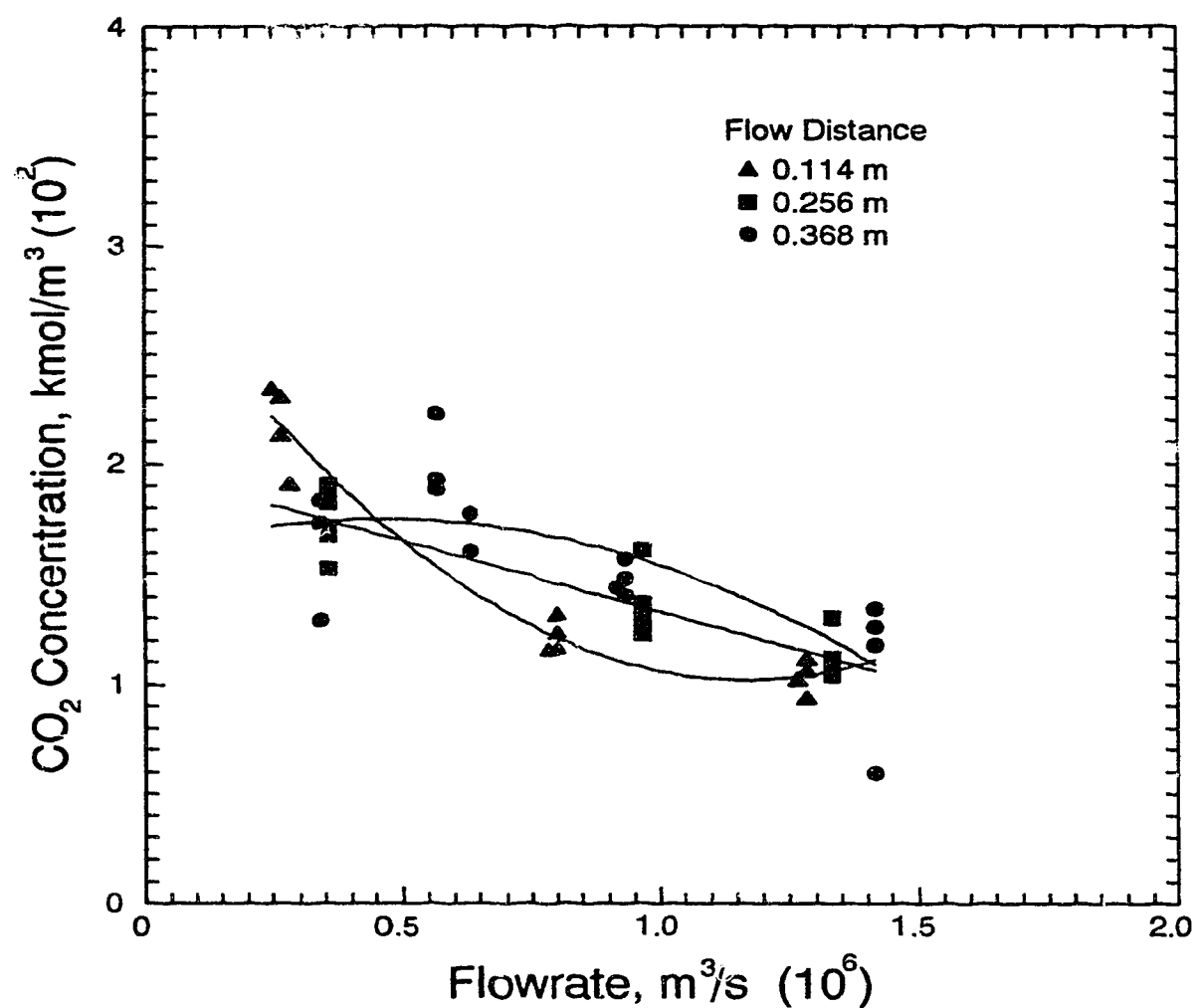


Figure 7.3: Absorption results for a Plate Inclination of 45° Showing the Effect of Flow Rate and Flow Distance. Absorption Results Calculated Using Difference in Weight Method. All of the Data Collected. Fixed Weir Sampling Mechanism.

	Average Peak Area	Standard Deviation
With CO ₂ Flow	3882	177
Without CO ₂ Flow	3912	252

Table 7.1: Effect of CO₂ Flow Rate on Absorption. $\alpha = 45^\circ$.

on the liquid surface thereby increasing absorption and changing the velocity profile inside the rivulet (zero shear on the rivulet free interface was assumed as one of the boundary conditions in the solution of the Navier-Stokes equation).

To test the effect of CO₂ flow on the absorption, the following test was done. The small opening at the top end of the inclined flow plate, through which the CO₂ exited, was blocked and the gas forced out the liquid overflow in the bottom of the liquid collection box. In this arrangement, the rivulet would still be exposed to a CO₂ environment but the gas would no longer be flowing past the rivulet. In the second part of the experiment, the opening at the top of the plate was reopened and gas was allowed to flow as usual past the rivulet at the rate of 750 mL/min (STP). The data collected from these runs are shown in Table F.8. For this data, the average absorptions are shown in Table 7.1. From these results it can be seen that, within experimental error, there is no significant difference between the two sets of data. Therefore, the flow rate of CO₂ used in these studies did not affect the amount of absorption.

7.4 Absorption Results

The investigation of CO₂ absorption by water flowing in discrete rivulets was performed using different flow rates, flow distances and plate angles to determine the effect of each of these parameters. The interrupted flow procedure from the

rivulet dimension analysis described in Chapter 5, Section 5.3 was used to establish the flowing rivulet on the plate as it produced a rivulet that was most consistent in size and shape and was well characterized by the contact angle measured in the flowing rivulet.

The liquid flow rates examined in this absorption study varied from a low of $3.333 \times 10^{-7} \text{ m}^3/\text{s}$ to a high of $1.633 \times 10^{-6} \text{ m}^3/\text{s}$. This flow rate range was chosen as a suitable range to study based upon flow stability knowledge gained in the rivulet dimension studies. For the upper limit of the liquid flow rate, the flows were stable for all plate inclinations. For the lower limit of the liquid flow rate, the corresponding value gave flows which were stable at all plate inclinations and easy to establish—lower flow rates would have caused problems with excess meandering at low plate inclinations.

Finally, absorption data was gathered at plate inclinations of 15° , 30° , 45° , and 60° but not at 90° . The reason that the 90° data was not gathered was that the liquid sampling mechanism which was used in this study could not adequately collect liquid at this steep plate angle—the liquid pooled excessively in the cup before flowing out the sampling line.

7.4.1 Concentration versus Liquid Flow Rate

Figures 7.4 to 7.7 show the experimental absorption data versus flow rate as a function of both flow distance and plate inclination. The triangles represent a flow distance of 0.114 m , the rectangles a distance of 0.256 m , and the circles a distance of 0.368 m . In these figures, the data presented is the calculated values of CO_2 concentration including end effects and the lines drawn through the data sets are best fit lines.

Figure 7.4 shows the absorption data for a plate angle of 15° . When these data are compared with the data of Figure 7.1, it can be seen that the sampling cup used to collect these data eliminates the problems associated with the fixed weir; these data can be connected by parallel lines and the data slopes from upper left to bottom right exactly as expected.

The absorption data in Figure 7.5 are for a plate inclination of 30° and are very similar to the 15° plate inclination data. One difference, however, is the data point for a flow distance of 0.114 m and a low flow rate, which appears to be lower than expected based upon the rest of the data sets. As with one of the data points in the 45° data, this point illustrates that there is some variability in the absorption results as absolute consistency in all of the rivulet flows could not be achieved.

Figure 7.6 shows the absorption data for a plate inclination of 45° and, except for the data point for a flow distance of 0.256 m and a high flow rate, this set looks very similar to the previous two.

Finally, Figure 7.7 shows the absorption data for a plate inclination of 60° . This data set is somewhat different than the previous sets as the concentration values for all three flow distances at the lowest flow rate are lower than expected relative to the other data points in this figure and based upon the results of the previous figures. Apart from this fact, these data are consistent with the previous results obtained.

7.4.2 Boundary Layer Development

The raw experimental absorption data just presented are important since they can be used to see the trends in the absorption data but they do not provide directly meaningful information as they still contains end effects. As well, the Sherwood

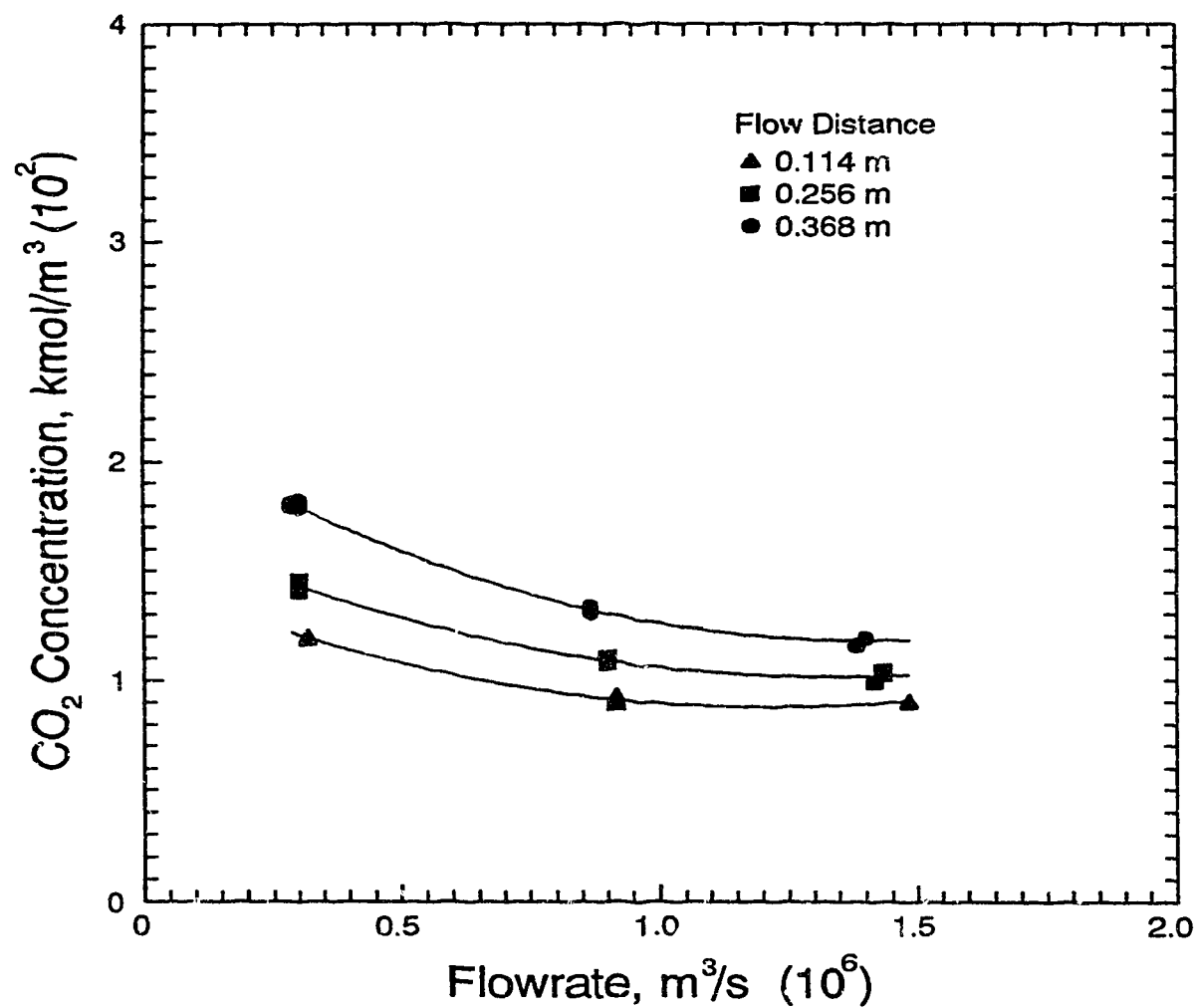


Figure 7.4: Absorption Results for a Plate Inclination of 15° Showing the Effect of Flow Rate and Flow Distance.

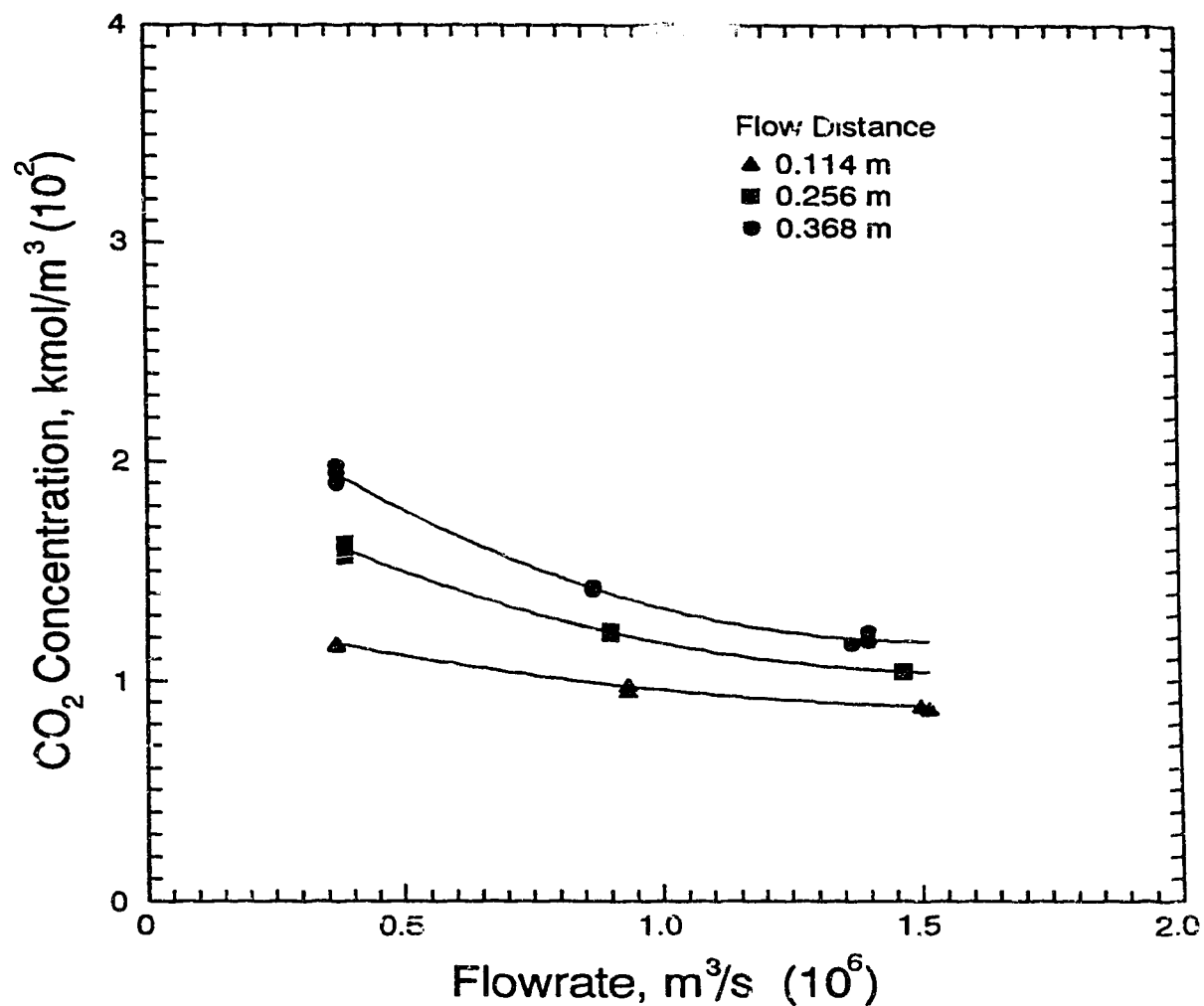


Figure 7.5: Absorption Results for a Plate Inclination of 30° Showing the Effect of Flow Rate and Flow Distance.

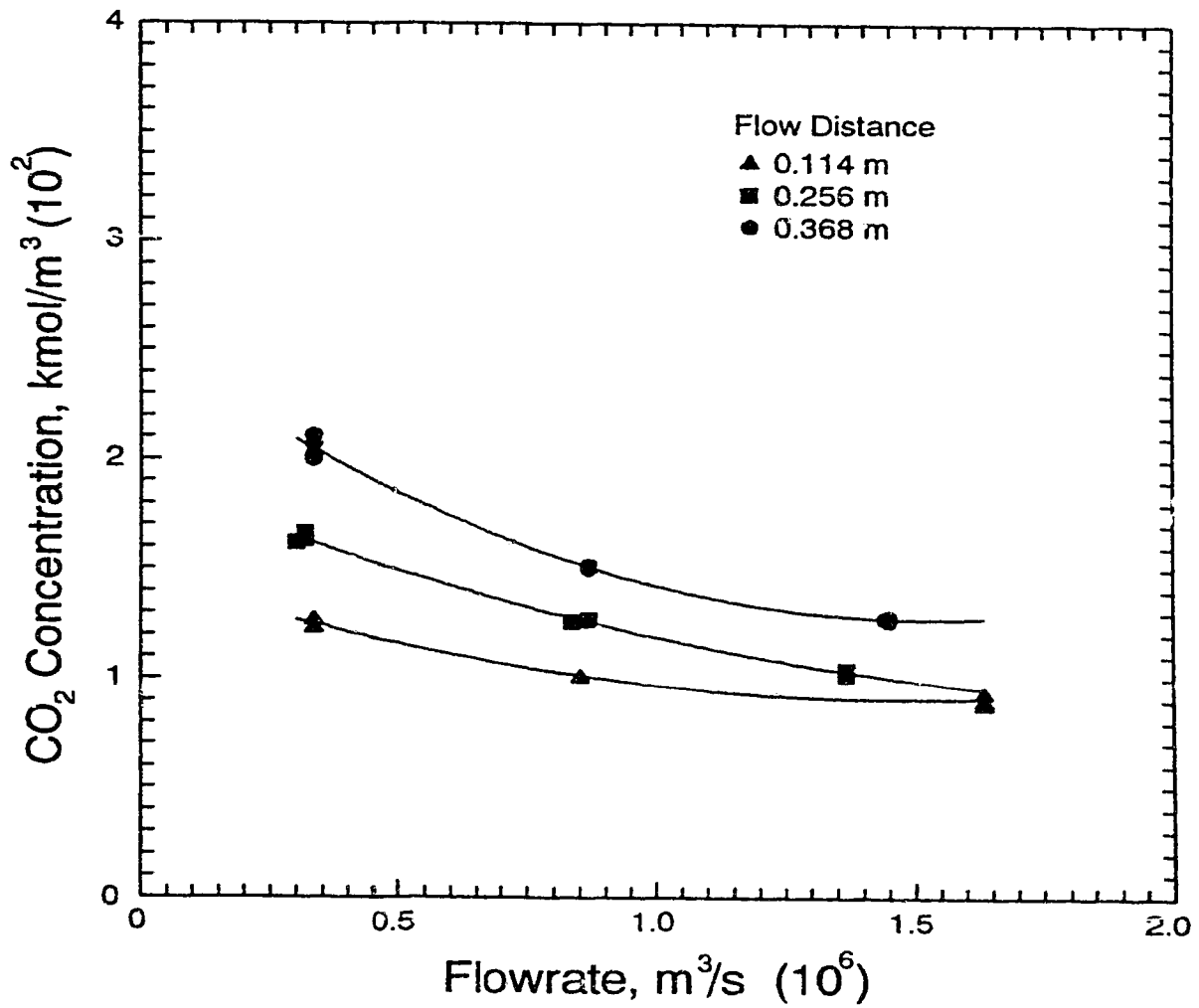


Figure 7.6: Absorption Results for a Plate Inclination of 45° Showing the Effect of Flow Rate and Flow Distance.

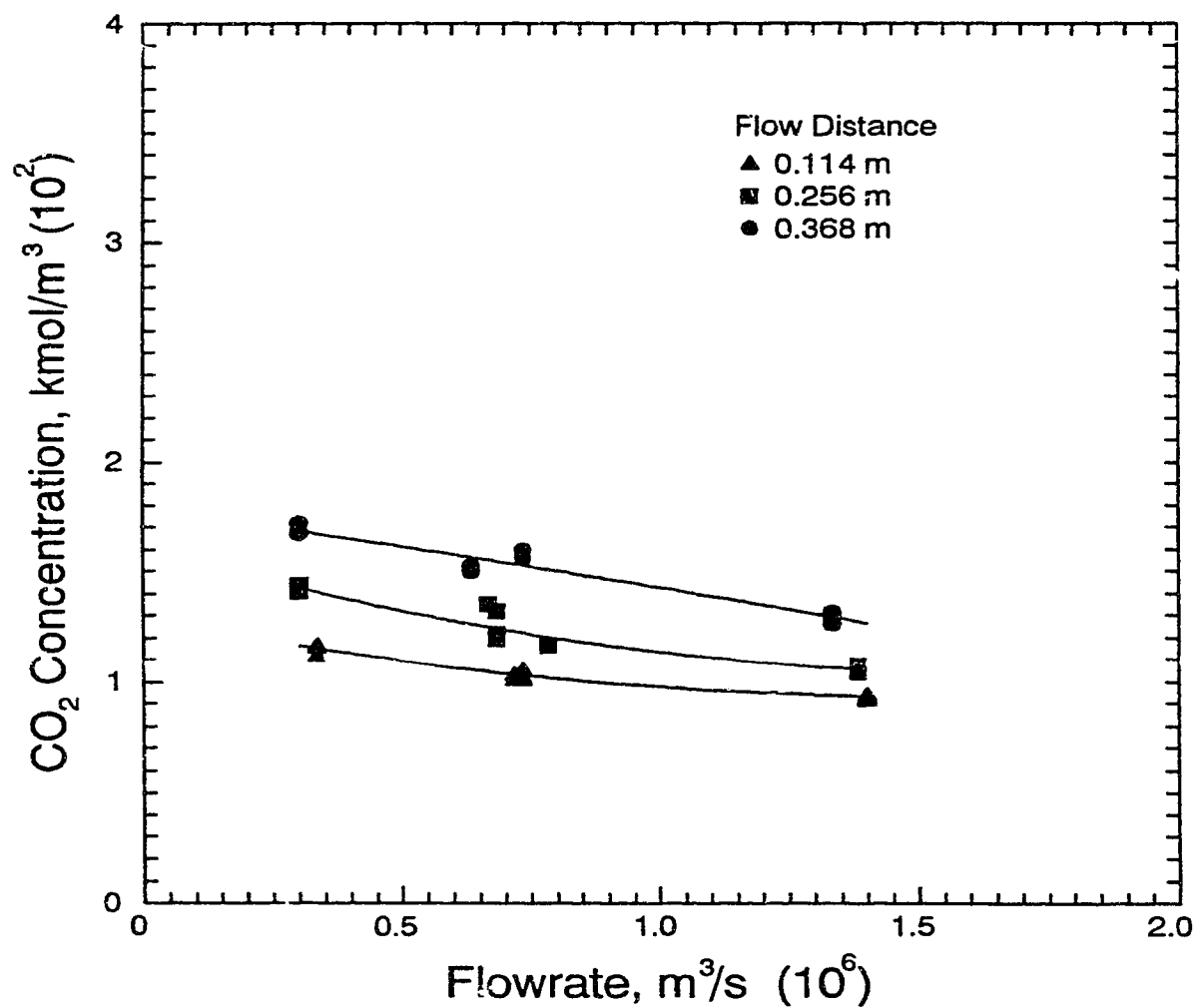


Figure 7.7: Absorption Results for a Plate Inclination of 60° Showing the Effect of Flow Rate and Flow Distance.

number and not the actual absorption results is the key information desired from a study such as the one described here. In order to evaluate the Sherwood number, further calculations are required. These calculations are summarized in the following sections and described in detail in Appendix D.

From the data in Figures 7.4 to 7.7, the value of the overall liquid-side mass transfer coefficient, $K_{\bar{x}}$, can be calculated from the following relationship

$$\tilde{N}_A = K_{\bar{x}} (\tilde{x}_A^* - \tilde{x}_A)_{lm} \quad (7.1)$$

which, when rearranged and expanded, leads to the following relationship

$$K_{\bar{x}} = \frac{(C_{A,0} - C_{A,1}) q_L}{s'_p \text{Dist} \Delta \tilde{x}_{lm}} \quad (7.2)$$

where:

$$\Delta \tilde{x}_{lm} = \frac{(\tilde{x}_A^* - \tilde{x}_A)_0 - (\tilde{x}_A^* - \tilde{x}_A)_1}{\ln((\tilde{x}_A^* - \tilde{x}_A)_0 / (\tilde{x}_A^* - \tilde{x}_A)_1)} \quad (7.3)$$

which was actually used to calculate the mass transfer coefficient. The value of the arc length was taken from the theoretical simulations based on the results from the rivulet dimension analysis.

For the rivulet problem analyzed in this work, the Sherwood number can be defined as follows

$$N_{Sh} = \frac{K_{\bar{x}} (2x'_p) (MW)}{\rho_L \mathcal{D}_{AB}} \quad (7.4)$$

To present the values of the Sherwood number in a meaningful manner, these values can be plotted versus the inverse Graetz number, which is defined as follows for the rivulet flow problem

$$N_{Gz^{-1}} = \frac{\text{Dist}}{(2x'_p) N_{Re} N_{Sc}} \quad (7.5)$$

Figure 7.8 presents both the experimental and the theoretical absorption results as just described. From this dimensionless analysis, some interpretation of the results is possible.

The first characteristic of importance in these data is the fact that the experimental data lie considerably above the theoretical results. As explained in Appendix D, the error in the experimental Sherwood numbers accounts for only 30% of the discrepancy between these two data sets. Therefore, it must be assumed that additional absorption is occurring in the experimental data which is not accounted for in the theoretical model.

The second characteristic is the fact that the slopes of the experimental and theoretical Sherwood numbers are different. This difference in the two slopes may be explained in terms of end effects. Low values of Gz^{-1} indicate a short flow distance and/or large flow rates where end effects would be most significant. Conversely, large values of Gz^{-1} indicate longer flow distances and/or smaller flow rates where end effects would be less significant. The curve, which is drawn in Figure 7.8, was constructed using the above reasoning and assumed that the experimental absorption data at the highest Gz^{-1} contained insignificant end effects. This curve, the slope for which was taken from the theoretical data which contain no end effects, indicates the values of the experimental Sherwood numbers in the absence of end effects. Even after correcting the Sherwood numbers, it can be seen that the experimental values remain considerably larger than the theoretical ones.

A third characteristic, which is illustrated in this plot, is the fact that the plate inclination has no significant effect on the experimental or theoretical absorption results since all of the data lie in straight lines. This effect is unexpected but indicates that, as the plate inclination increases, the rivulet changes in such a manner that the amount of absorption remains constant.

Finally, the results in this figure show that the concentration boundary layer is still developing in the flows analyzed in this work. This result is obvious since the Sherwood number is decreasing with increasing inverse Graetz number.

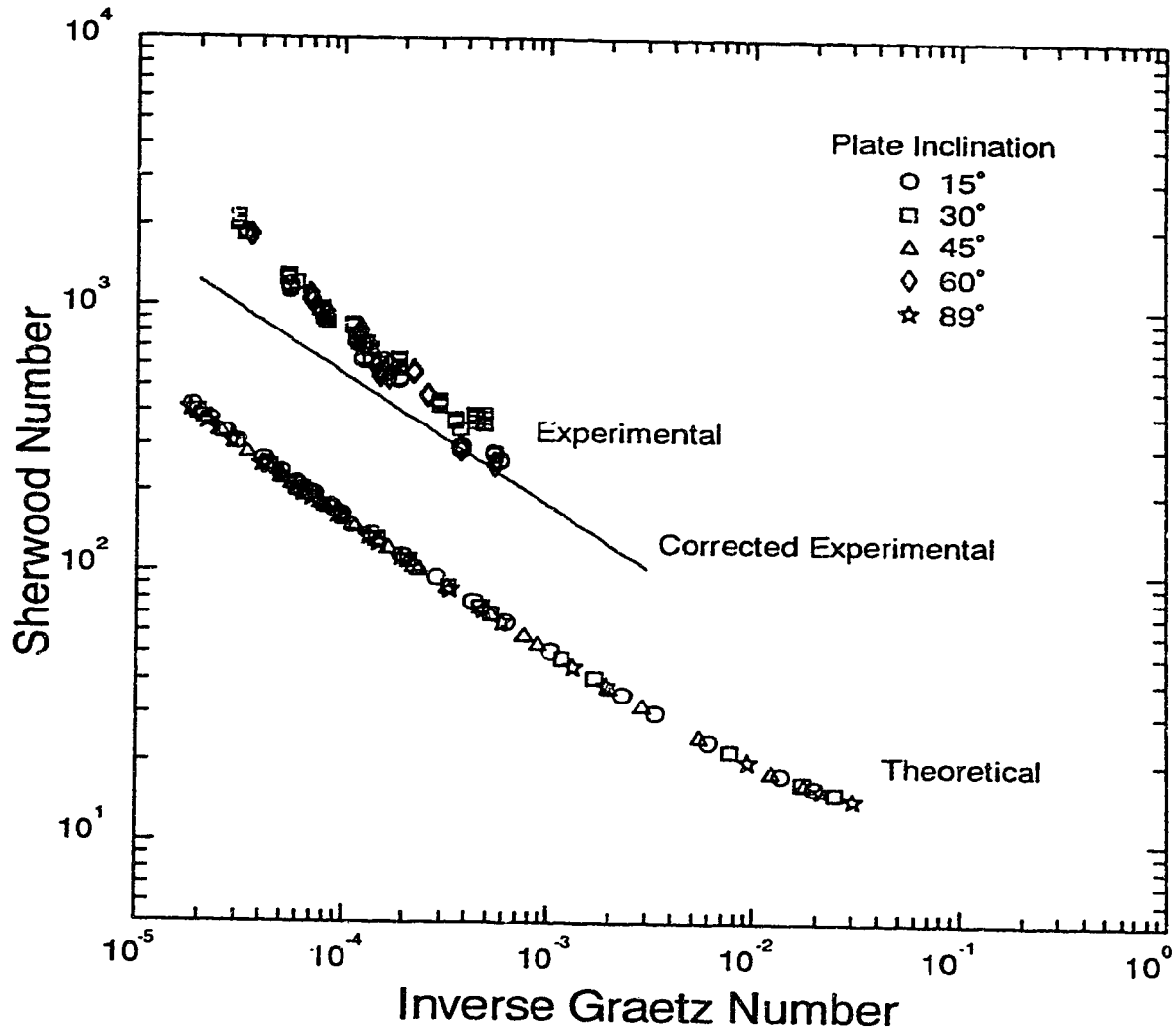


Figure 7.8: Dimensionless Number Analysis for Experimental and Theoretical Absorption Results Indicating Development of the Concentration Boundary Layer.

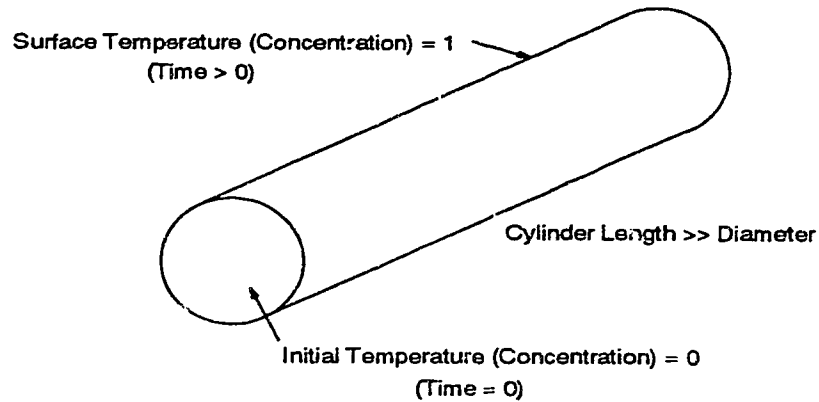


Figure 7.9: Transient Conduction/Diffusion Problem in a Cylinder of Infinite Length

7.4.3 Analytical versus Numerical Solution

To ensure that the computational solutions generated were correct, a comparison of these solutions with an analytical solution was performed. The problem chosen as the standard to which to compare the computational solutions is illustrated in Figure 7.9 and can be identified as either transient heat conduction or transient mass transfer into a cylinder of infinite length. This model allows verification of the conduction but not the complete convection-diffusion model in the computational code.

Figure 7.10 shows the results of both the analytical and computational solutions and, for small exposure times (0.005), the two solutions agree exactly. For longer exposure times, when heat or mass transfer has reached the center of the cylinder, there is some difference between the two solutions but this discrepancy is due to the finite differencing technique and application of the boundary condition at the solid surface in the rivulet absorption problem. With further grid refinement

near the solid surface, where the boundary condition is of the neuman type, better agreement between the two solutions would be obtained. As discussed in Chapter 4, Section 4.3.5, finer grids than the one used in this study (31×51) would not have significantly improved the solutions obtained.

7.4.4 Experimental versus Theoretical Absorption

With the excess absorption due to end effects eliminated from the experimental absorption results, these data can now be compared to the theoretically simulated data, which assumed a linear rivulet with laminar flow in the absence of surface waves or secondary flow. Figure 7.11 shows these data plotted as CO_2 absorption versus flow rate as a function of flow distance and plate inclination. In all cases, the theoretical data lie considerably below the experimental values even after the end effects have been eliminated. Even with the large discrepancy in the data, the same characteristics of downwardly sloping data and asymptotic approach with increasing flow rate remain. As explained in Section 7.4.2, and illustrated in this figure, there is no significant difference in absorption due to plate inclination for each of the three different flow distances studied.

7.4.5 Flow Structure

To investigate the stability and reproducibility of the absorption results which have just been presented, several experiments were conducted; the result of the most significant one is shown in Figure 7.12. In this absorption experiment, the inclined flow plate was first adjusted to 30° and a rivulet with a flow rate of $3.5 \times 10^{-7} \text{ m}^3/\text{s}$ established. The flow plate was then carefully adjusted to a plate inclination of 60° and liquid samples withdrawn every 30 min to see the effect of this adjustment on

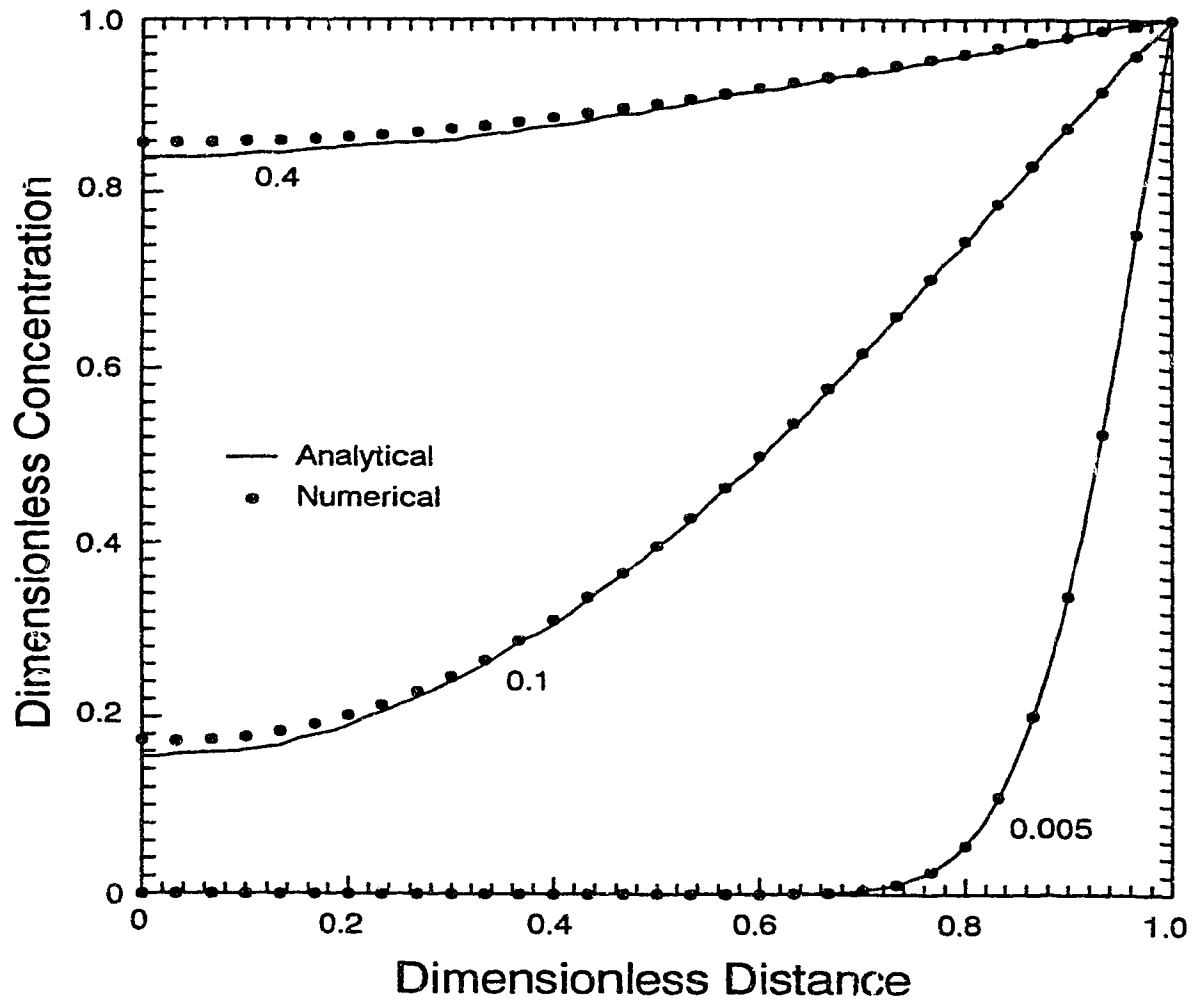


Figure 7.10: Comparison of Analytical and Computational Solutions for Transient Diffusion (Mass or Heat) in an Infinite Cylinder. Dimensionless Time as Indicated.

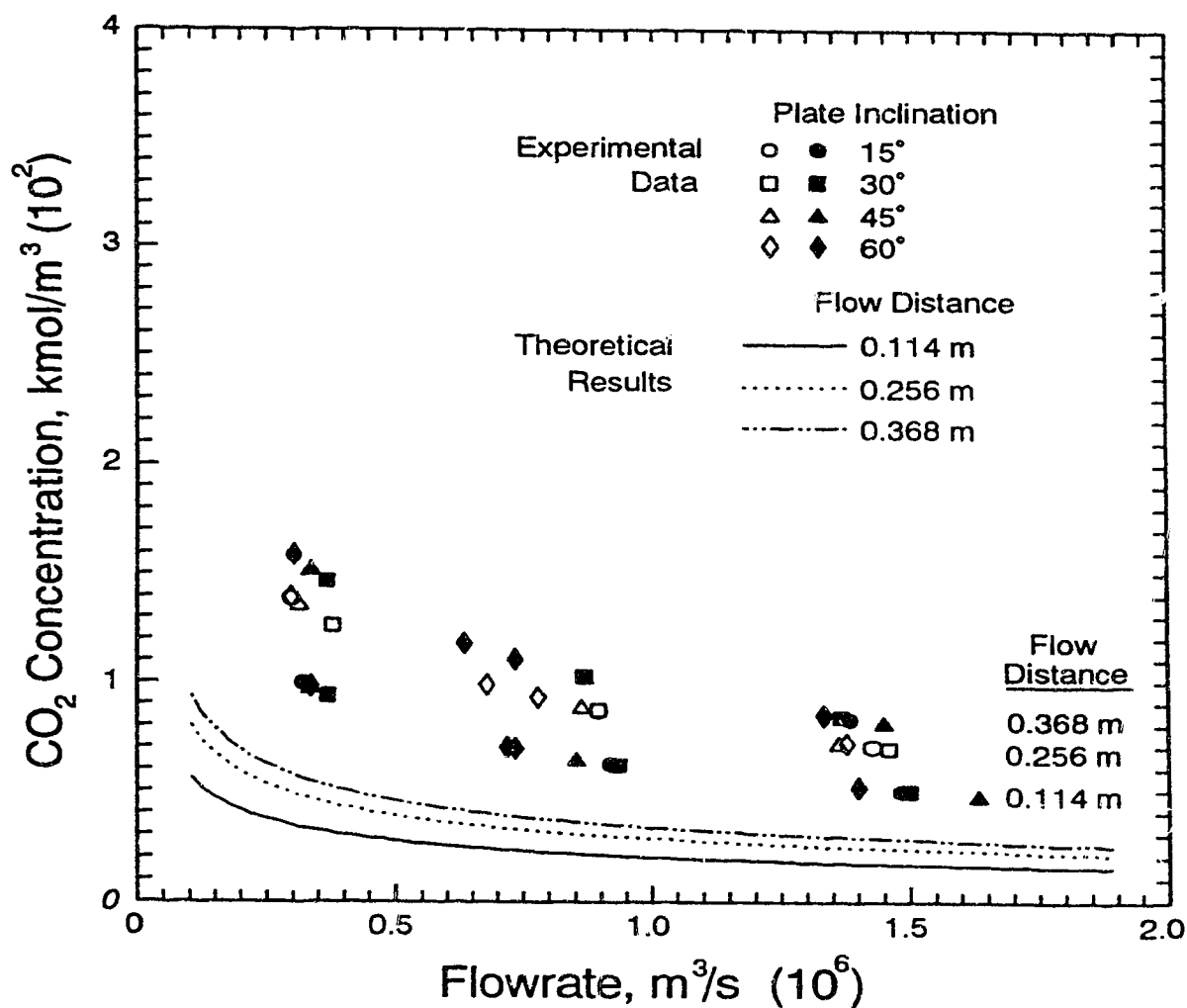


Figure 7.11: Comparison of Corrected Experimental and Theoretical CO₂ Absorption versus Flow Rate. Experimental Data are for the Plate Inclinations as Shown. Theoretical Prediction is For $\alpha = 15^\circ$.

the absorption. As can be seen from the figure, there was a significant reduction in the absorption values obtained over the course of the experiment—approximately four hours in total. What this plot shows, which was observed visually, is that the rivulets have a stable configuration to which they will tend if they have been disturbed. In this case, the rivulet began as a wider, lower rivulet at 30° and changed to a narrower, lower rivulet at 60° with increased average velocity. This decrease in the dimensions of the rivulet resulted in a decreased surface area and increased average flow rate thereby reducing the absorption. More importantly, however, the final values of the absorption recorded in this figure agree exactly with those shown in Figure 7.7 for the same flow distance and volumetric flow rate. This agreement lends much credibility to the experimental results presented here as the same absorption results were determined using two completely different procedures.

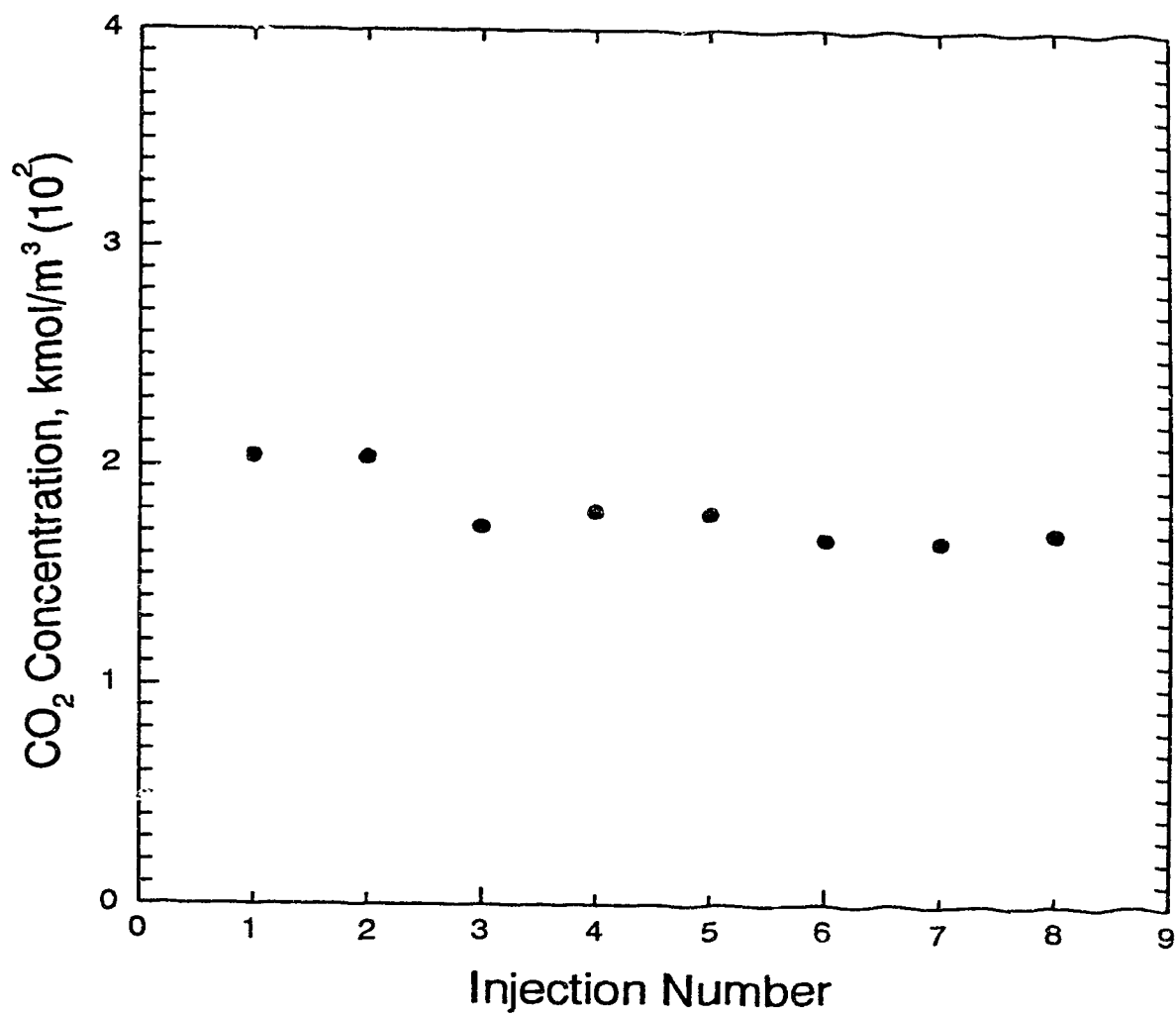


Figure 7.12: Effect of Change in Flow Plate Inclination on Experimental Absorption Results. $\alpha = 60^\circ$, $Dist = 0.368\text{ m}$.

Chapter 8

Conclusions and Recommendations

8.1 Conclusions

The use of basic, theoretical rivulet modelling to describe the specific process of gas absorption using structured packing is viable. Packing height, initial distribution and maldistribution and liquid-solid contact angle are shown to affect significantly the column performance. Predicted values of the mass transfer coefficient and height of the overall gas-side transfer unit agree well with literature values.

Construction of a suitable grid upon which to solve the governing equations is accomplished through a graphical technique. The numerical techniques of Gauss-Seidel successive over-relaxation and Crank-Nicolson are satisfactory for solving the simplified z -momentum Navier-Stokes and convection-diffusion equations, respectively.

Considerable variation is present in the values of the advancing, receding,

equilibrium and flowing rivulet contact angle. Averaged contact angle values from this study, however, do compare well with literature values.

Hysteresis characteristics exist in the values of the rivulet widths and heights. The theoretical rivulet model describes this behaviour using experimentally determined values of the advancing, receding and flowing rivulet contact angle.

The theoretical convection-diffusion equation did not fit the experimental absorption data. Additional absorption is shown in the experimental data which is unaccounted for in the theoretical model.

8.2 Recommendations

Further characterization of the liquid distribution in the column as well as the rivulet flow and mass transfer processes is required. More experimental absorption data from well designed and larger scale columns, incorporating both liquid-phase and gas-phase controlled absorption, is also required. The fundamental experimental problems of maldistribution and end effects must be reduced in order to produce meaningful results.

A more complete hydrodynamic model incorporating secondary flow and surface waves is desired to more accurately describe the flow field inside the rivulet. The Laplace equation must be incorporated into the Navier-Stokes equation to eliminate the assumptions created by the separate treatment of these equations. Solution of the developing hydrodynamic boundary layer problem is also required. The convection-diffusion equation must be modified to reflect the more detailed Navier-Stokes equation.

Better characterization of the contact angle in the flowing rivulets is required. Changes in the experimental apparatus to provide a hydrodynamic development

length would be desirable so that the hydrodynamic entry region could be controlled or eliminated in the absorption studies. Absorption data must also be collected in the developed concentration boundary layer region to fully describe the absorption process. Flow visualization in the rivulet could also be done to reveal the exact flow structure.

References

- [1] N.K. Adam. The chemical structure of solid surfaces as deduced from contact angles. In *Contact Angle, Wettability and Adhesion*, page 52, Washington, D.C., April 1964. American Chemical Society. Advances in Chemistry Series No. 43.
- [2] N.K. Adam and G.E.P. Elliot. Contact angles of water against saturated hydrocarbons. *J. Chem. Soc.*, page 2206, June 1962.
- [3] A.W. Adamson. *Physical Chemistry of Surfaces*. John Wiley and Sons, New York, New York, third edition, 1976.
- [4] M.A. Albright. Packed tower distributors tested. *Hydrocarbon Process.*, page 173, September 1984.
- [5] R.F. Allen and C.M. Biggin. Longitudinal flow of a lenticular liquid filament down an inclined plane. *Phys. Fluids*, 17(2):287, 1974.
- [6] A.I. Bailey. Discussion on solid surfaces. In *Second International Congress of Surface Activity. III. Electrical Phenomena and Solid-Liquid Interface*, page 189, 1957.
- [7] A.I. Bailey and S.M. Kay. A direct measurement of influence of vapour of liquid

- and of oriented monolayers on interfacial energy of mica. *Proc. R. Soc., Ser. A.*, 301:47, 1967.
- [8] H.R. Baker, E.G. Shafrin, and W.A. Zisman. The adsorption of hydrophobic monolayers of carboxylic acids. *J. Phys. Chem.*, 56:405, 1952.
- [9] D.H. Bangham. The Gibbs adsorption equation and adsorption on solids. *Trans. Faraday Soc.*, 33:805, 1937.
- [10] D.H. Bangham and R.I. Razouk. Adsorption and the wettability of solid surfaces. *Trans. Faraday Soc.*, 33:1459, 1937.
- [11] F.E. Bartell and K.E. Bristol. Wetting characteristics of solid surfaces covered with adsorbed films. *J. Phys. Chem.*, 44:86, 1940.
- [12] F.E. Bartell and P.H. Cardwell. Reproducible contact angles on reproducible metal surfaces. III. Contact angles of saturated aqueous solutions of different organic liquids on silver and gold. *J. Am. Chem. Soc.*, 64:1641, 1942.
- [13] F.E. Bartell and J.W. Shepard. Surface roughness as related to hysteresis of contact angles. I. The system paraffin-water-air. *J. Phys. Chem.*, 57:211, 1953.
- [14] F.E. Bartell and J.W. Shepard. Surface roughness as related to hysteresis of contact angles. II. The systems paraffin-3 molar calcium chloride solution-air and paraffin-glycerol-air. *J. Phys. Chem.*, 57:455, 1953.
- [15] F.E. Bartell and J.W. Shepard. Surface roughness as related to hysteresis of contact angles. III. The systems paraffin-ethylene glycol-air, paraffin-methyl cellusolve-air and paraffin-methanol-air. *J. Phys. Chem.*, 57:458, 1953.

- [16] F.E. Bartell and J.T. Smith. Alteration of surface properties of gold and silver as indicated by contact angle measurements. *J. Phys. Chem.*, 57:165, 1953.
- [17] F. Bashforth and J.C. Adams. *An Attempt to Test the Theories of Capillary Action*. University Press, Cambridge, England, 1883.
- [18] G.G. Bemmer and F.J. Zuiderweg. Radial liquid spread and maldistribution in packed columns under different wetting conditions. *Chem. Eng. Sci.*, 33:1637, 1978.
- [19] M. Bentwich, D. Glasser, J. Kern, and D. Williams. Analysis of rectilinear rivulet flow. *AIChE J.*, 22(4):772, 1976.
- [20] M.K. Bennett and W.A. Zisman. Effect of adsorbed water on the critical surface tension of water on metal surfaces. *J. Colloid Interface Sci.*, 28:243, 1968.
- [21] M.K. Bennett and W.A. Zisman. Effect of adsorbed water on wetting properties of borosilicate glass, quartz and sapphire. *J. Colloid Interface Sci.*, 29:413, 1969.
- [22] W.C. Bigelow, D.L. Pickett, and W.A. Zisman. Oleophobic monolayers. I. Films adsorbed from solution in non-polar liquids. *J. Colloid Sci.*, 1:513, 1946.
- [23] J.J. Bikerman. A method of measuring contact angles. *Ind. Eng. Chem., Anal. Ed.*, 13:443, 1941.
- [24] J.J. Bikerman. Surface roughness and contact angle. *J. Phys. Colloid Chem.*, 54:653, 1950.

- [25] J.J. Bikerman. Solid surfaces. In *Second International Congress of Surface Activity. III. Electrical Phenomena and Solid-Liquid Interface*, page 125, London, England, September 1957. Butterworth Scientific Publications.
- [26] R. Billet. Optimisation and comparison of mass transfer columns. *Inst. Chem. Eng. Symp. Ser. No. 32*, page 4:42, 1969.
- [27] R. Billet. Performance of low pressure drop packings. *Chem. Eng. Commun.*, 54:93, 1987.
- [28] R. Billet and J. Mackowiak. Application of modern packings in thermal separation processes. *Chem. Eng. Technol.*, 11:213, 1988.
- [29] W.L. Bolles and J.R. Fair. Performance and design of packed distillation columns. *Inst. Chem. Eng. Symp. Ser. No. 56*, page 3.3/35, 1979.
- [30] J.L. Bravo, J.A. Rocha, and J.R. Fair. Mass transfer in gauze packings. *Hydrocarbon Process.*, 64:91, January 1985.
- [31] J.L. Bravo, J.A. Rocha, and J.R. Fair. How surface treatment and geometry affect the performance of structured packing, 1990. preprints, annual meeting of AIChE, Chicago.
- [32] P. Brimblecombe. *Air Composition and Quality*. Cambridge University Press, Cambridge, 1986.
- [33] P.H. Calderbank. Physical rate processes in industrial fermentation. Part I. The interfacial area in gas-liquid contacting with mechanical agitation. *Trans. Inst. Chem. Eng.*, 36:443, 1958.
- [34] P.H. Calderbank. Physical rate processes in industrial fermentation. Part II. Mass transfer coefficients in gas-liquid contacting with and without

- mechanical agitation. *Trans. Inst. Chem. Eng.*, 37:173, 1959.
- [35] J.J. Carroll, J.D. Slupsky, and A.E. Mather. The solubility of carbon dioxide in water at low pressure. *J. Phys. Chem. Ref. Data*, 20(6):1201, 1991.
- [36] H.S. Carslaw and J.C. Jaeger. *Conduction of Heat in Solids*. Oxford University Press, London, England, 2nd edition, 1959.
- [37] A.B.D. Cassie. Contact angles. *Discuss. Faraday Soc*, 3:11, 1948.
- [38] A.B.D. Cassie and S. Baxter. Wettability of porous surfaces. *Trans. Faraday Soc.*, 40:546, 1944.
- [39] G.W. Castellan. *Physical Chemistry*. Addison-Wesley, Reading, Massachusetts, third edition, 1983.
- [40] K.T. Chuang and A.I. Miller. Performance of packings for water distillation. *Can. J. Chem. Eng.*, 66:377, June 1988.
- [41] Z. Cihla and O. Schmidt. A study of the flow of liquid when freely trickling over the packing in a cylindrical tower. *Collect. Czech. Chem. Commun.*, 22(3):896, 1957.
- [42] J.B. Culkin and S.H. Davis. Meandering of water rivulets. *AIChE J.*, 30(2):263, 1984.
- [43] C.G. Dassori, J.A. Deiber, and A.E. Cassano. Mass transfer with chemical reaction in partially wetted flat plate catalyst pellets: Rivulet flow analysis. *Chem. Eng. Commun.*, 51:105, 1987.
- [44] J.T. Davies and E. Rideal. *Interfacial Phenomena*. Academic Press, New York, 1961.

- [45] P.L. de Laplace. *Mechanique Celeste, Suppl. Au X Livre*. Coureier, Paris, 1805.
- [46] B.V. Derjaguin. On the dependence of the contact angle on the microrelief or roughness of a wetted solid surface. *Dokl. Akad. Nauk. SSSR.*, 51:361, 1946.
- [47] R.H. Dettre and R.E. Johnson, Jr. Contact angle hysteresis. II. Contact angle measurements on rough surfaces. *Adv. Chem. Ser.*, 43:136, 1964.
- [48] R.H. Dettre and R.E. Johnson, Jr. Contact angle hysteresis. IV. Contact angle measurements on heterogeneous surfaces. *J. Phys. Chem.*, 69:1507, 1965.
- [49] R.H. Dettre and R.E. Johnson, Jr. Contact angle hysteresis—porous surfaces. In *Wetting. A Discussion Covering Both Fundamental and Applied Aspects of the Subject of Wetting and Wettability*, page 144, London, England, September 1967. Society of Chemical Industry Monograph 25.
- [50] K.C. Dorma, 1992. personal communications.
- [51] A. Dupré. *Théorie Mécanique de la Chaleur*. Gauthier-Villars, Paris, France, 1869.
- [52] R. Duraiswami and A. Prosperetti. Orthogonal mapping in two dimensions. *J. Comput. Phys.*, 98:254, 1992.
- [53] E.B. Dussan V. On the spreading of liquids on solid surfaces: Static and dynamic contact lines. *Annu. Rev. Fluid Mech.*, 11:371, 1979.
- [54] E. Dutkai and E. Ruckenstein. Liquid distribution in packed columns. *Chem. Eng. Sci.*, 23:1365, 1968.

- [55] B.S. Ellefson and N.W. Taylor. Surface properties of fused salts and glasses. I. Sessile drop method of determining surface tension and density of viscous liquids at high temperatures. *J. Am. Ceram. Soc.*, 21:193, 1938.
- [56] J.R. Fair and J.L. Bravo. Distillation columns containing structured packing. *Chem. Eng. Prog.*, 86:19, 1990.
- [57] I.M. Fedotkin, G.A. Mel'nichuk, F.F. Koval, and E.V. Klimkin. Hydrodynamics of rivulet flow on a vertical surface. *J. Eng. Phys. (Engl. Transl.)*, 46(1):9, 1984.
- [58] C.A.J. Fletcher. *Computational Techniques for Fluid Dynamics. 2. Specific Techniques for Different Flow Categories*. Springer-Verlag, New York, 1988.
- [59] T. Fort, Jr. and H.T. Patterson. A simple method for measuring solid-liquid contact angles. *J. Colloid Interface Sci.*, 18:217, 1963.
- [60] F.M. Fowkes and W.D. Harkins. The state of monolayers adsorbed at the interface solid-aqueous solution. *J. Am. Chem. Soc.*, 62:3377, 1940.
- [61] H.W. Fox and W.A. Zisman. The spreading of liquids on low energy surfaces. I. Polytetrafluoroethylene. *J. Colloid Sci.*, 5:514, 1950.
- [62] G.A. Funk, M.P. Harold, and K.M. Ng. Effectiveness of a partially wetted catalyst for bimolecular reaction kinetics. *AIChE J.*, 34:1361, 1988.
- [63] G.A. Funk, M.P. Harold, and K.M. Ng. A novel model for reaction in trickle beds with flow maldistribution. *Ind. Eng. Chem. Res.*, 29:738, 1990.
- [64] G.A. Funk, M.P. Harold, and K.M. Ng. Experimental study of reaction in a partially wetted catalytic pellet. *AIChE J.*, 37(2):202, 1991.

- [65] J.W. Gibbs. *Collected Works of J. Willard Gibbs*. Yale University Press, New Haven, Connecticut, one edition, 1928.
- [66] R.J. Good. A thermodynamic derivation of Wenzel's modification of Young's equation for contact angles; together with a theory of hysteresis. *J. Am. Chem. Soc.*, 74:5041, 1952.
- [67] V.R. Gray. Contact angles, their significance and measurement. In *Wetting. A Discussion Covering Both Fundamental and Applied Aspects of the Subject of Wetting and Wettability*, page 99, London, England, September 1967. Society of Chemical Industry Monograph 25.
- [68] P. Griffith and J.D. Wallis. The role of surface conditions in nucleate boiling. *J. Colloid Interface Sci.*, 129(1):49, 1988.
- [69] P. Groenhof. *De invloed van vergroting van de diameter van kolommen met vullichamen up het scheident vermogen en het vloeistofgedrag*. PhD thesis, Groningen, 1972.
- [70] J. Guastalla. Wetting balance method and its applications. In *Second International Congress of Surface Activity. III. Electrical Phenomena and Solid-Liquid Interface*, page 143, London, England, September 1957. Butterworth Scientific Publications.
- [71] W.D. Harkins. *The Physical Chemistry of Surface Films*. Reinhold Publishing Corporation, New York, 1952.
- [72] S. Hartland and R.W. Hartley. *Axisymmetric Fluid-Liquid Interfaces*. Elsevier Scientific Publishing Company, New York, 1976.
- [73] R. Higbie. The rate of absorption of a pure gas into a still liquid during short periods of exposure. *Trans. Am. Inst. Chem. Eng.*, 31:365, 1935.

- [74] P.J. Hoek, J.A. Wesselingh, and F.J. Zuiderweg. Small scale and large scale liquid maldistributions in packed columns. *Chem. Eng. Res. Des.*, 64:431, November 1986.
- [75] M. Huber and W. Meier. Sulzer columns for vacuum rectification and mass transfer. *Sulzer Tech. Rev.*, 57(1):3, 1975.
- [76] J.R. Hufton, J.L. Bravo, and J.R. Fair. Scale-up of laboratory data for distillation columns containing corrugated metal-type structured packing. *Ind. Eng. Chem. Res.*, 27:2096, 1988.
- [77] R.E. Johnson Jr. Conflicts between Gibbsian thermodynamics and recent treatments of interfacial energies in solid-liquid-vapour systems. *J. Phys. Chem.*, 63(10):1655, 1959.
- [78] R.E. Johnson, Jr. and R.H. Dettre. Contact angle hysteresis. I. Study of an idealized rough surface. *Adv. Chem. Ser.*, 43:112, 1964.
- [79] R.E. Johnson, Jr. and R.H. Dettre. Contact angle hysteresis. III. Study of an idealized heterogeneous surface. *J. Phys. Chem.*, 68:1744, 1964.
- [80] R.E. Johnson Jr. and R.H. Dettre. Wettability and contact angles. *Surf. Colloid Sci.*, 2:85, 1969.
- [81] H.F. Johnstone and R.L. Pigford. Distillation in a wetted-wall column. *Trans. Am. Inst. Chem. Eng.*, 38:25, 1942.
- [82] J. Kern. Zur hydrodynamik der rinnsale. *verfahrenstechnik*, 3(10):425, 1969.
- [83] J. Kern. Stabilitätsprobleme der rinnsalströmung. *verfahrenstechnik*, 5(7):289, 1971.

- [84] E. Kneen and W.W. Benton. A simplified technique for the determination of contact angles and its application to studies on wetting. *J. Phys. Chem.*, 41:1195, 1937.
- [85] H. Kosuge, J. Matsudaira, K. Aoki, and K. Asano. Experimental approach to mass transfer in binary packed column distillation. *J. Chem. Eng. Jpn.*, 23(5):593, 1990.
- [86] E. Krell. The solid-liquid boundary in chemical engineering. *Br. Chem. Eng.*, 12(4):562, 1967.
- [87] J. Landau, J. Boyle, H.G. Gomma, and A.M. Al Taweel. Comparison of methods for measuring interfacial areas in gas-liquid dispersions. *Can. J. Chem. Eng.*, 55:13, 1977.
- [88] J. Landau, H.G. Gomma, and A.M. Al Taweel. Measurement of large interfacial areas by light attenuation. *Trans. Inst. Chem. Eng.*, 55:212, 1977.
- [89] I. Langmuir. *Collected Works*. Pergamon Press, New York, 1960.
- [90] I. Langmuir and V.J. Schaeffer. The effect of dissolved salts on insoluble monolayers. *J. Am. Chem. Soc.*, 59:2405, November 1937.
- [91] B. Lespinasse. Recherches sur le fonctionnement des colonnes à garnissage pour absorption gaz-liquide. II. etude du cheminement du liquide à travers le garnissage d'une colonne d'absorption gaz-liquide. *Rev. Inst. Fr. Pet. Ann. Combust. Liq.*, 17(11):21, 1962.
- [92] G.R. Lester. Contact angle of liquids at deformable solid surfaces. *J. Colloid Sci.*, 16:315, 1961.

- [93] G.R. Lester. Contact angles on deformable solids. In *Wetting. A Discussion Covering Both Fundamental and Applied Aspects of the Subject of Wetting and Wettability*, page 57, London, England, September 1967. Society of Chemical Industry Monograph No. 25.
- [94] O. Levine and W.A. Zisman. Physical properties of monolayers adsorbed at the solid-air interface. II. Mechanical durability of aliphatic polar compounds and effect of halogenation. *J. Phys. Chem.*, 61:1188, 1957.
- [95] S. Liu, 1992. personal communications.
- [96] M.J. Lockett and A.A. Safekourdi. Light transmission through bubble swarms. *AIChE J.*, 23:395, 1977.
- [97] G.L. Mack. The determination of contact angles from measurements of the dimensions of small bubbles and drops. I. The spheroidal method for acute angles. *J. Phys. Chem.*, 40:159, 1936.
- [98] G.L. Mack and D.A. Lee. The determination of contact angles from measurements of the dimensions of small bubbles and drops. II. The sessile drop method for obtuse angles. *J. Phys. Chem.*, 40:169, 1936.
- [99] D. Mackay, M. Medir, and D.E. Thornton. Interfacial behavior of oil under ice. *Can. J. Chem. Eng.*, 54:72, 1976.
- [100] W. Meier. Sulzer columns for rectification and absorption. *Sulzer Tech. Rev.*, 2:221, 1979.
- [101] W. Meier and M. Huber. Measurements of the number of theoretical plates in packed columns with artificial maldistribution. *Inst. Chem. Eng. Symp. Ser. No. 32*, page 4:31, 1969.

- [102] W. Meier, R. Hunkeler, and D. Stöcker. Performance of the new regular tower packing "Mellapak". *Inst. Chem. Eng. Symp. Ser. No. 56*, page 3.3/1, 1979.
- [103] W. Meier, W.D. Stoecker, and B. Weinstein. Performance of a new high efficiency packing. *Chem. Eng. Prog.*, 73:71, November 1977.
- [104] A.S. Michaels and S.W. Dean, Jr. Contact angle relationships on silica aquagel surfaces. *J. Phys. Chem.*, 66:1790, 1962.
- [105] R.W. Michell and I.A. Furzer. Trickle flow in packed beds. *Trans. Inst. Chem. Eng.*, 50:334, 1972.
- [106] M.D. Murray and B.W. Darvell. A protocol for contact angle measurement. *J. Phys. D: Appl. Phys.*, 23:1150, 1990.
- [107] T. Nakagawa and J.C. Scott. Stream meanders on a smooth hydrophobic surface. *J. Fluid Mech.*, 149:89, 1984.
- [108] P.A. Nawrocki, Z.P. Xu, and K.T. Chuang. Mass transfer in structured corrugated packing. *Can. J. Chem. Eng.*, 69(6):1336, 1991.
- [109] K. Onda. Mass transfer coefficients between gas and liquid phases in packed columns. *J. Chem. Eng. Jpn.*, 1:56, 1968.
- [110] K. Onda, H. Takeuchi, Y. Meada, and N. Takeuchi. Liquid distribution in a packed column. *Chem. Eng. Sci.*, 28:1677, 1973.
- [111] W. Peier, A.B. Ponter, and S. Fabre. Wetting of a vertical plate by a liquid flowing through a vertical nozzle. *Chem. Eng. Sci.*, 32:1491, 1977.
- [112] A.B. Ponter, G.A. Davies, W. Beaton, and T.K. Ross. The measurement of contact angles under the conditions of heat transfer when a liquid film breaks on a vertical surface. *Int. J. Heat and Mass Transfer*, 10:1633, 1967.

- [113] A.B. Ponter and M. Yekta-Fard. The influence of environment on the drop size-contact angle relationship. *Colloid Polym. Sci.*, 263(8):673, 1985.
- [114] K.E. Porter. Liquid flow in packed columns. Part I. The rivulet model. *Trans. Inst. Chem. Eng.*, 46:T69, 1968.
- [115] K.E. Porter and M.C. Jones. A theoretical prediction of liquid distribution in a packed column with wall effects. *Trans. Inst. Chem. Eng.*, 41:240, 1963.
- [116] D.J. Ryley and B.H. Khoshaim. A new method of determining the contact angle made by a sessile drop upon a horizontal surface (sessile drop contact angle). *J. Colloid Interface Sci.*, 59(2):243, 1977.
- [117] G. Ryskin and L.G. Leal. Orthogonal mapping. *J. Comput. Phys.*, 50:71, 1983.
- [118] P. Schmuki and M. Laso. On the stability of rivulet flow. *J. Fluid Mech.*, 215:125, 1990.
- [119] F. Schulman and W.A. Zisman. The spreading of liquids on low energy surfaces. V. Perfluorodecanoic acid monolayers. *J. Colloid Sci.*, 7:465, 1952.
- [120] A.M. Schwartz and F.W. Minor. A simplified thermodynamic approach to capillarity. II. Applications to contact angle and spreading phenomena. *J. Colloid Sci.*, 14:584, 1959.
- [121] F.W. Sears, M.W. Zemansky, and H.D. Young. *University Physics*. Addison-Wesley, 6th edition, 1982.
- [122] R. Semiat, D. Moalem-Maron, and S. Sideman. Transfer characteristics of convex and concave rivulet flow on inclined surfaces with straight-edged grooves. *Desalination*, 34:267, 1980.

- [123] E.G. Shafrin and W.A. Zisman. Hydrophobic monolayers and their adsorption from aqueous solution. In *Monomolecular Layers*. American Association for the Advancement of Science, Washington, DC, 1954.
- [124] E.G. Shafrin and W.A. Zisman. Effect of adsorbed water on the spreading of organic liquids on soda-lime glass. *J. Am. Ceram. Soc.*, 50:478, 1967.
- [125] M.G. Shi and A.G. Mersmann. Effective interfacial area in packed columns. *Ger. Chem. Eng.*, 8:87, 1985.
- [126] H.L. Shulman and W.G. Mellish. Performance of packed columns. Part VIII. Liquid flow patterns and velocities in packed beds. *AIChE J.*, 13(6):1137, 1967.
- [127] R. Shuttleworth and G.L.J. Bailey. The spreading of a liquid over a rough solid. *Discuss Faraday Soc*, 3:16, 1948.
- [128] L. Spiegel and W. Meier. Correlations of the performance characteristics of the various Mellapak types (capacity, pressure drop and efficiency). *Inst. Chem. Eng. Symp. Ser. No. 104*, page A203, 1987.
- [129] V. Staněk and V. Kolář. Distribution of liquid over random packing. *Collect. Czech. Chem. Commun.*, 30:1054, 1965.
- [130] V. Staněk and V. Kolář. The radial spread and the number of rivulets in a trickle bed. *Collect. Czech. Chem. Commun.*, 39:2007, 1974.
- [131] R. Stikkelman, J. de Graauw, Z. Olujic, H. Teeuw, and H. Wesselingh. A study of gas and liquid distribution in structured packings. *Chem. Eng. Technol.*, 12:445, 1989.

- [132] R.M. Stikkelman and J.A. Wesselingh. Liquid and gas flow patterns in packed columns. *Inst. Chem. Eng. Symp. Ser. No. 104*, page B155, 1987.
- [133] F. Stoter, Z. Olujic, and J. de Graauw. Measurement and modelling of liquid distribution in structured packings, 1990. preprints, annual meeting of AIChE, Chicago.
- [134] A.A. Stravs and U. von Stocker. Measurement of interfacial areas in gas-liquid dispersions by ultrasonic pulse transmission. *Chem. Eng. Sci.*, 40(7):1169, 1985.
- [135] C.G. Sumner. An apparatus for the measurement of contact angles by the plate method. In *Symposium on Detergency*, page 41, New York, 1937. Chemical Publishing Company.
- [136] K. Svoboda and M. Rylek. Measurement of interfacial area and mass transfer coefficients by the chemical method of CO₂ absorption into aqueous solutions of NaOH in a model column with expanded metal sheet packing. *Chem. Eng. Commun.*, 3:399, 1979.
- [137] P.A. Thiessen and E. Schoon. Work of adhesion on surfaces of solid organic compounds [and the groups of atoms present in the surface layer]. *Z. Elektrochem.*, 46:170, 1940.
- [138] J.F. Thompson. Grid generation techniques in computational fluid dynamics. *AIAA J.*, 22(11):1505, 1984.
- [139] J.F. Thompson, Z.U.A. Warsi, and C.W. Mastin. Boundary-fitted coordinate systems for numerical solution of partial differential equations—A review. *J. Comput. Phys.*, 47(1):1, 1982.
- [140] W. Thompson. On the thermal effects of drawing out a film of liquid. *Proc. R. Soc. London*, 9:255, 1858.

- [141] W. Thompson. On the thermal effects of drawing out a film of liquid. *Philos. Mag.*, 17(111):61, 1859.
- [142] G.D. Towell and L.B. Rothfeld. Hydrodynamics of rivulet flow. *AIChE J.*, 12(5):972, 1966.
- [143] I.J. Urua and M.C.G. del Cerro. Measurement of large gas-liquid interfacial areas by the light transmission method. *Can. J. Chem. Eng.*, 65:565, August 1987.
- [144] R.N. Wenzel. Resistance of solid surfaces to wetting by water. *Ind. Eng. Chem.*, 28:988, 1936.
- [145] R.N. Wenzel. Surface roughness and contact angle. *J. Phys. Colloid Chem.*, 53:1466, 1949.
- [146] A.M. Worthington. On the error involved in Professor Quinke's method of calculating surface tensions from the dimensions of flat drops and bubbles. *Philos. Mag.*, 20:51, 1885.
- [147] C. Xu, J. Lou, and Z. Jiang. Liquid distribution for metallic corrugated plate packings. *J. Chem. Ind. Eng. (China)*, 4:402, 1986.
- [148] M. Yekta-Fard and A.B. Ponter. Surface treatment and its influence on contact angles of water drops residing on polymers and metals. *Phys. Chem. Liq.*, 15:19, 1985.
- [149] M. Yekta-Fard and A.B. Ponter. The influence of vapor environment and temperature on the contact angle-drop size relationship. *J. Colloid Interface Sci.*, 126(1):134, 1988.

- [150] T. Young. An essay on the cohesion of fluids. *Philos. Trans. R. Soc. London*, 95:65, 1805.
- [151] J.B. Zech and A.B. Mersmann. Liquid flow and liquid phase mass transfer in irrigated packed columns. *Inst. Chem. Eng. Symp. Ser. No. 56*, page 2.5/39, 1979.
- [152] W.A. Zisman. Relationship of equilibrium contact angle to liquid and solid constitution. In *Contact Angle, Wettability and Adhesion*, page 1, Washington, D.C., April 1964. American Chemical Society. Advances in Chemistry Series No. 43.
- [153] W.A. Zisman. Surface energetics of wetting, spreading and adhesion. *J. Paint Technol.*, 44(564):42, 1972.

Appendix A

Equipment Specifications

The following tables list the equipment used in this research as well as the specifications for each item.

For the gas chromatograph used in this study, the minimum detectable limit for CO₂ is 10 *PPM* based on a peak with a retention time of less than two minutes and a five-to-one signal-to-noise ratio. The minimum quantifiable limit for CO₂ is 30 *PPM* based on a peak with a retention time of less than two minutes and a ten-to-one signal-to-noise ratio.

Equipment	Specifications
CO ₂ Cylinder	Commercial Grade CO ₂ Cylinder Size 1A (27.22 <i>kg</i>) Sum of N ₂ , O ₂ and CH ₄ < 0.5%
CO ₂ Regulator	Matheson Single Stage Brass CO ₂ -type Pressure on outlet 0–100 <i>psig</i>
Rotameter	Matheson Model FM1051S-HA E700 High Accuracy Stainless Steel Valve 6.35 <i>mm</i> tube (glass–stainless steel balls)
Thermocouples	Type-J (iron–constantan) 2–1.5875 <i>mm</i> dia by 150 <i>mm</i> length 1–3.175 <i>mm</i> dia by 335 <i>mm</i> length Temperature values +0.5°C of true value
Liquid Crystal Display	Omega Model DP701J Temperature Range -50–640°C ± 0.05%
Pump	Cole-Parmer Variable Speed Mag. Coupled Gear Pump with Controller, Model N-07144-04 180–360 <i>rpm</i> Micropump Series A Model 07002-27 Pump Head 0.18–0.302 <i>mL/min</i>
Pump	Cole Parmer Magnetically Coupled Centrifugal Pump 1 <i>L/min</i>
Temperature Bath	30 <i>L</i> water 2.5 <i>kW</i> cooling, 1 <i>kW</i> heating Stir-Pak Laboratory Stirrer Model 9M922 $\frac{1}{15}$ <i>hp</i> , 5000 <i>rpm</i> maximum
Gas Chromatograph	Varian Model 3700 2.646 <i>m</i> Porapak-Q Column 50–80 <i>mesh</i> styrene–divinylbenzene
Integrator	Hewlett-Packard Model 3380A Peak traces generated using 216 × 279 thermal paper

Table A.1: Experimental Equipment and Specifications

Equipment	Specifications
Camera and Lens	Nikon 35 <i>mm</i> Nikon Micro-NIKKOR 55 <i>mm</i> 1:35
Insulation	Self-adhering Streamline foam insulating tape 50.8 <i>mm</i> wide \times 3.175 <i>mm</i> thick
Stainless Steel for Flow Plate	AISI-304
Stainless Steel Sheeting	16 <i>gage</i> AISI-304 for all parts except the sampling cup which was 20 <i>gage</i> AISI-304
Storage tank	16 <i>gage</i> AISI-304 stainless steel sheeting 610 <i>mm</i> high by 565 <i>mm</i> diameter
Metal Dowels	AISI-304 stainless steel rod 15.875 <i>mm</i> dia by 90 <i>mm</i> length
Sandpaper	240 <i>grit</i> emery cloth 320 <i>grit</i> wet-dry 600 <i>grit</i> wet-dry crocus cloth
Plexiglass	4.75 <i>mm</i> clear cast acrylic sheeting
Buffing Wheel	Cloth pad buffing wheel Standard fine grain buffing compound
Micrometer	Mitutoyo Series 128 depth micrometer Smallest division, 0.001 <i>in</i>
Barometer	Nova barometer Calibrated in both inches and millimeters Attached thermometer scaled to nearest 1°C
Dry Gas Meter	Singer 1 <i>L/rev</i> dry gas meter Hewlett-Packard 100 <i>mL</i> bubble flow meter
Talysurf Equipment	Taylor-Hobson Talysurf 4 Surface Measuring Instrument Taylor-Hobson Rectilinear Recorder

Table A.2: Experimental Equipment and Specifications

Appendix B

Physical Properties

For this study, the physical property data used was that of pure water at 20°C. The necessary data included:

$$\rho_L = 998.23 \text{ kg/m}^3$$

$$\mu_L = 1.0019 \times 10^{-3} \text{ kg/(m s)}$$

$$\sigma_L = 72.75 \times 10^{-3} \text{ N/m}$$

The above data was taken from the *CRC Handbook of Chemistry and Physics* 66th edition, pp. F-10, F-35 and F-32, respectively. Using the above values, the kinematic viscosity, ν_L , can be calculated as follows:

$$\nu_L = \frac{\mu_L}{\rho_L} = 1.004 \times 10^{-6} \text{ m}^2/\text{s}$$

The diffusivity of CO₂ in water was also required at 20°C:

$$D_{AB} = 1.77 \times 10^{-9} \text{ m}^2/\text{s} \quad (\text{error} = \pm 3\%)$$

The above value was taken from the *International Critical Tables of Numerical Data, Physics, Chemistry and Technology*, Volume 5, 1st edition, p.65, 1929.

Appendix C

Calibration Technique

C.1 Gas Chromatograph

As explained in Chapter 5, Section 5.3, the calibration curve presented here was obtained by injecting known volumes of gaseous CO₂ into the gas chromatograph (GC) and recording the CO₂ peak area for each sample. For the liquid samples which were ultimately analyzed, the CO₂ peak areas from the liquid samples were matched with corresponding gas volumes as determined from the calibration curve. The concentration of CO₂ in the liquid could then be calculated from these results as explained in Appendix D.

Figure C.1 shows the actual calibration curve used in this study and, as can be seen from the figure, the curve is slightly non-linear with an apparent non-zero intercept. The equation used to characterize the curve was

$$V_{\text{CO}_2}, \mu L = 0.631159 + 3.11199 \times 10^{-4} (PA) - 6.98078 \times 10^{-9} (PA)^2 \\ + 2.02924 \times 10^{-13} (PA)^3 - 2.56877 \times 10^{-18} (PA)^4$$

where : PA = peak area of CO₂ as integrated

The conditions in the lab at the time the calibration curve was done were

Air Temperature = 22.0°C

Air Pressure = 94.352 kPa

CO_2 Temperature = 22.0°C

The non-zero intercept of the calibration curve can be explained in terms of the range of data studied and the fact that the curve can be non-linear in this region. Firstly, the $\text{CO}_2\text{-H}_2\text{O}$ solutions in this research are very dilute ($<1000\text{ PPM}$) and, subsequently, the calibration curve illustrated in the figure shows only the lower end of the entire calibration curve for this system. In focusing in on a small segment of the curve, any small error in the intercept, which would be unnoticed when the entire curve was used, would be greatly exaggerated when the small portion of the curve shown in Figure C.1 was used.

Secondly, the calibration curve may be non-linear in this region and, in fact, may not be continuous all the way to the origin due to the sensitivity limit of the GC. The important fact is that the calibration curve does cover the range of liquid CO_2 concentrations studied in this research and no extrapolation off the curve was required.

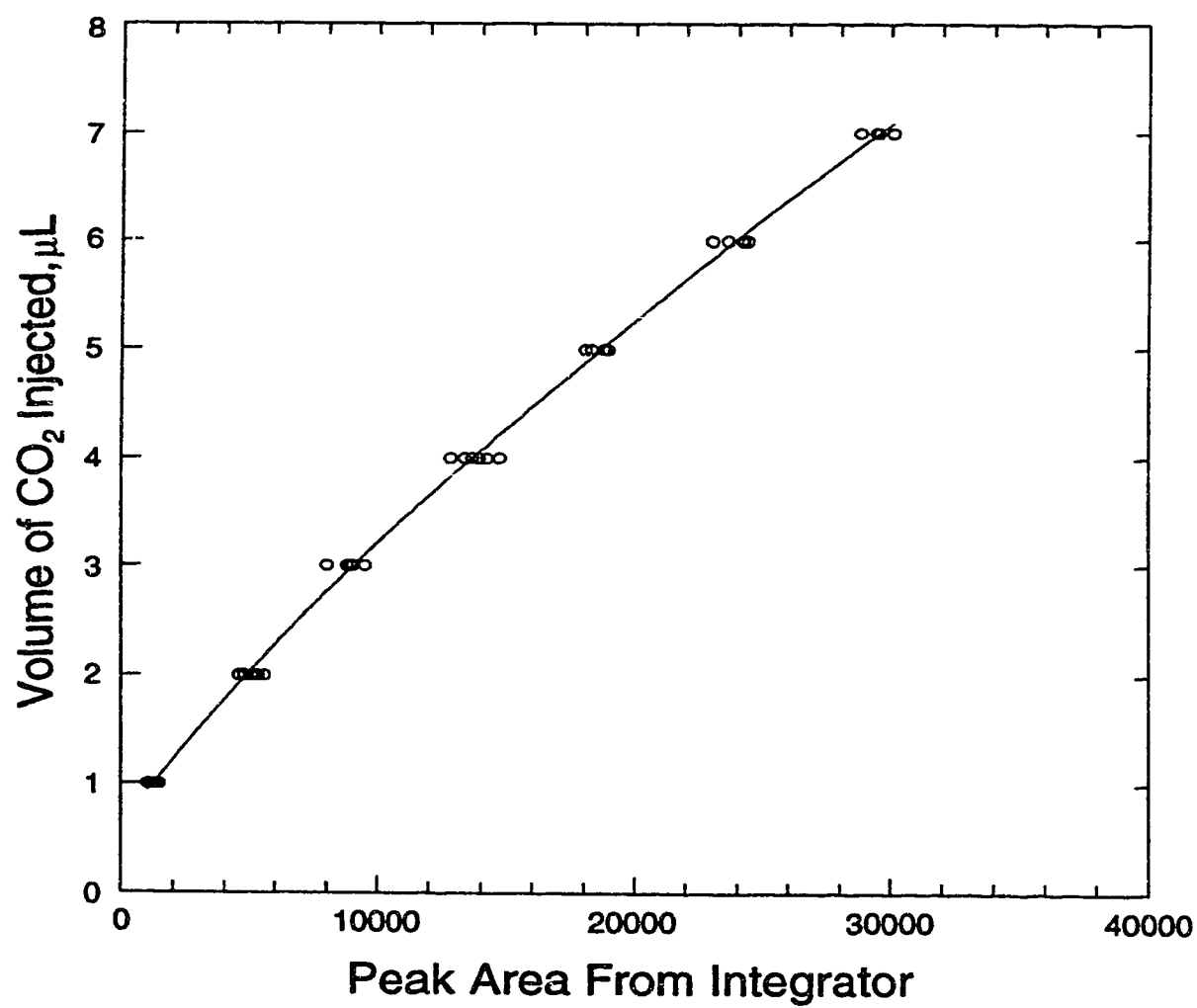


Figure C.1: Calibration Curve for Analyzing Dissolved CO₂ in Water. $T=20^{\circ}\text{C}$

Appendix D

Sample Calculations

D.1 Absorption Results

The following series of calculations were required in order to convert the raw experimental data of CO₂ peak area from the GC output to CO₂ concentration in *kmol/m³* in the absence of end effects.

D.1.1 Carbon Dioxide Concentration in Water Before Absorption

To determine the amount of CO₂ in the water before any absorption occurred, two techniques were tested. In the first, liquid samples from the distributor tube, which carried liquid to the plate, were collected and analyzed in the gas chromatograph (GC). Although a reproducible signal was obtained, the CO₂ peak area obtained was too small to be analyzed using the calibration curve. This technique was therefore abandoned in favour of using literature values for the

concentration of CO_2 in water at ambient conditions. The calculation of the concentration of CO_2 in water using the latter method is described below.

The mole fraction of CO_2 in dry, unpolluted air has been reported by Brimblecombe [32] as

$$\tilde{y}_{\text{CO}_2} = 340 \times 10^{-6}$$

although this value is variable.

The partial pressure of CO_2 in the air at the average laboratory conditions of 22°C and 94.352 kPa can therefore be determined as follows:

$$P_{\text{CO}_2} = 340 \times 10^{-6} (94.352 \text{ kPa}) = 3.208 \times 10^{-2} \text{ kPa}$$

The value of the Henry's Law constant at 20°C can be calculated via the correlation described in the work of Carroll *et al.* [35].

$$\ln \left(\frac{H_{AB}}{\text{MPa}} \right) = -6.8346 + \frac{1.2817 \times 10^6}{T} - \frac{3.7668 \times 10^6}{T^2} + \frac{2.997 \times 10^8}{T^3}$$

$$(\text{valid for } 273 < T < 433 \text{ K})$$

$$= -6.8346 + \frac{1.2817 \times 10^6}{295.15 \text{ K}} - \frac{3.7668 \times 10^6}{(295.15 \text{ K})^2} + \frac{2.997 \times 10^8}{(295.15 \text{ K})^3}$$

$$H_{AB} = 146.0 \text{ MPa}/(\text{mol frac})$$

The mole fraction of CO_2 in the liquid which would be in equilibrium with the surrounding air of mole fraction, $\tilde{y}_{\text{CO}_2} = 340 \times 10^{-6}$, would be

$$\tilde{x}_{\text{CO}_2} = \frac{P_{\text{CO}_2}}{H_{AB}} = \frac{3.208 \times 10^{-2} \text{ kPa}}{146 \times 10^3 \frac{\text{kPa}}{\text{mol frac}}} = 2.197 \times 10^{-7}$$

The concentration of CO_2 in the water can now be calculated from the definition of mole fraction using the dilute solution approximation

$$\text{mole fraction} = \frac{\text{kmol CO}_2}{\text{kmol H}_2\text{O} + \text{kmol CO}_2} \approx \frac{\text{kmol CO}_2}{\text{kmol H}_2\text{O}}$$

and the concentration of CO₂ in water at ambient conditions is

$$C_{\text{CO}_2} = 2.197 \times 10^{-7} \times 998.23 \frac{\text{kg}}{\text{m}^3} \times \frac{\text{kmol}}{18.016 \text{ kg}}$$

$$C_{\text{CO}_2} = 1.217 \times 10^{-5} \text{ kmol/m}^3$$

D.1.2 Converting Carbon Dioxide Peak Area to Concentration

The experimental data point used in the following sample calculations is taken from the experimental conditions

Plate Inclination, $\alpha = 15^\circ$

Flow Distance, $Dist = 0.114 \text{ m}$

Volumetric Flow Rate, $q_L = 19 \text{ mL/min}$

for which the peak area is

Peak Area, $PA = 3272$

To convert the CO₂ peak area to concentration, the fitted line from the calibration curve is used to determine the volume of CO₂ present in the water sample

$$V_{\text{CO}_2} = 0.631159 + 3.11199 \times 10^{-4} (3272 - 121) - 6.98078 \times 10^{-9} (3272 - 121)^2 + 2.02924 \times 10^{-13} (3272 - 121)^3 - 2.56877 \times 10^{-18} (3272 - 121)^4$$

$$V_{\text{CO}_2} = 1.54853 \mu\text{L}$$

where the peak area is corrected by a standard value of 121. This correction is done because injections of pre-absorption water samples revealed an average peak area of this amount was always present.

The ideal gas law can be used to convert this CO_2 volume value to kmol CO_2 using the pressure and temperature in the laboratory on the day the calibration curve was obtained

$$\begin{aligned} n_{\text{CO}_2} &= \frac{P V_{\text{CO}_2}}{RT} \\ &= \frac{(0.9312 \text{ atm})(1.54853 \times 10^{-6} \text{ L})}{(82.05 \frac{\text{L atm}}{\text{kmol K}})(295.15 \text{ K})} \\ n_{\text{CO}_2} &= 5.954 \times 10^{-11} \text{ kmol CO}_2 \end{aligned}$$

The volume of the liquid injected was read directly from the syringe used to inject the liquid and was always $5 \mu\text{L}$. Converting this value to m^3

$$V_{\text{sample}} = 5 \mu\text{L} \times \frac{\text{L}}{1 \times 10^6 \mu\text{L}} \times \frac{\text{m}^3}{1000 \text{ L}} = 5 \times 10^{-9} \text{ m}^3$$

The concentration of CO_2 in the liquid sample is then

$$\begin{aligned} C_{\text{CO}_2} &= \frac{n_{\text{CO}_2}}{V_{\text{sample}}} = \frac{5.954 \times 10^{-11} \text{ kmol CO}_2}{5 \times 10^{-9} \text{ m}^3} \\ C_{\text{CO}_2} &= 1.191 \times 10^{-2} \text{ kmol CO}_2/\text{m}^3 \end{aligned}$$

Expressed in terms of mole fraction

$$\begin{aligned} \tilde{x}_{\text{CO}_2} &= 1.191 \times 10^{-2} \frac{\text{kmol CO}_2}{\text{m}^3} \times \frac{\text{m}^3}{998.23 \text{ kg}} \times 18.016 \frac{\text{kg}}{\text{kmol}} \\ \tilde{x}_{\text{CO}_2} &= 2.149 \times 10^{-4} \end{aligned}$$

As can be seen from these results, the equilibrium CO_2 concentration in water at ambient conditions is negligible compared to the absorption which occurred while the liquid was flowing down the inclined plate. However, for completeness, this value is used in the calculation of the overall liquid-side mass transfer coefficient.

D.1.3 Overall Liquid-Side Mass Transfer Coefficient

The overall liquid-side mass transfer coefficient, $K_{\tilde{x}}$, can be expressed as

$$K_{\tilde{x}} = \frac{(C_{\text{CO}_2, \text{out}} - C_{\text{CO}_2, \text{in}}) q_L}{s'_p \text{Dist } \Delta \tilde{x}_{lm}} \quad (\text{D.1})$$

$$\text{where : } \Delta \tilde{x}_{lm} = \frac{(\tilde{x}_{\text{CO}_2}^* - \tilde{x}_{\text{CO}_2})_{\text{out}} - (\tilde{x}_{\text{CO}_2}^* - \tilde{x}_{\text{CO}_2})_{\text{in}}}{\ln((\tilde{x}_{\text{CO}_2}^* - \tilde{x}_{\text{CO}_2})_{\text{out}} / (\tilde{x}_{\text{CO}_2}^* - \tilde{x}_{\text{CO}_2})_{\text{in}})}$$

which requires information for the arc length of the rivulet, s'_p , and the liquid mole fraction which is in equilibrium with the surrounding gas, \tilde{x}_A . The value of s'_p is computed using the theoretical relationship for s'_p versus q_L , which for a plate inclination of 15° and a flow rate of 19 mL/min is

$$\begin{aligned} s'_p &= 0.167397 q_L^{0.258735} \\ &= 0.167397 (3.167 \times 10^{-7} \frac{\text{m}^3}{\text{s}})^{0.258735} \\ s'_p &= 3.484 \times 10^{-3} \text{ m} \end{aligned}$$

The value for $\tilde{x}_{\text{CO}_2}^*$ is taken from the paper by Carroll *et al.* [35]

$$\tilde{x}_{\text{CO}_2}^* = 6.642 \times 10^{-4}$$

With the above values for s'_p and $\tilde{x}_{\text{CO}_2}^*$, along with the results from the previous sections, $K_{\tilde{x}}$ can be computed

$$\begin{aligned} K_{\tilde{x}} &= \frac{(1.191 \times 10^{-2} - 1.217 \times 10^{-5}) \frac{\text{kmol}}{\text{m}^3} (3.167 \times 10^{-7} \frac{\text{m}^3}{\text{s}})}{(3.484 \times 10^{-3} \text{ m}) (0.114 \text{ m}) (5.496 \times 10^{-4})} \\ K_{\tilde{x}} &= 1.726 \times 10^{-2} \text{ kmol}/(\text{m}^2 \text{ s}) \end{aligned}$$

$$\begin{aligned} \text{where : } \Delta \tilde{x}_{lm} &= \frac{(6.642 \times 10^{-4} - 2.149 \times 10^{-4}) - (6.642 \times 10^{-4} - 2.197 \times 10^{-7})}{\ln((6.642 \times 10^{-4} - 2.149 \times 10^{-4}) / (6.642 \times 10^{-4} - 2.197 \times 10^{-7}))} \\ \Delta \tilde{x}_{lm} &= 5.496 \times 10^{-4} \end{aligned}$$

D.1.4 Dimensionless Number Analysis

Calculation of the dimensionless Sherwood and inverse Graetz numbers was performed to determine if the concentration boundary layer had developed. The Sherwood and inverse Graetz numbers are defined for this system as follows

$$N_{Sh} = \frac{K_{\bar{z}} (2x'_p) (MW)}{\rho_L \mathcal{D}_{AB}}$$

$$N_{Gz^{-1}} = \frac{Dist}{(2x'_p) N_{Re} N_{Sc}}$$

Experimental Data

The width of the rivulet at a flow rate of $3.167 \times 10^{-7} \text{ m}^3/\text{s}$ can be determined from the theoretical relationship for $2x'_p$ versus q_L , which for a plate inclination of 15° , is, from Appendix E

$$(2x'_p) = 0.157051 q_L^{0.261296}$$

$$= 0.157051 (3.167 \times 10^{-7} \frac{\text{m}^3}{\text{s}})^{0.261296}$$

$$(2x'_p) = 3.146 \times 10^{-3} \text{ m}$$

The Reynolds number is also required and can be calculated from the following expression, which is valid for rivulet flows

$$N_{Re} = \frac{4 q_L}{\nu_L (2x'_p)}$$

$$= \frac{4 (3.167 \times 10^{-7} \frac{\text{m}^3}{\text{s}})}{(1.004 \times 10^{-6} \frac{\text{m}^2}{\text{s}})(3.146 \times 10^{-3} \text{ m})}$$

$$N_{Re} = 401$$

The value of the Schmidt number is also required and is calculated as follows

$$N_{Sc} = \frac{\nu_L}{\mathcal{D}_{AB}}$$

$$N_{Sc} = \frac{1.004 \times 10^{-6} \frac{m^2}{s}}{1.77 \times 10^{-9} \frac{m^2}{s}} = 567$$

With the above calculated values and the value of K_z determined previously, the Sherwood and inverse Graetz numbers can now be calculated

$$N_{Sh} = \frac{(1.726 \times 10^{-2} \frac{kmol}{m^2 s})(3.146 \times 10^{-3} m)(18.016 \frac{kg}{kmol})}{(998.23 \frac{kg}{m^3})(1.77 \times 10^{-9} \frac{m^2}{s})}$$

$$N_{Sh} = 554$$

$$N_{Gz^{-1}} = \frac{0.114 m}{(3.146 \times 10^{-3} m)(401)(567)}$$

$$N_{Gz^{-1}} = 1.594 \times 10^{-4}$$

Theoretical Results

To calculate the Sherwood and inverse Graetz numbers for the theoretical data, the same relationships can be used as were used for the experimental data. The theoretical conditions, which are to be used in these calculations, are

Plate Inclination, $\alpha = 15^\circ$

Contact Angle, $\theta = 46^\circ$

Curvature at Apex, $\log_{10} B = 0.0$

Flow Distance, $Dist = 0.114 m$

The theoretical rivulet which is formed from these conditions has the following properties

Width, $2x_p' = 3.633 \times 10^{-3} m$

Reynolds Number, $N_{Re} = 626$

Arc Length, $s_p' = 4.025 \times 10^{-3} m$

$$\text{Volumetric Flow Rate, } q_L = 5.704 \times 10^{-7} \text{ m}^3/\text{s}$$

$$\text{Outlet Concentration, } C_{\text{CO}_2, \text{out}} = 2.4 \times 10^{-3} \text{ kmol/m}^3$$

From these results, the mass transfer coefficient can be calculated from Equation D.1

$$K_{\bar{x}} = \frac{(2.4 \times 10^{-3} - 0) \frac{\text{kmol}}{\text{m}^3} (5.704 \times 10^{-7} \frac{\text{m}^3}{\text{s}})}{(4.025 \times 10^{-3} \text{ m}) (0.114 \text{ m}) (6.42 \times 10^{-4})}$$

$$K_{\bar{x}} = 4.64 \times 10^{-3} \text{ kmol}/(\text{m}^2 \text{s})$$

$$\text{where: } \Delta \tilde{x}_{lm} = \frac{(6.642 \times 10^{-4} - 4.33 \times 10^{-5}) - (6.642 \times 10^{-4} - 0)}{\ln((6.642 \times 10^{-4} - 4.33 \times 10^{-5})/(6.642 \times 10^{-4} - 0))}$$

$$\Delta \tilde{x}_{lm} = 6.42 \times 10^{-4}$$

The Sherwood and inverse Graetz numbers can now be calculated for the theoretical results

$$N_{Sh} = \frac{(4.64 \times 10^{-3} \frac{\text{kmol}}{\text{m}^2 \text{s}})(3.633 \times 10^{-3} \text{ m})(18.016 \frac{\text{kg}}{\text{kmol}})}{(998.23 \frac{\text{kg}}{\text{m}^3})(1.77 \times 10^{-9} \frac{\text{m}^2}{\text{s}})}$$

$$N_{Sh} = 172$$

$$N_{Gz^{-1}} = \frac{0.114 \text{ m}}{(3.633 \times 10^{-3} \text{ m})(626)(567)}$$

$$N_{Gz^{-1}} = 3.1 \times 10^{-5}$$

Correction of Experimental Data

As explained in Chapter 7 the experimental data can be corrected for end effects, which are present in the data. The equation of the corrected experimental data line from Figure 7.8 is

$$N_{Sh} = 5.92348 (Gz^{-1})^{-0.493428}$$

The above calculated value of the Sherwood number from the experimental results can now be corrected using this equation

$$N_{Sh} = 5.92348 (1.594 \times 10^{-4})^{-0.493428} = 443$$

The corrected value of $K_{\bar{x}}$ can now be calculated from the definition of the Sherwood number

$$\begin{aligned} K_{\bar{x}} &= \frac{\rho_L N_{Sh} \mathcal{D}_{AB}}{(2x_p')(MW)} \\ &= \frac{(998.23 \frac{kg}{m^3})(443)(1.77 \times 10^{-9} \frac{m^2}{s})}{(3.146 \times 10^{-3} m)(18.016 \frac{kg}{kmol})} \\ K_{\bar{x}} &= 1.381 \times 10^{-2} kmol/(m^2 s) \end{aligned}$$

With this value of the corrected $K_{\bar{x}}$, the corrected outlet concentration can be determined. To find this concentration, Equation D.1 can be simplified by converting the concentration terms in the numerator to mole fractions, which then cancel with the numerator of the equation for $\Delta \tilde{x}_{lm}$. The resulting equation, when rearranged for the outlet mole fraction of CO_2 , and subsequent value for the corrected outlet concentration is

$$\tilde{x}_{CO_2,out} = \tilde{x}_{CO_2,out}^* - (\tilde{x}_{CO_2}^* - \tilde{x}_{CO_2})_{in} \exp \left(- \frac{K_{\bar{x}} s_p' Dist}{q_L} \frac{18.016 \frac{kg}{kmol}}{998.23 \frac{kg}{m^3}} \right)$$

The above results can be substituted into the above equation as follows

$$\begin{aligned} \tilde{x}_{CO_2,out} &= 6.642 \times 10^{-4} - (6.642 \times 10^{-4} - 2.197 \times 10^{-7}) \\ &\quad \exp \left(- \frac{(1.381 \times 10^{-2} \frac{kmol}{m^2 s})(3.484 \times 10^{-3} m)(0.114 m)}{(3.167 \times 10^{-7} \frac{m^3}{s})} \frac{(18.016 \frac{kg}{kmol})}{(998.23 \frac{kg}{m^3})} \right) \\ \tilde{x}_{CO_2,out} &= 1.78 \times 10^{-4} \end{aligned}$$

Expressing the corrected outlet mole fraction in terms of concentration yields

$$C_{CO_2,out} = 1.78 \times 10^{-4} \times 998.23 \frac{kg}{m^3} \times \frac{18.016 kg}{kmol} = 9.89 \times 10^{-3} kmol/m^3$$

D.2 Analytical Diffusion Model

Carslaw and Jaeger [36], in their book *Conduction of Heat in Solids*, describe the solution to the problem of transient heating of an infinite cylinder where the surface

temperature is kept at a constant value and the interior is initially at a temperature of zero. The diagram describing this problem is shown in Figure 7.9 but in order to use this problem as a benchmark solution, it is necessary to simulate a similar problem with the computer code. The solution which turns out to be equivalent to this problem for the rivulet flow case is a half cylinder with zero flux at the solid surface and a flat velocity profile. The exact rivulet profile used is shown in Figure 4.6.

From p.200 of Carslaw and Jaeger's book, a figure similar to the one in Figure 7.10 is shown from which were taken the analytical solutions. From the definition of the dimensionless time used in the figure,

$$t = \frac{t' D_{AB}}{(x'_p)^2}$$

it is possible to determine the correct exposure time to be used in the rivulet problem to obtain relevant comparison results.

Required Data: Diffusivity, $D_{AB} = 1.77 \times 10^{-9} \text{ m}^2/\text{s}$

Radius, $x'_p = 2.72 \times 10^{-4} \text{ m}$

Grid Density = 31×51

Plate Inclination, $\alpha = 0.01^\circ$

Average Velocity, $u_{z,av} = 2.887 \times 10^{-5} \text{ m/s}$

The dimensionless times listed in Figure 7.9 are 0.005, 0.1 and 0.4 and lead to exposure times in the rivulet problem of

$$\begin{aligned} t'_{0.005} &= \frac{(0.005) (2.720 \times 10^{-4} \text{ m})^2}{1.77 \times 10^{-9} \frac{\text{m}^2}{\text{s}}} = 0.209 \text{ s} \\ t'_{0.1} &= \frac{(0.1) (2.720 \times 10^{-4} \text{ m})^2}{1.77 \times 10^{-9} \frac{\text{m}^2}{\text{s}}} = 4.18 \text{ s} \\ t'_{0.4} &= \frac{(0.4) (2.720 \times 10^{-4} \text{ m})^2}{1.77 \times 10^{-9} \frac{\text{m}^2}{\text{s}}} = 16.72 \text{ s} \end{aligned}$$

From these exposure times and the average velocity calculated in the rivulet, the required flow distances which must be simulated can be determined.

$$Dist_{0.005} = t'_{0.005} u_{z,av} = (0.209 \text{ s}) (2.887 \times 10^{-5} \frac{m}{s}) = 6.034 \times 10^{-6} \text{ m}$$

$$Dist_{0.1} = t'_{0.1} u_{z,av} = (4.18 \text{ s}) (2.887 \times 10^{-5} \frac{m}{s}) = 1.207 \times 10^{-4} \text{ m}$$

$$Dist_{0.4} = t'_{0.4} u_{z,av} = (16.72 \text{ s}) (2.887 \times 10^{-5} \frac{m}{s}) = 4.827 \times 10^{-4} \text{ m}$$

Simulations were also done using an average velocity of $5.774 \times 10^{-5} \text{ m/s}$ to test if the flow rate had any effect on the solution.

D.3 Negligible Z-Diffusion Assumption

In Chapter 4, Section 4.1.3, the assumption is made that z -diffusion in the convection-diffusion equation is negligible compared to the convection which is occurring in the rivulet. This assumption seems reasonable based on the size of the diffusion coefficient for CO_2 , $\mathcal{D}_{AB} = 1.77 \times 10^{-9} \text{ m}^2/\text{s}$. The following calculations present an analysis of this problem using the Peclet number, which is defined as follows

$$N_{Pe} = N_{Re} N_{Sc} = \frac{4 q_L}{(2x'_p) \mathcal{D}_{AB}}$$

and is a ratio of the inertial effects to the mass diffusivity. The assumption of negligible z -diffusion will be least justified when the volumetric flow rate of the liquid is small and the plate inclination is low. Therefore, for a flow rate of $3 \times 10^{-7} \text{ m}^3/\text{s}$, which is the smallest flow rate studied in the absorption study, and a plate inclination of 15° , the rivulet width will be

$$\begin{aligned} 2x'_p &= 0.157051 q_L^{0.261296} \\ &= 0.157051 (3 \times 10^{-7})^{0.261296} \\ 2x'_p &= 3.1 \times 10^{-3} \text{ m} \end{aligned}$$

and the Peclet number is

$$N_{Pe} = \frac{4(3 \times 10^{-7} \frac{m^3}{s})}{(3.1 \times 10^{-3} m)(1.77 \times 10^{-9} \frac{m^2}{s})}$$

$$N_{Pe} = 2.19 \times 10^5$$

From this analysis, it can be seen that the inertial effects dominate in this absorption problem and the assumption of negligible z -diffusion is justified.

D.4 Error Analysis

This section presents an analysis of the errors which were present in the experimental results together with calculations to determine their magnitude. The experimental point, which has been chosen for analysis, is the same experimental point which has been used in the previous calculations. The calculations which are done here are to determine the lower error bound for the experimental data to see if the error in the experimental data includes the theoretical data.

Analysis of the calibration curve in Appendix C reveals that the value of the volume of CO_2 injected could range between

$$1.33 < V_{CO_2} < 1.73 \mu L$$

The errors associated with reading the barometer and temperature are taken as

$$\text{Pressure} \Rightarrow \pm 1 \text{ mmHg} \quad \text{Temperature} \Rightarrow \pm 1^\circ C$$

which give a range of pressure and temperature for this data point of

$$0.9299 < P < 0.9325 \text{ atm} \quad 294.15 < T < 296.15 \text{ K}$$

Calculating the number of kmoles of CO_2

$$\begin{aligned} n_{\text{CO}_2} &= \frac{P V_{\text{CO}_2}}{RT} \\ &= \frac{(0.9299 \text{ atm})(1.33 \times 10^{-6} \text{ L})}{(82.05 \frac{\text{L atm}}{\text{kmol K}})(296.15 \text{ K})} \\ n_{\text{CO}_2} &= 5.090 \times 10^{-11} \text{ kmol CO}_2 \end{aligned}$$

The error in the volume of liquid injected was taken to be $\pm 0.1 \mu\text{L}$ which gives a range in the liquid volume of

$$4.9 < V_{\text{sample}} < 5.1 \mu\text{L}$$

and a sample volume of

$$V_{\text{sample}} = 5.1 \mu\text{L} \times \frac{\text{L}}{1 \times 10^6 \mu\text{L}} \times \frac{1 \text{ m}^3}{1000 \text{ L}} = 5.1 \times 10^{-9} \text{ m}^3$$

The concentration of CO_2 in the sample is

$$\begin{aligned} C_{\text{CO}_2} &= \frac{n_{\text{CO}_2}}{V_{\text{sample}}} = \frac{5.090 \times 10^{-11} \text{ kmol CO}_2}{5.1 \times 10^{-9} \text{ m}^3} \\ C_{\text{CO}_2} &= 9.980 \times 10^{-3} \text{ kmol CO}_2/\text{m}^3 \end{aligned}$$

Expressed in terms of mole fraction

$$\begin{aligned} \tilde{x}_{\text{CO}_2} &= 9.980 \times 10^{-3} \frac{\text{kmol CO}_2}{\text{m}^3} \times \frac{\text{m}^3}{998.23 \text{ kg}} \times 18.016 \frac{\text{kg}}{\text{kmol}} \\ \tilde{x}_{\text{CO}_2} &= 1.801 \times 10^{-4} \end{aligned}$$

The interfacial area for this data point can be calculated assuming an error in the volumetric flow rate of $\pm 1 \text{ mL/min}$

$$\begin{aligned} s'_p &= 0.167397 q_L^{0.258735} \\ &= 0.167397 (3.0 \times 10^{-7} \frac{\text{m}^3}{\text{s}})^{0.258735} \\ s'_p &= 3.44 \times 10^{-3} \text{ m} \end{aligned}$$

The above calculation does not account for any error that would occur if the above relationship does not adequately represent the interfacial area. This relationship is assumed to adequately represent the interfacial area because the agreement between the experimental and theoretical rivulet widths and heights was very good. An error of 5% is assumed to account for any error in this relationship, which would give a value of s'_p of $3.61 \times 10^{-3} m$.

The error in the flow distance is taken to be $0.005 m$, which gives a range of flow distance of

$$0.109 < Dist < 0.119 m$$

The error in the saturation concentration of CO_2 is taken to be 5%, which gives a range in this value of

$$6.326 \times 10^{-4} < \tilde{x}_{CO_2}^* < 6.974 \times 10^{-4}$$

Calculating the logarithmic mean driving force

$$\Delta \tilde{x}_{lm} = \frac{(6.974 \times 10^{-4} - 1.801 \times 10^{-4}) - (6.974 \times 10^{-4} - 2.197 \times 10^{-7})}{\ln((6.974 \times 10^{-4} - 1.801 \times 10^{-4}) / (6.974 \times 10^{-4} - 2.197 \times 10^{-7}))}$$

$$\Delta \tilde{x}_{lm} = 6.028 \times 10^{-4}$$

Calculating the overall liquid-side mass transfer coefficient

$$K_{\tilde{x}} = \frac{(9.980 \times 10^{-3} - 1.217 \times 10^{-5}) \frac{kmol}{m^3} (3.0 \times 10^{-7} \frac{m^3}{s})}{(3.608 \times 10^{-3} m) (0.119 m) (6.028 \times 10^{-4})}$$

$$K_{\tilde{x}} = 1.16 \times 10^{-2} kmol/(m^2 s)$$

The rivulet width which corresponds to these conditions is

$$2x'_p = 0.157051 q_L^{0.261296}$$

$$= 0.157051 (3 \times 10^{-7} \frac{m^3}{s})^{0.261296}$$

$$2x'_p = 3.102 \times 10^{-3} m$$

As with the relationship for interfacial area, an additional error of 5% is included here, which gives a rivulet width of $2.947 \times 10^{-3} m$.

The value of the Sherwood number can now be computed

$$\begin{aligned}
 N_{Sh} &= \frac{K_{\bar{x}}(2x'_p)(MW)}{\rho_L \mathcal{D}_{AB}} \\
 &= \frac{(1.159 \times 10^{-2} \frac{kmol}{m^2 s})(2.947 \times 10^{-3} m)(18.016 \frac{kg}{kmol})}{(998.23 \frac{kg}{m^3})(1.77 \times 10^{-9} \frac{m^2}{s})} \\
 N_{Sh} &= 348
 \end{aligned}$$

The previously corrected Sherwood numbers were corrected approximately 20%. If this same correction is performed here on the lower error bound, the corrected lower limit for the Sherwood number is 278.

From Figure 7.8, the theoretical Sherwood number for the same conditions is approximately 120. Clearly, the experimental Sherwood numbers are considerably higher than the theoretical ones indicating enhanced absorption in the experimental data.

Appendix E

Best Fit Lines

The following information is a summary of the equations of the best fit lines of the curves which have been drawn in the figures of this thesis. The equations are tabulated by figure number and whether the results are experimental, analytical or calculated from the experimental data or by the computer code.

For the rivulet width results computed using the computer code, the equations are as follows:

Figure 6.4, Computer Code

$$\begin{aligned}\theta = 26^\circ & \quad 2x'_p = 0.304183 q_L^{0.272324} \\ \theta = 46^\circ & \quad 2x'_p = 0.157051 q_L^{0.261296} \\ \theta = 72^\circ & \quad 2x'_p = 0.0959509 q_L^{0.256951} \\ \theta = 88^\circ & \quad 2x'_p = 0.0756516 q_L^{0.256836}\end{aligned}$$

Figure 6.5, Computer Code

$$\begin{aligned}\theta = 26^\circ & \quad 2x'_p = 0.220417 q_L^{0.26339} \\ \theta = 46^\circ & \quad 2x'_p = 0.123381 q_L^{0.256969} \\ \theta = 72^\circ & \quad 2x'_p = 0.0779344 q_L^{0.254655} \\ \theta = 88^\circ & \quad 2x'_p = 0.0619341 q_L^{0.255053}\end{aligned}$$

Figure 6.6, Computer Code

$$\theta = 26^\circ \quad 2x'_p = 0.188241 q_L^{0.259731}$$

$$\begin{aligned}
\theta = 46^\circ & \quad 2x'_p = 0.108655 q_L^{0.254806} \\
\theta = 72^\circ & \quad 2x'_p = 0.0698222 q_L^{0.253481} \\
\theta = 88^\circ & \quad 2x'_p = 0.0552484 q_L^{0.253585}
\end{aligned}$$

Figure 6.7, Computer Code

$$\begin{aligned}
\theta = 26^\circ & \quad 2x'_p = 0.168161 q_L^{0.256379} \\
\theta = 46^\circ & \quad 2x'_p = 0.0998062 q_L^{0.252807} \\
\theta = 72^\circ & \quad 2x'_p = 0.0649273 q_L^{0.252269} \\
\theta = 88^\circ & \quad 2x'_p = 0.0514126 q_L^{0.2524}
\end{aligned}$$

Figure 6.8, Computer Code

$$\begin{aligned}
\theta = 26^\circ & \quad 2x'_p = 0.145123 q_L^{0.250163} \\
\theta = 46^\circ & \quad 2x'_p = 0.0915605 q_L^{0.250085} \\
\theta = 72^\circ & \quad 2x'_p = 0.060256 q_L^{0.250112} \\
\theta = 88^\circ & \quad 2x'_p = 0.0475796 q_L^{0.25005}
\end{aligned}$$

For the rivulet height results computed using the computer code, the equations are as follows:

Figure 6.9, Computer Code

$$\begin{aligned}
\theta = 26^\circ & \quad y'_p = 0.0190085 q_L^{0.238516} \\
\theta = 46^\circ & \quad y'_p = 0.0246246 q_L^{0.244474} \\
\theta = 88^\circ & \quad y'_p = 0.0308309 q_L^{0.24769}
\end{aligned}$$

Figure 6.10, Computer Code

$$\begin{aligned}
\theta = 26^\circ & \quad y'_p = 0.0175161 q_L^{0.243234} \\
\theta = 46^\circ & \quad y'_p = 0.0216781 q_L^{0.246562} \\
\theta = 88^\circ & \quad y'_p = 0.0264947 q_L^{0.248353}
\end{aligned}$$

Figure 6.11, Computer Code

$$\begin{aligned}
\theta = 26^\circ & \quad y'_p = 0.0166436 q_L^{0.245043} \\
\theta = 46^\circ & \quad y'_p = 0.0202814 q_L^{0.247641} \\
\theta = 88^\circ & \quad y'_p = 0.0245169 q_L^{0.248838}
\end{aligned}$$

Figure 6.12, Computer Code

$$\begin{aligned}
\theta = 26^\circ & \quad y'_p = 0.0163271 q_L^{0.246742} \\
\theta = 46^\circ & \quad y'_p = 0.019599 q_L^{0.248593} \\
\theta = 88^\circ & \quad y'_p = 0.0234594 q_L^{0.249196}
\end{aligned}$$

Figure 6.13, Computer Code

$$\begin{aligned}
 \theta = 26^\circ & & y_p' &= 0.0166746 q_L^{0.249922} \\
 \theta = 46^\circ & & y_p' &= 0.0193786 q_L^{0.249928} \\
 \theta = 88^\circ & & y_p' &= 0.0229368 q_L^{0.249955}
 \end{aligned}$$

For the rivulet arc length results computed using the computer code, the equations are as follows:

Figure 6.16, Computer Code

$$\begin{aligned}
 \alpha = 15^\circ & & s_p' &= 0.167397 q_L^{0.258735} \\
 \alpha = 30^\circ & & s_p' &= 0.133852 q_L^{0.255417} \\
 \alpha = 45^\circ & & s_p' &= 0.118939 q_L^{0.253729} \\
 \alpha = 60^\circ & & s_p' &= 0.110033 q_L^{0.252142} \\
 \alpha = 89^\circ & & s_p' &= 0.102157 q_L^{0.250069}
 \end{aligned}$$

For the rivulet cross-sectional area results computed using the computer code, the equations are as follows:

Figure 6.17, Computer Code

$$\begin{aligned}
 \alpha = 15^\circ & & v_p' &= 0.00279093 q_L^{0.508261} \\
 \alpha = 30^\circ & & v_p' &= 0.00189863 q_L^{0.505094} \\
 \alpha = 45^\circ & & v_p' &= 0.00155118 q_L^{0.50356} \\
 \alpha = 60^\circ & & v_p' &= 0.00136628 q_L^{0.502063} \\
 \alpha = 89^\circ & & v_p' &= 0.00122539 q_L^{0.500061}
 \end{aligned}$$

For the rivulet width results computed using the computer code and film approximation model, the equations are as follows:

Figure 6.18, Computer Code

$$\begin{aligned}
 \alpha = 15^\circ & & 2x_p' &= 0.169709 q_L^{0.260728} \\
 \alpha = 30^\circ & & 2x_p' &= 0.133698 q_L^{0.256638} \\
 \alpha = 45^\circ & & 2x_p' &= 0.11787 q_L^{0.254568} \\
 \alpha = 60^\circ & & 2x_p' &= 0.108387 q_L^{0.25267} \\
 \alpha = 89^\circ & & 2x_p' &= 0.0995295 q_L^{0.250037}
 \end{aligned}$$

The equations for the rivulet model (the other curve in each figure) are the same as those listed for Figures 6.4 to 6.8 for $\theta = 46^\circ$.

For the rivulet height results computed using the computer code and film approximation model, the equations are as follows:

Figure 6.19, Computer Code

$$\begin{aligned}
\alpha = 15^\circ & \quad y_p' = 0.0191163 q_L^{0.246405} \\
\alpha = 30^\circ & \quad y_p' = 0.0166182 q_L^{0.247762} \\
\alpha = 45^\circ & \quad y_p' = 0.0154327 q_L^{0.248426} \\
\alpha = 60^\circ & \quad y_p' = 0.0148382 q_L^{0.249076} \\
\alpha = 89^\circ & \quad y_p' = 0.0145446 q_L^{0.249915}
\end{aligned}$$

The equations for the rivulet model (the other curve in each figure) are the same as those listed for Figures 6.9 to 6.13 for $\theta = 46^\circ$.

For the rivulet arc length results computed using the computer code and film approximation model, the equations are as follows:

Figure 6.20, Computer Code

$$\begin{aligned}
\alpha = 15^\circ & \quad y_p' = 0.206910 q_L^{0.257539} \\
\alpha = 30^\circ & \quad y_p' = 0.156807 q_L^{0.254723} \\
\alpha = 45^\circ & \quad y_p' = 0.148609 q_L^{0.253185} \\
\alpha = 60^\circ & \quad y_p' = 0.137997 q_L^{0.251844} \\
\alpha = 89^\circ & \quad y_p' = 0.128514 q_L^{0.249956}
\end{aligned}$$

The equations for the rivulet model (the other curve in each figure) are the same as those listed for Figure 6.16 for $\theta = 46^\circ$.

For the experimental rivulet absorption data including end effects, the equations are as follows:

Figure 7.4, Experimental Data

$$\begin{aligned}
Dist = 0.114 \text{ m} & \quad C'_{CO_2} = 0.0145849 - 9579.16 q_L + 3.94325 \times 10^9 q_L^2 \\
Dist = 0.256 \text{ m} & \quad C'_{CO_2} = 0.0170749 - 10413.5 q_L + 3.91625 \times 10^9 q_L^2 \\
Dist = 0.368 \text{ m} & \quad C'_{CO_2} = 0.0217495 - 14270.7 q_L + 5.11633 \times 10^9 q_L^2
\end{aligned}$$

Figure 7.5, Experimental Data

$$\begin{aligned}
Dist = 0.114 \text{ m} & \quad C'_{CO_2} = 0.0135375 - 5576.53 q_L + 1.61486 \times 10^9 q_L^2 \\
Dist = 0.256 \text{ m} & \quad C'_{CO_2} = 0.0201069 - 12156 q_L + 3.79443 \times 10^9 q_L^2 \\
Dist = 0.368 \text{ m} & \quad C'_{CO_2} = 0.0250693 - 17498.7 q_L + 5.77725 \times 10^9 q_L^2
\end{aligned}$$

Figure 7.6, Experimental Data

$$\begin{aligned}
Dist = 0.114 \text{ m} & \quad C'_{CO_2} = 0.0147442 - 7638.22 q_L + 2.56511 \times 10^9 q_L^2 \\
Dist = 0.256 \text{ m} & \quad C'_{CO_2} = 0.0190384 - 9328.6 q_L + 2.14643 \times 10^9 q_L^2 \\
Dist = 0.368 \text{ m} & \quad C'_{CO_2} = 0.0253986 - 16624.6 q_L + 5.44494 \times 10^9 q_L^2
\end{aligned}$$

Figure 7.7, Experimental Data

$$Dist = 0.114\ m \quad C'_{CO_2} = 0.0128434 - 4484.82\ q_L + 1.4141 \times 10^9\ q_L^2$$

$$Dist = 0.256\ m \quad C'_{CO_2} = 0.0161228 - 6866.2\ q_L + 2.08256 \times 10^9\ q_L^2$$

$$Dist = 0.368\ m \quad C'_{CO_2} = 0.0178227 - 3234.56\ q_L + 3.19092 \times 10^8\ q_L^2$$

For the theoretical absorption results generated by the computer code, the equations are as follows:

Figure 7.11, Computer Code

$$Dist = 0.114\ m \quad C'_{CO_2} = 3.18779 \times 10^{-6}\ q_L^{-0.46243}$$

$$Dist = 0.256\ m \quad C'_{CO_2} = 4.49239 \times 10^{-6}\ q_L^{-0.463814}$$

$$Dist = 0.368\ m \quad C'_{CO_2} = 5.75824 \times 10^{-6}\ q_L^{-0.458168}$$

For the calibration curve for the gas chromatograph, the equation is as follows:

Figure C.1, Experimental

$$V_{CO_2} (\mu L) = 0.631159 + 3.11199 \times 10^{-4} (PA) - 6.98078 \times 10^{-9} (PA)^2 + 2.02924 \times 10^{-13} (PA)^3 - 2.56877 \times 10^{-18} (PA)^4$$

Appendix F

Raw Experimental Data

F.1 Experimental Absorption Data

The following data was that collected for the CO₂ absorption studies. For all of the data, the following conditions were maintained:

Sample Size, $V_{sample} = 5 \mu L$

CO₂ Flow Rate = 750 mL/min

Water Bath Temperature, $T_{bath} = 20.0^{\circ}C$

One other variable which was monitored but did vary slightly was the temperature of the CO₂. Listed below is the range of temperatures which were recorded over the course of this study.

CO₂ Temperature, $T_{CO_2} = 20.3\text{--}20.6^{\circ}C$

For most of the runs, however, the temperature of the CO₂ was either 20.4°C or 20.5°C.

The temperature in the laboratory during the absorption runs was $20.4^{\circ}\text{C} \pm 0.6^{\circ}\text{C}$. The room temperature was not recorded during the measurement of the rivulet dimensions. The temperature, however, is expected to have varied between 20°C and 20°C , which is not significant in these studies.

For each data set which is listed in the following table, the corresponding laboratory conditions on the day of the experiment are also listed. These values include the ambient air temperature, the barometric pressure, and the temperature of the water being delivered to the plate. In the first four columns of the table, an entry is made only when a specific value changes or a new flow distance begins. For example, in column four the pressure is only listed for certain data points and the assumption made is that the pressure remains the same for each data point which follows until a new entry of pressure is made. Likewise for the other columns. With this format, the following tables are less cluttered.

F.2 Surface Roughness Analysis

In order to accurately characterize the flow surface used in this study, surface roughness measurements were taken using a Taylor-Hobson Talysurf Surface Measuring Instrument. With this instrument, surface profiles were produced and are shown in Figure F.1. The top profile is taken directly from the flow plate used in this study while the bottom one is taken from a similar piece of untreated stainless steel. It should be noted that the two profiles do not have the same scale—the top profile has double the vertical magnification of the bottom profile. As well, for the flow plate profile, there is a valley at the location at which the roughness measurement was taken. However, this valley is of the order 10^{-6} m deep and does not create any problems in the flow experiments.

15° Plate Inclination							
Flow Distance (<i>m</i>)	Water Temperature (° <i>C</i>)	Air Temperature (° <i>C</i>)	Barometric Pressure (<i>mm Hg</i>)	Volumetric Flow Rate (<i>mL/min</i>)	Peak Area		
0.114	20.0	20.7	705.9	19	3272		
				19	3325		
				19	3272		
	19.9	19.8	703.9	55	1897		
				20.0	55	2057	
				19.9	55	1974	
	19.8			89	1931		
				89	1960		
				89	1947		
	0.256	20.0	20.7	705.9	18	4310	
					19.9	18	4968
					20.0	18	4557
					18	4128	
18					4534		
18					5356		
				18	4357		
				19.9	54	2738	
				54	2764		
				54	2857		
				19.8	86	2564	
				20.0	85	2337	
19.9		86	2492				

Table F.1: Experimental Absorption Data for a Plate Inclination of 15°.

15° Plate Inclination					
Flow Distance (<i>m</i>)	Water Temperature (°C)	Air Temperature (°C)	Barometric Pressure (<i>mm Hg</i>)	Volumetric Flow Rate (<i>mL/min</i>)	Peak Area
0.368	20.1	20.3	700.2	17	8650
				18	8664
				18	6842
				18	7424
				18	7680
	20.0			18	6451
				18	6257
				18	6348
				17	6278
				17	6381
	19.9	20.7	705.9	52	3839
				52	3916
				52	3968
	19.8	19.8	703.9	83	3114
				84	3271
				84	3275

Table F.2: Experimental Absorption Data for a Plate Inclination of 15°.

30° Plate Inclination					
Flow Distance (<i>m</i>)	Water Temperature (° <i>C</i>)	Air Temperature (° <i>C</i>)	Barometric Pressure (<i>mm Hg</i>)	Volumetric Flow Rate (<i>mL/min</i>)	Peak Area
0.114	20.2	20.0	704.0	22	3196
	20.1			22	3189
	20.2			22	3149
	20.1			56	2190
				56	2294
				56	2292
	20.0			90	1841
				90	1857
				90	2039
				91	1804
0.256	20.2	19.7	706.5	23	5121
	20.3			23	5231
				23	5548
				23	5441
				23	5402
	20.0	20.0	704.0	54	3426
				54	3383
				54	3482
				88	2970
				88	2600
				88	2602
				88	2547

Table F.3: Experimental Absorption Data for a Plate Inclination of 30°.

30° Plate Inclination						
Flow Distance (<i>m</i>)	Water Temperature (°C)	Air Temperature (°C)	Barometric Pressure (<i>mm Hg</i>)	Volumetric Flow Rate (<i>mL/min</i>)	Peak Area	
0.368	20.2	19.7	706.5	22	5962	
				21	5499	
	20.1			22	3302	
				22	4771	
				22	5736	
				22	6289	
				22	6634	
				22	7134	
	20.2			22	6877	
				22	7301	
		20.0	20.0	704.0	52	4442
					52	4423
					52	4378
	20.2	20.0		82	3169	
				84	3428	
				84	3769	
				84	3218	

Table F.4: Experimental Absorption Data for a Plate Inclination of 30°.

45° Plate Inclination					
Flow Distance (<i>m</i>)	Water Temperature (°C)	Air Temperature (°C)	Barometric Pressure (<i>mm Hg</i>)	Volumetric Flow Rate (<i>mL/min</i>)	Peak Area
0.114	20.0	21.0	712.4	23	4857
				23	5910
				23	5356
				23	5321
				23	4640
				23	5525
				23	6049
				23	4560
				23	4084
				22	4280
	20.2	20.7	705.5	20	3073
	20.3			20	3162
	20.2			20	3659
				20	3498
				20	3489
	19.9	21.0	705.2	52	3040
				52	1564
				51	2602
	20.0	20.7	705.2	52	3061
	19.9			51	2418
				51	2436
				98	2099
				98	1937
	19.8			98	1022
				98	1600
	19.9			98	1884

Table F.5: Experimental Absorption Data for a Plate Inclination of 45°.

45° Plate Inclination					
Flow Distance (<i>m</i>)	Water Temperature (°C)	Air Temperature (°C)	Barometric Pressure (<i>mm Hg</i>)	Volumetric Flow Rate (<i>mL/min</i>)	Peak Area
0.256	20.0	20.7	705.5	18	4647
				17	6557
				17	5240
				16	6647
				17	6720
				16	6578
				22	5087
				20	6529
				20	7441
				19	2644
				19	5597
				18	5386
				19	5453
	19.9			52	3650
				52	3612
				50	4026
				50	3586
	20.1			82	2773
				82	2452
				82	2535
				82	2559
	20.0				

Table F.6: Experimental Absorption Data for a Plate Inclination of 45°.

45° Plate Inclination					
Flow Distance (<i>m</i>)	Water Temperature (°C)	Air Temperature (°C)	Barometric Pressure (<i>mm Hg</i>)	Volumetric Flow Rate (<i>mL/min</i>)	Peak Area
0.368	20.2	20.8	705.2	22	7181
				22	6282
				21	6130
				20	5781
				20	7617
				19	9058
				18	7335
				18	6879
				18	6049
				18	6059
				18	6242
	20.2	20.7	705.5	20	5678
				20	7493
				20	7396
	20.3			20	8006
				20	7792
	19.9	20.7	705.2	52	4815
				52	4047
				52	4878
				52	4791
	19.8			87	3718
				87	3617
				86.5	3683

Table F.7: Experimental Absorption Data for a Plate Inclination of 45°.

45° Plate Inclination					
Flow Distance (<i>m</i>)	Water Temperature (°C)	Air Temperature (°C)	Barometric Pressure (<i>mm Hg</i>)	Volumetric Flow Rate (<i>mL/min</i>)	Peak Area
CO ₂ flow 0.368	19.9	19.2	708.9	49	3779
				49	4067
	20.0			48	3600
				49	4117
	19.9			49	3827
				48	3897
				48	3885
No CO ₂ flow 0.368	19.9	19.2	708.9	47	3824
				47	4272
				47	3546
				47	3825
	19.8			46	3727
				46	4089
				46	4103

Table F.8: Experimental Absorption Data for a Plate Inclination of 45°. Effect of CO₂ Flow on the Degree of Absorption.

60° Plate Inclination					
Flow Distance (<i>m</i>)	Water Temperature (°C)	Air Temperature (°C)	Barometric Pressure (<i>mm Hg</i>)	Volumetric Flow Rate (<i>mL/min</i>)	Peak Area
0.114	19.9	20.5	711.2	20	3176
				20	2957
				20	3111
	19.9	20.5	703.5	43	2369
				43	2431
				43	1671
				43	2553
				43	2317
	19.8			43	2568
				43	2459
	19.9	20.1	706.9	44	1610
				44	1050
				44	2448
				44	2669
	19.8			44	2501
	19.9	21.1	698.5	84	2030
				84	2063
				84	2132

Table F.9: Experimental Absorption Data for a Plate Inclination of 60°.

60° Plate Inclination					
Flow Distance (<i>m</i>)	Water Temperature (°C)	Air Temperature (°C)	Barometric Pressure (<i>mm Hg</i>)	Volumetric Flow Rate (<i>mL/min</i>)	Peak Area
0.256	20.0	20.5	711.2	18	5456
				18	4761
				18	4841
				18	4307
				18	4484
	19.9			18	4351
	19.8	20.1	706.9	41	3892
				41	2643
				41	3907
				40	3365
				40	4045
	19.9				
		20.5	703.5	41	2517
				41	3589
				41	2436
				41	3304
				41	3276
				41	3405
				41	3375
		20.1	701.3	47	3445
				47	3164
				47	2938
				47	3127
				47	3161
	20.0	21.1	698.5	83	2584
				83	2183
				83	2707
				83	2733

Table F.10: Experimental Absorption Data for a Plate Inclination of 60°.

60° Plate Inclination					
Flow Distance (m)	Water Temperature (°C)	Air Temperature (°C)	Barometric Pressure (mm Hg)	Volumetric Flow Rate (mL/min)	Peak Area
0.368	19.7	20.5	711.2	18	5396
	19.8			18	5923
	20.0			18	4553
				18	5661
				18	5716
	19.9	20.1	706.9	18	5914
	20.0			18	6049
	19.9			18	5179
				38	4860
	19.8			38	4783
				38	4931
	19.9	20.1	701.3	44	3808
				44	5089
				44	5125
				44	4718
				44	5277
		21.1	698.5	80	3620
				80	3780
	20.0			80	3877

Table F.11: Experimental Absorption Data for a Plate Inclination of 60°.

60° Plate Inclination					
Flow Distance (m)	Temperature (°C)	Air Temperature (°C)	Barometric Pressure (mm Hg)	Volumetric Flow Rate (mL/min)	Peak Area
0.114	20.3	21.4	705.3	23	5248
				21	3703
				18	4026
				18	4887
				17	4711
				16	4518
				16	4905
				16	4942
0.256	20.1	21.1	700.0	23	4224
				23	4943
				23	4913
	20.0			23	4613
				23	4952
				23	4267
				23	5078
				23	5087
				23	4691
				23	4668
	20.1			23	4872
				23	4828
0.368	20.1	21.1	700.0	21	7538
				21	7511
				21	5830
				21	6193
				21	6139
				21	5514
				21	5507
				21	5673

Table F.12: Experimental Absorption Data for a Change in Plate Inclination from 30° to 60°.

The average roughness measurements of the two samples were determined to be $1.8 \times 10^{-7} m$ for the flow plate sample and $3.8 \times 10^{-7} m$ for the untreated sample. Looking at the two profiles and the results of the surface analysis, it is clear that the flow plate used in this study was smoother than a plain sheet of stainless steel but that it did have similar roughness characteristics.

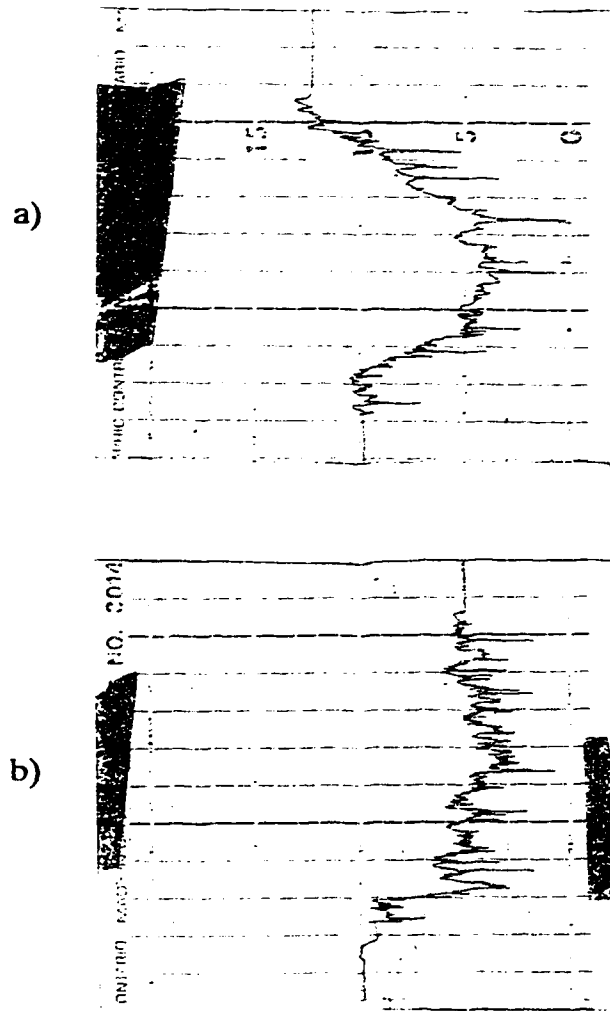


Figure F.1: Surface Roughness Profiles. a) Flow Plate. Vertical Scale = $5.08 \times 10^{-6} m$ b) Stainless Steel Sample. Vertical Scale = $10.16 \times 10^{-6} m$

Appendix G

Computer Code and Implementation

The formulations of the profile, Navier-Stokes and convection-diffusion equations described in Chapter 4 were solved using a FORTRAN-77 program in double precision on an IBM RISC/6000 Model 320. Computational times varied from several minutes to several hours depending upon the shape of the rivulet profile and the flow distance being simulated.

The flowsheet for the computer code is illustrated in Figure G.1. The structure of the program was that of a main program which accessed the code contained in four subroutines. Each of these subroutines performed a separate task, and when fully integrated, led to the simulated results presented in this study.

The subroutine CURVE contains the code which solved the equations for the rivulet profile. This section also located the points of intersection of the constant η -lines with the free interface of the surface and the volumetric flow rate for the simplified rivulet model.

The subroutine INIT was used to construct the computational grid using the graphical construction technique described in Section 4.2.1. Calculation and output of the metric coefficients was done in this subroutine.

FLOWP was the subroutine in which the z -momentum Navier-Stokes equation was solved using Gauss-Seidel successive over-relaxation.

Finally, CONCP was used to solve the convection-diffusion equation using the method of Crank-Nicolson. Output of the grid points, velocity and concentration profile was done from within this subroutine.

The input file for the program is as shown in Table G.1.

G.1 Generation of Theoretical Results

The theoretical results required to compare with the experimental data were rivulet width and height versus volumetric flow rate. In order to generate these types of results, the appropriate values of the plate inclination, α , and contact angle, θ , were inputted and the logarithm of the value of the curvature at the apex of the rivulet, $\text{Log}_{10}B$, was varied to generate different size profiles with correspondingly different flow rates as determined from the solution of the Navier-Stokes equation inside each profile. Each theoretical result, therefore, has its own unique set of values of width and height versus flow rate.

```

Files to which to read output
    'riv.dat', 'riv.xy', 'riv.flow', 'riv.dn'
    'riv.met', 'riv.conc', 'riv.err'
Angle of inclination of flow plate, degrees
    45
Log of the radius of curvature of the rivulet at the apex
    0.05
Contact angle of the liquid, degrees
    46
Liquid Properties: Density (kg/m3), Kinematic Viscosity (m2/s)
    Surface Tension (N/m), Diffusivity (m2/s)
    998.23,1.004E-6,72.75E-3,1.77E-9
Saturation concentration of CO2 in H2O (kmol/m3)
    3.68E-2
Grid size, XI direction (M), ETA direction (N)
    31,51
Simulated flow distance (m), step size (m), rate of step size
    increase, and maximum step size (m)
    0.368, 1E-7, 1.1, 1E-3
Printing interval for Sherwood and Reynolds numbers.
    Print every PIDN'th value
    10.0
Overrelaxation factors, WX,WY,WU
    1.3,1.3,0.8
Iteration tolerance, TOLXY,TOLU,TOLC
    1.0E-3,1.0E-4,1.0E-6
Maximum iterations allowed, MITER,MXY,MITERU,MITERC
    500,10000,10000,500
Calculate velocity (IFLOWP=1) or read from file (IFLOWP=0)
    1

```

Table G.1: Input File for Computer Code

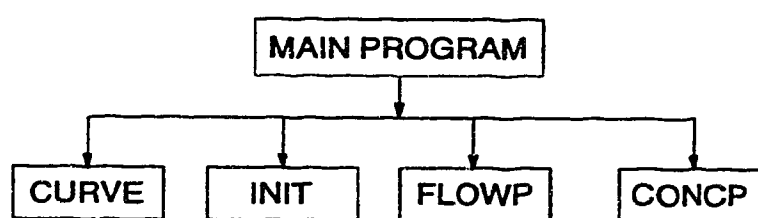


Figure G.1: Flowsheet Structure for Computer Code